

MRI methods for the planning and evaluation of High Intensity Focused Ultrasound tumor treatment

Citation for published version (APA):

Hectors, S. J. C. G. (2015). *MRI methods for the planning and evaluation of High Intensity Focused Ultrasound tumor treatment*. [Phd Thesis 1 (Research TU/e / Graduation TU/e), Biomedical Engineering]. Technische Universiteit Eindhoven. <https://doi.org/10.6100/IR783134>

DOI:

[10.6100/IR783134](https://doi.org/10.6100/IR783134)

Document status and date:

Published: 13/01/2015

Document Version:

Publisher's PDF, also known as Version of Record (includes final page, issue and volume numbers)

Please check the document version of this publication:

- A submitted manuscript is the version of the article upon submission and before peer-review. There can be important differences between the submitted version and the official published version of record. People interested in the research are advised to contact the author for the final version of the publication, or visit the DOI to the publisher's website.
- The final author version and the galley proof are versions of the publication after peer review.
- The final published version features the final layout of the paper including the volume, issue and page numbers.

[Link to publication](#)

General rights

Copyright and moral rights for the publications made accessible in the public portal are retained by the authors and/or other copyright owners and it is a condition of accessing publications that users recognise and abide by the legal requirements associated with these rights.

- Users may download and print one copy of any publication from the public portal for the purpose of private study or research.
- You may not further distribute the material or use it for any profit-making activity or commercial gain
- You may freely distribute the URL identifying the publication in the public portal.

If the publication is distributed under the terms of Article 25fa of the Dutch Copyright Act, indicated by the "Taverne" license above, please follow below link for the End User Agreement:

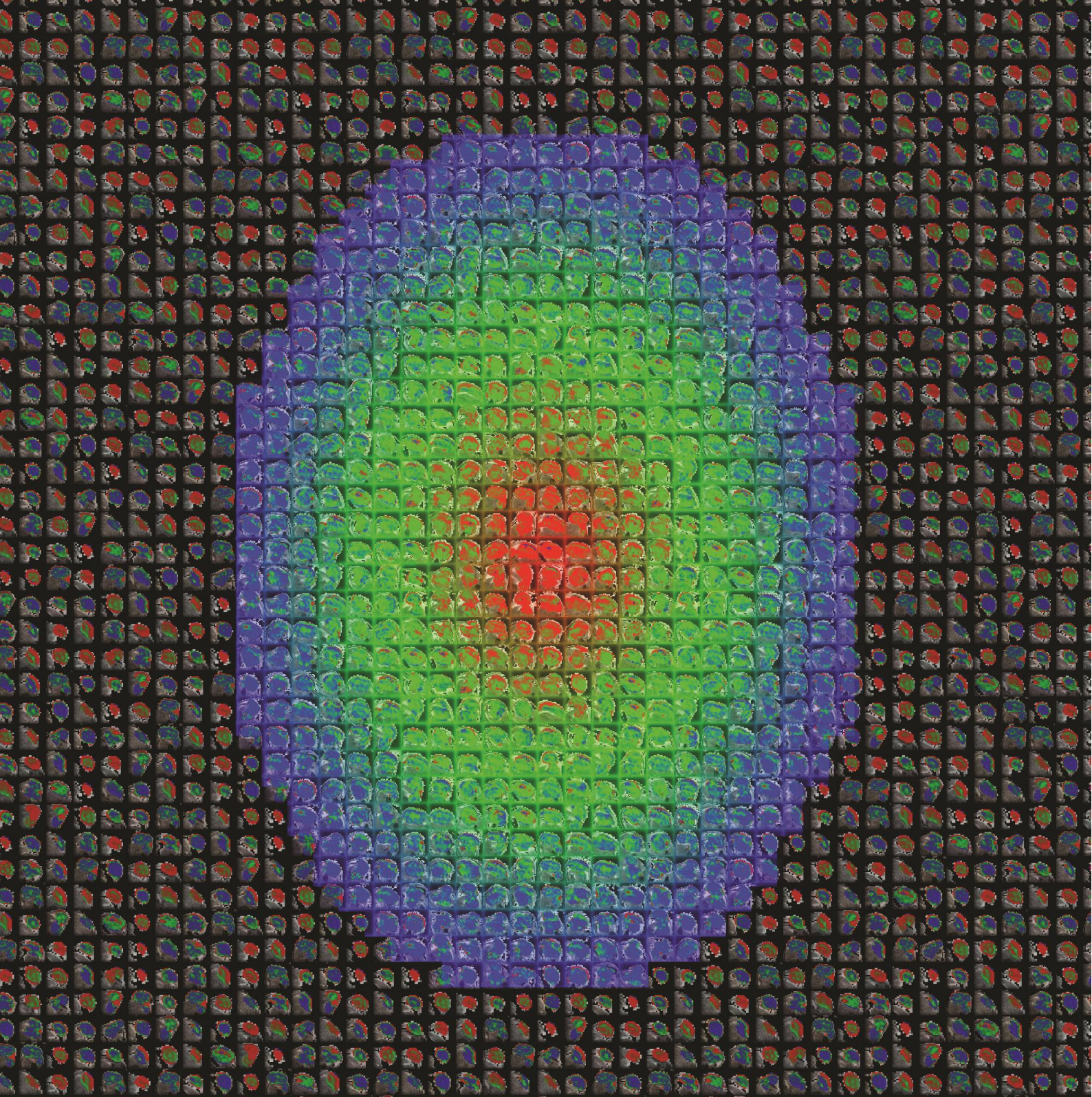
www.tue.nl/taverne

Take down policy

If you believe that this document breaches copyright please contact us at:

openaccess@tue.nl

providing details and we will investigate your claim.



MRI methods for the
planning and evaluation of
High Intensity Focused Ultrasound
tumor treatment

Stefanie Hector

**MRI methods for the
planning and evaluation of
High Intensity Focused Ultrasound
tumor treatment**

Stefanie Hectors

Financial support by Philips Research and KR Analytical for the publication of this thesis is gratefully acknowledged.

This research was performed within the framework of the Center for Translational Molecular Medicine, project VOLTA (grant 05T-201).

A catalogue record is available from the Eindhoven University of Technology Library.

ISBN: 978-90-386-3755-6

Cover design: Stefanie Hectors

Printed by: Ipskamp Drukkers

Copyright © Stefanie Hectors, 2014

MRI methods for the planning and evaluation of High Intensity Focused Ultrasound tumor treatment

PROEFSCHRIFT

ter verkrijging van de graad van doctor aan de Technische Universiteit
Eindhoven, op gezag van de rector magnificus prof.dr.ir. C.J. van
Duijn, voor een commissie aangewezen door het College voor
Promoties, in het openbaar te verdedigen op dinsdag 13 januari 2015
om 16.00 uur

door

Stefanie Jacoba Cornelia Geertruda Hectors

geboren te Roosendaal

Dit proefschrift is goedgekeurd door de promotor en de samenstelling van de promotiecommissie is als volgt:

voorzitter:	prof. dr. ir. F.P.T. Baaijens
promotor:	prof. dr. K. Nicolay
copromotor:	dr. ir. G.J. Strijkers
leden:	prof. dr. W. Gedroyc (Imperial College London)
	dr. U.A. van der Heide (NKI)
	prof. dr. J.P.W. Pluim
	prof. dr. H.W.M. van Laarhoven (UvA)
	prof. dr. C.T.W. Moonen (UU-UMC)

Contents

Chapter 1 General introduction	9
Chapter 2 Automatic Segmentation of Subcutaneous Mouse Tumors by Multiparametric MR Analysis based on Endogenous Contrast	31
Chapter 3 Multiparametric MRI Analysis for the Identification of High Intensity Focused Ultrasound-treated Tumor Tissue.....	51
Chapter 4 Amide Proton Transfer Imaging of High Intensity Focused Ultrasound-treated Tumor Tissue.....	77
Chapter 5 $T_{1\rho}$ Mapping for the Evaluation of High Intensity Focused Ultrasound Tumor Treatment	95
Chapter 6 Cluster analysis of DCE-MRI-derived pharmacokinetic parameters to identify regional vascular changes after tumor treatment with High Intensity Focused Ultrasound	113
Chapter 7 Multiparametric Magnetic Resonance Imaging analysis for the evaluation of Magnetic Resonance-guided High Intensity Focused Ultrasound treatment.....	137
Chapter 8 General discussion and future directions	169
Summary	178
Glossary of abbreviations and acronyms	180
List of publications	182
Acknowledgements / dankwoord	185
Curriculum Vitae	188

Chapter 1

General introduction

Based on:

Stefanie Hectors, Igor Jacobs, Chrit Moonen, Gustav Strijkers, Klaas Nicolay

MRI methods for the evaluation of High Intensity Focused Ultrasound tumor treatment –
current status and future needs

Under review

Magnetic Resonance-guided High Intensity Focused Ultrasound

Thermal ablation using High Intensity Focused Ultrasound (HIFU) allows for non-invasive tumor treatment by selective tissue heating. The first therapeutic trial with focused ultrasound beams dates back to the 1940s (1). The therapeutic application of focused ultrasound was initially restricted to the treatment of neurological disorders, such as Parkinson's disease. The Fry brothers were the first to report successful HIFU-induced local lesions in the central nervous system (2). Tumor treatment using HIFU was introduced in the 1970s (3). Since then, major technical advancements in HIFU set-ups have accelerated the clinical introduction of cancer therapy using HIFU. Nowadays, HIFU is applied for the treatment of a large range of tumor types, including uterine fibroids (4,5) and prostate (6-9), breast (10,11), liver (12-14) and bone (15) tumors. Particularly for treatment of malignant lesions, it is of key importance that the HIFU procedure can be accurately planned, monitored and evaluated. HIFU is therefore commonly performed under image guidance, either by ultrasound (US) or magnetic resonance imaging (MRI). While US is more time- and cost-effective than MRI, the use of MRI guidance seems preferred. Although multiple techniques for US real-time thermometry have been developed, e.g. based on the temperature dependence of the ultrasound propagation velocity (16), MR thermometry that uses the linear relationship between temperature increase and the proton resonance frequency shift (17) allows for a more accurate estimation of the temperature during the HIFU procedure. The dynamic temperature profile can be used to determine the thermal dose that was delivered to the tissue. A thermal dose of 240 equivalent minutes (EM) is generally considered as the threshold for complete cell death. However, the thermal sensitivity may vary between species and organs, which implies that the thermal dose threshold is dependent on tissue type (18,19). In addition, the effects of HIFU are not only based on heating. Depending on the settings, mechanical effects, such as cavitation and radiation forces, may also induce damage (20). Apart from direct effects of the combined thermal and mechanical damage to the tissue, such as those leading to coagulative necrosis, HIFU also causes initially sublethal tissue changes that may become fatal at a later time point after treatment (21). Therefore, for complete assessment of the success of the HIFU procedure, next to treatment monitoring, also extensive evaluation of the intervention should be performed. MRI offers a large variety of distinct contrast mechanisms that are sensitive to different effects of the HIFU treatment. Ideally, the MR protocol should be highly sensitive to acute tissue changes to allow for accurate evaluation of HIFU treatment effects directly after the intervention. If residual viable tumor tissue is detected, immediate re-treatment could eventually be performed, which would minimize the number of required hospital visits and maximize long-term outcome for the patient. Next to HIFU, also other methods, such as chemotherapy or radiotherapy, could be used as adjuvant therapy to treat residual tumor tissue after HIFU. Extensive MRI evaluation of the HIFU treatment would then also allow for localization and characterization of the residual tumor tissue and thereby aid in the planning of the adjuvant therapy. Multiple MRI methods have been assessed previously for their suitability for the evaluation of HIFU cancer treatment. While several of these

methods seem promising regarding their sensitivity to HIFU-induced changes, there is ample room for improvement of MRI-based HIFU treatment evaluation. In this chapter, the major effects of thermal treatment with HIFU are discussed. In addition, MRI methods that could detect these effects are discussed. At the end of the chapter, future directions with respect to MRI methods for the evaluation of HIFU treatment are discussed.

Basic principle of HIFU treatment

During the HIFU procedure, ultrasound waves generated by a therapeutic transducer are focused into a very small volume, which greatly increases the intensity of the sound waves and thereby induces energy deposition in the target tissue. The energy that is absorbed by the tissue in the focal point of the transducer generates heat that can cause immediate coagulative necrosis in the tissue. Typically, treatment schemes are designed in such way that the tissue temperature rapidly increases to approximately 60 °C (22). As stated above, next to thermal effects, HIFU may also, depending on the settings, have a substantial mechanical influence on the tissue. One of these mechanical effects is cavitation, during which small gas bubbles in the tissue will start to grow and oscillate under the influence of the varying acoustic pressure during HIFU sonication. During inertial cavitation, these oscillating bubbles can eventually collapse, which leads to cell destruction and local high temperatures. Another mechanical effect of HIFU involves the generation of acoustic radiation forces. When ultrasound is applied at relatively high intensities, non-linear acoustic conditions may occur. Under these conditions, momentum can be transferred from the ultrasound waves to the tissue, which generates a unidirectional force, which is known as a radiation force. These radiation forces can induce local displacements of tissue in the focal point of the transducer (20,23). Repetitive displacements may lead to structural damage changes in the tissue, through the development of local strains (24).

The focal point of the HIFU transducer can, either manually or electronically, be steered to allow for volumetric ablation of the tumor. The ablated lesion present after HIFU treatment generally consists of three zones: the central zone located in the target volume that undergoes immediate coagulative necrosis; the peripheral zone that was subjected to hyperthermia due to thermal conduction from the central zone; and the surrounding tissue that was not affected (21). A schematic drawing of the different tissue zones after HIFU treatment is shown in Figure 1.

In the next paragraphs, the acute and delayed treatment effects in the central and peripheral zones are described. In addition, MRI methods that could provide imaging biomarkers for the treatment effects will be addressed. An overview of these treatment effects and the MRI methods that have been or could be used to detect these is listed in Table 1.

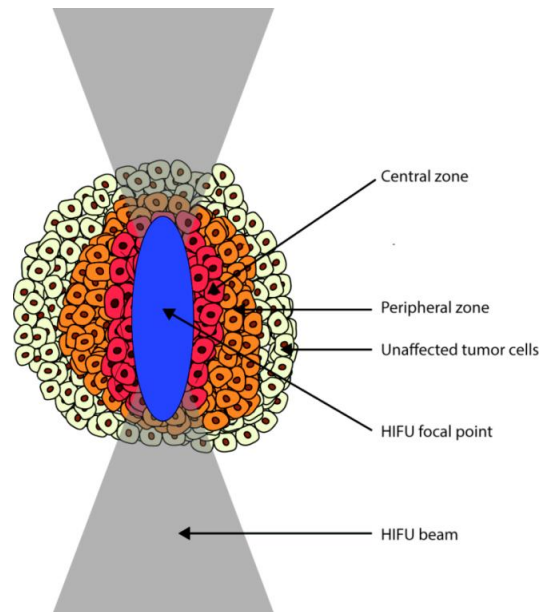


Figure 1. Schematic representation of the presence of a central zone of coagulative necrosis, a peripheral zone and a zone of unaffected tumor tissue after HIFU treatment of tumor tissue.

Table 1. Overview of acute and delayed HIFU treatment effects and the MRI methods that have been or could be used to detect the treatment effects. ↑ and ↓ indicate an increase and decrease in the measured parameter after HIFU treatment, respectively. ≈ indicates an absent or heterogeneous change in the parameter. - indicates that there are no studies published (yet) in which the referred MRI method was used to evaluate thermal treatment.

Acute treatment effects			Delayed treatment effects		
Effect	MRI method	Findings	Effect	MRI method	Findings
Protein denaturation and aggregation	MT imaging APT imaging T _{1ρ} mapping MR elastography	MTR ↑(25-27) chapter 4, 7 chapter 5, 7 Stiffness ↑(ex vivo) (28,29) and ↓ (in vivo) (28) Signal intensity ↑ (30)	Inflammatory response and edema formation	Macrophage imaging with nanoparticles T _{2w} imaging	- Edema extent ↑ in first 2 days, then ↓ (31) K ^{trans} ↑ (32)
	CE-MRI upon MS-325 injection			DCE-MRI	
Damage of cellular and nuclear membranes	ADC mapping ²³ Na MRI	ADC ↑ (27,33,34) and ↓ (35-38) Signal intensity ↑ (36)	Ischemia and latent cell death due to vascular damage	(D)CE-MRI APT imaging BOLD MRI ADC mapping Hyperpolarized ¹³ C	Presence NPV (39-42) chapter 4, 7 - ADC ↑ (27,43) -
Halted metabolism	¹ H MRS Hyperpolarized ¹³ C	[choline+creatine]/citrate ↓ (44) -			
Vascular collapse and hemorrhage	CE-MRI	Presence NPV (4,7,34,36,39,43,45-53) K ^{trans} ↓ (32,40,54,55), v _e ↓ and ↑ (32,40,55) Signal intensity ≈ (33,34) and ≈/↑ (56,57) T ₁ ↓(27) Signal intensity ≈ (7,47,56,57) T ₂ ↑ (34) and ≈ (27,34)	Apoptosis	ADC mapping Hyperpolarized ¹³ C	ADC ↑ (27,43) - -
	DCE-MRI				
	T _{1w} imaging				
	T ₁ mapping T _{2w} imaging				
Hyperaemia	T ₂ mapping			CE-MRI after injection of PS-targeting contrast agents	
	CE-MRI	Enhancing rim (7,34,43,45-51) K ^{trans} ↑, v _e ↑ (55)			
	DCE-MRI ASL IVIM	- - -			

Acute treatment effects

A schematic overview of the acute HIFU treatment effects, for which MRI might provide imaging readouts is given in Figure 2 for the central and the peripheral zone. In the central zone, direct cell death occurs due to a combination of different effects, including protein denaturation, affected cell membrane integrity, structural changes inducing mitochondrial dysfunction and inhibition of DNA replication (21). The major acute effects that are potentially detectable by MRI are protein denaturation and aggregation, damage of cellular and nuclear membranes, halted metabolism and vascular collapse and hemorrhage (21,55,58). In the peripheral zone, there could be a temporarily increased blood flow (hyperaemia) and halted/impaired metabolism due to hyperthermic conditions (21). Furthermore, the permeability of the vascular endothelium could be altered in this area, because hyperthermia can induce reversible morphological changes to the endothelial cell cytoskeleton, which may result in changes in the endothelial cell lining (59).

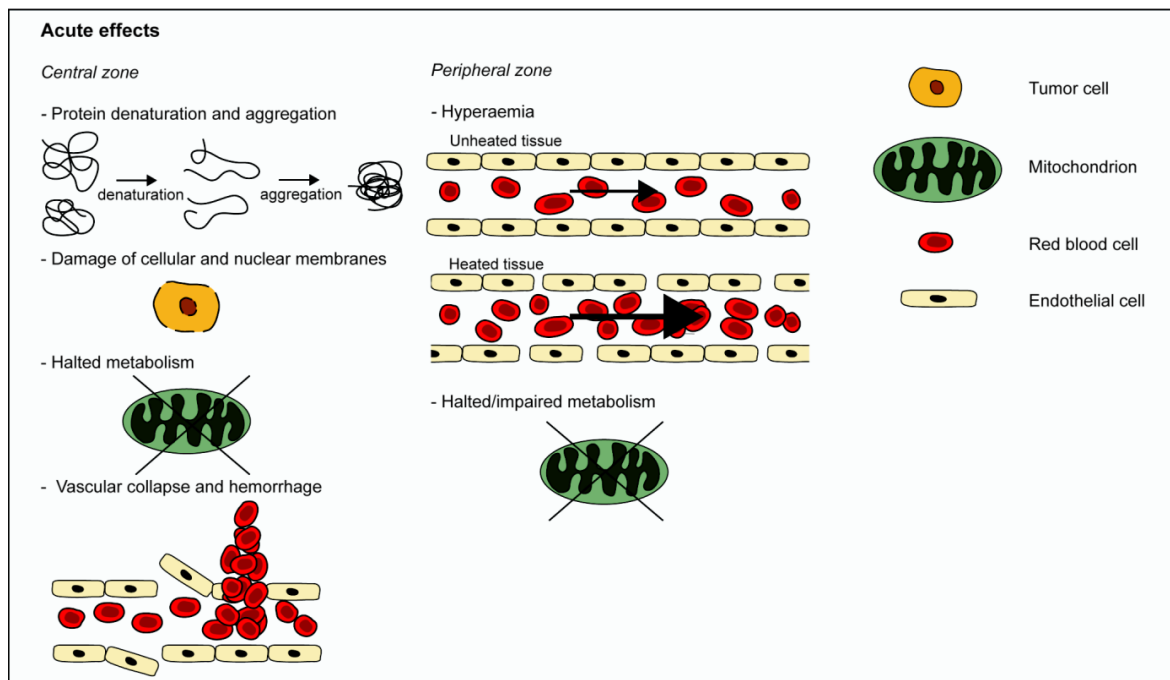


Figure 2. Schematic drawing of acute HIFU treatment effects in the central and peripheral zone. For detailed explanation see text.

Protein denaturation and aggregation

The high temperatures reached during HIFU treatment lead to instant protein denaturation in the central zone. In addition, protein aggregation may eventually occur due to interactions between hydrophobic sites on the unfolded proteins (60,61). Extensive protein denaturation is immediately cytotoxic and leads to coagulative necrosis (21). Different MRI parameters that are considered directly sensitive to the presence of (denatured) proteins have been studied for their suitability for the evaluation of HIFU treatment. In several studies the effect of HIFU on the magnetization transfer ratio (MTR) was assessed. The

MTR is a measure for the level of magnetization exchange between protons of mobile water molecules and protons associated with semi-solid macromolecules, such as structural proteins (62). In *in vivo* magnetization transfer (MT) measurements on mouse subcutaneous tumors (27) an MTR increase was observed directly after HIFU application. Carasso et al. developed an MT-based MRI method, named magnetization exchange imaging (MEXI), that is more directly sensitive to the magnetization exchange rate than a conventional MT experiment (25). They observed an increase in the magnetization exchange after HIFU treatment of rat muscle, which may be interpreted as an MTR increase. This apparent MTR increase is consistent with MT measurements after HIFU treatment of *ex vivo* porcine muscle (26), while an MTR decrease was observed after thermal treatment of different *ex vivo* tissues (63). The MTR decrease in the latter study was explained by protein denaturation, while the generally observed MTR increase might be caused by increased access of water molecules to semi-solid macromolecules due to membrane disruption. The MTR is thus sensitive to multiple HIFU treatment effects and therefore not uniquely specific to protein denaturation. An MRI method that is potentially more specifically sensitive to protein denaturation is amide proton transfer (APT) imaging (64). APT imaging employs the saturation transfer between water protons and amide protons of mobile protein/peptide backbones. The contrast in APT-weighted images is dependent on both the concentration of amide protons as well as the exchange rate. It is expected that HIFU-induced protein denaturation and aggregation strongly influence the accessibility of water molecules to the amide-proton-rich protein backbones, which consequently alters the saturation transfer between the water and amide protons and thereby the observed APT-weighted signals. Another MRI parameter of interest to study protein denaturation is $T_{1\rho}$. $T_{1\rho}$ is a measure for the decay of magnetization in the transverse plane during a spin-lock pulse that is applied parallel to the magnetization vector. $T_{1\rho}$ is sensitive to interactions between water molecules and macromolecules that occur around the carrier frequency of the applied spin-lock pulse. Tissue $T_{1\rho}$ values are predominantly influenced by protein-water interactions (65). While APT measurements are sensitive to the relatively slowly exchanging amide protons in tissue, on-resonance $T_{1\rho}$ measurements are mainly sensitive to fast exchanging protons. $T_{1\rho}$ mapping may thus provide complimentary information on the thermally denatured tissue compared to APT imaging.

An MRI method that has been used to probe HIFU-induced protein denaturation and aggregation indirectly by quantification of HIFU-induced tissue stiffness changes is MR elastography (MRE), which measures tissue stiffness by imaging of the propagation of mechanical waves (66). HIFU treatment introduces major structural changes to tissue and it was hypothesized that particularly protein denaturation and aggregation increase tissue stiffness. *Ex vivo* MRE studies on thermal treatment of bovine muscle tissue (29) and on HIFU treatment of turkey breast (28) confirmed that tissue stiffness increased after treatment. HIFU treatment of *in vivo* rat brain rather resulted in tissue softening directly after and up to at least 3 weeks after treatment, which was attributed to the presence of

edema. These results suggested that tissue elasticity is more sensitive to edema than to tissue necrosis (28).

Vogel et al. demonstrated that MS-325 may be a suitable MR contrast agent for the characterization of coagulated tumor tissue after laser ablation (30). MS-325 is a contrast agent that binds to serum albumin and it has previously been shown that coagulation induces a conformational change to serum albumin, which facilitates improved binding of the contrast agent (67). In addition, the binding of MS-325 to albumin increases the relaxivity of the contrast agent (68). A pronounced signal intensity increase was observed on T_1 -weighted images during and after laser thermal treatment of pig muscle in the presence of MS-325, while the signal intensity decreased in the presence of gadolinium (Gd)-DTPA and in absence of contrast agent. This suggests that MS-325 can indeed be used to image tissue coagulation. A potential disadvantage of this method is that it requires presence of contrast agent during treatment, which could induce entrapment of Gd^{3+} in the tissue with a toxicity hazard and errors in MR thermometry (69,70).

Damage of cellular and nuclear membranes

The thermal and mechanical effects of HIFU may disrupt the cellular and nuclear membranes of cells. The apparent diffusion coefficient (ADC), which is a measure of the diffusion of water molecules in tissue, could serve as a sensitive readout for membrane damage as this disruption in the membranes is expected to increase the ADC. Indeed, an increase in ADC was measured after thermal treatment of various ex vivo tissues (63). The effect of HIFU treatment on the tissue ADC has also been studied quite extensively in vivo, both in preclinical (27,33,34,71,72) and clinical studies (35-38,43). Similar to the ex vivo study an ADC increase was observed instantly after HIFU treatment of subcutaneous mouse tumors (27,33,34) and muscle tissue (33). In contrast, a decrease in ADC was found directly after treatment of uterine fibroids (35-38) (Figure 3A). The ADC decline was attributed to cytotoxic edema, which is caused by dysfunction of the cell membrane and is associated with cell swelling (36). Apparently, the change in ADC after the HIFU intervention is dependent on tissue type. In addition, also treatment settings likely influence the observed ADC contrast directly after HIFU. If the combined mechanical and thermal effects are large enough to induce substantial damage to the cell membranes, the ADC will probably increase upon HIFU treatment. However, if the treatment is applied in a more subtle manner, the cell membrane integrity may be maintained, which allows for the formation of cytotoxic edema and subsequently leads to an ADC decline. The observed bidirectional effects of HIFU on the ADC could hamper the interpretation of ADC maps early after treatment.

An alternative MRI method that is directly sensitive to cell membrane dysfunction is sodium MRI, which allows for a quantitative measurement of the sodium concentration in tissue. Cells in healthy tissue maintain a large sodium concentration gradient (high extracellular concentration vs. low intracellular concentration), which is mainly controlled by the sodium-potassium pump (73). Alterations to cell membrane integrity may lead to

failure of the cells to maintain this sodium concentration gradient. In addition, the performance of the sodium-potassium pump may also be affected by the halted metabolism after HIFU treatment, since the exchange of sodium and potassium across the cell membrane is energy-dependent. As a consequence of the cell membrane damage, there will be an inflow of the sodium ions from the extracellular space and the blood pool, resulting in higher sodium concentrations in the affected tissue. This increased sodium concentration can potentially be detected with sodium MRI. Jacobs et al. have performed preliminary sodium MRI measurements after HIFU treatment of uterine fibroids (36). They observed a pronounced increase in the signal intensity of the sodium MR images (Figure 3), which suggested that the HIFU-induced loss of cell membrane integrity can indeed be probed with sodium MRI.

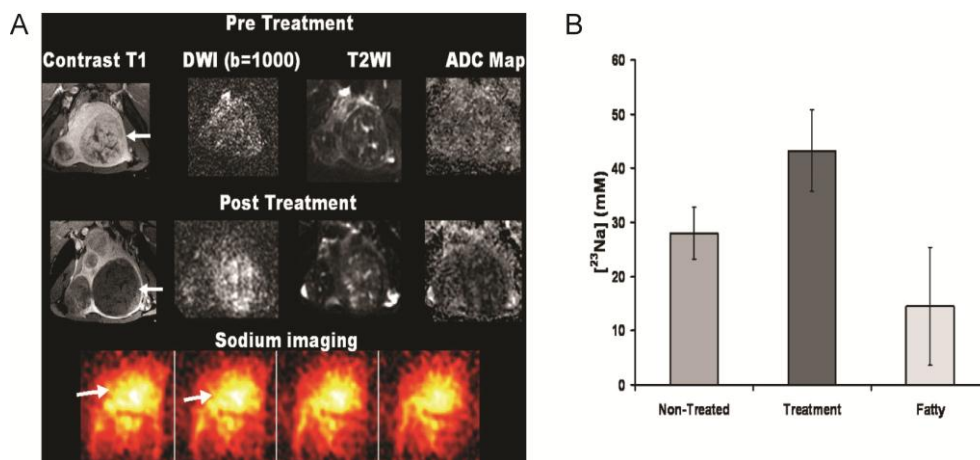


Figure 3. A) Contrast-enhanced T_1 -weighted image, diffusion-weighted image, T_2 -weighted image and quantitative ADC map of a uterine fibroid before and after HIFU treatment. Lack of perfusion and a decreased ADC were observed after therapy. At the bottom of the figure, sodium MR images obtained after treatment are displayed. These showed a marked increase in sodium concentration compared to baseline measurements. B) Sodium concentrations obtained from sodium MR acquisitions in non-treated uterine fibroid, treated fibroid and fatty tissue, showing an increase in sodium concentration in the treated fibroids compared to non-treated fibroids. Adapted with permission from (36).

Halted metabolism

The protein denaturation in the central zone of coagulation directly affects the cellular metabolism, which depends on enzymatic activity. In addition, the hyperthermic conditions in the peripheral zone may also partly impair the metabolism in that zone, since exposure to temperatures of approximately 43°C has shown to promote the leakage of protons through the inner mitochondrial membrane, which induces mitochondrial dysfunction (21,74). Changes in metabolism may be probed by MR spectroscopy (MRS). It has previously been shown that ^1H MRS is a potentially suitable method to detect residual tumor tissue at several months after HIFU treatment of prostate cancer (44). Due to the difference in metabolism, successfully treated tumor tissue generally has a lower [choline+creatine]/citrate ratio than residual tumor tissue, determined by proton MRS. Although there are no reports on ^1H MRS directly after HIFU treatment, it is expected that this technique is also suited for the direct assessment of HIFU therapy, since the

metabolic changes occur instantly during treatment. Another metabolite of interest that can be measured by ^1H MRS is lactate. As opposed to healthy cells that metabolize glucose via the citric acid cycle and subsequent oxidative phosphorylation, glucose in highly proliferating tumors is primarily metabolized by aerobic glycolysis which produces lactate (75,76). Lactate may thus be a suitable biomarker to distinguish between metabolically arrested treated tumor tissue and normally metabolizing residual tumor tissue after HIFU treatment, provided that lactate present in the tumor tissue before treatment does not become entrapped in the coagulated tissue. However, clinical utility of ^1H MRS for the measurement of lactate is hampered by low lactate concentrations, even in high-grade prostate tumors (77). For detection of such low concentrations, a relatively coarse spatial resolution of this particular MRS method, as well as for MRS methods in general, is often unavoidable, which would limit the sensitivity of MRS for the detection of local spots of residual tumor tissue after HIFU treatment. A promising technique for sensitive detection of tumor-associated metabolic activity is hyperpolarized ^{13}C MR. Hyperpolarization of ^{13}C -enriched substrates alters the Boltzmann distribution of spins, which drastically ($>10^4$ fold) increases the sensitivity for detection of these substrates and the products of metabolic conversions (78). Recently, Rodrigues et al. have shown that hyperpolarized ^{13}C MR allows for real-time imaging of the glycolytic flux of injected ^{13}C -labeled glucose into lactate (79). This technique may become very suitable for the detection of early tumor response to various treatments, including HIFU therapy. Another metabolism-sensitive ^{13}C hyperpolarized MR method that has shown promising results for the early detection of tumor necrosis employs the production of ^{13}C -labeled malate from intravenously administered ^{13}C -labeled fumarate, both of which are intermediates in the citric acid cycle. The production of labeled malate increases in a binary fashion during the onset of necrosis, due to increased access of fumarate to the enzyme fumarase that catalyzes the reaction from fumarate to malate (80). This enhanced access of fumarate is caused by higher permeability of the cellular membrane due to necrosis. This technique can be used to detect necrosis after anti-angiogenic tumor therapy (81). However, its suitability for the detection of the coagulative necrosis in the central zone instantly after thermal treatment seems questionable, since it requires uncompromised functioning of the fumarase enzyme, while thermal treatment will likely induce denaturation of this enzyme. This method could however be suitable for the detection of delayed necrosis in the peripheral zone (see section Delayed treatment effects).

Vascular collapse and hemorrhage

Similar to tumor cells, tumor blood vessels also undergo coagulative necrosis during thermal ablation. Histological analysis of HIFU-treated solid malignancies in patients confirmed severe damage to the tumor vasculature (58). This vascular damage causes impaired blood flow and potentially also hemorrhage. For the identification of the impaired blood flow commonly contrast-enhanced MRI (CE-MRI) is employed, which is by far the mostly used MR method for the evaluation of HIFU treatment. The CE-MRI methods generally consist of two T_1 -weighted acquisitions, one before and one after injection of a low-molecular weight Gd-based contrast agent. The region of coagulated tissue is then

characterized by a lack of signal enhancement after injection and referred to as the non-perfused volume (NPV). In several studies, the NPV was quantitatively compared to the estimated treatment volume derived from the temperature maps and to the necrotic volume from histopathology. Directly after HIFU treatment, the NPV was generally larger than the estimated treated volume (4,38,39,52,53), probably caused by destruction of large blood vessels that perfuse tissue outside the HIFU-treated volume. In addition, histopathological analysis of HIFU-treated rabbit tumors showed that the NPV underestimated the extent of necrosis early (up to 3 days) after treatment (39). In contrast, an overestimation of the extent of non-viable tumor tissue by the NPV was observed directly after HIFU treatment of subcutaneous tumors (40). These findings suggest that care must be taken with the interpretation of CE-MRI performed directly after HIFU treatment. Moreover, the NPV is often surrounded by an enhancing rim (7,34,43,45-51,82). An example of a contrast-enhanced T_1 -weighted image showing an enhancing rim around the HIFU-treated breast tumor is displayed in Figure 4. This enhancing rim has been attributed to hyperaemia in the peripheral zone (47), but also to residual tumor tissue. At later time points after treatment, also inflammation and fibrotic tumor tissue may contribute to this peripheral enhancement (7). The presence of this enhancing rim is another factor that complicates the interpretation of CE-MRI images obtained after HIFU treatment.

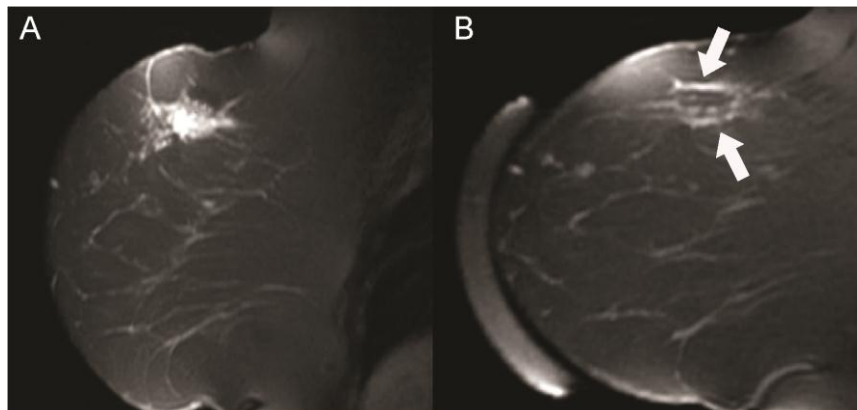


Figure 4. Sagittal contrast-enhanced T_1 -weighted image of a differentiated invasive ductal carcinoma before (A) and 3 days after (B) HIFU treatment. After treatment, a rim of contrast enhancement (white arrows) was observed around the treated lesion. Adapted with permission from (82).

DCE-MRI may have additional value for the evaluation of HIFU treatment compared to conventional CE-MRI. In DCE-MRI the signal intensity is measured dynamically before, during and after injection of a contrast agent. Quantitative analysis of the DCE-MRI data can be performed by pharmacokinetic modeling. With the widely applied Standard Tofts model the transfer constant K^{trans} and the extravascular, extracellular volume fraction v_e can be estimated (83). A few studies have performed pharmacokinetic modeling of DCE-MRI data from HIFU-treated tissue. A significant decrease in tumor K^{trans} was reported after HIFU treatment of subcutaneous rat tumors (54). Cheng et al. performed an extensive analysis of the K^{trans} and v_e values in the tissue surrounding the central zone upon ablation of rabbit skeletal muscle tissue (32,55) (Figure 5). After HIFU, the central

zone was characterized by low K^{trans} and low v_e values. Adjacent to this zone, a region of low K^{trans} and high v_e was observed, which was associated with structural disruption, vascular congestion, hemorrhage and vacuolation. A tissue region located further away from the central zone was characterized by higher K^{trans} and v_e , caused by edema, hyperaemia, mild inflammation and increased vascular permeability. To the best of our knowledge, there are no studies on HIFU-treated tumor tissue in which the distinct vascular changes in the regions surrounding the central zone of ablation were investigated by quantitative pharmacokinetic modelling of DCE-MRI data. Nevertheless, the above-mentioned study on muscle already shows that extensive pharmacokinetic analysis of DCE-MRI data gives improved insights in the vascular effects of HIFU treatment. Quantitative DCE-MRI analysis could aid in assessment of the consequences of the different vascular changes after HIFU for the microenvironment and fate of the tissue and the sensitivity of the tumor to additional therapies.

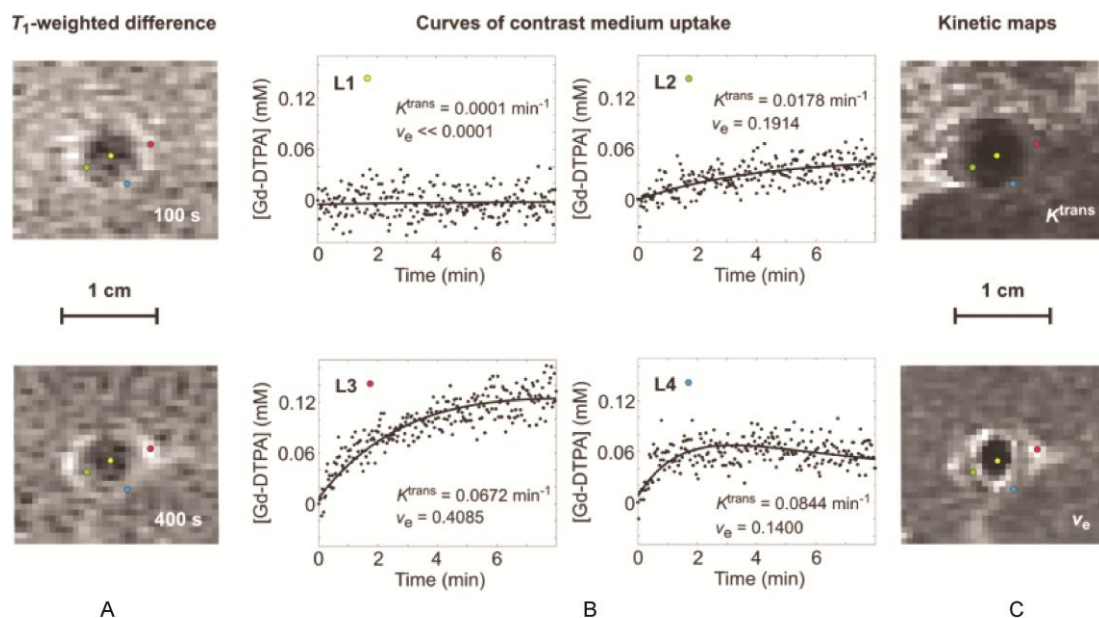


Figure 5. Dynamic tissue contrast agent (Gd-DTPA) concentration curves derived from DCE-MRI measurements performed after HIFU treatment of rabbit muscle tissue. A) Contrast-enhanced T_1 -weighted difference images at 100 and 400 s after bolus injection of Gd-DTPA. B) Dynamic Gd-DTPA concentration curves at select locations L1-L4 (indicated with the colored dots in the left and right images). The experimental data (dots) were fitted to the Tofts model (solid lines). The estimated parameter values for K^{trans} and v_e are shown bottom right in each graph. C) K^{trans} and v_e parameter maps. Adapted with permission from (55).

In addition to contrast-enhanced MRI, also a number of intrinsic contrast MRI parameters are sensitive to HIFU-induced changes to the tissue vasculature. For instance, the HIFU-induced damage to blood vessels can lead to hemorrhage that is associated with an increase in the concentration of paramagnetic deoxygenated hemoglobin, which influences the tissue T_1 and T_2 relaxation times. T_1 - and T_2 -weighted imaging have been used extensively for the evaluation of HIFU treatment. However, no consistent results have been reported. In preclinical studies of HIFU treatment of muscle (33) and subcutaneous tumors (34) no significant treatment-induced change in the T_1 -weighted

signal intensity was observed. In two clinical studies of HIFU treatment of uterine fibroids (56) and pancreatic cancer (57), the treated lesion appeared hyperintense on T_1 -weighted images. However, this hyperintense region was heterogeneous (56) and not seen in all cases (57). A significant decrease in T_1 was found after HIFU treatment of mouse subcutaneous tumors (27), which is consistent with hyperintensity on T_1 -weighted images. On T_2 -weighted images, a heterogeneous appearance of the HIFU-treated tissue was reported after treatment of uterine fibroids (56), prostate (7,47) and pancreatic (57) tumors. This is consistent with findings after HIFU treatment of mouse subcutaneous tumors, in which a broad range of T_2 values was observed in the HIFU-treated tumor tissue (27). Hundt et al. observed a significant increase in T_2 after HIFU treatment of mouse muscle tissue, while T_2 did not change significantly after treatment of subcutaneous tumors (34). The apparently conflicting results on T_1 and T_2 responses after HIFU treatment are probably caused by the fact that T_1 and T_2 are sensitive to multiple, possibly counteracting, effects of the HIFU intervention. Next to vascular damage, also other HIFU effects such as membrane disruption and protein denaturation/aggregation will affect the general tissue structure and thus T_1 and T_2 , leading to the reported heterogeneous changes in these parameters after HIFU treatment.

Hyperaemia

The hyperthermic conditions in the peripheral zone may cause a temporarily increased blood flow (hyperaemia). In preclinical tumor models, it is generally observed that the blood flow in this region indeed increases upon heating after which it gradually declines to pre-treatment values again. However, in human tumors there seems to be no such clear unidirectional effect of hyperthermia on tumor blood flow (84). Apart from the influence of tumor type, the effect of hyperthermia on blood flow is strongly dependent on the temperature and the duration for which the tissue was exposed to this temperature. Similar to the vascular damage in the central zone, the effect of hyperthermia on the blood flow in the peripheral zone could be probed with (D)CE-MRI. On CE-MRI images, hyperaemia can be observed as an enhancing rim around the central ablation volume. However, as discussed earlier, residual tumor tissue could also contribute to this peripheral enhancement. DCE-MRI may allow for better characterization of hyperaemic effects and possibly also for quantitative estimates of changes in blood flow and vascular permeability. As indicated above, Cheng et al. observed a hyperaemic region with high K^{trans} and v_e around the central ablation volume (55). Quantification of the hyperaemic effect may be particularly interesting if one would like to exploit this effect for example for the stimulation of local delivery of chemotherapeutic agents (85,86). Adjuvant chemotherapy could be performed after HIFU treatment to treat residual tumor tissue present at the ablation margins (87). DCE-MRI has been used previously to measure tumor perfusion after hyperthermia (88). Importantly, the authors noted that for accurate quantification of the change in perfusion after hyperthermia one has to take into account that the arterial input function, which is needed for quantitative DCE-MRI analysis, also changes due to hyperthermia. Arterial spin labelling (ASL) may be another suitable MR method for direct measurement of the tumor perfusion after HIFU treatment. In ASL

experiments, proximal labeling of arterial water spins is applied, which, after a certain transit time, leads to a perfusion-dependent decline in magnetization in the tissue of interest due to exchange of the tissue water spins with the labeled water spins (89). An alternative MRI method that could be employed for perfusion measurements is intravoxel incoherent motion (IVIM) imaging, which estimates both tissue perfusion and diffusion based on a series of diffusion-weighted acquisitions with low and high b-values (90). An advantage of ASL and IVIM imaging compared to (D)CE-MRI is that these methods do not require the injection of a contrast agent and therefore can be more readily combined with MRI guidance of HIFU and repeated at will to assess the dynamics of perfusion changes.

Delayed treatment effects

Delayed effects occurring at several days after HIFU treatment that are potentially detectable by MRI are illustrated in Figure 6. The HIFU treatment could lead to a systemic inflammatory response and formation of edema in and around the treated tumor. In addition, the vascular damage may result in ischemic conditions in tumor tissue outside the central ablation zone, which could eventually cause latent cell death (21). Heat stress in the peripheral zone during ablation may lead to apoptosis (91).

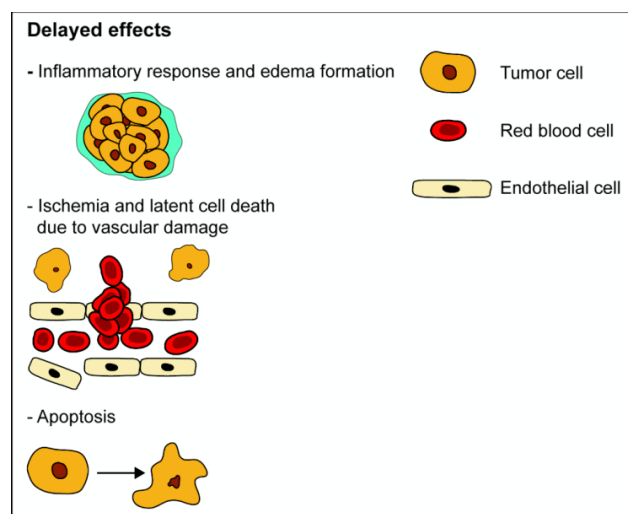


Figure 6. Schematic drawing of delayed HIFU treatment effects. Details are provided in the main text.

Inflammatory response and edema formation

In the process of tissue repair, the inflammatory activity in the ablated lesion will increase in the first days after HIFU treatment. After HIFU ablation of a rabbit tumor, a clear rim of neutrophilic granulocytes and macrophages was observed at day 1 and 3 after treatment. No signs of inflammation were visible in the central region of ablation (39). The macrophages may be visualized with MRI by the injection of nanoparticles, that are passively targeted to macrophages by employing the naturally high endocytotic activity of these inflammatory cells. Examples of nanoparticles that have been used for MRI detection of macrophages are iron oxide particles and ^{19}F MRI-detectable perfluorocarbon emulsions (92,93). Macrophage imaging with nanoparticles has been applied quite extensively in multiple pathologies, including cancer, atherosclerosis, myocardial infarction

and stroke (94). While probably not suitable for the direct visualization of inflammatory cells, intrinsic MRI contrast methods could be used for the detection of edema around the central ablation zone. This edematous tissue is associated with the inflammatory infiltration and can be visualized with MRI based on either T_2 or ADC contrast mechanisms because of the high-water and low-cellular content in edema. Mórocz et al. have followed the development of edema after HIFU ablation of rabbit brain tissue with T_2 -weighted images. The extent of peripheral edema increased during the first 2 days after treatment, after which it gradually decreased again during the next five days (31). Cheng et al. used DCE-MRI to assess delayed effects of HIFU treatment of rabbit thigh muscles. At 40 hrs and 3 days after treatment, a pronounced ring of inflammatory edema, that was characterized by high K^{trans} values, was observed around the central zone of ablation (32).

Ischemia and latent cell death due to vascular damage

The vascular damage induced by the HIFU treatment could lead to diminished oxygen and nutrient delivery to regions of tumor tissue extending beyond the central zone of ablation if the damaged vessels perfused these regions, leading to ischemic conditions in the peripheral zone. In the first days after HIFU treatment, the perfusion can be partially restored due to increased blood supply by peripheral blood vessels and the collateral circulation (91). In addition, HIFU-induced vascular occlusion can be transient and be followed by partial reperfusion of the ischemic tumor tissue (95). Similar to early after HIFU, the vascular status of the tumor tissue at a later stage after HIFU treatment can be assessed by (D)CE-MRI. It has been shown that the NPV derived from (D)CE-MRI measurements correlates better with the extent of tissue necrosis at later time points (>3 days) after treatment compared to directly after treatment (39,40). Also, strong correlations between semi-quantitative DCE-MRI parameters and the amount of residual tumor tissue have been reported at 3-14 days after treatment (41,42). Khiat et al. showed that the correlation between semi-quantitative DCE-MRI parameters and the amount of residual tumor tissue was highest at least 7 days after treatment (42). The mismatch between the extent of necrosis and the (D)CE-MRI findings early after treatment was explained by the influence of other treatment effects such as hemorrhage, edema, inflammation and fibrosis. Furthermore, also the transient vascular damage and latent cell death could negatively influence the accuracy of (D)CE-MRI for the early evaluation of HIFU.

To the best of our knowledge, there are no reports on the direct MR visualization of ischemia after HIFU treatment. Nevertheless, it is of high importance to detect hypoxic residual tumor tissue after HIFU treatment, since there may be a considerable risk of metastatic spread induced by hypoxia. Hypoxia could trigger the activation of the hypoxia inducible factors HIF-1 α and HIF-2 α , which may eventually lead to angiogenesis by increased expression of vascular endothelial growth factor (96,97). Subsequently, the residual tumor cells can migrate through the newly formed blood vessels, which may lead to tumor progression and the development of metastases. Several MRI methods exist that are potentially sensitive to HIFU-induced ischemia. The hypoxic conditions may for

example be imaged by blood oxygen level-dependent (BOLD) MRI. BOLD MRI has been used quite extensively to assess tumor tissue oxygenation (98). Preliminary data on BOLD MRI after chemotherapy of rat liver tumors (99) and human breast tumors (100) indicate that this technique may provide a suitable biomarker for the assessment of treatment response. Another method that is being used to assess ischemia during stroke is APT imaging. The decline in intracellular pH during ischemia produces contrast on APT-weighted images, because the chemical exchange between amide and water protons becomes slower when the tissue pH decreases (101-103).

The ADC is a promising MR biomarker for the detection of latent, ischemia-induced necrosis. Cell lysis that is associated with necrosis generally leads to elevated tissue ADC values. Indeed, an ADC increase has been observed at 1 week after HIFU treatment of human liver tumors (43) and at 3 days after treatment of mouse subcutaneous tumors (27). While less suitable for the detection of the direct coagulative necrosis (see above), hyperpolarized ^{13}C MR that employs the production of ^{13}C -labeled malate from intravenously injected ^{13}C -labeled fumarate could be a promising method for the detection of the latent ischemia-induced necrosis, since the functioning of the fumarase enzyme in the tissue outside the central zone of coagulation is likely not affected by the HIFU treatment. It has been reported that the increased production of ^{13}C -labeled malate occurs parallel to the onset of necrosis induced by anti-angiogenic therapy and precedes any change in tumor ADC (81). This suggests that hyperpolarized ^{13}C MR may allow for an earlier assessment of latent cell death after HIFU treatment compared to ADC measurements.

Apoptosis

Instead of necrosis, cells in parts of the peripheral zone may undergo apoptosis after HIFU treatment. It has been reported that the maximum level of apoptosis was reached at 72 h after HIFU treatment of rabbit liver tumors (91). The particular reason for the onset of apoptosis is unknown. Apoptosis may be induced by the release of reactive oxygen species due to either hyperthermic or ischemia-reperfusion processes that can occur due to increased blood flow in the collateral circulation. In addition, apoptosis can be induced by mitochondrial dysfunction (91). Similar to necrosis, apoptosis may be visualized by diffusion-weighted MRI. Apoptosis-related cell shrinkage, cell blebbing and phagocytosis all cause an elevation in the tissue ADC value (104). Next to ischemia-induced necrosis, apoptosis may thus also partly explain the observed elevated ADC values at later stages after HIFU treatment (27,43). Because of the similar effect of apoptosis and necrosis on the tumor ADC, it is difficult, if not impossible, to distinguish these different types of cell death based on diffusion-weighted imaging alone. Hyperpolarized MRI with ^{13}C -labeled fumarate (80) may provide a means to distinguish between these types of cell death, since the increased malate production during necrosis mainly relies on permeabilization of the cell membrane, which does not occur during the early phase of apoptosis. HIFU-induced apoptosis might also be specifically detected by CE-MRI after the injection of phosphatidylserine (PS)-targeting MR contrast agents. PS is a membrane phospholipid

that is normally exclusively present in the inner leaflet of the cell membrane. At the onset of apoptosis, PS is exposed at the outer leaflet as well to promote phagocytosis by inflammatory cells (105). Two peptides that have shown strong affinity to PS are annexin A5 (106) and the C2A domain of synaptotagmin I (107). The latter peptide is much smaller than annexin A5 and therefore allows for better access to, and clearance from, the tumor interstitium (108). Krishnan et al. showed with CE-MRI that the accumulation of Gd3+ chelate conjugates of C2A was higher in chemotherapy-treated tumor-bearing mice compared to non-treated animals. Histological validation indicated that tumor regions that showed accumulation of the contrast agent co-localized with areas of apoptosis (108).

Multiparametric MRI for the evaluation of HIFU treatment

As described above, multiple MRI methods have been employed for the evaluation of HIFU treatment, each providing sensitivity to (a number of) changes after HIFU treatment. Instead of evaluating changes in a single MRI parameter, with multiparametric MRI the effect of the HIFU treatment on a number of MR parameters can be assessed. Since the different MRI parameters are each sensitive to different treatment effects, a multiparametric MR approach may provide a more complete assessment of the HIFU intervention. The potential value of multiparametric MRI has recently been addressed in a review on prostate focused ultrasound therapy (6). In several studies, a multiparametric MRI protocol was employed for HIFU treatment evaluation. As an example, Jacobs et al. evaluated thermal ablation of uterine fibroids with multiparametric MRI that consisted of T₂-weighted imaging, ADC mapping, sodium MRI and contrast-enhanced T₁-weighted imaging (36) (Figure 3). Partanen et al. performed contrast-enhanced and diffusion-weighted MRI directly after HIFU treatment of canine prostate and subsequently did a correlation analysis between non-viable tumor tissue identified on each of the scans and in histology. Preliminary observations indicated a strong correlation between histology and each of the MRI methods (72).

Instead of assessing changes in the individual parameters of the multiparametric MRI protocol, the information of the different parameters can also be combined into a single, automated analysis. This could potentially allow for automatic segmentation of successfully treated and residual non-treated tumor tissue. Jacobs et al. employed a multiparametric analysis using diffusion-weighted and contrast-enhanced T₁-weighted images to segment successfully treated and non-treated tissue directly after HIFU treatment of uterine fibroids. Excellent agreement was observed between the segmentations based on both MRI methods (37). Cluster algorithms that segment the multiparametric data into groups of pixels, i.e. clusters, with similar MR parameter values seem promising for automatic tumor treatment evaluation based on multiple MR contrast mechanisms. While not applied for the evaluation of HIFU treatment yet, cluster analysis based on multiparametric MRI data, consisting of quantitative values of T₂, ADC and proton density, has been employed for the identification of non-viable tumor tissue after chemotherapy (109) and radiotherapy (110) in preclinical tumor models. A strong agreement between the extent of non-viable tumor tissue in the clustering results and in

histology was observed in both studies. These results suggest that cluster analysis of multiparametric MRI data may provide a suitable tool for automated treatment evaluation.

MRI-based HIFU treatment planning

Next to extensive evaluation of the HIFU intervention, also accurate treatment planning is necessary to ensure that the entire tumor is included in the treatment volume, while the surrounding tissue should be minimally affected. MR-HIFU treatment planning protocols generally include the acquisition of contrast-enhanced T_1 -weighted images on which the highly perfused tumor is generally well visible (82,111). However, a disadvantage of the use of CE-MRI for HIFU treatment planning is that it requires the injection of a contrast agent. If the HIFU treatment is to be performed directly after treatment planning, the presence of the Gd-based contrast agent may introduce errors in the MR thermometry measurements acquired during treatment (70). In addition, the contrast agent could become entrapped in the treated tumor tissue, possibly leading to tissue retention of (toxic) Gd^{3+} (69). While the tumor is generally less visible on non-contrast-enhanced MR images, a cluster analysis that is based on multiple intrinsic contrast MRI parameters may allow for accurate tumor delineation before HIFU treatment without the need for injection of contrast agent.

Aim and outline of this thesis

The goal of this thesis was to identify suitable MRI methods for accurate HIFU treatment planning and evaluation. To that aim, a series of preclinical studies in subcutaneous tumor models was performed.

The study in **chapter 2** describes a fully automatic tumor segmentation algorithm that is solely based on intrinsic contrast MRI. The described cluster analysis was performed with all possible feature vectors, i.e. subsets of the acquired MRI parameters (T_1 , T_2 and ADC). The automatic segmentations of the different feature vectors were quantitatively compared to manual tumor segmentations to determine the optimal combination of MRI parameters for accurate tumor delineation.

The major part of the thesis consists of the identification of suitable MRI biomarkers for accurate HIFU treatment evaluation. In the majority of the studies (**chapter 3, 4, 5 and 6**), the HIFU treatment was performed outside the high-field (6.3 or 7 Tesla) animal scanner with a preclinical therapeutic ultrasound transducer. In these studies, a mouse subcutaneous tumor model was used.

In **chapter 3** a multiparametric cluster analysis was employed to segment successfully treated non-viable tumor tissue from residual or recurrent viable tumor tissue. The multiparametric MRI protocol, that was performed before, directly after and at 3 days after HIFU treatment, consisted of quantitative assessment of T_1 , T_2 , ADC and MTR. The cluster analysis was again performed on all possible feature vectors. The optimal feature vector for accurate assessment of the extent of non-viable tumor tissue after HIFU

treatment was determined by quantitative comparison between clustering-derived and histology-derived non-viable tumor fractions.

In **chapter 4** and **5** the sensitivity of APT imaging and $T_{1\rho}$ mapping, respectively, to HIFU-induced tissue changes was assessed. A quantitative analysis of HIFU-induced changes in these advanced MRI parameters was performed in these studies.

Chapter 6 describes a cluster analysis on pharmacokinetic parameters K^{trans} and v_e derived from DCE-MRI data of HIFU-treated tumors. The cluster algorithm was employed to identify regions of distinct HIFU-induced vascular changes around the NPV.

In the final study in **chapter 7** all assessed MRI methods (T_1 , T_2 , ADC, $T_{1\rho}$ mapping, APT imaging and DCE-MRI) were combined into a single, multiparametric MRI protocol. To advance clinical translation of the described multiparametric approach for HIFU treatment evaluation, the thermal ablation was performed in a clinical MR-HIFU system at 3 Tesla. An extensive analysis of HIFU-induced effects on the different MRI parameters was performed in subcutaneous rat tumors. In addition, the final optimal subset of MRI biomarkers for HIFU treatment assessment was determined by quantitative comparison of the clustering results with histology.

In **chapter 8** the main findings in the studies described in this thesis and future directions are discussed.

References

1. **Lynn JG, Zwemer RL, Chick AJ, Miller AE.** J Gen Physiol 1942;26:179-193.
2. **Fry WJ, Mosberg WH, Jr., Barnard JW, Fry FJ.** J Neurosurg 1954;11:471-478.
3. **Kremkau FW.** J Clin Ultrasound 1979;7:287-300.
4. **Tempany CM, Stewart EA, McDannold N, Quade BJ, Jolesz FA, Hynynen K.** Radiology 2003;226:897-905.
5. **Hesley GK, Gorny KR, Woodrum DA.** Cardiovasc Intervent Radiol 2013;36:5-13.
6. **Rouviere O, Gelet A, Crouzet S, Chapelon JY.** Nat Rev Clin Oncol 2012;9:721-727.
7. **Kirkham AP, Emberton M, Hoh IM, Illing RO, Freeman AA, Allen C.** Radiology 2008;246:833-844.
8. **Murat FJ, Poissonnier L, Pasticier G, Gelet A.** Cancer Control 2007;14:244-249.
9. **Gelet A, Chapelon JY, Bouvier R, Rouviere O, Lasne Y, Lyonnet D, Dubernard JM.** J Endourol 2000;14:519-528.
10. **Merckel LG, Bartels LW, Kohler MO, van den Bongard HJ, Deckers R, Mali WP, Binkert CA, Moonen CT, Gilhuijs KG, van den Bosch MA.** Cardiovasc Intervent Radiol 2013;36:292-301.
11. **Schmitz AC, Gianfelice D, Daniel BL, Mali WP, van den Bosch MA.** Eur Radiol 2008;18:1431-1441.
12. **Leslie TA, Kennedy JE, Illing RO, Ter Haar GR, Wu F, Phillips RR, Friend PJ, Roberts IS, Cranston DW, Middleton MR.** Br J Radiol 2008;81:564-571.
13. **Leslie T, Ritchie R, Illing R, Ter Haar G, Phillips R, Middleton M, F. W, Cranston D.** Br J Radiol 2012;85:1363-1370.
14. **Wijlemans JW, Bartels LW, Deckers R, Ries M, Mali WP, Moonen CT, van den Bosch MA.** Cancer Imaging 2012;12:387-394.
15. **Gianfelice D, Gupta C, Kucharczyk W, Bret P, Havill D, Clemons M.** Radiology 2008;249:355-363.
16. **Seip R, Ebbini ES.** IEEE Trans Biomed Eng 1995;42:828-839.
17. **Ishihara Y, Calderon A, Watanabe H, Okamoto K, Suzuki Y, Kuroda K.** Magn Reson Med 1995;34:814-823.
18. **Dewhirst MW, Viglianti BL, Lora-Michiels M, Hanson M, Hoopes PJ.** Int J Hyperthermia 2003;19:267-294.
19. **Yarmolenko PS, Moon EJ, Landon C, Manzoor A, Hochman DW, Viglianti BL, Dewhirst MW.** Int J Hyperthermia 2011;27:320-343.

20. **Miller DL, Smith NB, Bailey MR, Czarnota GJ, Hynynen K, Makin IR.** *J Ultrasound Med* 2012;31:623-634.
21. **Chu KF, Dupuy DE.** *Nat Rev Cancer* 2014;14:199-208.
22. **Kennedy JE.** *Nat Rev Cancer* 2005;5:321-327.
23. **Frenkel V.** *Advanced Drug Delivery Reviews* 2008;60:1193-1208.
24. **Stone MJ, Frenkel V, Dromi S, Thomas P, Lewis RP, Li KC, Horne M, 3rd, Wood BJ.** *Thromb Res* 2007;121:193-202.
25. **Carasso D, Hanannel A, Navon G.** *NMR Biomed* 2008;21:637-643.
26. **Peng HH, Huang TY, Tseng WY, Lin EL, Chung HW, Wu CC, Wang YS, Chen WS.** *J Magn Reson Imaging* 2009;30:596-605.
27. **Hectors SJ, Jacobs I, Strijkers GJ, Nicolay K.** *PLoS One* 2014;9:e99936.
28. **Larrat B, Pernot M, Aubry JF, Dervishi E, Sinkus R, Seilhean D, Marie Y, Boch AL, Fink M, Tanter M.** *Phys Med Biol* 2010;55:365-388.
29. **Wu T, Felmlee JP, Greenleaf JF, Riederer SJ, Ehman RL.** *Magn Reson Med* 2001;45:80-87.
30. **Vogel MW, Entius CA, Pattynama PM.** *Invest Radiol* 2004;39:661-665.
31. **Morocz IA, Hynynen K, Gudbjartsson H, Peled S, Colucci V, Jolesz FA.** *J Magn Reson Imaging* 1998;8:136-142.
32. **Cheng HL, Purcell CM, Bilbao JM, Plewes DB.** *J Magn Reson Imaging* 2004;19:329-341.
33. **Hundt W, Yuh EL, Steinbach S, Bednarski MD, Guccione S.** *Eur Radiol* 2008;18:993-1004.
34. **Hundt W, Yuh EL, Steinbach S, Bednarski MD.** *Technol Cancer Res Treat* 2009;8:85-98.
35. **Jacobs MA, Herskovits EH, Kim HS.** *Radiology* 2005;236:196-203.
36. **Jacobs MA, Ouwerkerk R, Kamel I, Bottomley PA, Bluemke DA, Kim HS.** *J Magn Reson Imaging* 2009;29:649-656.
37. **Jacobs MA, Gultekin DH, Kim HS.** *Med Phys* 2010;37:4768-4776.
38. **Pilatou MC, Stewart EA, Maier SE, Fennessy FM, Hynynen K, Tempny CM, McDannold N.** *J Magn Reson Imaging* 2009;29:404-411.
39. **Wijlemans JW, Deckers R, van den Bosch MA, Seinstra BA, van Stralen M, van Diest PJ, Moonen CT, Bartels LW.** *Invest Radiol* 2013;48:381-386.
40. **Jacobs I, Hectors SJ, Strijkers GJ, Nicolay K.** *Proceedings of the 14th International Symposium on Therapeutic Ultrasound, Las Vegas, NV, USA 2014.*
41. **Gianfelice D, Khat A, Amara M, Belblidia A, Boulanger Y.** *Breast Cancer Res Treat* 2003;82:93-101.
42. **Khat A, Gianfelice D, Amara M, Boulanger Y.** *Br J Radiol* 2006;79:308-314.
43. **Zhang Y, Zhao J, Guo D, Zhong W, Ran L.** *Eur J Radiol* 2011;79:347-352.
44. **Muto S, Kaminaga T, Horiuchi A, Kitamura K, Saito K, Isotani S, Yamaguchi R, Ide H, Furui S, Horie S.** *Int J Urol* 2014;doi:10.1111/iju.12442.
45. **Bohris C, Jenne JW, Rastert R, Simiantonakis I, Brix G, Spoo J, Hlavac M, Nemeth R, Huber PE, Debus J.** *Magn Reson Imaging* 2001;19:167-175.
46. **Curiel L, Souchon R, Rouviere O, Gelet A, Chapelon JY.** *Ultrasound Med Biol* 2005;31:1461-1468.
47. **Hazle JD, Diederich CJ, Kangasniemi M, Price RE, Olsson LE, Stafford RJ.** *J Magn Reson Imaging* 2002;15:409-417.
48. **McDannold, Hynynen K, Wolf D, Wolf G, Jolesz F.** *J Magn Reson Imaging* 1998;8:91-100.
49. **Ren XL, Zhou XD, Zhang J, He GB, Han ZH, Zheng MJ, Li L, Yu M, Wang L.** *J Ultrasound Med* 2007;26:201-212.
50. **Ritchie RW, Leslie T, Phillips R, Wu F, Illing R, ter Haar G, Protheroe A, Cranston D.** *BJU Int* 2010;106:1004-1009.
51. **Vykhodtseva N, Sorrentino V, Jolesz FA, Bronson RT, Hynynen K.** *Ultrasound Med Biol* 2000;26:871-880.
52. **McDannold N, Tempny CM, Fennessy FM, So MJ, Rybicki FJ, Stewart EA, Jolesz FA, Hynynen K.** *Radiology* 2006;240:263-272.
53. **Venkatesan AM, Partanen A, Pulanic TK, Dreher MR, Fischer J, Zurawin RK, Muthupillai R, Sokka S, Nieminen HJ, Sinaii N, Merino M, Wood BJ, Stratton P.** *J Vasc Interv Radiol* 2012;23:786-794 e784.
54. **Hijnen NM, Heijman E, Kohler MO, Ylihautala M, Ehnholm GJ, Simonetti AW, Grull H.** *Int J Hyperthermia* 2012;28:141-155.
55. **Cheng HL, Purcell CM, Bilbao JM, Plewes DB.** *J Magn Reson Imaging* 2003;18:585-598.
56. **Fukunishi H, Funaki K, Ikuma K, Kaji Y, Sugimura K, Kitazawa R, Kitazawa S.** *Int J Gynecol Cancer* 2007;17:724-728.
57. **Sung HY, Jung SE, Cho SH, Zhou K, Han JY, Han ST, Kim JI, Kim JK, Choi JY, Yoon SK, Yang JM, Han CW, Lee YS.** *Pancreas* 2011;40:1080-1086.
58. **Wu F, Chen WZ, Bai J, Zou JZ, Wang ZL, Zhu H, Wang ZB.** *Ultrasound Med Biol* 2002;28:535-542.
59. **Kong G, Braun RD, Dewhirst MW.** *Cancer Res* 2001;61:3027-3032.
60. **Bellmann K, Charette SJ, Nadeau PJ, Poirier DJ, Loranger A, Landry J.** *Cell Stress Chaperones* 2010;15:101-113.
61. **Zhang Y, Calderwood SK.** *Int J Hyperthermia* 2011;27:409-414.

62. **Wolff SD, Balaban RS.** Radiology 1994;192:593-599.
63. **Graham SJ, Stanisiz GJ, Kecojevic A, Bronskill MJ, Henkelman RM.** Magn Reson Med 1999;42:1061-1071.
64. **van Zijl PC, Zhou J, Mori N, Payen JF, Wilson D, Mori S.** Magn Reson Med 2003;49:440-449.
65. **Grohn OH, Lukkariinen JA, Silvennoinen MJ, Pitkanen A, van Zijl PC, Kauppinen RA.** Magn Reson Med 1999;42:268-276.
66. **Mariappan YK, Glaser KJ, Ehman RL.** Clin Anat 2010;23:497-511.
67. **Lauffer RB, Dunham SO;** Contrast-enhanced diagnostic imaging method for monitoring interventional therapies patent WO 99/17809. 1999.
68. **Caravan P, Cloutier NJ, Greenfield MT, McDermid SA, Dunham SU, Bulte JW, Amedio JC, Jr., Looby RJ, Supkowski RM, Horrocks WD, Jr., McMurry TJ, Lauffer RB.** J Am Chem Soc 2002;124:3152-3162.
69. **Hijnen NM, Elevelt A, Grull H.** Invest Radiol 2013;48:517-524.
70. **Hijnen NM, Elevelt A, Pikkemaat J, Bos C, Bartels LW, Grull H.** Journal of Therapeutic Ultrasound 2013;1:8.
71. **Cohen ZR, Zaubermann J, Harnof S, Mardor Y, Nass D, Zadicario E, Hananel A, Castel D, Faibel M, Ram Z.** Neurosurgery 2007;60:593-600.
72. **Partanen A, Yerram NK, Trivedi H, Dreher MR, Oila J, Hoang AN, Volkin D, Nix J, Turkbey B, Bernardo M, Haines DC, Benjamin CJ, Linehan WM, Choyke P, Wood BJ, Ehnholm GJ, Venkatesan AM, Pinto PA.** BJU Int 2013;112:508-516.
73. **Madelin G, Lee JS, Regatte RR, Jerschow A.** Prog Nucl Magn Reson Spectrosc 2014;79:14-47.
74. **Willis WT, Jackman MR, Bizeau ME, Pagliassotti MJ, Hazel JR.** Am J Physiol Regul Integr Comp Physiol 2000;278:R1240-1246.
75. **Vander Heiden MG, Cantley LC, Thompson CB.** Science 2009;324:1029-1033.
76. **Warburg O.** Science 1956;123:309-314.
77. **Kobus T, Wright AJ, Van Asten JJ, Heerschap A, Scheenen TW.** Magn Reson Med 2014;71:26-34.
78. **Brindle KM, Bohndiek SE, Gallagher FA, Kettunen MI.** Magn Reson Med 2011;66:505-519.
79. **Rodrigues TB, Serrao EM, Kennedy BW, Hu DE, Kettunen MI, Brindle KM.** Nat Med 2014;20:93-97.
80. **Gallagher FA, Kettunen MI, Hu DE, Jensen PR, Zandt RI, Karlsson M, Gisselsson A, Nelson SK, Witney TH, Bohndiek SE, Hansson G, Peitersen T, Lerche MH, Brindle KM.** Proc Natl Acad Sci U S A 2009;106:19801-19806.
81. **Bohndiek SE, Kettunen MI, Hu DE, Brindle KM.** Cancer Res 2012;72:854-864.
82. **Zhou YF.** World J Clin Oncol 2011;2:8-27.
83. **Tofts PS, Kermode AG.** Magn Reson Med 1991;17:357-367.
84. **Vaupel PW, Kelleher DK.** Int J Hyperthermia 2010;26:211-223.
85. **de Smet M, Hijnen NM, Langereis S, Elevelt A, Heijman E, Dubois L, Lambin P, Grull H.** Invest Radiol 2013;48:395-405.
86. **Hijnen N, Langereis S, Grull H.** Advanced Drug Delivery Reviews 2014;72C:65-81.
87. **Hijnen N, De Smet M, Kneepkens E, Langereis S, Grull H.** European Molecular Imaging Meeting 2013:22.
88. **Ludemann L, Wust P, Gellermann J.** Int J Hyperthermia 2008;24:91-96.
89. **Golay X, Hendrikse J, Lim TC.** Top Magn Reson Imaging 2004;15:10-27.
90. **Takahara T, Kwee TC.** J Magn Reson Imaging 2012;35:1266-1273.
91. **Luo W, Zhou X, Gong X, Zheng M, Zhang J, Guo X.** J Ultrasound Med 2007;26:477-485.
92. **Temme S, Bonner F, Schrader J, Fogel U.** Wiley interdisciplinary reviews Nanomedicine and nanobiotechnology 2012;4:329-343.
93. **Stoll G, Basse-Lusebrink T, Weise G, Jakob P.** Wiley interdisciplinary reviews Nanomedicine and nanobiotechnology 2012;4:438-447.
94. **Weissleder R, Nahrendorf M, Pittet MJ.** Nature materials 2014;13:125-138.
95. **Hynynen K, Chung AH, Colucci V, Jolesz FA.** Ultrasound Med Biol 1996;22:193-201.
96. **Wu L, Fu Z, Zhou S, Gong J, Liu CA, Qiao Z, Li S.** PLoS One 2014;9:e88913.
97. **Moon EJ, Sonveaux P, Porporato PE, Danhier P, Gallez B, Batinic-Haberle I, Nien YC, Schroeder T, Dewhirst MW.** Proc Natl Acad Sci U S A 2010;107:20477-20482.
98. **Li SP, Padhani AR, Makris A.** J Natl Cancer Inst Monogr 2011;2011:103-107.
99. **Choi JW, Kim H, Kim HC, Lee Y, Kwon J, Yoo RE, Cho HR, Choi SH, Chung JW.** Anticancer Res 2013;33:1887-1892.
100. **Fan B, Wang XY, Yang XD, Zhong H, Wu CX, Jiang XX.** Magn Reson Imaging 2011;29:153-159.
101. **Zhou J, Payen JF, Wilson DA, Traystman RJ, van Zijl PC.** Nat Med 2003;9:1085-1090.
102. **Sun PZ, Zhou J, Huang J, van Zijl P.** Magn Reson Med 2007;57:405-410.
103. **Zhou J, van Zijl PC.** Transl Stroke Res 2011;3:76-83.
104. **Thoeny HC, Ross BD.** J Magn Reson Imaging 2010;32:2-16.
105. **Fadok VA, Bratton DL, Frasch SC, Warner ML, Henson PM.** Cell Death Differ 1998;5:551-562.
106. **Boersma HH, Kietselaer BL, Stolk LM, Bennaghmouch A, Hofstra L, Narula J, Heidendal GA, Reutelingsperger CP.** J Nucl Med 2005;46:2035-2050.
107. **Zhao M, Beauregard DA, Loizou L, Davletov B, Brindle KM.** Nat Med 2001;7:1241-1244.

108. **Krishnan AS, Neves AA, de Backer MM, Hu DE, Davletov B, Kettunen MI, Brindle KM.** Radiology 2008;246:854-862.
109. **Carano RA, Ross AL, Ross J, Williams SP, Koeppen H, Schwall RH, Van Bruggen N.** Magn Reson Med 2004;51:542-551.
110. **Henning EC, Azuma C, Sotak CH, Helmer KG.** Magn Reson Med 2007;57:501-512.
111. **Jolesz FA.** Annu Rev Med 2009;60:417-430.

Chapter 2

Automatic Segmentation of Subcutaneous Mouse Tumors by Multiparametric MR Analysis based on Endogenous Contrast

Stefanie Hectors, Igor Jacobs, Gustav Strijkers, Klaas Nicolay

Published in Magn Reson Mater Phy 2014;doi:10.1007/s10334-014-0472-1

Abstract

Purpose

Contrast-enhanced T_1 -weighted imaging is generally included in MRI protocols for automatic tumor segmentation. However, the use of an MR contrast agent may be unfavorable in several applications. We assessed whether automatic tumor segmentation is feasible using a multiparametric cluster analysis that uses intrinsic MRI contrast only.

Materials and Methods

Multiparametric MRI consisting of quantitative T_1 , T_2 and apparent diffusion coefficient (ADC) mapping was performed on mice bearing subcutaneous tumors ($n=21$). k-means and fuzzy c-means clustering with all possible combinations of MRI parameters, i.e. feature vectors, and 2 to 7 clusters were performed on the multiparametric data. The clusters associated with tumor tissue were selected using the relative signal intensity of tumor tissue in T_2 -weighted images. The optimal segmentation method was determined by quantitative comparison of the automatic segmentation with manual segmentations performed by three observers. In addition, the automatically segmented tumor volumes from 7 separate tumor data sets were quantitatively compared to histology-derived tumor volumes.

Results

The highest similarity index between the manual and automatic segmentations ($SI_{\text{manual,automatic}}=0.82\pm 0.06$) was observed for k-means clustering with feature vector $\{T_2, \text{ADC}\}$ and 4 clusters. A strong linear correlation between the automatically and manually segmented tumor volumes ($R^2=0.99$) was observed for this segmentation method. The automatically segmented tumor volumes were also strongly correlated to the histology-derived tumor volumes ($R^2=0.96$).

Conclusions

Accurate, automatic segmentation of mouse subcutaneous tumors can be achieved based on endogenous MR contrast only.

Introduction

Accurate tumor volume delineation is often necessary, both in (pre)clinical cancer research and in clinical practice. Tumor size measurements are generally used to assess tumor treatment efficacy (1). Furthermore, image-guided cancer treatment techniques, including MRI-guided High Intensity Focused Ultrasound (HIFU) and radiotherapy, require accurate tumor demarcation to define the target volume for the treatment. Currently, tumor delineation is generally performed by manual segmentation of the tumor tissue, which is time-consuming and prone to inter-observer variability. Automatic tumor segmentation would aid in more robust, fast, objective and reproducible delineation of the tumor tissue.

Multiple methods for (semi)automatic tumor segmentation based on MRI images have been described for different tumors, including breast (2-6), prostate (7,8), brain (9-11) and head and neck (12) tumors. Various segmentation algorithms were employed in these studies, including volume growing, threshold-based methods and clustering algorithms, such as fuzzy c-means and fuzzy connectedness. Contrast-enhanced imaging is commonly included in the MRI protocols for automated tumor segmentation. However, if tumor segmentation needs to be performed shortly before treatment, the presence of the gadolinium (Gd) contrast agent during the treatment might cause adverse effects. It has recently been reported that presence of Gd during HIFU treatment may be unfavorable, because Gd-induced magnetic susceptibility changes in the tissue cause inaccuracies in the temperature maps acquired during treatment (13). Furthermore, tumor ablation with HIFU could induce entrapment of Gd in the treated tissue, which possibly results in prolonged retention of Gd in the body and potential release of free Gd^{3+} ions from the chelates (14). These free Gd^{3+} ions have been strongly associated with the development of Nephrogenic Systemic Fibrosis (NSF) (15). The drawbacks of contrast-enhanced T_1 -weighted imaging for treatment planning are however not restricted to HIFU treatment. Presence of the MR contrast agent may also be disadvantageous if treatment evaluation with MRI needs to be performed directly after treatment, because the influence of the contrast agent on the post-treatment MRI data could lead to misinterpretation of the treatment effects. Furthermore, apart from treatment-related drawbacks of injection of Gd contrast agents, in clinical practice, the injection of Gd contrast agent is contraindicated in patients with severely impaired renal function, because of the increased risk of NSF (16). Cancer patients are especially vulnerable to renal toxicity of contrast agents, because they are frequently exposed to nephrotoxic chemotherapeutics and may be dehydrated because of chemotherapy- and cancer-related nausea and vomiting (17).

Only a few studies have reported on automatic tumor segmentation methods based on endogenous contrast MRI. Hsieh et al. reported a method for automatic segmentation of meningiomas based on T_1 - and T_2 -weighted images (18). Although successful segmentation was obtained for most tumors, the method failed in approximately 20% of the cases. The authors reported that noticeable edema was present in the brain in these failure cases, indicating that the method could not distinguish between tumor and edematous tissue. Recently, in a preclinical study semi-automatic size measurements of

tumors that were subcutaneously inoculated in the neck region of mice were demonstrated (19). A threshold-based method was applied on T_2 -weighted images to segment the tumor tissue from the surrounding tissue. Additional manual delineation needed to be performed to exclude regions where the segmentation had failed.

These previous reports on automated tumor segmentation based on endogenous contrast suggest that a more advanced MR protocol is required to improve the accuracy of automatic tumor segmentation. Specifically, we hypothesize that inclusion of apparent diffusion coefficient (ADC) mapping to the endogenous contrast MRI methods may result in improved discrimination between tumor tissue and surrounding tissue, such as edema. Cancerous tissue typically has a lower ADC than non-cancerous tissue, because of high cellular density and thereby increased effects of diffusion-hindering obstacles, such as cell membranes and other macromolecular structures (20). In contrast, the peri-tumoral edematous tissue generally has a high ADC because of low cellularity. It was previously shown that the combination of ADC maps and T_2 -weighted images improves the sensitivity and specificity of prostate cancer detection by visual inspection (21).

The goal of the present study was to assess whether accurate, automatic tumor segmentation can be achieved based on combined analysis of quantitative T_1 , T_2 and ADC parameter maps. Clustering-based algorithms were used as segmentation method, since these algorithms are particularly suitable for segmentation based on multiparametric data. The study was aimed to assess the general feasibility of clustering algorithms based on endogenous MRI parameters for automatic tumor segmentation. Therefore, as a first step, the implemented algorithms were applied to segmentation of subcutaneous mouse tumors. To determine the optimal clustering method for automatic delineation of the tumor tissue, k-means clustering and fuzzy c-means clustering were performed with all possible combinations of MR parameters, i.e. feature vectors. Furthermore, the number of clusters was varied for each feature vector. The optimal segmentation method, i.e. the method that yielded the best segmentation of the tumor, was determined by quantitative comparison between the automatic tumor segmentations and manual tumor segmentations performed by three experienced observers. In addition, a quantitative correlation analysis between automatically segmented tumor volumes and histology-derived tumor volumes was performed.

Materials and Methods

Tumor model

CT26.WT mouse colon carcinoma cells (American Type Culture Collection (ATCC; CRL-2638)) were cultured as a monolayer at 37°C and 5% CO_2 in RPMI-1640 medium (Invitrogen, Breda, The Netherlands), supplemented with 10% fetal bovine serum (Greiner Bio-One, Alphen a/d Rijn, The Netherlands) and 50 U/ml penicillin/streptomycin (Lonza Bioscience, Basel, Switzerland). Early passages (5-10) of the original ATCC batch were used for inoculation.

10-12 week-old Balb/c mice (n=21; Charles River, Maastricht, The Netherlands) were inoculated with 2×10^6 CT26.WT cells subcutaneously in the right hind limb. Approximately 10 days after inoculation, tumors became palpable in all animals. All animal experiments were performed according to the Directive 2010/63/EU of the European Parliament and approved by the Animal Care and Use Committee of Maastricht University.

MRI measurements

MRI measurements were performed with a 6.3 T scanner (Bruker BioSpin, Ettlingen, Germany) using a 3.2-cm-diameter quadrature birdcage RF coil (Rapid Biomedical, Rimpfing, Germany). The mice were positioned in a custom-made cradle, equipped with a mask for anesthetic gas (1-2% isoflurane). Respiration was monitored with a balloon sensor. Animal temperature was monitored and maintained at body temperature with a warm water pad. For reduction of susceptibility artifacts in the Echo Planar Imaging (EPI) sequences, the tumor-bearing limb was covered with degassed ultrasound gel (Aquasonic® 100, Parker Laboratories). Artifacts were further reduced by local shimming of the tumor-bearing limb.

The multi-slice imaging protocol, covering the whole tumor, consisted of fat-suppressed T_2 -weighted imaging (spin-echo, echo time TE=30 ms, repetition time TR=1000 ms, number of averages NA=1), quantitative T_1 mapping (Inversion Recovery Look-Locker EPI, TE=8 ms, TR=10000 ms, inversion time=30 ms, flip angle=20°, pulse separation=400 ms, number of points=15, NA=2), T_2 mapping (MLEV-prepared GE-EPI (22), 7 TE's ranging from 1 to 82 ms, TR=2000 ms, NA=2) and ADC mapping (double spin-echo prepared EPI, TE=41 ms, TR=4000 ms, b-values 0, 100, 200 and 400 s/mm^2 , 3 orthogonal directions, NA=4). All acquired images had a matrix size of 128x128, FOV of $4 \times 4 \text{ cm}^2$ and 1 mm slice thickness. Regardless of tumor size, a minimum of twelve slices was acquired. For tumors extending outside these twelve slices, the number of slices was increased (to up to sixteen slices at maximum) to cover the entire tumor volume.

Image processing and generation of parameter maps

Image analysis was performed in Mathematica 8.0 (Wolfram Research, Champaign, IL, USA). Parameter maps were calculated on a pixel-by-pixel basis in each slice. The parameter values were only determined in pixels with substantial signal intensity (> 0.05 times the maximum signal intensity) in the T_2 -weighted images. T_1 maps were generated as described previously (23). T_2 maps were calculated from mono-exponential fitting of the multi-echo data. For the generation of ADC maps, mono-exponential fitting was performed through the signal intensities at the different b-values for each diffusion-encoding direction separately. Next, ADC values of the different directions were averaged to obtain the final (orientation-invariant) ADC value for each pixel.

Automatic tumor segmentation

A flow chart of the automatic tumor segmentation method is shown in Figure 1. Tumor segmentation based on the acquired parameter maps was performed by either k-means or fuzzy c-means clustering. Fuzzy c-means clustering is a soft version of k-means

clustering, in which each pixel has a certain degree of membership to each cluster. In applications where there is overlap between the clusters in the data set, fuzzy c-means clustering is more suitable than k-means (24). Clustering was performed with all possible feature vectors, namely $\{T_1\}$, $\{T_2\}$, $\{ADC\}$, $\{T_1, ADC\}$, $\{T_2, ADC\}$, $\{T_1, T_2\}$ and $\{T_1, T_2, ADC\}$ and with various numbers of clusters, ranging from 2 to 7. For fuzzy c-means clustering the fuzziness index was set to 2. The clustering algorithms were iterated until the method converged or the maximum number of iterations of 50 was reached.

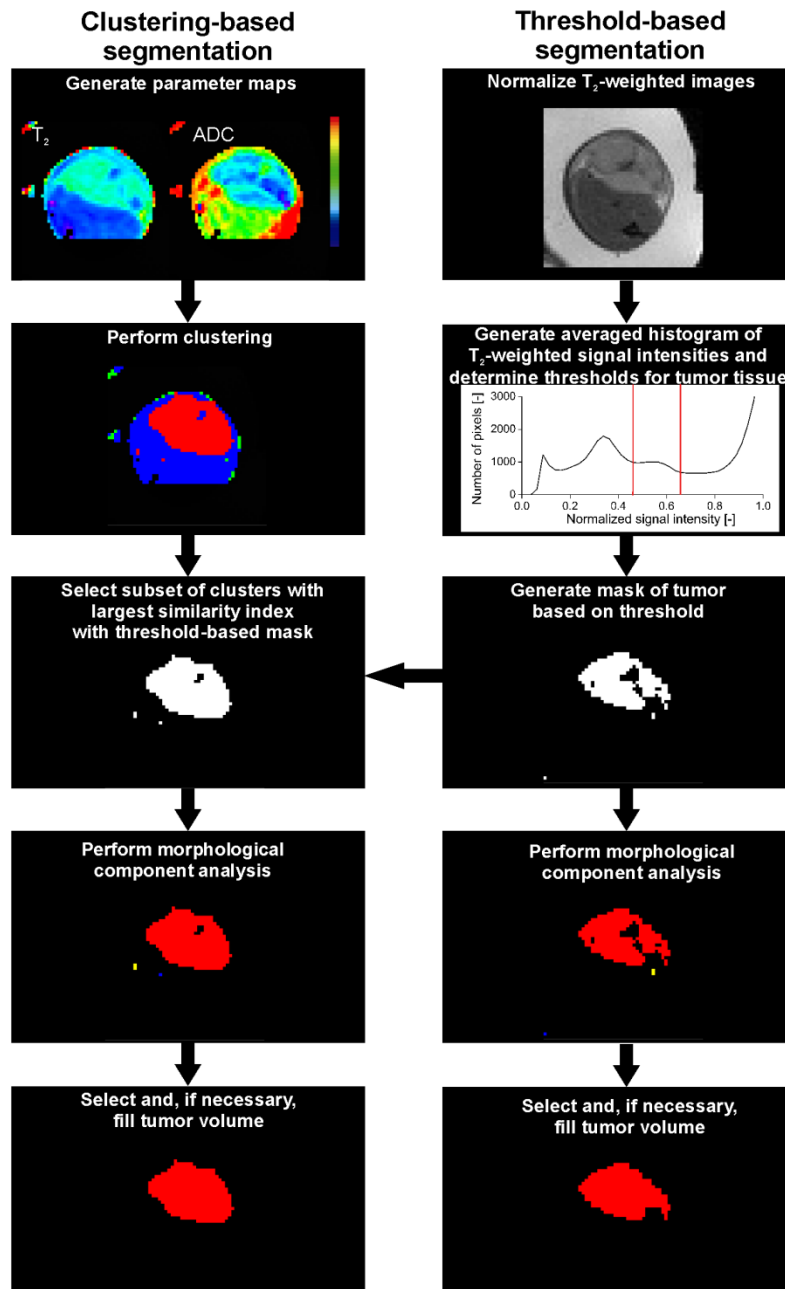


Figure 1. Flowchart of the clustering-based and threshold-based tumor segmentation methods. The tumor mask resulting from the threshold-based segmentation method was used for automatic selection of the tumor clusters in the clustering-based segmentation method. For details see text.

The segmentation method was performed on large rectangular regions around the tumor-bearing limb. These regions contained tumor tissue and surrounding muscle, oedema and bone. Prior to segmentation, pixels within the ultrasound gel were excluded from the defined rectangular regions by application of a threshold to the T_2 -weighted images. This led to segmentation of the hyperintense ultrasound gel and the relatively hypo-intense tissue. To correct for scaling differences between the different parameters, features were normalized (mean = 0, standard deviation SD = 1) before clustering was performed.

Certain prior knowledge on specific characteristics of the tumor tissue is needed to allow the algorithm to automatically assign clusters as tumor and non-tumor tissue. In the example of the subcutaneous tumors presented here, we made use of the typically higher signal intensity of the tumor tissue compared to the surrounding muscle tissue in T_2 -weighted images. An initial tumor mask was generated by a threshold-based segmentation method that was based on the T_2 -weighted images. The threshold-based tumor segmentation is illustrated at the right-hand side of Figure 1. For this method, the T_2 -weighted images from the different animals were normalized by dividing the pixel intensities by the average signal intensity of the ultrasound gel surrounding the tumor-bearing limb. Next, a histogram of the normalized signal intensities in the T_2 -weighted images averaged for all animals was generated. A clear peak that, based on visual inspection, belonged to the tumor tissue was observed in this averaged histogram. The minimum and maximum intensity values of this peak were found to be 0.45 and 0.65, respectively. Subsequently, all pixel values between these minimum and maximum intensities were set to 1, which resulted in a tumor mask that could be used as input for the clustering-based algorithm to allow for automatic determination of the subset of clusters belonging to the tumor tissue. The Similarity Index (SI) between the threshold-based tumor segmentation and the clustering-based segmentation method was determined for all possible subsets of clusters. The SI is a measure of the area defined as tumor tissue by both methods relative to the total segmented area and was determined according to equation 1 (9,25).

$$SI_{\text{threshold,clustering}} = \frac{2 \cdot S_{\text{threshold}} \cap S_{\text{clustering}}}{2 \cdot S_{\text{threshold}} \cap S_{\text{clustering}} + S_{\text{threshold}} \cap S_{\text{clustering}} + S_{\text{clustering}} \cap S_{\text{threshold}}} \quad (1)$$

In this equation $S_{\text{threshold}}$ and $S_{\text{clustering}}$ are the tumor segmentations resulting from the threshold-based and clustering-based segmentation, respectively. The \cap symbol represents intersection.

The tumor clusters were determined by automatic selection of the subset of clusters for which the $SI_{\text{threshold,clustering}}$ was maximal. To eliminate small groups of pixels outside the large tumor volume that were assigned to (one of) the tumor cluster(s), connected components analysis was performed on all pixels that were assigned to the tumor cluster(s) (Mathematica command `MorphologicalComponents`). This connected components method segments an image into different groups of connected pixels. The largest component resulting from this analysis was assumed to be the tumor. Region

growing was applied on this component to include pixels within the tumor that were not assigned to the tumor cluster(s), e.g. because of naturally occurring necrotic tumor tissue that has different MR parameter values than viable tumor tissue and may therefore initially not be selected as tumor tissue by the segmentation method. To compare the performance of the clustering-based segmentation methods to that of the threshold-based segmentation method, the same procedure of morphological component analysis and region growing was also applied on the generated threshold-based tumor mask.

Manual tumor segmentation

Manual segmentation was performed by three independent observers (O_1 , O_2 and O_3). All three observers have substantial experience (>4 years) in MRI of subcutaneous mouse tumors. Regions of interest (ROIs) around the tumor tissue were drawn on the 3rd echo images of the T_2 mapping protocol, because this image has approximately the same echo time (28 ms) as the spin-echo T_2 -weighted image (30 ms). ROI definition was performed on the images from the T_2 mapping rather than the spin-echo T_2 -weighted images, because, although maximum effort was taken to minimize the effects of susceptibility artifacts in the EPI acquisitions, minimal geometric distortions could still be present in the EPI acquisitions. These distortions could lead to a slight misregistration between the spin-echo T_2 -weighted imaging and the EPI-based T_1 , T_2 and ADC acquisitions.

Evaluation of automatic segmentation methods

To determine the optimal automatic segmentation method, the tumor delineations resulting from the various segmentation methods were quantitatively compared to the manual tumor delineations. The performance of the segmentation methods was assessed by calculation of the specificity, sensitivity and the similarity index ($SI_{\text{manual,automatic}}$) between the manual and automatic tumor segmentations. An SI above 0.7 is indicative of a good segmentation (26).

The sensitivity, specificity and $SI_{\text{manual,automatic}}$ were determined by Equation 2, 3 and 4, respectively:

$$\text{Sensitivity} = \frac{TP}{TP+FN} \quad (2)$$

$$\text{Specificity} = \frac{TN}{TN+FP} \quad (3)$$

$$SI_{\text{manual,automatic}} = \frac{2 \cdot TP}{2 \cdot TP + FP + FN} \quad (4)$$

In these equations, TP is the number of true-positive pixels, FP is the number of false-positive pixels, TN is the number of true-negative pixels, and FN is the number of false-negative pixels (see Figure 2).

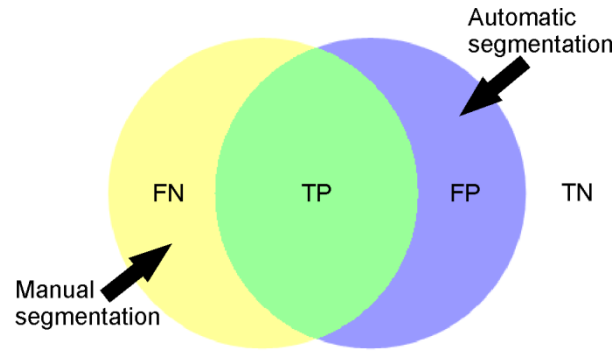


Figure 2. Illustration of calculation of true positive (TP), true negative (TN), false positive (FP) and false negative (FN) values based on comparison between automatically (blue) and manually (yellow) segmented tumor regions.

Assessment of inter-observer variability

The manual segmentations of the different observers were compared by calculation of the above-mentioned SI. The SI between two different manual segmentations was assessed by the following equation:

$$SI_{O_i, O_j} = \frac{2 \cdot S_i \cap S_j}{2 \cdot S_i \cap S_j + S_i \cap \bar{S}_j + S_j \cap \bar{S}_i} \quad (5)$$

, in which S_i and S_j are the manual segmentations of observers O_i and O_j , respectively.

Comparison of the optimal automatic segmentation method with histology

The segmentation method that was considered optimal based on the above measures of performance was run on 7 separate MRI data sets of the same tumor model, that were acquired according to the same MRI protocol as described above. For these data sets, histological sections of the tumors, that were excised directly after acquisition of the MRI data, were available. The 5- μ m-thick cryosections covered the entire tumor volume and were cut with a 300 μ m inter-section distance. The cryosections were stained for nicotinamide adenine dinucleotide diaphorase (NADH) activity, which is a marker for cell viability (for protocol, see **chapter 3**). All sections were imaged with brightfield microscopy, that consisted of mosaic acquisition at 5x magnification. Analysis of the microscopy images was done in Mathematica. ROIs were manually drawn around the entire tumor tissue on each section. Subsequently, histology-derived tumor volumes were calculated by multiplication of the sum of the areas of tumor tissue in all sections with the inter-section distance.

Statistics

All data are presented as mean \pm SD. The $SI_{\text{manual,automatic}}$ values of the different segmentation methods were statistically compared with a paired t-test. The effect of a difference in observer on the $SI_{\text{manual,automatic}}$ values was assessed with ANOVA for repeated measures. In case the influence of observer on the $SI_{\text{manual,automatic}}$ proved to be significant, Bonferroni post-hoc tests were performed to compare the $SI_{\text{manual,automatic}}$ values of the individual observers. For all tests, the level of significance was set to $\alpha=0.05$.

The automatically and manually segmented tumor volumes were compared by linear

regression that consisted of fitting of the data points to the line $y=a*x+b$. A similar analysis was performed for comparison between tumor volumes from histology and automatically segmented tumor volumes. Outliers that significantly affected the linear regression were identified by calculation of the Cook's distance of each data point. A data point was considered as outlier if its Cook's distance was higher than $4/(n-k-1)$, in which n is the number of data points and k the number of fitted parameters (2) (27).

Results

Inter-observer variability

Three observers manually delineated the tumor tissue on the T_2 -weighted images of all tumors. The inter-observer variability was assessed by calculation of the similarity index (SI). The SI values between the different manual segmentations are listed in Table 1, showing good agreement between the segmentations of the different observers.

Table 1. Average Similarity Index between the three manual tumor segmentations. Values are given as mean \pm SD (n=21).

Observer	O ₁	O ₂	O ₃
O ₁	1	0.86 \pm 0.04	0.84 \pm 0.04
O ₂	-	1	0.87 \pm 0.04
O ₃	-	-	1

Performance of k-means clustering

Average sensitivity and specificity values of the k-means methods with the different feature vectors as function of the number of clusters are displayed in Figure 3A and B, respectively. Generally, a rise in specificity of the automatic segmentation method with increasing number of clusters was observed. Selection of the optimal k-means method for accurate tumor delineation was based on the $SI_{\text{manual,automatic}}$ values, which are displayed in Figure 3C for the different methods. The highest $SI_{\text{manual,automatic}}$ value (0.82 \pm 0.06) was observed for feature vector $\{T_2, \text{ADC}\}$ with 4 clusters. For this k-means method the sensitivity (Figure 3A) and specificity (Figure 3B) were 0.76 \pm 0.10 and 0.95 \pm 0.02, respectively. The $SI_{\text{manual,automatic}}$ value of this method was significantly larger than that of most of the other k-means methods. Only the k-means methods with feature vector $\{T_1, \text{ADC}\}$ with 4 clusters, feature vector $\{T_1, T_2, \text{ADC}\}$ with 4 and 5 clusters and feature vector $\{T_2, \text{ADC}\}$ with 3, 5 and 6 clusters did not have a significantly lower $SI_{\text{manual,automatic}}$ than the optimized k-means method with feature vector $\{T_2, \text{ADC}\}$ and 4 clusters. The $SI_{\text{manual,automatic}}$ value for the automatic segmentation using k-means with feature vector $\{T_2, \text{ADC}\}$ and 4 clusters was higher than 0.7 (indicative of good agreement, see Materials and Methods) for 20 out of 21 tumors.

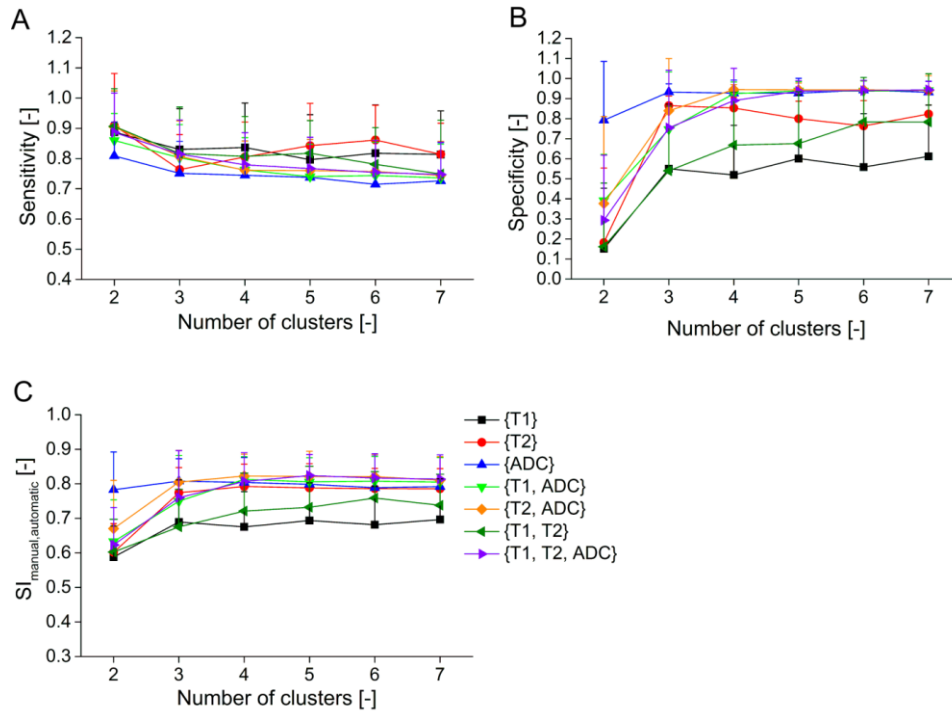


Figure 3. Mean sensitivity (A), specificity (B) and the $SI_{\text{manual,automatic}}$, i.e. the similarity index between the manual and automatic tumor segmentation, (C) values averaged over the observers for the different feature vectors (see bottom right) as function of the number of clusters for the k-means clustering-based segmentation method. The error bars represent the standard deviation between the different animals ($n=21$).

The $SI_{\text{manual,automatic}}$ values between the manual segmentation of each observer and the automatic segmentation with k-means clustering with feature vector $\{T_2, \text{ADC}\}$ and 4 clusters were 0.85 ± 0.05 , 0.82 ± 0.08 and 0.80 ± 0.07 for observer O_1 , O_2 and O_3 , respectively. These high $SI_{\text{manual,automatic}}$ values are indicative of good agreement between the automatic segmentation and the individual manual segmentations. Statistical analysis showed that there was a significant effect of observer on the $SI_{\text{manual,automatic}}$ values ($P < 0.001$). The $SI_{\text{manual,automatic}}$ values of observer O_1 were significantly higher than those of observer O_2 and O_3 . Furthermore, significantly higher $SI_{\text{manual,automatic}}$ values were found for observer O_2 as compared to observer O_3 .

Figure 4 shows three representative examples of automatic tumor segmentation with k-means clustering with feature vector $\{T_2, \text{ADC}\}$ and 4 clusters. On the right-hand side of the figure, the automatic tumor segmentation as well as the manual tumor segmentation of each observer are overlaid on the T_2 -weighted images. Close agreement between the manual and automated tumor segmentation was observed for all observers. The algorithm accurately segmented the tumor tissue, even for tumors with a heterogeneous appearance on the T_2 -weighted images, such as the tumors in the 2nd and 3rd row of Figure 4. In these heterogeneous tumors, the (most likely necrotic) regions within the tumor that exhibited a low signal intensity on the T_2 -weighted images were generally not assigned to one of the tumor clusters. However, they were included in the final segmented tumor volume by the region growing algorithm that was applied in the last step of the algorithm (see Figure 1 and Materials and Methods).

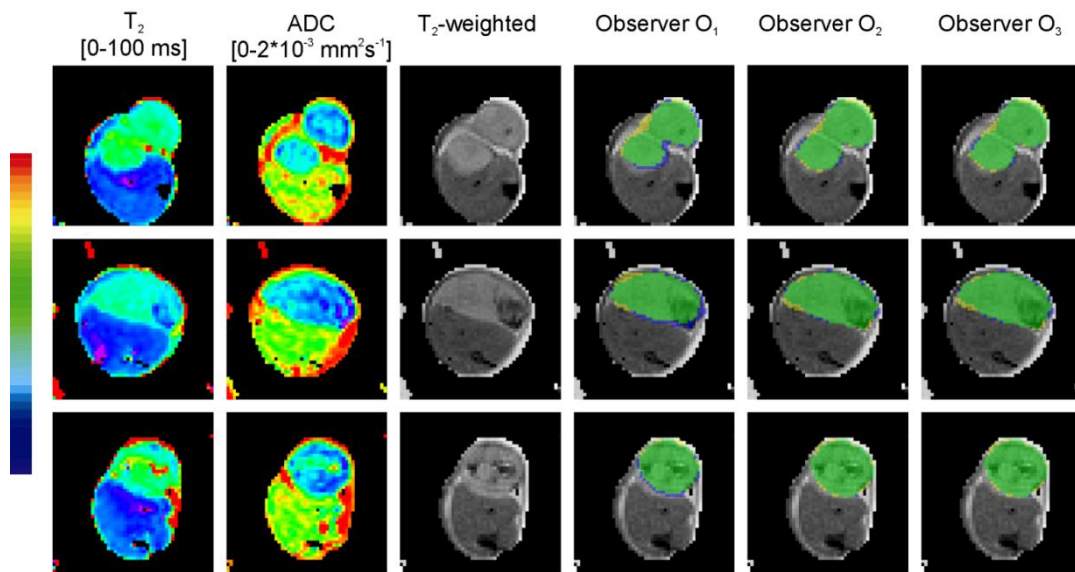


Figure 4. Three representative examples of the results of k-means clustering with feature vector $\{T_2, ADC\}$ and 4 clusters. The T_2 and ADC maps of the tumor-bearing paws are shown in the first and second column, respectively. The third column shows the corresponding T_2 -weighted images. In the fourth, fifth and sixth column the automatic tumor segmentation (blue) and manual segmentation (yellow) of observer O_1 , O_2 and O_3 , respectively, are overlaid on the T_2 -weighted image.

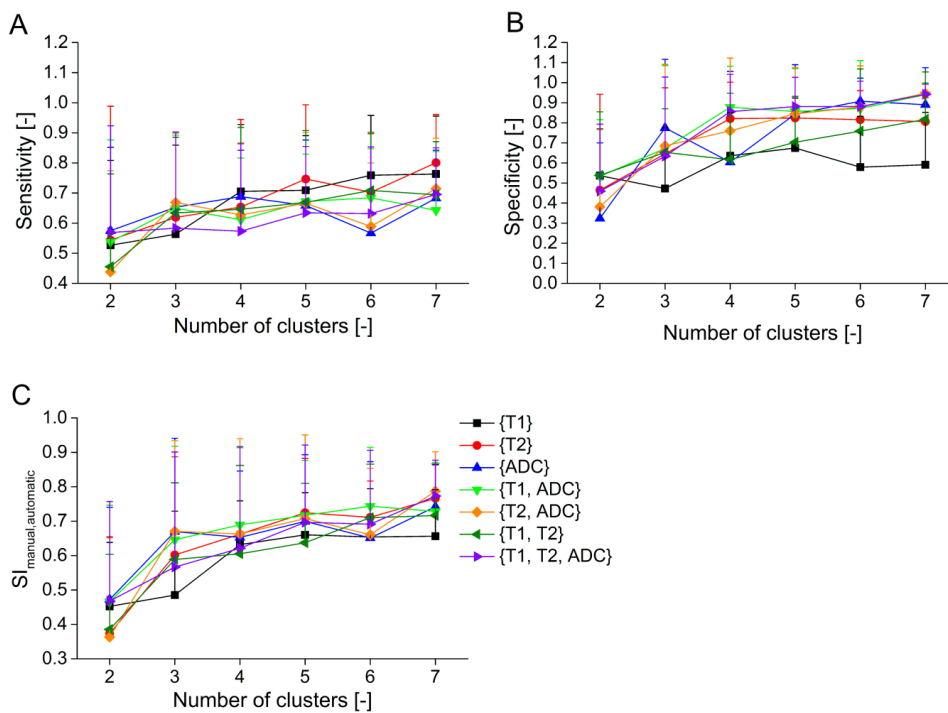


Figure 5. Mean sensitivity (A), specificity (B) and $SI_{\text{manual,automatic}}$, i.e. the similarity index between the manual and automatic tumor segmentation, (C) averaged over the observers for the different feature vectors (see bottom right) as function of the number of clusters for the fuzzy c-means clustering-based segmentation method. The error bars represent the standard deviation between the different animals ($n=21$).

Performance of fuzzy c-means clustering

Average sensitivity, specificity and $SI_{\text{manual,automatic}}$ values for the different fuzzy c-means methods are shown in Figure 5A, B and C, respectively. All values were generally lower

than those obtained for k-means clustering (Figure 3). For fuzzy c-means clustering, the highest $SI_{\text{manual,automatic}}$ was noted for feature vector $\{T_2, \text{ADC}\}$ and 7 clusters. For this fuzzy c-means method, the $SI_{\text{manual,automatic}}$ was 0.79 ± 0.11 , which tended to be lower ($P=0.053$) than the $SI_{\text{manual,automatic}}$ of the optimal k-means method.

Performance of threshold-based segmentation method

For the threshold-based segmentation method, which only made use of T_2 -weighted images, a mean $SI_{\text{manual,automatic}}$ of 0.69 ± 0.14 was found, which is significantly lower than the $SI_{\text{manual,automatic}}$ values for both the optimized k-means ($P<0.001$) and fuzzy c-means ($P<0.01$) clustering methods.

Comparison between tumor volumes from automatic and manual segmentation

Figure 6A shows the tumor volumes resulting from k-means clustering with feature vector $\{T_2, \text{ADC}\}$ and 4 clusters vs. the average tumor volumes derived from manual tumor segmentations by the three observers. A high linear correlation ($R^2=0.99$) was observed between the manually and automatically segmented tumor volumes. However, the slope of the linear fit was 0.88, indicative of either an underestimation of the tumor volume in the automatic segmentation or an overestimation of the tumor volume in the manual segmentation. Figure 6B shows a Bland-Altman plot of the difference in tumor volume between the manual and automatic segmentations resulting from the optimized segmentation method vs. the mean of the manually and automatically segmented tumor volumes. This plot further illustrates that the automatically segmented tumor volumes were consistently smaller than the manually segmented tumor volumes.

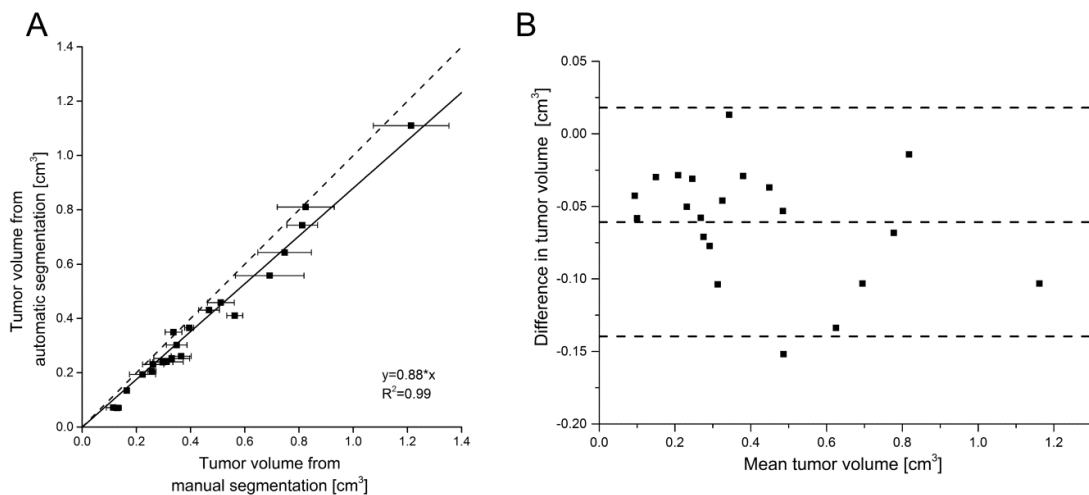


Figure 6. A) Tumor volumes derived from automatic tumor segmentation with k-means clustering with feature vector $\{T_2, \text{ADC}\}$ and 4 clusters vs. average tumor volumes derived from the manual tumor segmentations. The error bars represent the standard deviation between the manually segmented tumor volumes of the different observers ($n=3$). The fit to the data points is plotted with the solid line. The corresponding fit parameters are shown bottom right. The line of identity (dashed line) is added as visual reference. B) Bland-Altman plot of the difference in tumor volume between the manually and automatically segmented tumors (i.e., automatically segmented tumor volume minus the observer-averaged manually segmented tumor volume) vs. the mean of the manually and automatically segmented tumor volumes. The dashed lines represent the mean and 95% confidence interval for the difference in tumor volume.

Comparison between tumor volumes from automatic segmentation and histology

Figure 7 shows a correlation plot between histology-derived tumor volumes and tumor volumes derived from automatic segmentation of 7 separate data sets. A strong linear correlation ($R^2=0.96$) was observed after omitting the data point that was identified as outlier. For all tumors, the automatically segmented tumor volume was larger than the tumor volume derived from histology.

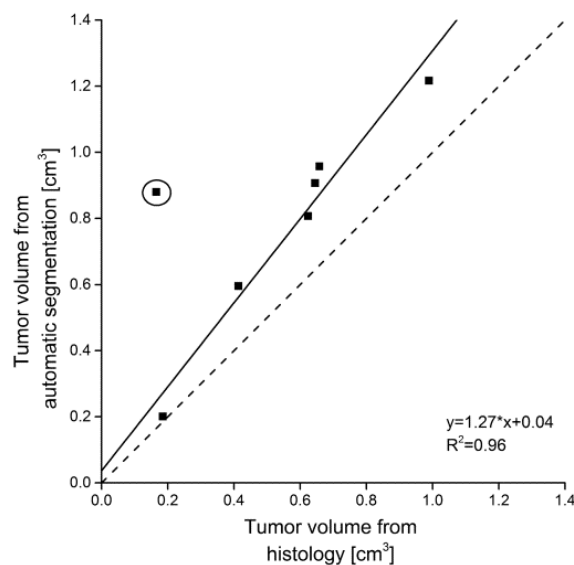


Figure 7. Tumor volumes resulting from automatic segmentation with k-means clustering with feature vector $\{T_2, ADC\}$ and 4 clusters vs. tumor volumes derived from whole-tumor based histology. The fit to the data points is plotted with the solid line. The corresponding fit parameters are shown bottom right. The line of identity (dashed line) is added as visual reference. One data point was identified as outlier and is indicated with a black circle.

Discussion and Conclusions

An automatic segmentation method for delineation of tumor tissue based on endogenous MR contrast was described. For optimization of the segmentation method, automatic tumor delineations were quantitatively compared to manual segmentations performed by three observers. The largest overlap between the automatic and manual segmentations was observed for k-means clustering with feature vector $\{T_2, ADC\}$ and 4 clusters. Visual inspection of the 4 clusters originating from this k-means method showed that three clusters corresponded to tumor tissue, peritumoral edema and muscle tissue. The fourth cluster generally originated from small regions of a few pixels in muscle or tumor tissue. The bone tissue in the tumor-bearing limb was typically excluded from analysis, since parameter values were not calculated in bone pixels because the signal intensity in these pixels was at noise level (see Materials and Methods). The $SI_{\text{manual,automatic}}$ of k-means clustering with $\{T_2, ADC\}$ and 4 clusters was not significantly better than the k-means method with feature vectors $\{T_1, ADC\}$ (4 clusters) and $\{T_1, T_2, ADC\}$ (4 and 5 clusters), which indicated that clustering based on ADC and either T_1 or T_2 worked equally well for the segmentation of these tumors.

Fuzzy c-means clustering did not improve the tumor segmentation as compared to k-means clustering, which implies that the contrast between the clusters of the different tissue types was well-defined. In clinical applications of automated tumor segmentation, fuzzy c-means clustering is widely used in various tumor types (3-5,9,10). In human tumors, the tissue around the tumor is generally very different from the surrounding tissue (muscle, oedema, bone) in the subcutaneous tumor model here. The contrast between tumor and surrounding tissue could be less well-defined, which may explain the additive value of fuzzy c-means clustering in the clinical setting. Furthermore, the resolution of clinical MR images is generally lower than the resolution used in our study ($0.31 \times 0.31 \times 1 \text{ mm}^3$), leading to larger partial volume effects at the tumor borders and a less well-defined demarcation between tumor and surrounding tissue. In such cases, a soft segmentation method, such as fuzzy c-means, could prove beneficial.

A strong linear correlation was observed between tumor volumes from the optimized automated segmentation and manual segmentations (Figure 6). However, the automatically segmented tumor volumes were on average smaller than those from the manual segmentations, which corresponds to the finding that the sensitivity of the optimized segmentation method was lower (0.76) compared to its specificity (0.95). Although the partial volume effects were relatively small, as stated above, they could partly explain the smaller tumor volumes for the automatic segmentation. Visual inspection of the segmentations revealed that pixels at the tumor rim were generally included in the manual segmentations, whereas they were not always included in the automatic segmentation because of partial volume effects with adjacent muscle or edematous tissue. These partial volume effects should be carefully taken into account when the segmentation method is used for image-guided treatment planning. It would be advisable to include a safety margin around the segmented tumor volume to prevent undertreatment. Safety margins are generally already included in image-guided therapy, for example during HIFU procedures (28), to account for the possible presence of occult tumor cells outside the tumor mass that are not visible with the used imaging method. The deviation between the automatically and manually segmented tumor volumes was also partly caused by errors in the manual tumor segmentations. The manual tumor delineations were based on T_2 -weighted images only. The border between tumor tissue and peri-tumoral edema was sometimes hardly visible, which led to incorrect inclusion of edematous tissue in the manual segmentations of several tumors, and underlines the need for automatic segmentation methods. Possible susceptibility artifacts that arise from EPI that was used as readout in the parameter mapping acquisitions most likely did not cause the observed mismatch between the automatically and manually segmented tumor volumes, because both the manual and automatic segmentation were performed based on EPI images. No apparent geometric differences between the EPI images of the T_1 , T_2 and ADC mapping protocol were observed. In addition, susceptibility artifacts at air-tissue interfaces were small anyway because of application of ultrasound gel on the tumor-bearing limb (see Materials and Methods).

The inter-observer variability was assessed by calculation of the SI between the different manual segmentations (Table 1). Strong agreement (average SI of 0.86 ± 0.02) was observed between the tumor delineations of the different observers. Visual inspection of the manual segmentations showed that differences in the tumor delineations were mainly caused by the aforementioned inclusion of peri-tumoral edema. In a future study, the accuracy of the manual tumor delineations could be improved by inclusion of diffusion-weighted images as a visual reference. The contrast between tumor and edematous tissue is generally improved on diffusion-weighted images compared to T_2 -weighted images, because of the large difference in apparent diffusion coefficient of water in tumor tissue and edema (29). In addition, the manual tumor segmentations could also be performed on contrast-enhanced T_1 -weighted images. These tumor delineations could then be compared to the automatic segmentations by the proposed intrinsic MR contrast-based method to assess whether our method could rival tumor delineations based on contrast-enhanced MRI that are considered as gold-standard in the clinic. The present study can be regarded as a feasibility study in which we assessed whether automatic tumor segmentation based on intrinsic MR contrast can be performed in a subcutaneous tumor model. Since T_2 -weighted images are generally used for manual segmentations of these subcutaneous tumors rather than contrast-enhanced T_1 -weighted images (e.g., (30-32)), manual tumor delineations from T_2 -weighted images were considered as gold-standard in this study.

Selection of the clusters associated with the tumor tissue was performed based on a threshold-based segmentation method (see Figure 1 and Materials and Methods). The $SI_{\text{manual,automatic}}$ was significantly lower for the threshold-based segmentation method compared to the clustering-based segmentation methods. Although a clear peak that corresponded to tumor tissue was observed in the averaged histogram of signal intensities in the T_2 -weighted images (Figure 1), this peak considerably overlapped with other peaks in the histogram. Consequently, next to the tumor tissue, also regions of other types of tissue were incorrectly assigned as tumor tissue by the threshold-based segmentation. In addition, in individual animals, the tumor peak in the histogram could be slightly shifted compared to the histogram averaged for all animals, resulting in incomplete segmentation of the tumor by the threshold-based segmentation. Nevertheless, the threshold-based segmentation method provided a suitable initial tumor segmentation from which the tumor clusters could be selected in the clustering-based segmentation methods. However, care must be taken on the definition of the thresholds for the T_2 -weighted signal intensity values. To address this, we evaluated the influence of varying the thresholds on the $SI_{\text{manual,automatic}}$ values of the optimized segmentation method. Application of a smaller range of normalized intensity values (0.5-0.6) as threshold did not influence the $SI_{\text{manual,automatic}}$ values, while a larger range (0.4-0.7) did lead to a lower performance of the method ($SI_{\text{manual,automatic}}=0.78\pm 0.11$ compared to $SI_{\text{manual,automatic}}=0.82\pm 0.06$ for the threshold range that was used in this study (0.45-0.65)). This finding suggests that the threshold intensity range can better be chosen conservatively. A too broad range leads to a larger overlap of the tumor peak with peaks of other tissue and consequently to substantial

misclassification of surrounding non-tumor tissue as tumor tissue.

The threshold-based segmentation may however not be applicable for certain (clinical) tumor types in which the contrast between tumor and surrounding tissue is less defined on T_2 -weighted images. For those tumor types, the threshold-based segmentation method may be applied to T_1 -weighted or diffusion-weighted images, if the contrast between tumor and other tissue is better visible on those images. While the threshold-based method likely requires re-definition of the set thresholds for each tumor type, the automatic selection of clusters could possibly also be done based on features that are more specific to tumors in general, such as shape, size (18) and tissue homogeneity (9). Recently, Linguraru et al. showed that liver tumors can be accurately detected on contrast-enhanced computed tomography images by using a set of features that describe the intensity, shape, size and homogeneity of identified objects of interest in the liver (33). Apart from their potential utility for cluster selection, such tumor features could also be employed to select the tumor volume from the results of the morphological component analysis. In the present study the largest component was assumed to be the tumor volume, but this procedure would not be applicable in data sets in which more than one tumor is present. In those cases, the tumor volumes could be automatically selected based on the above-mentioned tumor features.

Furthermore, the clustering-based segmentation may also be performed without input of prior knowledge on tumor tissue characteristics. The expert observer/radiologist could then manually select the cluster(s) associated with tumor tissue and subsequently the tumor volume(s). Although this would imply some user interaction, manual selection of the tumor clusters may still yield a more accurate and faster segmentation than tumor segmentation that is purely based on laborious manual delineations.

Manual segmentation was considered as 'gold standard' for tumor demarcation in the present study. In other reports on automatic segmentation of tumors, manual segmentation is also often used as reference for the evaluation of the performance of the presented segmentation method (3,6,9,10,12). However, the above-discussed inter-observer variability might suggest that manual segmentation is not the best reference for optimization of automatic segmentation methods. The ideal validation of the proposed segmentation method would consist of spatial correlation analysis between the segmented tumors and histological tumor sections. However, spatial registration between MRI and histology is known to be very challenging and would have required an intermediate MRI scan of the excised tumors and a robust anatomical reference (34). Instead of assessment of spatial correlation between MRI and histology, in the present study whole-tumor histology was used to calculate the tumor volume of a small set of tumors. A strong correlation between the automatically segmented tumor volumes and the histology-derived tumor volumes was observed. However, the tumor volumes from histology were consistently smaller than the automatically segmented tumor volumes. This finding can most probably be explained by tissue shrinkage during preparation of the tumors for cryosectioning. In addition, histological processing can induce substantial tissue deformations, which may explain the outlier observed in Figure 7. Visual inspection

of the automatically segmented tumor volume corresponding to the outlier showed that the algorithm had accurately identified the tumor tissue. Tumor weight could provide an alternative measure for tumor volume. Strong correlations between tumor mass and MRI-derived measurements of tumor burden in mouse lung (35) and subcutaneous (19) tumor models have been described earlier.

Clinical translation of the automatic segmentation method seems feasible, since the proposed MRI protocols are already clinically available. However, as indicated above, differences in the properties of the surrounding tissue and the typically lower spatial resolution in clinical MR imaging could affect the accuracy of the proposed algorithm. Furthermore, the typical lower field strength of clinical scanners could influence the observed contrast between tumor and surrounding tissue, since most MR parameters, such as T_1 and T_2 , are dependent on the magnetic field strength. Because of these potential challenges regarding the translation of the proposed method from the subcutaneous mouse tumor model to human tumor types, the algorithm needs to be tested in different tumors to gain insight in its clinical applicability. Adaptations to the algorithm to allow for segmentation of a broader range of tumor types may include the use of other tumor features than the relative signal intensity in the T_2 -weighted images for the automatic selection of the clusters associated with the tumor tissue, as indicated above.

Apart from having potential clinical utility, the proposed method may also be useful for various preclinical applications. Analysis of preclinical MRI data of various tumor models is currently generally performed based on manually drawn ROIs. An observer-independent tumor volume measure could increase the reproducibility in these preclinical studies. Application of the algorithm in several orthotopic animal tumor models is necessary to assess the full suitability of the method in preclinical MR cancer research in general, since segmentation of these orthotopic tumors may, similarly to human tumors, require adaptations to the algorithm.

For practical application of the proposed method in a larger variety of tumor types, the implemented algorithms should be integrated into software package with a graphical user interface (GUI) that facilitates user-friendly MRI data processing and subsequent automatic tumor segmentation. This GUI should allow for user interaction, such as the addition of information on tumor characteristics and manual adjustments to the automatic segmentations. In addition, previous knowledge derived from automatic segmentations of different tumor types could be stored in this software to improve the accuracy of the automatic segmentation of subsequent tumors.

In conclusion, we have shown that accurate, automatic and time-efficient segmentation of tumor tissue subcutaneously growing in the mouse hindleg can be achieved based on endogenous MR contrast only, without the need of injection of a contrast agent. We believe that this automatic segmentation method will be beneficial for various clinical and preclinical applications.

Acknowledgements

This research was performed within the framework of CTMM, the Center for Translational Molecular Medicine (www.ctmm.nl), project VOLTA (grant 05T-201).

References

1. Partridge SC, Gibbs JE, Lu Y, Esserman LJ, Tripathy D, Wolverton DS, Rugo HS, Hwang ES, Ewing CA, Hylton NM. *AJR Am J Roentgenol* 2005;184:1774-1781.
2. Alderliesten T, Schlief A, Peterse J, Loo C, Teertstra H, Muller S, Gilhuijs K. *Invest Radiol* 2007;42:42-49.
3. Chen W, Giger ML, Bick U. *Acad Radiol* 2006;13:63-72.
4. Kannan SR, Ramathilagam S, Devi P, Sathya A. *J Med Syst* 2012;36:321-333.
5. Pang Y, Li L, Hu W, Peng Y, Liu L, Shao Y. *Comput Math Methods Med* 2012;2012:634907.
6. Vignati A, Giannini V, De Luca M, Morra L, Persano D, Carbonaro LA, Bertotto I, Martincich L, Regge D, Bert A, Sardanelli F. *J Magn Reson Imaging* 2011;34:1341-1351.
7. Vos PC, Barentsz JO, Karssemeijer N, Huisman HJ. *Phys Med Biol* 2012;57:1527-1542.
8. Ozer S, Langer DL, Liu X, Haider MA, van der Kwast TH, Evans AJ, Yang Y, Wernick MN, Yetik IS. *Med Phys* 2010;37:1873-1883.
9. Harati V, Khayati R, Farzan A. *Comput Biol Med* 2011;41:483-492.
10. Liu J, Udupa JK, Odhner D, Hackney D, Moonis G. *Comput Med Imaging Graph* 2005;29:21-34.
11. Fathi Kazerooni A, Mohseni M, Rezaei S, Bakhshandehpour G, Saligheh Rad H. *Magn Reson Mater Phy* 2014;doi:10.1007/s10334-014-0442-7
12. Lodder WL, Gilhuijs KG, Lange CA, Pameijer FA, Balm AJ, van den Brekel MW. *Head Neck* 2013;35:521-526.
13. Hijnen N, Elevelt A, Grüll H. *Proceedings of the 3rd MRgFUS Symposium, Washington DC, USA* 2012;ID P-116-EA.
14. Hijnen NM, Elevelt A, Grüll H. *Invest Radiol* 2013;48:517-524.
15. MacNeil S, Bains S, Johnson C, Idee JM, Factor C, Justin G, Fretellier N, Morcos SK. *Invest Radiol* 2011;46:711-717.
16. Kuo PH, Kanal E, Abu-Alfa AK, Cowper SE. *Radiology* 2007;242:647-649.
17. Amet S, Deray G. *Bull Cancer* 2012;99:295-307.
18. Hsieh TM, Liu YM, Liao CC, Xiao F, Chiang IJ, Wong JM. *BMC Med Inform Decis Mak* 2011;11:54.
19. Montelius M, Ljungberg M, Horn M, Forssell-Aronsson E. *BMC Med Imaging* 2012;12:12.
20. Herneth AM, Guccione S, Bednarski M. *Eur J Radiol* 2003;45:208-213.
21. Lim HK, Kim JK, Kim KA, Cho KS. *Radiology* 2009;250:145-151.
22. Levitt M, Freeman R. *J Magn Reson* 1981;43:56-80.
23. Karlsson M, Nordell B. *Magn Reson Imaging* 1999;17:1481-1488.
24. Omran MGH, Engelbrecht AP, Salman A. *Intelligent Data Analysis* 2007;11:583-605.
25. Zijdenbos AP, Dawant BM, Margolin RA, Palmer AC. *IEEE Trans Med Imaging* 1994;13:716-724.
26. Khayati R, Vafadust M, Towhidkhan F, Nabavi M. *Comput Biol Med* 2008;38:379-390.
27. Belsley DA, Kuh E, Welsch RE. *John Wiley & Sons, Inc.*; 2005.
28. Schmitz AC, Gianfelice D, Daniel BL, Mali WP, van den Bosch MA. *Eur Radiol* 2008;18:1431-1441.
29. Spuentrup E, Buecker A, Adam G, van Vaals JJ, Guenther RW. *AJR Am J Roentgenol* 2001;176:351-358.
30. Zhang CC, Yan Z, Giddabasappa A, Lappin PB, Painter CL, Zhang Q, Li G, Goodman J, Simmons B, Pascual B, Lee J, Levkoff T, Nichols T, Xie Z. *Cancer medicine* 2014;3:462-471.
31. Zhen Z, Tang W, Chuang YJ, Todd T, Zhang W, Lin X, Niu G, Liu G, Wang L, Pan Z, Chen X, Xie J. *ACS nano* 2014;8:6004-6013.
32. Zhang L, Zhou H, Belzile O, Thorpe P, Zhao D. *Journal of controlled release : official journal of the Controlled Release Society* 2014;183:114-123.
33. Linguraru MG, Richbourg WJ, Liu J, Watt JM, Pamulapati V, Wang S, Summers RM. *IEEE Trans Med Imaging* 2012;31:1965-1976.
34. Alic L, Haeck JC, Bol K, Klein S, van Tiel ST, Wielepolski PA, de Jong M, Niessen WJ, Bernsen M, Veenland JF. *PLoS One* 2011;6:e22835.
35. Tidwell VK, Garbow JR, Krupnick AS, Engelbach JA, Nehorai A. *Magn Reson Med* 2012;67:572-579.

Chapter 3

Multiparametric MRI Analysis for the Identification of High Intensity Focused Ultrasound-treated Tumor Tissue

Stefanie Hectors*, Igor Jacobs*, Gustav Strijkers, Klaas Nicolay

Published in PLoS One 2014;9(6):e99936

* authors contributed equally

Abstract

Purpose

In this study endogenous magnetic resonance imaging (MRI) biomarkers for accurate segmentation of High Intensity Focused Ultrasound (HIFU)-treated tumor tissue and residual or recurring non-treated tumor tissue were identified.

Materials and Methods

Multiparametric MRI, consisting of quantitative T_1 , T_2 , apparent diffusion coefficient (ADC) and magnetization transfer ratio (MTR) mapping, was performed in tumor-bearing mice before ($n=14$), 1 h after ($n=14$) and 72 h ($n=7$) after HIFU treatment. A non-treated control group was included ($n=7$). Cluster analysis using the Iterative Self Organizing Data Analysis (ISODATA) technique was performed on subsets of MRI parameters (feature vectors). The clusters resulting from the ISODATA segmentation were divided into a viable and non-viable class based on the fraction of pixels assigned to the clusters at the different experimental time points. ISODATA-derived non-viable tumor fractions were quantitatively compared to histology-derived non-viable tumor volume fractions.

Results

The highest agreement between the ISODATA-derived and histology-derived non-viable tumor fractions was observed for feature vector $\{T_1, T_2, ADC\}$. R_1 ($1/T_1$), R_2 ($1/T_2$), ADC and MTR each were significantly increased in the ISODATA-defined non-viable tumor tissue at 1 h after HIFU treatment compared to viable, non-treated tumor tissue. R_1 , ADC and MTR were also significantly increased at 72 h after HIFU.

Conclusions

This study demonstrates that non-viable, HIFU-treated tumor tissue can be distinguished from viable, non-treated tumor tissue using multiparametric MRI analysis. Clinical application of the presented methodology may allow for automated, accurate and objective evaluation of HIFU treatment.

Introduction

Thermal ablation of tumors with High Intensity Focused Ultrasound (HIFU) (1,2) is currently being introduced in the clinic for the treatment of both benign tumors, mainly uterine fibroids (3,4), and malignant tumors, such as prostate (5-7) and breast tumors (8) and liver metastases (9,10). HIFU treatment of malignant tumors should cover the entire tumor, which requires adequate treatment planning, monitoring and evaluation. HIFU therapy is therefore commonly performed under image guidance, often using magnetic resonance imaging (MRI) (11,12). MRI facilitates treatment planning because of its excellent soft tissue contrast. Furthermore, MR thermometry allows for real-time temperature feedback during the procedure (12). MRI is also well-suited for the evaluation of treatment outcome.

With MR thermometry, lethal thermal dose areas (i.e. tissue regions that received a thermal dose of at least 240 equivalent minutes (EM) at 43°C) can be identified (13). However, a recent study on MR-guided HIFU treatment of a rabbit tumor model showed that the 240-EM thermal dose limit underestimates the necrotic tissue area immediately after HIFU treatment (14), possibly caused by the dependence of thermal dose necrosis thresholds on tissue type (13,15).

For treatment evaluation commonly conventional MRI techniques are used, including T_2 -weighted and contrast-enhanced T_1 -weighted imaging. Kirkham et al. (7) reported a heterogeneous appearance of the tumor tissue on T_2 -weighted images up to 1 month after HIFU ablation of human prostate tumors, showing that T_2 -weighted imaging alone is inadequate for the assessment of necrosis. Furthermore, on contrast-enhanced T_1 -weighted imaging, an enhancing rim, surrounding the non-enhancing central core of necrosis, was observed, that can either originate from residual tumor tissue or from inflammation-induced hyperemia. A similar enhancement pattern was observed in other clinical studies on HIFU treatment of prostate tumors (6) and on radiofrequency (RF) ablation of kidney (16) and liver tumors (17). Furthermore, the aforementioned study of HIFU treatment of a rabbit tumor model reported that contrast-enhanced T_1 -weighted imaging underestimates the area of necrosis in histology directly after HIFU treatment (14). An additional drawback of contrast-enhanced T_1 -weighted imaging for the evaluation of HIFU treatment is the need for the injection of a Gadolinium (Gd) contrast agent. If immediate retreatment needs to be performed directly after treatment evaluation, the Gd contrast agent could interfere with the HIFU procedure. Presence of Gd in the tissue could induce susceptibility artifacts in the thermometry acquisitions, resulting in inaccurate temperature maps (18).

Several studies have reported on the evaluation of HIFU treatment with more advanced MRI protocols. In clinical studies, preliminary experiments were conducted in which diffusion-weighted imaging was used to evaluate HIFU treatment. A recent study on HIFU ablation of malignant liver lesions showed a significant increase in the apparent diffusion

coefficient (ADC) in the necrotic, HIFU-treated tumor tissue (19). In contrast, a decrease in ADC was observed after HIFU treatment of uterine fibroids (20,21). The magnetization transfer ratio (MTR) is another MRI parameter that has potential sensitivity for the distinction between HIFU-treated and non-treated tumor tissue. The MTR is a measure for the level of magnetization exchange between water protons and semi-solid macromolecular protons in tissue (22). An increase in tissue MTR has been observed after thermal treatment of ex vivo porcine muscle tissue (23).

Overall, multiple studies have been published in which different MRI parameters for HIFU treatment evaluation were proposed. However, no quantitative studies on the correlation between changes in the different MRI parameters and histological analysis of the HIFU-treated lesion have been reported. Recently, multiparametric MRI has been proposed as a possibly suitable approach for the evaluation of HIFU treatment of prostate tumors (24). To the best of our knowledge, multiparametric MR analysis consisting of quantitative assessment of HIFU-induced changes in the tumor tissue based on different combinations of MRI parameters has not yet been performed.

Therefore, the goal of the present study was to identify endogenous MRI biomarkers that can be used to distinguish between HIFU-treated and non-treated tumor tissue, using multiparametric MRI analysis combined with quantitative histological evaluation. Specifically, the multiparametric MRI protocol consisted of quantitative assessment of T_1 , T_2 , ADC and MTR and was used to assess changes in tumor tissue status as induced by HIFU treatment in a murine tumor model. The HIFU treatment consisted of partial ablation of the tumors to allow for internal reference between HIFU-treated and residual non-treated tumor tissue. MR evaluation of the tumor tissue was performed before and at 1 h and at 72 h after HIFU. The Iterative Self Organizing Data Analysis (ISODATA) clustering algorithm (25) was implemented and employed to segment the multispectral data into tissue populations with similar MRI parameter values. Cluster analysis was performed on different subsets of MRI parameters. The optimal set of MR parameters for the segmentation of HIFU-treated and non-treated tissue was determined by quantitative comparison between ISODATA-derived and histology-derived non-viable tumor volume fractions.

Materials and Methods

Ethics Statement

All animal experiments were performed according to the Directive 2010/63/EU of the European Parliament and approved by the Animal Care and Use Committee of Maastricht University.

Murine tumor model

CT26.WT murine colon carcinoma cells (American Type Culture Collection (ATCC; CRL-2638)) were cultured as a monolayer at 37°C and 5% CO₂ in RPMI-1640 medium

(Invitrogen, Breda, The Netherlands), supplemented with 10% fetal bovine serum (Greiner Bio-One, Alphen a/d Rijn, The Netherlands) and 50 U/ml penicillin/streptomycin (Lonza Bioscience, Basel, Switzerland). Early passages (5-10) of the original ATCC batch were used for inoculation.

10-12 week-old Balb/c mice (Charles River, Maastricht, The Netherlands) were inoculated with 2×10^6 CT26.WT cells subcutaneously in the right hind limb. Approximately 10 days after inoculation, tumors became palpable in all animals.

Study design

Animals were subjected to MRI examination 24 h before (n=14), 1 h after (n=14) and 72 h after HIFU treatment (n=7). A control group of non-treated animals (n=7) was included. The time points of MRI examinations of the control animals were the same as for the HIFU-treated animals and are referred to as Day 0, Day 1 and Day 4. Directly after the last MRI experiment, the mice were sacrificed, and the tumors were dissected and processed for histological analysis. This study design led to three different groups for quantitative histology: animals sacrificed after the MRI examination at 1 h after HIFU treatment (n=7, referred to as '1 h after HIFU'), animals sacrificed after the MRI examination at 72 h after HIFU treatment (n=7, referred to as '72 h after HIFU') and non-treated control animals (n=7, referred to as 'Control').

HIFU treatment

HIFU treatment was performed with the preclinical Therapy and Imaging Probe System (TIPS, Philips Research, Briarcliff Manor, NY, USA) (26), outside the MR system. Animals were initially anesthetized with 3% isoflurane in medical air and maintained with 1-2% isoflurane during HIFU treatment. Precautionary analgesia (buprenorphine, 0.1 mg/kg s.c.) was administered 30 min before treatment. The non-treated control animals received an equal dose of analgesia at the corresponding time point. Animal temperature was maintained with an infrared lamp controlled by feedback from a rectal temperature sensor, supplemented with a warm water pad. The tumor-bearing paw was positioned underneath the therapeutic transducer. The paw was fully covered with degassed ultrasound transmission gel (Aquasonic 100, Parker Laboratories, Fairfield, NJ, USA). An acoustic absorber (Aptflex F28P, Precision Acoustics, Dorchester, UK) was positioned underneath the paw to prevent far-field heating. A photograph and a schematic drawing of the HIFU set-up are shown in Supplemental Figure S1.

Partial tumor ablation was performed such that both HIFU-treated and non-treated tumor tissue were present after treatment. Positioning of the tumor in the focal point of the therapeutic transducer was confirmed by use of an ultrasound imaging system (HDI5000 imaging system combined with a P7-4 phased array transducer, Philips Ultrasound, Bothell, WA, USA). Ultrasound imaging was solely used for treatment planning; ultrasound-based treatment monitoring was beyond the scope of the present study. A square 4×4 mm² treatment grid consisting of 25 equally-spaced treatment points was defined within the tumor. A wait time of 120 s was applied between the point-wise HIFU

treatments to allow sufficient cooling of the tissue. Treatment settings were: frequency=1.4 MHz, pulse repetition frequency=20 Hz, acoustic power=12 W, duty cycle=50%, treatment time=30 s. In three pilot experiments, a thermocouple (T-type thermocouple; T-150A, Physitemp Instruments, Clifton, NJ, USA) was positioned in the focal point of the therapeutic transducer to monitor temperature during the treatment. The temperature increased to approximately 66°C during the sonication and decreased again to the pre-sonication temperature (approximately 35°C) during the wait time. A representative temperature profile is shown in Supplemental Figure S2. The thermocouple was not inserted during the treatment of the experimental groups to prevent non-HIFU-related damage to the tumor tissue.

MRI measurements

MRI measurements were performed with a 6.3 T scanner (Bruker BioSpin, Ettlingen, Germany) using a 3.2-cm-diameter quadrature birdcage RF coil (Rapid Biomedical, Rimpfing, Germany). Anesthesia was maintained with 1-2% isoflurane during the MRI experiments. The mice were positioned in a custom-made cradle, equipped with a mask for anesthetic gas. The tumor-bearing paw was fixed in the set-up by adhesive tape in order to prevent motion artifacts. No motion was observed between the images of the different sequences and therefore no further post-processing image registration proved necessary. Respiration was monitored with a balloon sensor. Body temperature was monitored and maintained with a warm water pad. For reduction of susceptibility artifacts in the echo planar imaging (EPI) sequence, the tumor-bearing paw was covered with degassed ultrasound gel (Aquasonic 100, Parker Laboratories). Artifacts were further reduced by local shimming of the tumor-bearing paw. To illustrate the obtained image quality of the EPI sequence, representative images of a conventional T_2 -weighted spin-echo acquisition and a T_2 -prepared gradient-echo EPI (GE-EPI) sequence are shown in Supplemental Figure S3. No apparent geometric distortion artifacts were present in the EPI images.

The multi-slice MRI protocol, covering the whole tumor, started with a fat-suppressed T_2 -weighted spin-echo sequence (echo time TE=30 ms, repetition time TR=1000 ms, number of averages NA=1) for anatomical reference. Subsequently, T_1 , T_2 , ADC and MTR mapping were performed. T_1 mapping was performed with an inversion recovery Look-Locker EPI method (TE=8 ms, TR=10000 ms, inversion time=30 ms, flip angle=20°, pulse separation=400 ms, number of points=15, NA=2). For T_2 mapping, a T_2 -weighted MLEV-prepared (27) GE-EPI sequence (TR=2000 ms, NA=2) was acquired with 7 TE's ranging from 1 to 82 ms. For ADC mapping, a diffusion-weighted double spin-echo prepared EPI sequence (TE=41 ms, TR=4000 ms, NA=4) was used to acquire images with 4 different b-values (0, 100, 200 and 400 s/mm²). The diffusion-sensitizing gradient was applied separately in three orthogonal directions. The MTR mapping protocol consisted of two GE-EPI acquisitions (TE=8 ms, TR=8000 ms, NA=2) with and without an off-resonance preparation pulse (4000 ms block pulse, $B_1=1.3$ μ T, -10 ppm from water resonance

frequency). All acquired images had a matrix size of 128x128, FOV of 4x4 cm² and 1 mm slice thickness. Twelve to 16 slices were acquired covering the whole tumor volume.

Image processing and generation of parameter maps

Image analysis was performed in Mathematica 7.0 (Wolfram Research, Champaign, IL, USA). Regions of interest (ROIs) were defined on the T₂-weighted images by manually drawing contours around the tumor tissue on each slice. Diffusion-weighted images were used as an additional reference for tumor demarcation. Parameter maps were calculated on a pixel-by-pixel basis in each slice. T₁ maps were generated as described previously (28). T₂ maps were calculated from mono-exponential fitting of the multi-echo data. For the generation of ADC maps, mono-exponential fitting was performed through the signal intensities at the different b-values for each diffusion-encoding direction separately. Next, ADC values of the different directions were averaged to obtain the final (orientation-invariant) ADC value. MTR maps were generated according to $MTR=(1-S/S_0)*100\%$, in which S and S₀ are the pixel signal intensities with and without off-resonance irradiation, respectively.

ISODATA analysis

ISODATA cluster analysis was employed to segment the multiparametric data into groups of pixels, i.e. clusters, with similar MR parameter values. The ISODATA technique was implemented in Mathematica 7.0 according to the description given by Jacobs et al. (25). A schematic overview of the ISODATA algorithm can be found in Supplemental Information S1. The ISODATA clustering technique is similar to the widely applied clustering algorithm k-means (29). However, as opposed to k-means, the number of clusters does not have to be determined a priori for the ISODATA algorithm. The number of clusters is rather adjusted iteratively according to the Euclidean distance between and within the clusters. ISODATA clustering was performed on the multi-slice parametric images of all animals (HIFU-treated and control) at all time points simultaneously. Prior to ISODATA clustering, features were normalized (mean $\mu=0$, standard deviation (SD)=1) to remove scaling differences between the different parameters. Pixels of which the signal intensity in the T₂-weighted images was at noise level, e.g. because of HIFU-induced hemorrhage, were excluded from ISODATA analysis. ISODATA clustering was performed on the following subsets of MRI parameters, termed feature vectors: {T₂}, {ADC}, {T₁,T₂}, {T₂,ADC}, {T₁,ADC}, {ADC,MTR}, {T₁,T₂,ADC}, {T₂,ADC,MTR}, {T₁,ADC,MTR}, {T₁,T₂,MTR} and {T₁,T₂,ADC,MTR}. The resulting clusters were divided into two different classes:

- Non-viable: clusters of which the fraction of assigned pixels increased significantly after HIFU (either at 1 h or 72 h) compared to before HIFU (paired Student's t-test, P<0.05);
- Viable: all remaining clusters.

Subsequently, all tumor pixels of both the HIFU-treated and non-treated animals at all experimental time points were assigned as either viable or non-viable based on the class of the cluster to which the pixel belongs.

A schematic view of the classification of the clusters into either non-viable or viable tumor tissue is given in Figure 1.

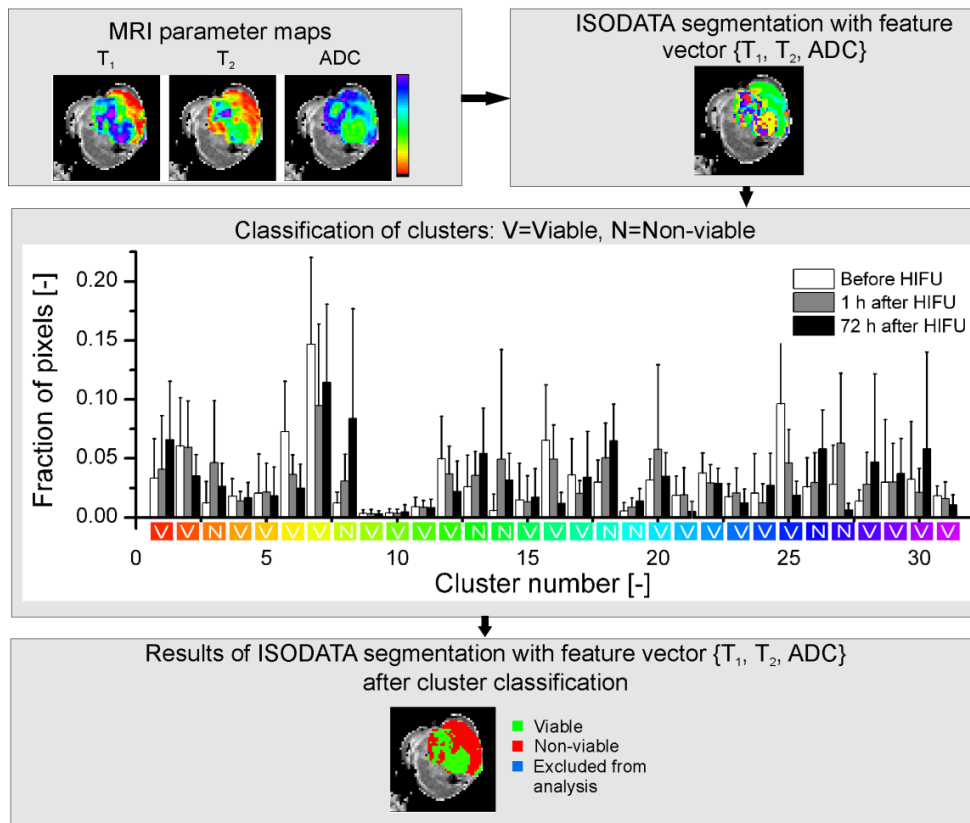


Figure 1. Flow chart of the classification of clusters resulting from ISODATA segmentation with feature vector $\{T_1, T_2, ADC\}$. MRI parameter maps were generated from the multiparametric MRI data (top left). The displayed MRI results originate from a tumor scanned at 72 h after HIFU treatment. Pixels were clustered into tissue populations with similar MRI parameters (top right; different colors represent different clusters). The resulting clusters were classified as either viable (labeled 'V' in the histogram) or non-viable (labeled 'N' in the histogram) based on the fraction of pixels assigned to the clusters at the different time points. Clusters of which the fraction of pixels had increased significantly (paired Student's t-test, $P < 0.05$) after HIFU compared to before HIFU were assigned to non-viable tumor tissue. The remaining clusters were assigned to viable tumor tissue. The histogram of the fractions of tumor pixels in each cluster at the different time points is displayed in the center of the figure. The white, grey and black bars represent mean \pm SD of the fractions of tumor pixels before, at 1 h after and at 72 h after HIFU, respectively. The color coding on the x-axis of the histogram corresponds to the cluster colors in the ISODATA segmentation results (top right). The result of the ISODATA segmentation after classification of the clusters as either viable or non-viable tumor tissue is shown in the bottom part of the figure. A small number of tumor pixels was excluded from ISODATA analysis, because of a low signal-to-noise ratio (see Materials and Methods).

Based on this classification, ISODATA-derived non-viable tumor volume fractions were calculated for each tumor for the different feature vectors. These tumor fractions were compared to histology-derived non-viable tumor volume fractions in order to select the optimal feature vector, i.e. the combination of MRI indices, which led to the best agreement with the histological differentiation between non-viable and viable tumor tissue.

Mean MRI parameter values in the pixels classified as viable and non-viable tumor tissue were calculated to quantify the effects of HIFU treatment on the measured MRI parameters.

Histological analysis

Dissected tumors were snap-frozen in isopentane and stored at -80°C . Tumors were cut into $5\ \mu\text{m}$ thick sections with a distance of approximately $300\ \mu\text{m}$ between the sections. The cryo-sections were briefly air-dried and subsequently stained for nicotinamide adenine dinucleotide (NADH) diaphorase activity to assess cell viability. NADH-diaphorase staining is a powerful histological tool for demarcation between viable and non-viable tumor tissue after HIFU treatment (30). Sections were incubated at 37°C for 1 h in Gomori-Tris-HCl buffer (pH 7.4) containing β -NAD reduced disodium salt hydrate (Sigma-Aldrich, St. Louis, MO, USA, 0.71 mg/ml buffer solution) and nitro blue tetrazolium (Sigma-Aldrich, 0.29 mg/ml buffer solution). Brightfield microscopy was performed on all sections and consisted of mosaic acquisition of the entire section at 5x magnification.

Analysis of the microscopy images was performed in Mathematica 7.0. ROIs were manually drawn around the pale non-viable tumor tissue and the entire tumor tissue on all sections of each tumor. From the ratio between the ROI areas of non-viable tumor tissue and entire tumor tissue on all tumor sections, a histology-derived non-viable tumor volume fraction was determined for each tumor.

Statistical analysis

Data are reported as mean \pm SD. For the determination of the optimal feature vector, non-viable tumor fractions derived from ISODATA segmentation with the different feature vectors were quantitatively compared to the histology-derived non-viable tumor volume fractions. Initial feature vector selection was based on the one-to-one correspondence between histology-derived and ISODATA-derived non-viable tumor fractions. The one-to-one correspondence was determined by calculation of the coefficient of determination (R^2) of the data points, consisting of the ISODATA-derived and the histology-derived non-viable tumor fraction of each tumor, to the line of identity ($y=x$). This initial selection led to the elimination of feature vectors for which the ISODATA-derived non-viable tumor fractions were either strongly over- or underestimated compared to the histology-derived non-viable tumor fractions. Subsequently, Pearson's correlation coefficients were determined between the histology-derived and ISODATA-derived tumor fractions, as a measure for the strength of the linear relationship between the histology-derived and ISODATA-derived non-viable tumor fractions. These correlation values were determined

for two different groups of animals: one group consisting of the animals sacrificed after the MRI examination at 1 h after HIFU and the non-treated control animals (referred to as '1 h after HIFU + Control') and one group consisting of the animals sacrificed after the MRI examination at 72 h after HIFU and the control animals (referred to as '72 h after HIFU + Control'). This division in groups was made to take into account the temporal changes in tumor tissue after HIFU treatment, which might lead to a different optimal feature vector for the different time points after HIFU. The control animals were included in both groups to increase the statistical power and to obtain a larger range of non-viable tumor fractions. Differences in correlation values between the different feature vectors were tested for significance with a Wolfe's test for Comparing Dependent Correlation Coefficients (31).

For the HIFU-treated animals, the MRI parameter values in ISODATA-defined non-treated tumor tissue at all time points were compared to the parameter values in ISODATA-defined non-viable tumor tissue at 1 h and 72 h after HIFU with a paired Student's t-test. For all tests the level of significance was set at $\alpha=0.05$.

Results

MRI parameter maps

Representative MRI parameter maps as measured before, 1 h and 72 h after HIFU treatment are shown in Figure 2. A heterogeneous appearance of the HIFU-treated lesion was visible on the T_2 -weighted images at both time points after HIFU treatment. Distinct regions with decreased T_1 and T_2 were observed at 1 h after HIFU. A further increase in the area of T_1 and T_2 decline was observed in these regions at 72 h after HIFU. Increased ADC and MTR values were observed in roughly the same regions of T_1 and T_2 change, both at 1 h and 72 h after HIFU. However, no sharp demarcation between HIFU-treated and non-treated tumor tissue was visible on the individual MRI parameter maps obtained after HIFU. Tumor regions with altered MRI parameters co-localized only partially for the different parameters. This implied that more advanced analysis of the multiparametric data is necessary to enable MRI-based identification of the HIFU-treated tumor tissue. Therefore, quantitative multiparametric analysis of the MRI parameter changes after HIFU treatment was performed using the ISODATA technique. Clusters resulting from the ISODATA segmentation were classified as either viable or non-viable based on the fraction of pixels assigned to the clusters at the different experimental time points (Figure 1). ISODATA clustering was applied on different combinations of the MRI parameters (i.e. feature vectors), to determine the feature vector that led to the most accurate segmentation between viable and non-viable tumor tissue.

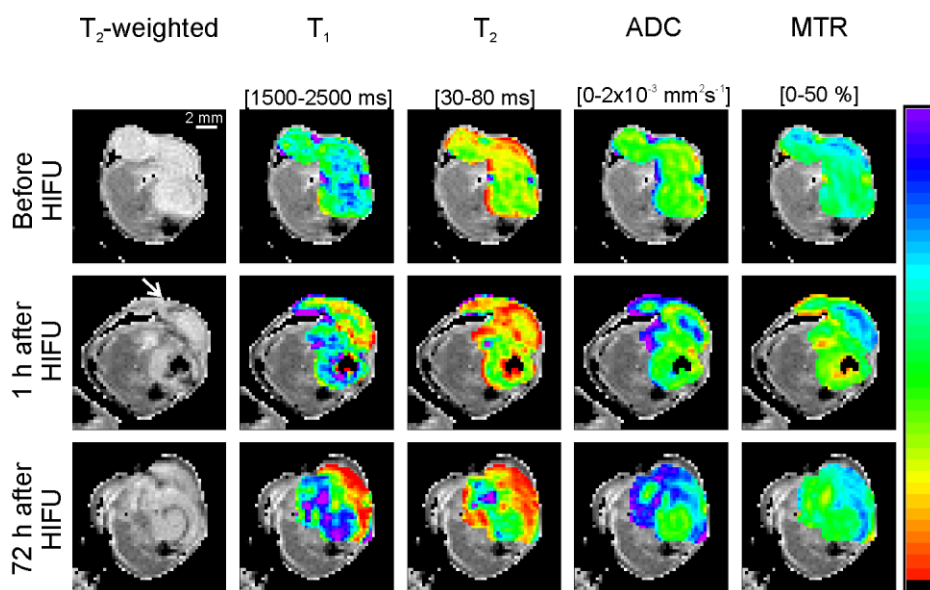


Figure 2. MRI parameter maps before and longitudinally after HIFU treatment. Representative example of multiparametric MRI of the hind limb region of a HIFU-treated tumor-bearing mouse before and 1 h and 72 h after HIFU treatment. T_2 -weighted images of an axial slice of the tumor-bearing paw are shown in the left panel. The hyper-intense tumor tissue is surrounded by hypo-intense muscle tissue. In the other panels the same T_2 -weighted images are displayed except that the tumor pixels are overlaid with MRI parameter maps. The parameter maps were scaled according to the color scale bar shown at the right-hand side of the figure. The corresponding parameter range for this scale bar is indicated above each panel. The approximate direction of the HIFU treatment is shown by the white arrow on the T_2 -weighted image, which was collected 1 h after HIFU treatment.

Feature vector selection

Selection of the optimal feature vector for the discrimination between HIFU-treated, non-viable and non-treated, viable tumor tissue was performed based on quantitative comparison between non-viable tumor fractions resulting from ISODATA segmentation with different feature vectors and non-viable tumor fractions derived from whole-tumor-based histology.

Plots of the histology-derived non-viable tumor fractions versus the ISODATA-derived non-viable tumor fractions were processed for all assessed feature vectors. The R^2 of the data points to the line of identity, indicative of the level of one-to-one correspondence between the results from ISODATA analysis and histology, was used as an initial criterion for feature vector selection. R^2 values for all assessed feature vectors are listed in Table 1. Relatively high R^2 values (>0.7) were observed for three feature vectors: {ADC}, $\{T_2, \text{ADC}\}$ and $\{T_1, T_2, \text{ADC}\}$, which were therefore considered candidates for the segmentation of HIFU-treated tumor tissue. Scatter plots of the ISODATA-derived and histology-derived non-viable tumor fractions are displayed in Figure 3 for these candidate feature vectors.

Table 1 R^2 values of ISODATA-derived versus histology-derived non-viable tumor fractions to the line of identity for all assessed feature vectors.

Feature vector	R^2 to line of identity [-]
{ T_2 }	0.60
{ADC}	0.74
{ T_1 , T_2 }	0.70
{ T_2 , ADC}	0.77
{ T_1 , ADC}	0.68
{ADC, MTR}	-1.67
{ T_1 , T_2 , ADC}	0.77
{ T_2 , ADC, MTR}	-0.09
{ T_1 , ADC, MTR}	0.42
{ T_1 , T_2 , MTR}	-0.79
{ T_1 , T_2 , ADC, MTR}	-0.16

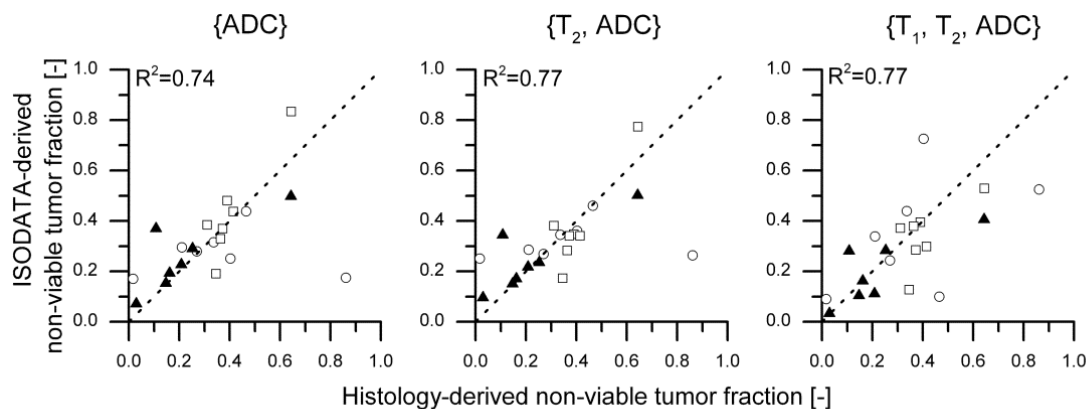


Figure 3. Scatter plots of the ISODATA-derived non-viable tumor fractions following segmentation with feature vectors {ADC}, { T_2 , ADC} and { T_1 , T_2 , ADC} as a function of the histology-derived non-viable tumor fractions. The symbols \circ , \square and \blacktriangle indicate groups '1 h after HIFU', '72 h after HIFU' and 'Control', respectively. The line of identity is shown as visual reference. The R^2 values of the data to the line of identity are shown in the top left corner of each plot.

The correlation between the histology-derived and ISODATA-derived non-viable tumor fractions was used as a second criterion for feature vector selection. The experimental groups were divided into two groups for this correlation analysis: '1 h after HIFU + Control' and '72 h after HIFU + Control' (see Methods). Correlation plots for the three candidate feature vectors are depicted in Figure 4 for both groups. For group '1 h after HIFU + Control' the strongest correlation was found for feature vector { T_1 , T_2 , ADC} ($r=0.62$, moderate correlation; Figure 4A). However, for this group, no statistically significant differences between the correlation values of the different candidate feature vectors were observed. A strong correlation was observed for all three feature vectors for group '72 h after HIFU + Control' (Figure 4B). The strongest correlation in this case was found for feature vector {ADC} ($r=0.83$), which was significantly higher than the correlation value found for feature vector { T_1 , T_2 , ADC} ($r=0.80$).

The third criterion for feature selection consisted of minimization of the number of pixels incorrectly assigned to non-viable tissue before ablation. Most notably for the feature vectors $\{\text{ADC}\}$ and $\{\text{T}_2, \text{ADC}\}$, a portion of pixels in the tumor rim was incorrectly assigned to non-viable tissue before HIFU, whereas this was observed to a lesser extent for feature vector $\{\text{T}_1, \text{T}_2, \text{ADC}\}$. The incorrect classification of the tumor pixels was caused by presence of peritumoral edema at the tumor rim. Visual inspection during excision of the tumors confirmed presence of edema around the HIFU-treated tumors. The fraction of rim pixels (rim thickness of 3 pixels) that was incorrectly assigned as non-viable before HIFU application was therefore used as a further selection measure. The fractions of incorrectly assigned rim pixels were significantly lower for feature vector $\{\text{T}_1, \text{T}_2, \text{ADC}\}$ (0.15 ± 0.09) as compared to feature vectors $\{\text{ADC}\}$ and $\{\text{T}_2, \text{ADC}\}$ (0.28 ± 0.10 and 0.25 ± 0.08 , respectively).

Based on the above three criteria, feature vector $\{\text{T}_1, \text{T}_2, \text{ADC}\}$ provided the optimal combination of MRI parameters for differentiation between HIFU-treated and non-treated tumor tissue.

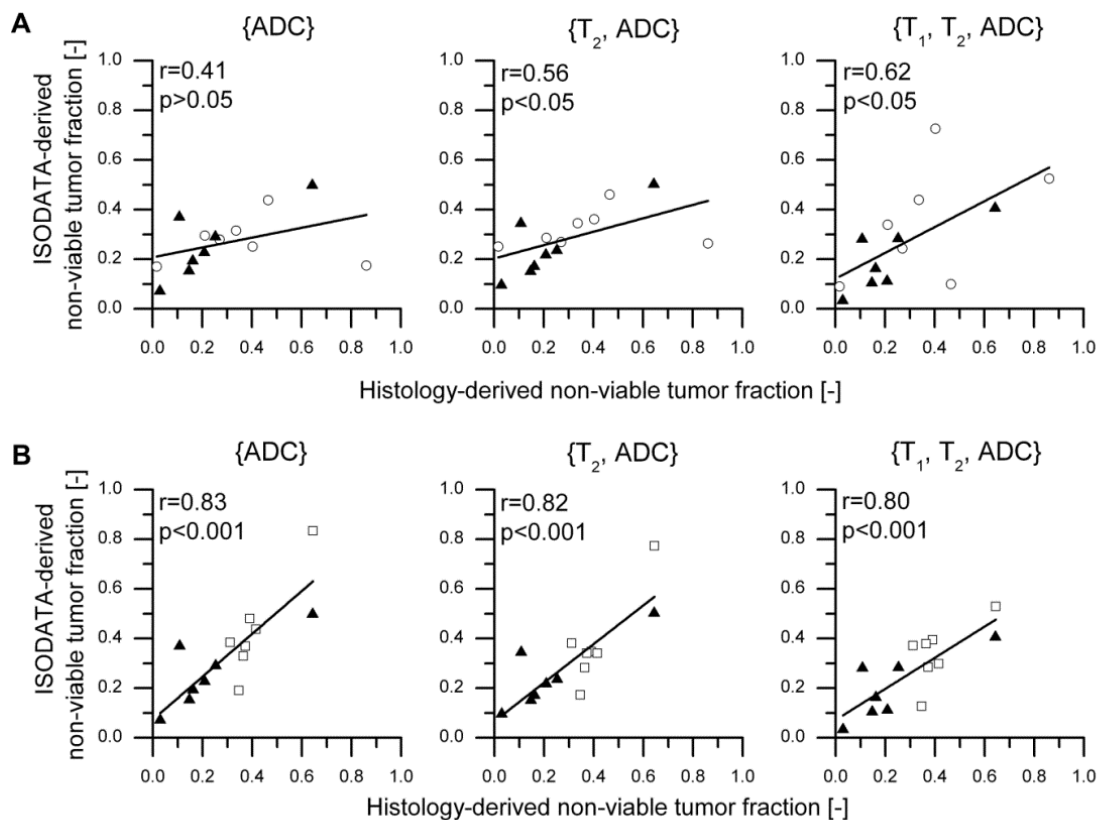


Figure 4. Correlation between histology-derived and ISODATA-derived non-viable tumor fractions. Correlation plots of ISODATA-derived non-viable tumor fractions following segmentation with feature vectors $\{\text{ADC}\}$, $\{\text{T}_2, \text{ADC}\}$ and $\{\text{T}_1, \text{T}_2, \text{ADC}\}$ as a function of the histology-derived non-viable tumor fractions for two different groups of animals: '1 h after HIFU + Control' (A) and '72 h after HIFU + Control' (B). The symbols \circ , \square and \blacktriangle indicate groups '1 h after HIFU', '72 h after HIFU' and 'Control', respectively. Correlation values between the ISODATA-derived and the histology-derived tumor fractions are listed in the top left corner of each plot.

In Figure 5A representative results of the ISODATA segmentation with feature vector $\{T_1, T_2, ADC\}$ are displayed for two HIFU-treated animals. As anticipated, at baseline the largest fraction of pixels (0.85 ± 0.10 for all HIFU-treated animals) was assigned to viable tumor tissue. At 1 h after HIFU a region emerged in which pixels were assigned to HIFU-treated, i.e. non-viable tumor tissue. At 72 h after HIFU this region had grown and showed good spatial agreement with a region of non-viable tumor tissue on an NADH-diaphorase stained section at approximately the same location within the tumor. In comparison, Figure 5B shows representative results of ISODATA segmentation of a non-treated control animal that was subjected to MRI examination at the same time points. Here only a small number of pixels was assigned to non-viable tumor tissue at all time points, in agreement with a fully viable tumor observed by NADH-diaphorase staining.

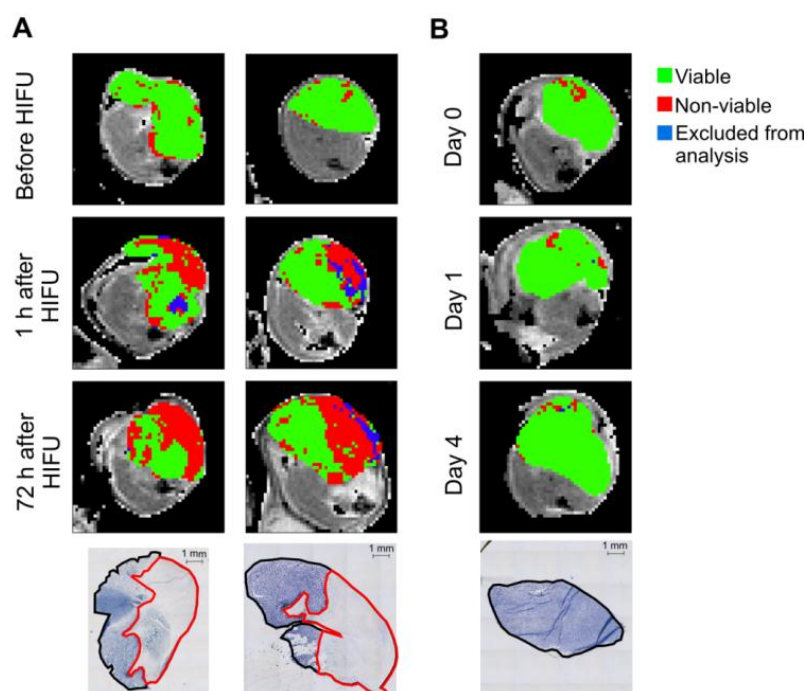


Figure 5. A) Representative T_2 -weighted images of the hind limb region of two HIFU-treated mice before, 1 h after and 72 h after HIFU. The results of ISODATA segmentation with feature vector $\{T_1, T_2, ADC\}$ are overlaid on the tumor pixels. NADH-diaphorase stained sections of tumors dissected at 72 h after HIFU were made at approximately the same location within the tumor and are shown at the bottom of each column. ROIs around the entire (black line) and non-viable (red line) tumor tissue were drawn manually. Data in the left column are from the animal presented in Figure 1. B) Similar data of a non-treated control mouse that was subjected to serial MRI measurements at the same time points (Day 0, Day 1 and Day 4) as the HIFU-treated animals. Scale bar = 1 mm.

Evaluation of MRI parameter changes

Average MRI parameter values of ISODATA-defined viable tumor tissue at all experimental time points and non-viable tumor tissue at both time points after HIFU are listed in Table 2 for feature vector $\{T_1, T_2, ADC\}$. R_1 ($1/T_1$), R_2 ($1/T_2$), ADC and MTR were significantly increased in the non-viable, HIFU-treated tumor tissue 1 h after HIFU compared to viable tumor tissue. R_1 , ADC and MTR remained significantly increased in

non-viable tumor tissue 72 h after HIFU. No significant differences in parameter values were observed between 1 h and 72 h after HIFU treatment.

Table 2. MRI parameter values (mean±SD) in viable tumor tissue (tumor tissue assigned as viable tumor tissue at all time points (n=14)), non-viable tumor tissue at 1 h after HIFU (n=14) and non-viable tumor tissue at 72 h after HIFU (n=7) of the HIFU-treated animals following ISODATA segmentation with feature vector $\{T_1, T_2, ADC\}$. * and ** denote a significant difference between viable and non-viable tumor tissue with $P<0.05$ and $P<0.001$, respectively (paired Student's t-test).

MRI parameter	Viable tumor tissue	Non-viable tumor tissue 1 h after HIFU	Non-viable tumor tissue 72 h after HIFU
$R_1 [s^{-1}]$	0.45±0.01	0.61±0.13 **	0.60±0.06 **
$R_2 [s^{-1}]$	21.7±1.4	35.8±19.5 **	34.0±21.0
ADC [$10^{-3} \text{ mm}^2 \text{ s}^{-1}$]	0.84±0.12	1.09±0.20 **	1.25±0.16 **
MTR [%]	23.3±1.2	26.4±2.7 **	26.4±3.5 *

Discussion and Conclusions

In the present study multiparametric MR analysis was performed to distinguish non-viable, HIFU-treated tumor tissue from viable, non-treated tumor tissue in a murine tumor model. The longitudinal multiparametric MRI measurements consisted of quantitative assessments of T_1 , T_2 , ADC and MTR. ISODATA segmentation was applied on various feature vectors. ISODATA-derived non-viable tumor volume fractions were compared to non-viable tumor fractions derived from quantitative histology to identify the optimal feature vector for differentiation between non-viable, HIFU-treated and viable, non-treated tumor tissue.

The most accurate distinction between HIFU-treated and non-treated tumor tissue was obtained with feature vector $\{T_1, T_2, ADC\}$. For this feature vector, the correlation between the histology-derived and ISODATA-derived fractions of non-viable tumor tissue was lower for group '1 h after HIFU + Control' than for group '72 h after HIFU + Control'. These results suggest that time is needed before HIFU-induced changes in the tumor tissue produce sufficient detectable contrast in the MRI images.

A multiparametric protocol consisting of T_1 , T_2 and ADC mapping was sufficient to segment HIFU-treated and non-treated tumor tissue. Inclusion of MTR to the protocol led to less agreement of the ISODATA segmentation with the histological analysis. Nevertheless, a significant increase in MTR was observed in the non-viable tumor tissue identified from ISODATA analysis with feature vector $\{T_1, T_2, ADC\}$ (Table 2). However, since this increase was only subtle, clustering with inclusion of MTR led to merging of clusters of non-viable and viable tumor tissue, resulting in a lower specificity and sensitivity of the cluster method.

ISODATA clustering with feature vector $\{T_1, T_2, ADC\}$ yielded 31 different clusters (Figure 1), which indicated a large heterogeneity of the HIFU-treated tumor tissue. Extensive analysis of each cluster separately would yield additional information about the status of the different segmented tissue populations. However, the focus of this study was the binary distinction between non-viable, HIFU-treated and viable, non-treated tumor tissue. Therefore, it was decided to allocate the clusters resulting from ISODATA segmentation to two distinct classes, designated as non-viable and viable. A cluster was assigned to the non-viable class if the fraction of pixels within the cluster significantly increased by HIFU treatment. This criterion could however also be met if the cluster is associated with reversible HIFU-induced tissue changes instead of with non-viable tumor tissue. Nevertheless, since a high one-to-one correspondence between histology-derived and ISODATA-derived non-viable tumor fractions was observed for the optimal feature vector $\{T_1, T_2, ADC\}$, it seems reasonable to assume that the majority of the non-viable clusters for that feature vector indeed represents non-viable tumor tissue.

A minor part of the tumor pixels after HIFU treatment (fractions of 0.05 ± 0.03 and 0.02 ± 0.02 of the entire tumor tissue at 1 h and 72 h after HIFU, respectively) needed to be excluded from the multiparametric MR analysis, because the signal intensity of these tumor pixels was at noise level in the T_2 -weighted images (see Methods). This low signal intensity was most likely caused by HIFU-induced hemorrhage. Exclusion of these hemorrhage-associated pixels from the analysis did not influence the correlation results presented here, because it only involved a very low fraction of tumor pixels.

Direct registration of the histological data with the MRI findings would allow for analysis of the spatial correlation between the ISODATA-segmented and histology-based non-viable volumes. However, 3D reconstruction of histological tumor sections was not performed in the present study. Accurate 3D histological reconstruction and its registration with MRI would have required an intermediate MRI scan after tumor excision, a robust anatomical reference and denser histological sampling (32). Additionally, spatial correlation of histology with MRI would require a higher spatial resolution of the MR images. This would lead to a substantially longer acquisition time of the multiparametric MR protocol and result in unacceptably long anesthesia times for the animals.

Instead of assessment of spatial correlation, the ISODATA analysis method was optimized based on the correlation between histology-derived and ISODATA-derived non-viable tumor fractions for different feature vectors. A similar correlation analysis has been performed for the detection of necrotic tumor tissue after radiotherapy, which yielded comparably strong correlations between clustering and histology (33), showing that this global correlation analysis is suitable for the optimization of clustering methods. For the optimized feature vector $\{T_1, T_2, ADC\}$, a strong spatial agreement between the region of ISODATA-derived non-viable tumor tissue and the region of non-viable tumor tissue on NADH-diaphorase-stained histological sections (Figure 5) was observed visually, which

indicates that the proposed methodology allows for accurate segmentation of HIFU-treated, non-viable tumor tissue.

Mean MRI parameter values were determined in non-viable and viable tumor tissue following ISODATA segmentation with feature vector $\{T_1, T_2, ADC\}$ (Table 2). R_1 was significantly increased in the non-viable, HIFU-treated tumor tissue both at 1 h and 72 h after HIFU as compared to viable, non-treated tumor tissue. Such increased R_1 (or decreased T_1) was previously also observed *ex vivo* in (non-cancerous) tissues after heat treatment (34), which was explained by a combination of coagulation of the blood volume fraction and disruption of biological barriers, which facilitates access of water molecules to paramagnetic sites in the coagulated blood. Decreased T_1 was also observed as a result of tissue necrosis after chemotherapy (35).

Graham et al. observed an increase in T_2 after heating of *ex vivo* tissue, which was explained as vacuolization of water molecules caused by increased hydrophobic interactions induced by protein denaturation (34). We observed significantly increased R_2 (and thus decreased T_2) in non-viable tumor tissue 1 h after HIFU treatment, whereas at 72 h after HIFU treatment no significant R_2 differences between non-viable and viable tumor tissue were observed. This initially decreased T_2 could be explained by the aforementioned increased access of water molecules to paramagnetic centers in the coagulated blood. Furthermore, the large standard deviation of R_2 in the non-viable, HIFU-treated tumor tissue (Table 2) indicated large T_2 heterogeneity due to the presence of areas with increased and decreased T_2 .

The observed increased ADC values in the non-viable tumor tissue have been described earlier *ex vivo* in thermally treated tissue samples (34) and *in vivo* in preclinical experiments on the effects of HIFU treatment in a murine tumor model (36) and in clinical studies of RF ablation of liver lesions (19). Diffusion of water molecules could have been facilitated by HIFU-induced disruption of obstructing barriers, leading to an increased ADC.

Reports on the effects of thermal treatment on the MTR are conflicting. Both a decreased (34) and increased (23) MTR have been observed in *ex vivo* thermally treated samples. An MTR decrease could be explained by denaturation of structural proteins (34), whereas an increase might be caused by increased access of water molecules to macromolecules due to disruption of barriers. Furthermore, T_1 effects may play a role, since the MTR is known to be affected by tissue T_1 (37). In the current study, a combination of these factors has probably influenced the observed MTR, which is also illustrated by the subtle yet significant increase in MTR in the non-viable, HIFU-treated tumor tissue compared to viable tumor tissue.

The HIFU treatment was performed outside the MR system, since the preclinical therapeutic ultrasound transducer is not (yet) MRI-compatible. In an MRI-guided HIFU set-up, results from the multiparametric MR analysis could be quantitatively compared to thermal dose maps derived from MR thermometry during HIFU treatment. Furthermore,

the MRI examinations before and directly after HIFU could then be combined within the same anesthesia period. This was not feasible in this study, since the ablation procedure was rather lengthy for the current set-up (~1 hour) and the subject would have to be positioned in the MR system twice. Nevertheless, no significant differences in MRI parameters were observed between the measurements of the control animals at Day 0 and Day 1, corresponding in time with the measurements of the HIFU-treated animals before and at 1 h after HIFU. This indicated that the time between the examinations before and after HIFU did not influence the results presented here.

A murine tumor model was used to assess the effects of HIFU treatment on tumor tissue status. The CT26 colon carcinoma was chosen because previous studies have shown that subcutaneous inoculations of CT26 cell suspensions lead to well-vascularized tumors (38) with limited necrosis (39). This is beneficial for the current study, because extensive natural necrosis could mask the effects of HIFU-induced necrosis. However, the method is not restricted to this tumor model, since similar approaches, consisting of multispectral MR imaging combined with cluster analysis, have been employed for the identification of viable and non-viable tissue after chemotherapy (40) and radiotherapy (33) in other preclinical tumor models.

Clinical translation of the multiparametric protocol is feasible, since MR sequences for acquisition of the proposed MRI parameters, T_1 , T_2 and ADC, are already clinically available. The total acquisition time of the multi-slice T_1 , T_2 and ADC protocol was approximately 25 minutes. Further reduction of the measurement time would facilitate inclusion of the multiparametric MR measurements in clinical HIFU treatment protocols. The MR parameter mapping acquisitions could be accelerated by for example rapid imaging techniques, such as parallel imaging and compressed sensing. Prior to clinical introduction of the proposed multiparametric MR analysis, it would be necessary to further confirm that the ISODATA-derived non-viable tumor tissue spatially corresponds to non-viable tumor tissue in histology. This could for example be achieved by image-guided biopsies from the ISODATA-derived viable and non-viable tumor tissue. Since clinical trials on HIFU treatment of malignant tumors generally use treat-and-resect protocols (41), it would be feasible to include image-guided biopsies in the workflow of these studies. Such extensive validation should be performed in different tumor subtypes to assess the full clinical potential of the proposed methodology.

In summary, we have shown that non-viable, HIFU-treated tumor tissue could be distinguished from non-treated tumor tissue using quantitative multiparametric MRI combined with the ISODATA clustering technique. Clustering with feature vector $\{T_1, T_2, ADC\}$ yielded a strong correlation between ISODATA-derived and histology-derived non-viable tumor fractions. The presented methodology not only offers clear insights in the HIFU-induced changes in MRI parameters, but could also ultimately be made suitable for clinical application and might offer the unique possibility to automatically detect residual or recurring tumor tissue after HIFU treatment in an objective manner. Furthermore, since

the proposed MRI analysis is solely based on endogenous contrast, immediate retreatment is possible when residual or recurring tumor tissue is detected, without the risk of inaccurate temperature mapping due to presence of a Gd-based contrast agent.

Acknowledgements

The authors thank Ralf Seip from Philips Research for his advice on the HIFU treatment settings. Furthermore, the authors want to acknowledge Holger Grüll from Eindhoven University of Technology and Philips Research for useful discussions.

References

1. **Kennedy JE.** *Nat Rev Cancer* 2005;5:321-327.
2. **ter Haar G.** *Prog Biophys Mol Biol* 2007;93:111-129.
3. **Hesley GK, Gorny KR, Woodrum DA.** *Cardiovasc Intervent Radiol* 2013;36:5-13.
4. **Voogt MJ, Trillaud H, Kim YS, Mali WP, Barkhausen J, Bartels LW, Deckers R, Frulio N, Rhim H, Lim HK, Eckey T, Nieminen HJ, Mougnot C, Keserci B, Soini J, Vaara T, Kohler MO, Sokka S, van den Bosch MA.** *Eur Radiol* 2012;22:411-417.
5. **Murat FJ, Poissonnier L, Pasticier G, Gelet A.** *Cancer Control* 2007;14:244-249.
6. **Rouviere O, Girouin N, Glas L, Ben Cheikh A, Gelet A, Mege-Lechevallier F, Rabilloud M, Chapelon JY, Lyonnet D.** *Eur Radiol* 2010;20:48-55.
7. **Kirkham AP, Emberton M, Hoh IM, Illing RO, Freeman AA, Allen C.** *Radiology* 2008;246:833-844.
8. **Schmitz AC, Gianfelice D, Daniel BL, Mali WP, van den Bosch MA.** *Eur Radiol* 2008;18:1431-1441.
9. **Leslie TA, Kennedy JE, Illing RO, Ter Haar GR, Wu F, Phillips RR, Friend PJ, Roberts IS, Cranston DW, Middleton MR.** *Br J Radiol* 2008;81:564-571.
10. **Leslie T, Ritchie R, Illing R, Ter Haar G, Phillips R, Middleton M, Bch B, Wu F, Cranston D.** *Br J Radiol* 2012;85:1363-1370.
11. **Hynynen K.** *Ultrasonics* 2010;50:221-229.
12. **Rieke V, Butts Pauly K.** *J Magn Reson Imaging* 2008;27:376-390.
13. **Yarmolenko PS, Moon EJ, Landon C, Manzoor A, Hochman DW, Viglianti BL, Dewhurst MW.** *Int J Hyperthermia* 2011;27:320-343.
14. **Wijlemans JW, Deckers R, van den Bosch MA, Seinstra BA, van Stralen M, van Diest PJ, Moonen CT, Bartels LW.** *Invest Radiol* 2013;48:381-386.
15. **Dewhurst MW, Viglianti BL, Lora-Michiels M, Hanson M, Hoopes PJ.** *Int J Hyperthermia* 2003;19:267-294.
16. **Merkle EM, Nour SG, Lewin JS.** *Radiology* 2005;235:1065-1071.
17. **Dromain C, de Baere T, Elias D, Kuoch V, Ducreux M, Boige V, Petrow P, Roche A, Sigal R.** *Radiology* 2002;223:255-262.
18. **Hijnen NM, Elevelt A, Pikkemaat J, Bos C, Bartels LW, Grüll H.** *Journal of Therapeutic Ultrasound* 2013;1:8.
19. **Zhang Y, Zhao J, Guo D, Zhong W, Ran L.** *Eur J Radiol* 2011;79:347-352.
20. **Jacobs MA, Ouwerkerk R, Kamel I, Bottomley PA, Bluemke DA, Kim HS.** *J Magn Reson Imaging* 2009;29:649-656.
21. **Pilatou MC, Stewart EA, Maier SE, Fennessy FM, Hynynen K, Tempany CM, McDannold N.** *J Magn Reson Imaging* 2009;29:404-411.
22. **Wolff SD, Balaban RS.** *Radiology* 1994;192:593-599.
23. **Peng HH, Huang TY, Tseng WY, Lin EL, Chung HW, Wu CC, Wang YS, Chen WS.** *J Magn Reson Imaging* 2009;30:596-605.
24. **Rouviere O, Gelet A, Crouzet S, Chapelon JY.** *Nat Rev Clin Oncol* 2012;9:721-727.
25. **Jacobs MA, Knight RA, Soltanian-Zadeh H, Zheng ZG, Goussev AV, Peck DJ, Windham JP, Chopp M.** *J Magn Reson Imaging* 2000;11:425-437.
26. **Seip R, Chin CT, Hall CS, Raju BI, Ghanem A, Tiemann K.** *IEEE Trans Biomed Eng* 2010;57:61-70.
27. **Levitt M, Freeman R.** *J Magn Reson* 1981;43:56-80.
28. **Karlsson M, Nordell B.** *Magn Reson Imaging* 1999;17:1481-1488.
29. **Omran MGH, Engelbrecht AP, Salman A.** *Intelligent Data Analysis* 2007;11:583-605.
30. **Hijnen NM, Heijman E, Kohler MO, Ylihautala M, Ehnholm GJ, Simonetti AW, Grull H.** *Int J Hyperthermia* 2012;28:141-155.
31. **Wolfe DA.** *Biometrika* 1976;63:214-215.
32. **Alic L, Haeck JC, Bol K, Klein S, van Tiel ST, Wielepolski PA, de Jong M, Niessen WJ, Bernsen M, Veenland JF.** *PLoS One* 2011;6:e22835.

33. **Henning EC, Azuma C, Sotak CH, Helmer KG.** Magn Reson Med 2007;57:501-512.
34. **Graham SJ, Stanisz GJ, Kecojevic A, Bronskill MJ, Henkelman RM.** Magn Reson Med 1999;42:1061-1071.
35. **McSheehy PM, Weidensteiner C, Cannet C, Ferretti S, Laurent D, Ruetz S, Stumm M, Allegrini PR.** Clin Cancer Res 2010;16:212-225.
36. **Hundt W, Yuh EL, Steinbach S, Bednarski MD.** Technol Cancer Res Treat 2009;8:85-98.
37. **Henkelman RM, Stanisz GJ, Graham SJ.** NMR Biomed 2001;14:57-64.
38. **Ogawara K, Un K, Minato K, Tanaka K, Higaki K, Kimura T.** Int J Pharm 2008;359:234-240.
39. **Aulino P, Berardi E, Cardillo VM, Rizzuto E, Perniconi B, Ramina C, Padula F, Spugnini EP, Baldi A, Faiola F, Adamo S, Coletti D.** BMC Cancer 2010;10:363.
40. **Carano RA, Ross AL, Ross J, Williams SP, Koeppen H, Schwall RH, Van Bruggen N.** Magn Reson Med 2004;51:542-551.
41. **Merckel LG, Bartels LW, Kohler MO, van den Bongard HJ, Deckers R, Mali WP, Binkert CA, Moonen CT, Gilhuijs KG, van den Bosch MA.** Cardiovasc Intervent Radiol 2013;36:292-301.

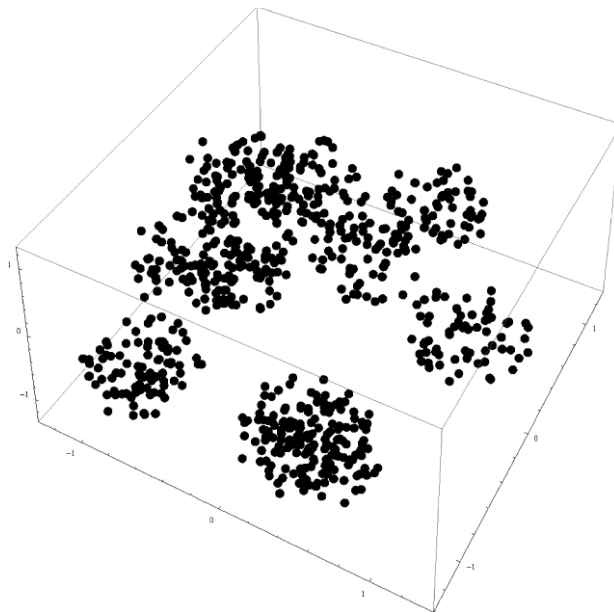
Supplemental Information

Supplemental Information S1

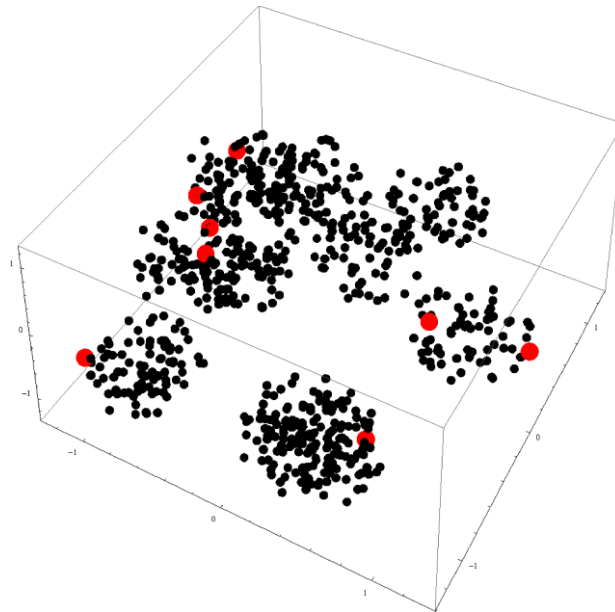
Theory: the ISODATA clustering algorithm

The ISODATA clustering described in the manuscript was performed with different feature vectors, consisting of either 1, 2, 3 or all 4 (T_1 , T_2 , ADC and MTR) MR contrast parameters. Extensive details of the ISODATA clustering algorithm can be found in the original paper by Jacobs et al. (1). A brief theoretical description of the concepts of the clustering algorithm is given below.

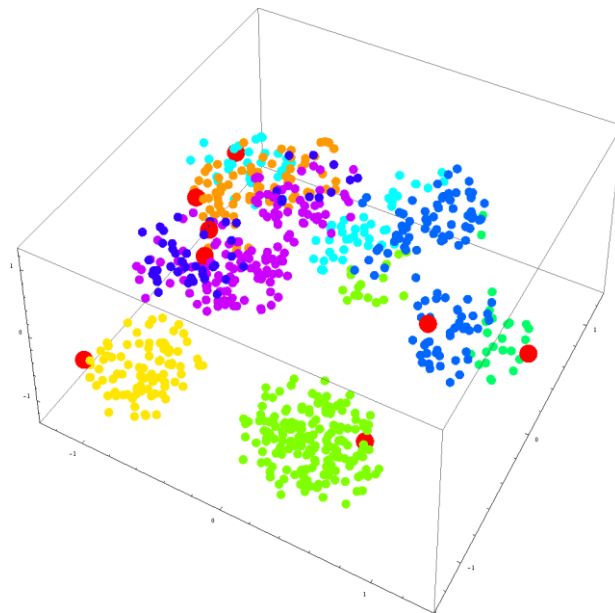
If the clustering would be performed with a feature vector consisting of for example three parameters, the values in the tumor pixels can be represented in a 3D space, as schematically shown below, in which each black spot represents a single tumor pixel. To explain the ISODATA concept and for reasons of clarity, the clustering steps described in the figures below were performed on simulated data describing a limited number of well-separated clusters. The actual tumor data yielded typically 20-40 clusters, which would make the figures unclear.



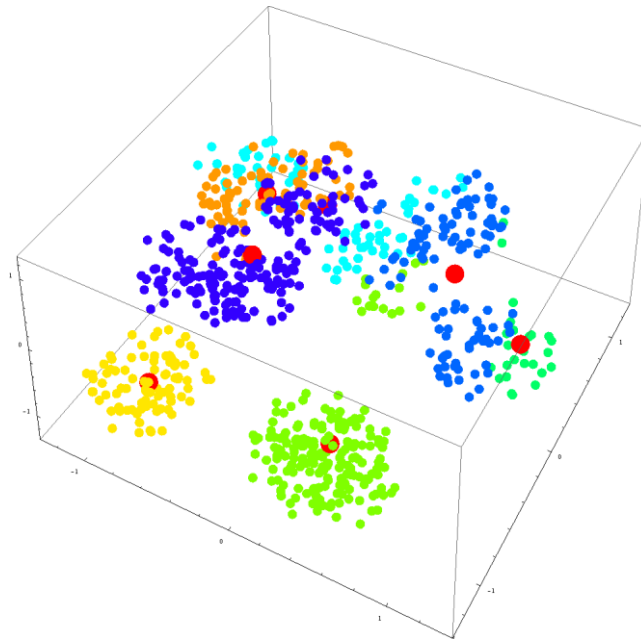
As the first step in the algorithm, an initial number of clusters is defined. In this example the initial number of clusters was set to 8. Cluster centroids (red spots below) are randomly defined for each cluster.



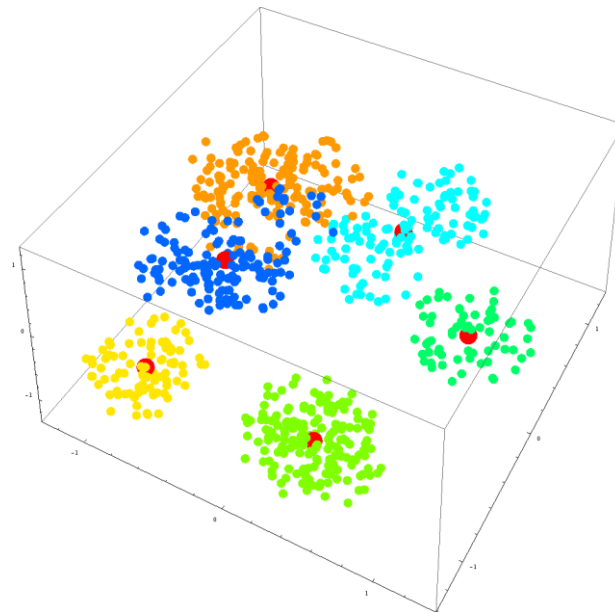
Next, pixels are assigned to the cluster of which the centroid is closest to the parameter values of the pixel. The different clusters that are the results of this step in the process are given by the different colors.



Subsequently, the centroids of each cluster are re-calculated. Clusters are split into two separate clusters, if the intra-Euclidean distances between the pixel vectors and the centroid of each cluster are larger than a pre-defined threshold. These intra-Euclidean distances are a measure of the spread within a certain cluster. Furthermore, pairs of clusters are merged into one cluster if the inter-Euclidean distance between the two cluster centroids is smaller than a pre-defined threshold, which means that the clusters are close to each other. In the example, the dark-blue and purple clusters were merged in this step, as can be seen below.

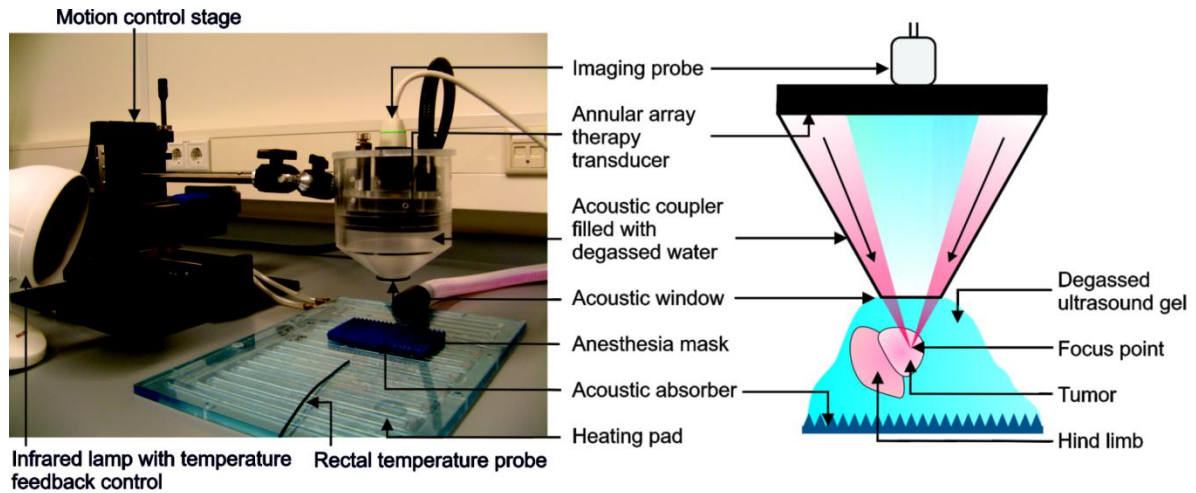


The previous step is repeated until convergence of the algorithm is reached. The algorithm is converged if the objective function (1) has not changed between subsequent iterations, which means that no alterations in the composition of the clusters occurred in the last iteration.

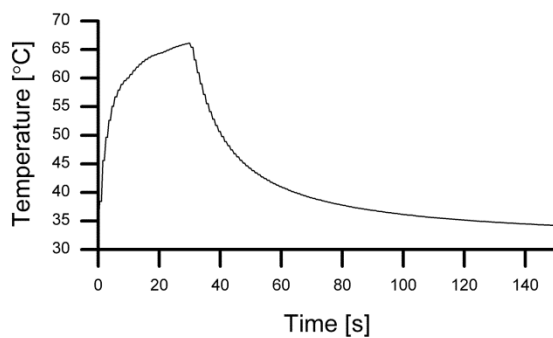


1. **Jacobs MA, Knight RA, Soltanian-Zadeh H, Zheng ZG, Goussev AV, Peck DJ, Windham JP, Chopp M. J Magn Reson Imaging 2000;11:425-437.**

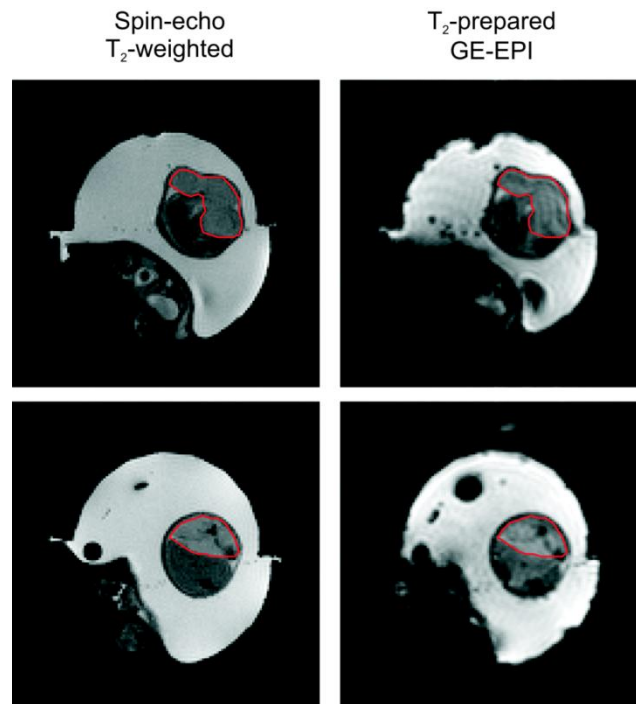
Supplemental Figures



Supplemental Figure S1. HIFU set-up. *Left* Photograph of the HIFU set-up. The animal was positioned underneath the acoustic coupler. Animal temperature was maintained with an infrared lamp with temperature feedback control from a rectal temperature probe. The motion control stage allowed for accurate movement of the therapy transducer between the pre-defined treatment points. *Right* Schematic drawing of the HIFU set-up, showing positioning of the tumor tissue in the focus point of the therapy transducer. The surrounding hind limb tissue was positioned outside the focal zone.



Supplemental Figure S2. Temperature profile. Typical example of a temperature profile during HIFU treatment. The tumor tissue temperature increased to 66 °C during the sonication of 30 seconds, followed by cooling of the tissue to pre-sonication temperature during the wait time of 120 seconds. The temperature information was acquired by a thermocouple, which was inserted into the tumor tissue during the pilot experiments. The focal point of the therapeutic transducer co-localized with the tip of the thermocouple. This co-localization was verified by multiple low-power sonications around the expected thermocouple position. The exact thermocouple position was determined as the position at which the highest temperature increase was observed during the sonication.



Supplemental Figure S3. Two representative examples of conventional T_2 -weighted spin-echo images (left column of panels) and T_2 -prepared GE-EPI images (right column of panels). The effective echo times are similar for both images (30 ms for the conventional T_2 -weighted images; 28 ms for the T_2 -prepared GE-EPI images). Regions of interest (ROIs) of the tumor tissue are indicated with the red lines, showing absence of apparent geometric distortion within the tumor tissue in the EPI images.

Chapter 4

Amide Proton Transfer Imaging of High Intensity Focused Ultrasound-treated Tumor Tissue

Stefanie Hectors, Igor Jacobs, Gustav Strijkers, Klaas Nicolay

Published in Magn Reson Med 2014;72:1113-22.

Abstract

Purpose

In this study the suitability of amide proton transfer (APT) imaging as a biomarker for the characterization of High Intensity Focused Ultrasound (HIFU)-treated tumor tissue was assessed.

Materials and Methods

APT imaging was performed on tumor-bearing mice before (n=15), directly after (n=15) and at 3 days (n=8) after HIFU treatment. A control group (n=7) of non-treated animals was scanned at the same time points. Histogram analysis of the tumor APT-weighted signal distributions was performed to assess HIFU-induced changes in the tumor APT contrast.

Results

Distinct regions of decreased APT-weighted signal were observed at both time points after HIFU treatment. Analysis of the tumor APT-weighted signal distribution showed a pronounced shift towards lower APT-weighted signal values after HIFU treatment. A significantly increased fraction of pixels with an APT-weighted signal value between -10 and -2% was observed both directly (0.37 ± 0.16) and at 3 days (0.49 ± 0.16) after HIFU treatment as compared to baseline (0.22 ± 0.16).

Conclusions

The presented results show that APT imaging is sensitive to HIFU-induced changes in tumor tissue and may thus serve as a new biomarker for monitoring the response of tumor tissue to HIFU treatment.

Introduction

High Intensity Focused Ultrasound (HIFU) is an emerging technique for the thermal treatment of solid tumors (1-3). During HIFU treatment, high-intensity ultrasound waves are focused in the target tissue, which leads to deposition of ultrasonic energy. This energy deposition leads to a temperature rise, which induces cell death in the target tissue with minimal collateral damage to surrounding tissue. For the application of HIFU for the treatment of malignant tumors, such as prostate (4-6) and breast tumors (7) and liver metastases (8,9), full tumor coverage of the treatment is essential. This requires, besides adequate treatment planning and monitoring, a treatment evaluation method that is capable of detecting local residual or recurrent tumor tissue after HIFU treatment. In **chapter 3**, it was demonstrated that residual non-treated tumor tissue can be detected by multiparametric MRI, consisting of quantitative assessment of T_1 , T_2 and the apparent diffusion coefficient (ADC), combined with cluster analysis. The highest correlation between MRI-derived HIFU-treated tumor fractions and histology-derived non-viable tumor fractions was observed at 3 days after HIFU. As a next step, we aimed to assess whether more advanced MRI parameters could give complementary, yet distinct, information on tumor tissue status after HIFU treatment. These parameters could be more sensitive to HIFU-induced changes in tumor tissue instantly after treatment, possibly allowing for accurate identification of successfully treated tissue directly after the HIFU procedure. Furthermore, treatment evaluation with these parameters could lead to improved insights in the interaction of HIFU with tumor tissue.

Specifically, MRI parameters that are sensitive to macromolecular content and the exchange between macromolecules and water protons will be assessed as possible biomarkers for the characterization and identification of HIFU-treated tumor tissue. It is expected that these MRI parameters change after HIFU-induced protein denaturation and coagulative necrosis. Magnetization transfer imaging has shown potential sensitivity for HIFU-induced macromolecular changes in an ex vivo study on HIFU treatment of porcine muscle tissue (10). However, in our previous study, we observed that magnetization transfer imaging has a lower sensitivity for the discrimination between HIFU-treated and non-treated tumor tissue as compared to T_1 , T_2 and ADC measurements. Only a subtle, yet significant, increase was found in the magnetization transfer ratio of HIFU-treated tumor tissue as compared to non-treated tumor tissue (**chapter 3**). Other, more specific, macromolecule-sensitive MRI methods, including amide proton transfer (APT) imaging, might be more suitable for the distinction between HIFU-treated and non-treated tumor tissue.

APT imaging is an emerging application of chemical exchange saturation transfer (CEST) imaging (11-13). The contrast in CEST imaging experiments originates from the change in water signal intensity due to chemical exchange of water protons with saturated solute protons. APT imaging employs the saturation transfer from amide protons of protein/peptide backbones, resonating at 3.5 ppm downfield of the water resonance frequency. The APT contrast depends on both the concentration of the amide protons and

the exchange rate. Since the exchange rate of the amide protons is dependent on tissue pH, APT imaging has been used to study pathologies associated with altered pH, such as cerebral ischemia (14-16). Furthermore, the dependence of the APT contrast on amide proton concentration has been exploited by imaging of brain tumors, both preclinical (17,18) and clinical (19-21), based on the increased cytosolic content of amide-proton-rich proteins and peptides in malignant brain tumors (22). The APT contrast has also been assessed in other tumors, including breast (23) and prostate (24) carcinomas.

Recently, APT imaging has been applied to monitor treatment response after radiotherapy of rat brain tumors. In that study, radiation necrosis could be differentiated from tumor progression using the APT contrast mechanism (25). Similar, preliminary findings were reported in a clinical study on APT imaging to monitor breast tumor response to chemotherapy treatment (23). To the best of our knowledge, no studies have reported on the use of APT imaging to evaluate HIFU treatment of tumors. Therefore, the goal of the present study was to investigate whether APT imaging can be used as a biomarker for tumor necrosis induced by HIFU treatment. To this aim, APT imaging was performed before, directly after and 3 days after HIFU treatment of a murine tumor model to assess the influence of HIFU treatment on the characteristics of APT contrast in the tumor.

Materials and Methods

Murine tumor model

CT26.WT murine colon carcinoma cells (American Type Culture Collection (ATCC; CRL-2638)) were cultured as a monolayer at 37°C and 5% CO₂ in RPMI-1640 medium (2 mM L-glutamine, 10 mM HEPES, 1 mM sodium pyruvate, 4500 mg/L glucose, and 1500 mg/L sodium bicarbonate) (Invitrogen, Breda, The Netherlands), supplemented with 10% fetal bovine serum (Greiner Bio-One, Alphen a/d Rijn, The Netherlands) and 50 U/ml penicillin/streptomycin (Lonza Bioscience, Basel, Switzerland). Early passages (5-10) of the original ATCC batch were used for inoculation.

10-12 week-old Balb/c mice (Charles River, Maastricht, The Netherlands) were inoculated with 2x10⁶ CT26.WT cells subcutaneously in the right hind limb. Approximately 10 days after inoculation, tumors became visible in all animals. The first MRI experiment was performed when tumors had reached a size of approximately 300 mm³. The animal experiments were approved by the animal experiment committee of Maastricht University (The Netherlands).

Study design

MRI examinations were performed 1 day before (n=15), directly after (n=15) and 3 days after (n=8) HIFU treatment. A control group (n=7) of non-treated animals was included. The time points of MRI examinations of the control animals were the same as for the HIFU-treated animals and are referred to as day -1, day 0 and day 3. Directly after the last MRI experiment, the mice were sacrificed, and the tumors were dissected and processed for histological analysis. This study design led to three different experimental groups:

HIFU-treated animals sacrificed after the MRI examination directly after treatment (n=7), HIFU-treated animals sacrificed after the MRI examination at 3 days after treatment (n=8) and non-treated control animals (n=7).

HIFU treatment

HIFU treatment was performed with the preclinical Therapy Imaging Probe System (TIPS, Philips Research, Briarcliff Manor, NY, USA), outside the MR system. Technical specifications and calibrations of the TIPS device are reported elsewhere (26). The transducer was coupled to the tumor tissue with degassed water and ultrasound gel. Reflections were avoided with an acoustic absorber (Aptflex F28P, Precision Acoustics, Dorchester, UK), which was positioned underneath the tumor-bearing paw. The tumors were treated under general anesthesia (1-2% isoflurane) and precautionary analgesia (buprenorphine, 0.1 mg/kg s.c., administered 30 min before treatment). The control animals received an equal dose of analgesia at the corresponding time point. The HIFU treatment involved partial tumor ablation, to allow for internal reference between HIFU-treated and non-treated tumor tissue. A square 4x4 mm² treatment grid consisting of 25 equally-spaced treatment points was defined within the tumor area. A wait time of 120 s was applied between sonication of the different treatment points to allow cooling of the tissue to body temperature. Treatment settings were: frequency 1.4 MHz, pulse repetition frequency 20 Hz, acoustic power 12 W, duty cycle 50%, treatment time 30 s. Three pilot experiments, in which a thermocouple (80- μ m-diameter bare-wire T-type thermocouple; T-150A, Physitemp Instruments, Clifton, NJ, USA) was inserted into the tumor tissue during the HIFU treatment, showed that a temperature of approximately 65°C was reached during sonication with the above-mentioned treatment settings. Directly after sonication of the last treatment point, the animals were transferred to the MRI system. The positioning of the animals in the MR scanner took approximately 15 minutes, which ensured recovery of the temperature of the HIFU-treated tissue to body temperature.

MRI measurements

MRI measurements were performed with a 6.3 T scanner (Bruker BioSpin, Ettlingen, Germany) using a 3.2-cm-diameter quadrature birdcage RF coil (Rapid Biomedical, Rimpar, Germany). The mice were positioned in a custom-made cradle, equipped with a mask for anesthetic gas (1-2% isoflurane). Respiration was monitored with a balloon sensor. Body temperature was monitored and maintained at approximately 37 °C with a warm water pad. An infusion line with contrast agent was placed in the tail vein to enable injection during the MRI experiment. For reduction of susceptibility artifacts in the echo planar imaging (EPI) sequence, the tumor-bearing paw was covered with degassed ultrasound gel (Aquasonic® 100, Parker Laboratories, Fairfield, NJ, USA).

For all MRI acquisitions a matrix size of 128 x 128 and a field of view of 4 x 4 cm² were used. Slice thickness was 1 mm for all experiments.

Prior to APT acquisitions, higher-order local shimming was performed on the tumor-bearing paw using the Bruker MAPSHIM routine to improve B₀ homogeneity. To assess

the influence of the local shimming procedure on the field homogeneity, a point-resolved spectroscopy (PRESS) sequence (echo time TE=20 ms, repetition time TR=2500 ms, number of averages NA=1) was acquired before and after local shimming on a single voxel surrounding the tumor-bearing paw. The average voxel size was $2.3 \pm 0.9 \text{ cm}^3$. To correct for possible deviations between the scanner frequency setting and the actual water frequency, a magnetization transfer spectrum with a low saturation power ($0.5 \mu\text{T}$, saturation time 4 s) and a narrow offset range (-0.6 to 0.6 ppm, interval 0.05 ppm) was acquired on the central tumor slice, as described previously (25). Signal read-out was performed with dual-shot gradient-echo EPI (TE=8 ms, TR=10000 ms, NA=1). The deviation of the magnetization transfer spectrum center frequency from 0 ppm was determined and used to adjust the scanner transmitter frequency.

Subsequently, multi-slice, high signal-to-noise ratio (SNR) APT imaging was performed. Twelve to 16 adjacent slices (0.1 mm slice gap) were defined, covering the whole tumor volume. The APT imaging protocol consisted of three acquisitions; two images with saturation at -3.5 ppm and 3.5 ppm from the water frequency, $S_{\text{sat}}(-3.5 \text{ ppm})$ and $S_{\text{sat}}(3.5 \text{ ppm})$ respectively, and one control image in the absence of RF saturation (S_0). The saturation consisted of a 4 s block pulse with a power level of $1.3 \mu\text{T}$, as described previously in a study on APT imaging of rat brain tumors (18). Signal read-out was performed with dual-shot gradient-echo EPI (TE=8 ms, TR=10000 ms, NA=8).

In addition to the APT imaging protocol, T_2 -weighted imaging (spin-echo, TE=30 ms, TR=1000 ms, NA=1) and contrast-enhanced T_1 -weighted imaging (spin-echo, TE=8 ms, TR=800 ms, NA=2, acquisitions before and directly after intravenous injection of Dotarem (0.3 mmol Gd/kg)) were performed with the same geometry as used for the high SNR APT images.

Data analysis

Image analysis was performed in Mathematica 7.0 (Wolfram Research, Champaign, IL, USA). Regions of interest (ROI's) were defined on the T_2 -weighted images by manually drawing contours around the tumor tissue on each slice. APT-weighted signal maps in the tumor ROI were generated according to:

$$\text{APT-weighted signal} = [(S_{\text{sat}}(-3.5 \text{ ppm}) - S_{\text{sat}}(3.5 \text{ ppm})) / S_0] * 100\%$$

For analysis of HIFU-induced changes in the APT-weighted signal distribution, histograms of the APT-weighted signals were generated for each tumor at each time point separately. The histogram characteristics were: 20 bins, bin width 1% and an APT-weighted signal range from -10 to 10%. Histograms of the animals within the different groups (HIFU-treated and control) were averaged for each time point and spline fitting through these averaged histograms was performed to visualize the APT-weighted signal distribution at the different time points for both groups.

From the contrast-enhanced acquisitions, the signal enhancement (SE) after Gadolinium injection was calculated in each pixel in the tumor ROI according to:

$$SE = [(SI_{\text{after injection}} - SI_{\text{before injection}}) / SI_{\text{before injection}}] * 100\%,$$

in which $SI_{\text{before injection}}$ and $SI_{\text{after injection}}$ are the signal intensities in the images before and after contrast agent injection, respectively.

For determination of non-perfused tumor fractions after HIFU treatment, the tumor pixels were assigned as either enhanced or non-enhanced. A pixel was assigned as enhanced if $SI_{\text{after injection}} > SI_{\text{before injection}} + 2 * SD_{\text{before injection}}$, in which $SD_{\text{before injection}}$ is the standard deviation of $SI_{\text{before injection}}$ in the tumor ROI. Subsequently, the non-perfused tumor fractions were calculated by dividing the number of non-enhanced tumor pixels by the total number of tumor pixels.

Histological analysis

Dissected tumors were snap-frozen in isopentane and stored at -80 °C. Tumors were cut into 5 µm thick sections with a distance of approximately 300 µm between the sections. Multiple sections were collected at each position to allow for different staining protocols. The cryo-sections were briefly air-dried and subsequently stained for nicotinamide adenine dinucleotide (NADH) diaphorase activity to assess cell viability. Sections were incubated at 37 °C for 1 h in Gomori-Tris-HCl buffer (pH 7.4) containing β-NAD reduced disodium salt hydrate (Sigma-Aldrich, St. Louis, MO, USA, 0.71 mg/ml buffer solution) and nitro blue tetrazolium (Sigma-Aldrich, 0.29 mg/ml buffer solution). Adjacent cryo-sections were stained with haematoxylin and eosin (H&E) to analyze general morphology. Brightfield microscopy was performed on selected stained sections and consisted of mosaic acquisition of the entire section at 5x magnification.

Statistical analysis

All data are presented as mean±standard deviation (SD). The histograms of APT-weighted signal values of the HIFU-treated tumors before and after HIFU were statistically compared by a paired Student's t-test. A similar analysis was performed to compare the APT-weighted signal distributions of the non-treated control tumors at the different time points. The APT-weighted signal distributions of the HIFU-treated and control tumors were compared with a Student's t-test. The difference in non-perfused tumor fractions and tumor fractions with HIFU-induced APT-weighted signal changes was tested for significance with a paired Student's t-test. In all analyses, the difference was considered significant at $P < 0.05$.

Results

To evaluate the effect of HIFU treatment on the APT-weighted signal in tumor tissue, APT imaging was performed before and at two time points after HIFU treatment. The APT imaging results were compared to conventional T_2 -weighted and contrast-enhanced T_1 -weighted images, which are routinely used in the clinic to monitor tumor treatment response. Figure 1A shows representative MRI results of a HIFU-treated animal before, directly after and 3 days after HIFU treatment. Before HIFU, a homogeneous appearance of the tumor tissue was observed, both in the T_2 -weighted images and the APT-weighted signal maps. Furthermore, substantial signal enhancement (SE) after Gd injection was observed throughout the entire tumor tissue before HIFU treatment. Both directly after and at 3 days after HIFU treatment, a heterogeneous appearance of the HIFU-treated lesion was observed on the T_2 -weighted images. From these images, successfully treated tumor tissue could not be distinguished from residual non-treated tumor tissue. Contrary, on the APT-weighted signal maps, a distinct tumor region with decreased APT-weighted signal as well as a smaller region with increased APT-weighted signal appeared directly after HIFU treatment. The region of decreased APT-weighted signal had increased in size at 3 days after HIFU. The SE maps derived from the contrast-enhanced T_1 -weighted images showed large non-perfused volumes, both directly and at 3 days after HIFU treatment. Interestingly, these non-perfused volumes were substantially larger than the regions with decreased APT-weighted signal.

To aid in the interpretation of the MRI results, histology was performed on excised tumor tissues. Figure 1B shows adjacent NADH-diaphorase and H&E-stained tumor sections obtained at 3 days after HIFU treatment. The tumor sections were collected at approximately the same location in the tumor as the MRI slice displayed in Figure 1A. A distinct, pale, non-viable tumor area was observed in the NADH-diaphorase-stained tumor section. This region of non-viable tumor tissue corresponded to necrotic tumor tissue on the H&E-stained tumor section. Furthermore, good spatial agreement between the region of decreased APT-weighted signal (Figure 1A, bottom row) and the region of non-viable, necrotic tumor tissue in histology was observed.

Non-treated control animals were scanned at the same time points to investigate the effects of tumor progression on the tumor APT-weighted signal and to assess whether the observed changes in the tumor APT-weighted signal distribution in the HIFU-treated animals could be purely attributed to the effects of HIFU treatment on tumor tissue status. Representative MRI results of a non-treated control animal are displayed in Figure 2A. A relatively homogeneous appearance of the tumor tissue was observed on the T_2 -weighted images and the tumor APT-weighted signal maps at all time points. Occasionally, local spots of decreased APT-weighted signal were observed, possibly associated with natural necrosis in the tumor tissue. The SE maps after Gd injection showed substantial contrast enhancement throughout the entire tumor tissue at all time points. The corresponding NADH-diaphorase- and H&E-stained tumor sections (Figure 2B) confirmed general viability of the tumor tissue, with small regions of necrosis.

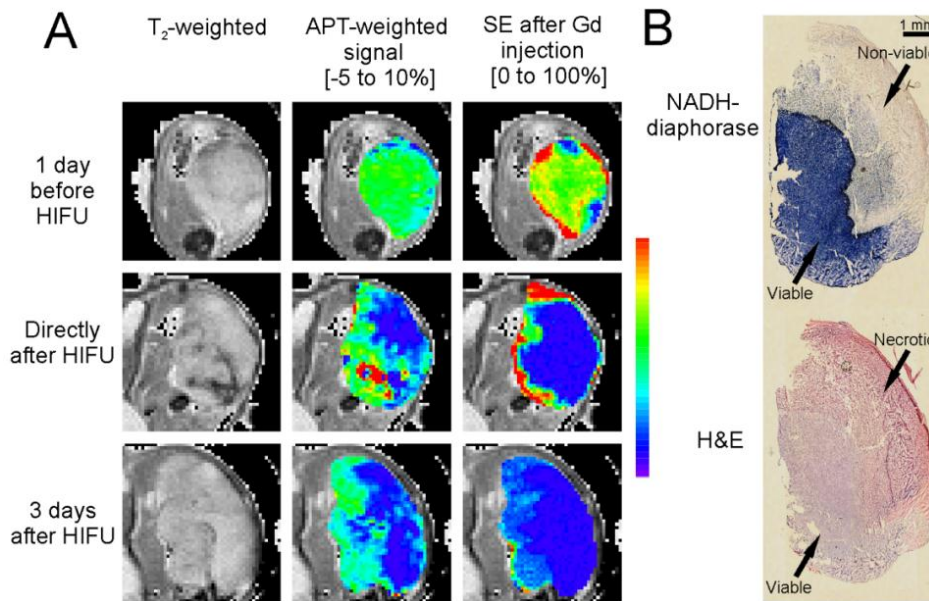


Figure 1. A) Representative example of MRI of a tumor-bearing leg before, directly after and 3 days after HIFU treatment. T_2 -weighted images of an axial slice of the tumor-bearing paw are shown in the left column of panels. The hyper-intense tumor tissue is surrounded by hypo-intense muscle tissue. In the center and right panels the APT-weighted signal maps and signal enhancement (SE) maps after Gd injection are overlaid on the tumor pixels, respectively. The parameter maps were scaled according to the color scale bar shown at the right-hand side of the figure. The corresponding parameter range for this scale bar is indicated above each column of panels. B) NADH-diaphorase (top) and H&E stained tumor sections (bottom) obtained at 3 days after HIFU at approximately the same location within the tumor. A region of non-viable (NADH-diaphorase negative), necrotic (H&E) tumor tissue was observed in the upper right part of the sections, next to viable (NADH-diaphorase positive, and normal on H&E staining) tumor tissue.

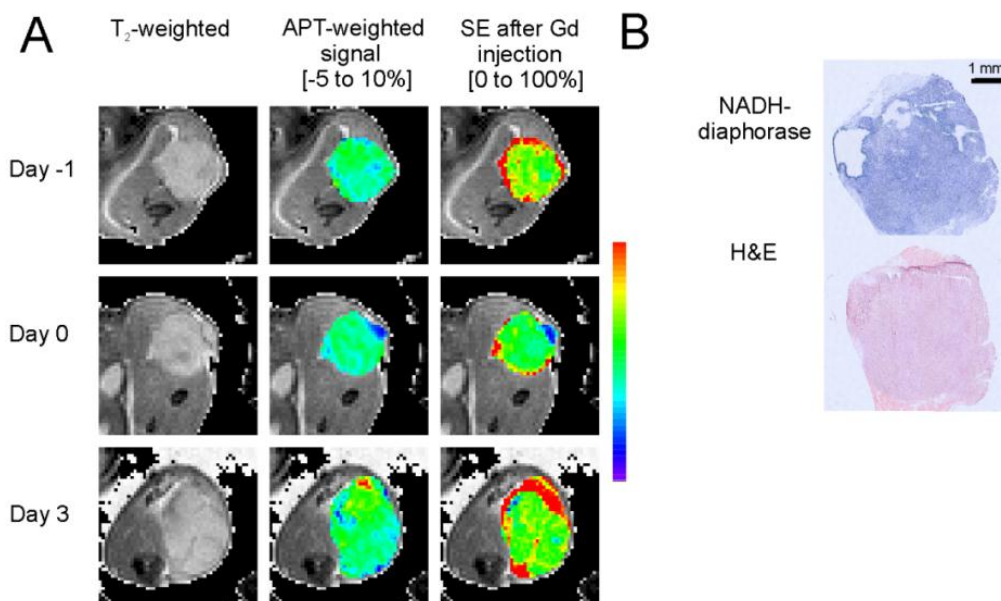


Figure 2. A) Representative example of MRI of a tumor-bearing leg of a non-treated control animal at day -1, day 0 and day 3. The structure of the figure is identical to the figure of representative MRI results of the HIFU-treated animals (Figure 1A). B) NADH-diaphorase and H&E stained tumor sections obtained at day 3 at approximately the same location within the tumor.

The changes in APT contrast after HIFU treatment were quantified by histogram analysis of the tumor APT-weighted signals. Histograms of the APT-weighted signal values were obtained for each tumor at the different experimental time points. These were averaged for each time point to visualize the effect of HIFU treatment on the tumor APT-weighted signal profiles. The averaged histograms of the HIFU-treated animals are shown in Figure 3A. Significantly increased fractions of tumor pixels with negative APT-weighted signal values ranging from -10% to -3% and positive APT-weighted signal values ranging from 4 to 10% were observed directly after HIFU as compared to before HIFU (paired Student's t-test, $P < 0.05$). The fractions of pixels with negative APT-weighted signal values ranging from -9 to -4% were further increased at 3 days after HIFU treatment. Spline fitting through these averaged histograms was performed to facilitate visualization of the HIFU-induced changes in tumor APT-weighted signal distribution. The resulting APT-weighted signal distribution plots are displayed in Figure 3B. A clear shift towards lower APT-weighted signal values was observed directly after HIFU treatment and this effect was more prominent at 3 days after HIFU. Figure 3C shows the difference in APT-weighted signal distribution between baseline values and directly and 3 days after HIFU treatment. A clear increase in fraction of pixels with an APT-weighted signal range between -10 and -2% was observed at both time points after HIFU. This APT-weighted signal range was assumed to be related to HIFU-induced changes in the tumor tissue. A highly significant increase in the fractions of pixels within this APT-weighted signal range was observed directly (0.37 ± 0.16) and 3 days (0.49 ± 0.16) after HIFU treatment as compared to baseline (0.22 ± 0.16) (Figure 3D).

For a quantitative comparison between the areas of decreased APT-weighted signal and the areas of decreased perfusion (i.e. decreased signal enhancement after contrast agent injection), non-perfused tumor fractions were determined for the HIFU-treated animals at both time points after HIFU treatment. Directly after HIFU treatment, the non-perfused tumor fraction (0.61 ± 0.21) was significantly larger than the tumor fraction with APT-weighted signals within the HIFU-related APT-weighted signal range (0.37 ± 0.16). At 3 days after HIFU treatment, the non-perfused tumor fraction continued to be larger (0.59 ± 0.22), yet non-significantly, than the tumor fraction within the HIFU-related APT-weighted signal range (0.49 ± 0.16).

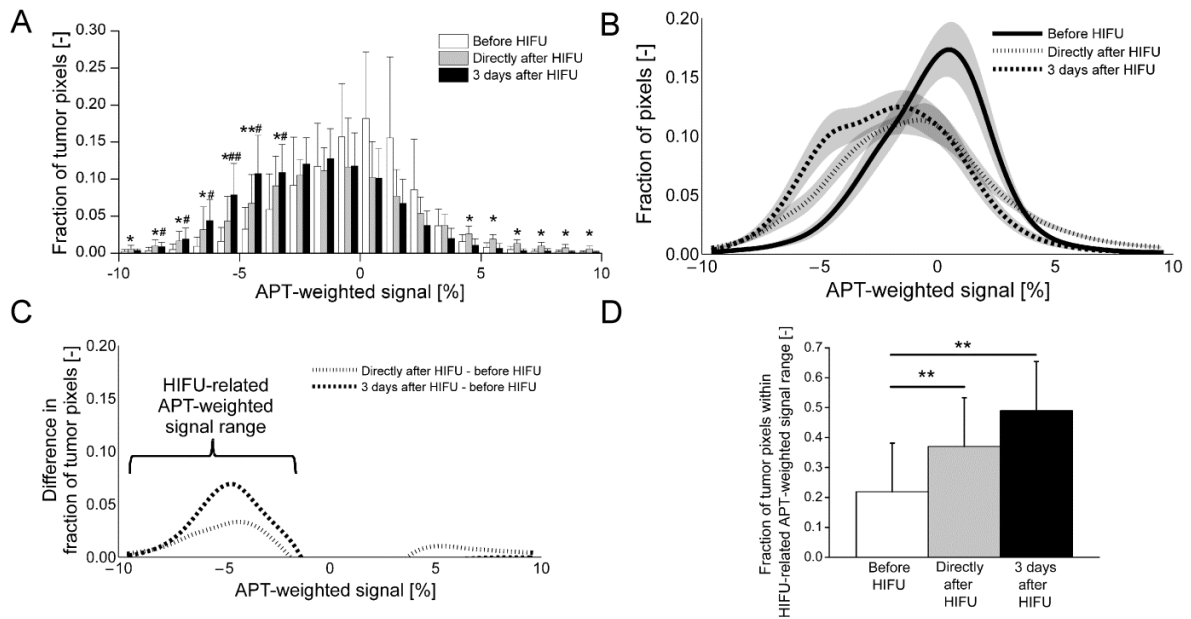


Figure 3. A) Average histogram of APT-weighted signal values in tumors before (white), directly after (gray) and 3 days after HIFU treatment (black). Bars represent mean±SD. * and # indicate significantly increased fractions of pixels directly and at 3 days after HIFU treatment, respectively, as compared to before HIFU with $P < 0.05$ (paired Student's t-test). ** and ## indicate a significant increase in the fractions of pixels directly after and at 3 days after HIFU respectively, as compared to baseline with $P < 0.001$. B) Average distribution of tumor APT-weighted signal values before (solid line), directly after (thin dashed line) and at 3 days after HIFU treatment (thick dashed line). The lines were generated by spline fitting through the averaged histograms. The transparent gray bands around the curves represent the standard error. C) Difference in distribution of tumor APT-weighted signal values directly after (thin dashed line) and at 3 days after HIFU (thick dashed line) with respect to baseline, generated by subtraction of the average distribution before HIFU from the average distributions directly and 3 days after HIFU, respectively. The APT-weighted signal range that showed a pronounced increase of fraction of pixels both directly and at 3 days after HIFU was assumed to be HIFU-related (APT-weighted signals between -10 and -2%). D) Fraction of tumor pixels (mean±SD) within the defined HIFU-related APT-weighted signal range before (white bar), directly after (gray bar) and 3 days after HIFU treatment (black bar). ** indicates a significantly increased fraction of pixels in the HIFU-related APT-weighted signal range after HIFU as compared to before HIFU (paired Student's t-test, $P < 0.001$).

Similarly to the HIFU-treated tumors, the APT-weighted signal distribution in the control tumors was determined at each time point. The resulting averaged histograms are displayed in Figure 4A. No significant differences were observed between the APT-weighted signal distribution at day -1 and day 0. However, small, yet significant, increases in the fractions of tumor pixels with lower APT-weighted signal values (-10 to -8% and -6% to -5%) were observed at day 3 as compared to day -1.

To take into account the influence of tumor progression on the observed changes in APT-weighted signal after HIFU treatment, a quantitative comparison between the tumor APT-weighted signal distributions of the non-treated control tumors at day 3 and the HIFU-treated tumors at 3 days after HIFU was performed. Spline fits through the averaged histograms of the HIFU-treated and non-treated control tumors at the last experimental time points were made. The resulting APT-weighted signal distribution plots are displayed in Figure 4B. The tumor APT-weighted signal distribution of the HIFU-treated animals was

obviously shifted towards lower values as compared to that of the control animals. A significant increase in the fraction of pixels within the above defined HIFU-related APT-weighted signal range was observed for the HIFU-treated tumors at 3 days after HIFU (0.49 ± 0.16) as compared to the control tumors at day 3 (0.23 ± 0.16) (Figure 4C).

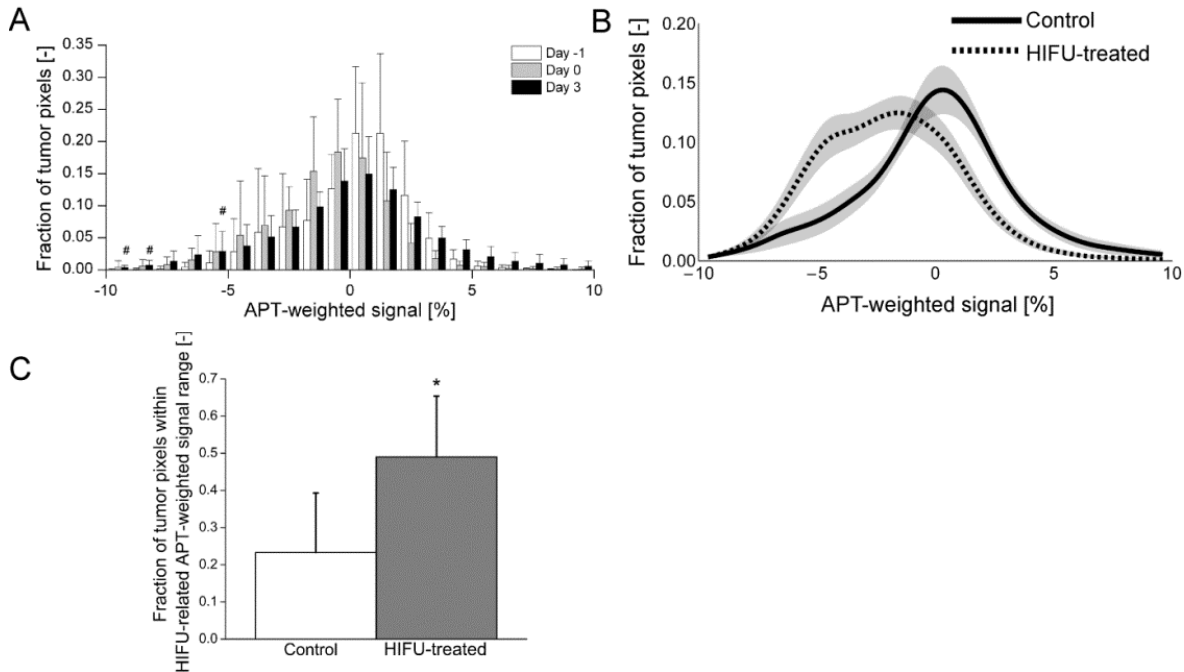


Figure 4. A) Average histogram of APT-weighted signal distribution in non-treated control tumors at day -1 (white), day 0 (gray) and day 3 (black). Bars represent mean \pm SD. # indicates a significantly increased fraction of pixels at day 3 as compared to day -1 (paired Student's t-test, $P < 0.05$). B) Average distribution of tumor APT-weighted signal values of the non-treated control animals at day 3 (solid line) and the HIFU-treated animals at 3 days after HIFU treatment (dashed line; identical to dashed line in Figure 2B). The lines were generated by spline fitting through the averaged histograms. The transparent gray bands around the curves represent the standard error. C) Mean \pm SD fraction of tumor pixels within the HIFU-related APT-weighted signal range for the control animals at day 3 (white bar) and the HIFU-treated animals at 3 days after HIFU (gray bar). * indicates a significantly increased fraction of tumor pixels within the HIFU-related APT-weighted signal range for the HIFU-treated animals as compared to the control animals ($P < 0.05$).

Discussion and Conclusions

In the present study, it was assessed whether APT imaging could be used as a novel biomarker for the characterization of HIFU-treated tumor tissue. APT imaging was performed before, directly after and at 3 days after HIFU treatment. A significant shift towards lower APT-weighted signal values (between -10% and -2%; termed HIFU-related APT-weighted signal range throughout this paper) was observed both directly and at 3 days after HIFU. These results can be compared to other studies in which APT imaging was used to monitor treatment response of tumor tissue. Zhou et al. reported a significant decrease in the tumor APT-weighted signal after radiotherapy of rat glioma (25). Similar findings were reported in a preliminary clinical study on the effects of chemotherapy on the APT signal in breast tumors (23). The observed decreased APT signals were attributed to decreased concentration of mobile proteins and peptides due to the loss of cytoplasm (25). The decreased APT signals in the present study were already observed

directly after HIFU treatment. It is unlikely that this early change in APT contrast is solely caused by decreased protein concentration, since the lymphatic drainage in tumor cells is known to be poor (27). Protein aggregation due to thermal stress during the HIFU treatment (28,29) likely also contributed to the observed decline in tumor APT-weighted signal, because aggregation of proteins causes a decrease in the number of amide protons that are available for exchange with the bulk water. Furthermore, HIFU-induced pH changes could have contributed to the observed decreased APT-weighted signal. It was previously reported that tumor pH decreases after hyperthermic treatment, probably because of lactate accumulation resulting from an increased metabolic rate of the tumor cells under hyperthermic conditions (30). In a future study, the contribution of pH changes to the observed decreased APT-weighted signal after HIFU treatment could be investigated by comparison between APT imaging and quantitative pH mapping. In vivo pH measurements could be obtained by various MRI techniques, including phosphorus spectroscopy (31) and imaging of pH-responsive CEST agents (32,33).

In addition to the observed shift towards lower APT-weighted signal values, also a small, yet significant, increase in fraction of tumor pixels with APT-weighted signal values ranging from 4 to 10% was observed directly after HIFU (Figure 3A). These small regions of increased APT-weighted signal were located outside the large region of decreased APT-weighted signal as evident from the APT-weighted signal maps acquired directly after treatment (Figure 1). Since these regions were outside the main ablation volume, (mild) hyperthermia in these regions may have caused unfolding of proteins. Since these unfolded, not (yet) aggregated proteins have more exchangeable amide protons on their surface, presence of these proteins possibly explains the small areas of increased APT-weighted signal directly after HIFU treatment.

Partial tumor ablation was performed to allow for internal comparison between the APT-weighted signal values of HIFU-treated and residual non-treated tumor tissue. Global analysis of the changes in APT-weighted signal in the tumor tissue by calculation of mean APT-weighted signal values in the tumor tissue would mask the effects of HIFU treatment on tumor APT-weighted signal because of the presence of unaffected viable tumor tissue. Therefore, histogram analysis was preferred, which is more sensitive to regional changes after treatment. A similar histogram analysis of tumor APT signals before and after treatment has also been performed in the aforementioned study on the effects of radiotherapy on the APT signal, in which a similar shift towards lower APT-weighted signal values was observed (25).

The histogram analysis was also carried out for non-treated control tumors of which APT imaging was performed at the same time points. Subtle, yet significant, increases in the fractions of pixels with lower APT-weighted signal values (-10 to -8% and -6% to -5%) were observed at day 3 as compared to day -1. This decrease in tumor APT-weighted signal was possibly caused by necrosis induced by tumor progression during the time between the experiments. Nevertheless, the shift towards decreased APT-weighted signal

values was much less pronounced than for the HIFU-treated animals. A significant increase was observed in the fraction of tumor pixels within the HIFU-related APT-weighted signal range for the HIFU-treated animals at 3 days after HIFU as compared to the control animals at the corresponding experimental time point (Figure 4C).

The APT imaging protocol consisted of a multi-slice acquisition, covering the whole tumor volume. APT imaging is known to be sensitive to B_0 field inhomogeneities. Since the APT-weighted signals in this study were derived from asymmetry analysis, the water resonance signals should be properly centered at the offset of 0 ppm. Sufficient B_0 homogeneity was achieved by higher-order local shimming of the tumor-bearing leg. As a quality assessment of the shimming routine, a PRESS sequence was run in the shimming volume before and after local shimming. From the spectra, the line width of the water signal was determined. The water line width at half height was significantly decreased by local shimming (0.17 ± 0.04 ppm before shimming, 0.12 ± 0.02 ppm after shimming), indicative of good B_0 homogeneity in the tumor tissue. Importantly, no significant difference between the water line widths of spectra of HIFU-treated and non-treated tumors was observed (0.12 ± 0.02 ppm and 0.11 ± 0.02 ppm, respectively). To further assure proper centering of the water resonance signal around 0 ppm, a magnetization transfer spectrum around 0 ppm was acquired at the center slice to correct for a possible deviation between the scanner transmitter frequency setting and the actual water frequency (see Materials and Methods). After local shimming and the frequency correction, accurate APT measurements could be performed in which significant contrast between HIFU-treated and non-treated tumor tissue was observed. In clinical practice, accurate water frequency determination and shimming might be considerably more challenging. Fortunately, extensive Z-spectrum acquisitions and analyses combined with voxel-by-voxel correction of the B_0 field inhomogeneities (19,34) and the development of APT imaging strategies that are more robust to B_0 inhomogeneities (35) have shown potential to improve the APT image quality in clinical studies.

A potential drawback of asymmetry analysis for the determination of the APT contrast, could be the possible influence of aliphatic protons, resonating at ~ -3.5 ppm. Direct saturation of these protons and a Nuclear Overhauser Effect (NOE) caused by cross-relaxation between aliphatic and water protons (36) could affect the measured APT-weighted signals. Recently, asymmetry analysis showed to be non-sufficient to discriminate between normal and necrotic tumor tissue in a subcutaneous mouse tumor model, possibly caused by the aliphatic effect (37). In those experiments, APT-weighted signals of approximately -4 % were observed for the tumor tissue. We observed an average tumor APT-weighted signal of $-0.07 \pm 1.20\%$ at baseline, indicating that the aliphatic effect probably had less effect in our experiments. Furthermore, a clear distinction between HIFU-induced tumor necrosis and viable tumor tissue was observed. The better performance of the asymmetry analysis in our experiments could be caused by the different tumor model used here. Furthermore, our APT measurements were performed with a higher amplitude of the saturation pulse ($1.3 \mu\text{T}$ vs. $0.6 \mu\text{T}$), which

probably increased the contrast in the asymmetry analysis (38). The influence of aliphatic protons could be assessed by extensive analysis of the z-spectrum, which was beyond the scope of this study.

The acquisition time of the multislice APT imaging protocol was 96-128 minutes for 12-16 slices. Since acquisition time is not a major issue during preclinical studies, a long TR (10 s) between the saturation pulses was chosen to minimize the dependence of the APT signals on T_1 relaxation. Furthermore, a relatively long low-power saturation pulse was used for saturation to reduce the effects of direct water saturation and conventional magnetization transfer effects. However, for human application, this long acquisition time would be unacceptable. Recently, multiple 3D and multislice CEST imaging protocols have been proposed that allow for APT imaging with large volume coverage within a clinically acceptable acquisition time (39-42).

The APT imaging results were compared to T_2 -weighted and contrast-enhanced T_1 -weighted imaging, which are conventional MRI techniques that are clinically used to assess tumor tissue status after HIFU treatment. A heterogeneous appearance of the HIFU-treated tumor tissue was observed in the T_2 -weighted images, which was also observed in previous studies on the evaluation of HIFU treatment of prostate tumors (5,6). The contrast-enhanced T_1 -weighted images showed a large, non-enhancing tumor volume after HIFU treatment that was substantially larger than the volume of decreased APT-weighted signal. Quantitative analysis showed that the non-perfused tumor fractions were larger than tumor fractions within the HIFU-related APT-weighted signal range at both time points after HIFU. Good visual agreement between necrotic, non-viable tumor tissue regions observed in histology and tumor regions with decreased APT-weighted signal was observed, which suggests that the contrast-enhanced T_1 -weighted imaging overestimated the extent of tissue necrosis. Contrary, a recent study on MR-guided HIFU treatment of a rabbit tumor model reported that contrast-enhanced T_1 -weighted imaging underestimates the area of necrosis in histology directly after HIFU treatment (43). The larger non-perfused volume in the present study was likely caused by the fact that the subcutaneous CT26 colon carcinoma is highly vascularized (44,45) and therefore probably more sensitive to tumor vessel destruction induced by the HIFU treatment (46).

In **chapter 3**, it was demonstrated that residual non-treated tumor tissue could be detected by multiparametric MR analysis, based on T_1 , T_2 and ADC. The strongest correlation between HIFU-treated tumor volume fractions derived from the multiparametric MR analysis and histology-derived non-viable tumor fractions was observed at 3 days after HIFU. In the current study, a significant change in the APT-weighted signal distribution in the tumor was already observed directly after HIFU treatment. This could indicate that inclusion of APT imaging in the previously described MRI protocol would allow for improved discrimination between successfully treated and residual non-treated tumor tissue directly after HIFU. Therefore, in a future study, APT imaging will be included in the previously described multiparametric MR protocol. Quantitative histology will be

performed to assess the complementary value of APT imaging as compared to more traditional MRI parameters for identification of HIFU-treated tumor tissue. In the current study, MR imaging was restricted to APT imaging, since the objective of this initial study was to assess whether tumor APT contrast changes by HIFU treatment.

In summary, tumor regions with substantially decreased APT-weighted signal were observed after HIFU treatment. These regions showed visual agreement with non-viable, necrotic tumor regions observed in histology. Analysis of the tumor APT-weighted signal distribution showed a pronounced shift towards lower APT-weighted signal values after HIFU. The fractions of pixels with APT-weighted signals between -10 and -2 % significantly increased after HIFU treatment. These results provide evidence that APT imaging may serve as a new biomarker for identification of HIFU-treated tumor tissue. In the near future, APT imaging will be added to the previously described multiparametric protocol to assess its complementary value for HIFU treatment evaluation.

Acknowledgements

This research was performed within the framework of CTMM, the Center for Translational Molecular Medicine (www.ctmm.nl), project VOLTA (grant 05T-201).

References

1. **Hynnen K.** *Ultrasonics* 2010;50:221-229.
2. **ter Haar G.** *Prog Biophys Mol Biol* 2007;93:111-129.
3. **Kennedy JE.** *Nat Rev Cancer* 2005;5:321-327.
4. **Murat FJ, Poissonnier L, Pasticier G, Gelet A.** *Cancer Control* 2007;14:244-249.
5. **Rouviere O, Girouin N, Glas L, Ben Cheikh A, Gelet A, Mege-Lechevallier F, Rabilloud M, Chapelon JY, Lyonnet D.** *Eur Radiol* 2010;20:48-55.
6. **Kirkham AP, Emberton M, Hoh IM, Illing RO, Freeman AA, Allen C.** *Radiology* 2008;246:833-844.
7. **Schmitz AC, Gianfelice D, Daniel BL, Mali WP, van den Bosch MA.** *Eur Radiol* 2008;18:1431-1441.
8. **Leslie TA, Kennedy JE, Illing RO, Ter Haar GR, Wu F, Phillips RR, Friend PJ, Roberts IS, Cranston DW, Middleton MR.** *Br J Radiol* 2008;81:564-571.
9. **Leslie T, Ritchie R, Illing R, Ter Haar G, Phillips R, Middleton M, Bch B, Wu F, Cranston D.** *Br J Radiol* 2012;85:1363-1370.
10. **Peng HH, Huang TY, Tseng WY, Lin EL, Chung HW, Wu CC, Wang YS, Chen WS.** *J Magn Reson Imaging* 2009;30:596-605.
11. **van Zijl PC, Yadav NN.** *Magn Reson Med* 2011;65:927-948.
12. **Liu G, Song X, Chan KW, McMahon MT.** *NMR Biomed* 2013;26:810-828.
13. **Vinogradov E, Sherry AD, Lenkinski RE.** *J Magn Reson* 2013;229:155-172.
14. **Jokivarsi KT, Grohn HI, Grohn OH, Kauppinen RA.** *Magn Reson Med* 2007;57:647-653.
15. **Sun PZ, Sorensen AG.** *Magn Reson Med* 2008;60:390-397.
16. **Zhou J, van Zijl PC.** *Transl Stroke Res* 2011;3:76-83.
17. **Zhou J, Lal B, Wilson DA, Larterra J, van Zijl PC.** *Magn Reson Med* 2003;50:1120-1126.
18. **Salhotra A, Lal B, Larterra J, Sun PZ, van Zijl PC, Zhou J.** *NMR Biomed* 2008;21:489-497.
19. **Jones CK, Schlosser MJ, van Zijl PC, Pomper MG, Golay X, Zhou J.** *Magn Reson Med* 2006;56:585-592.
20. **Zhou J.** *Methods Mol Biol* 2011;711:227-237.
21. **Zhou J, Blakeley JO, Hua J, Kim M, Larterra J, Pomper MG, van Zijl PC.** *Magn Reson Med* 2008;60:842-849.
22. **Howe FA, Barton SJ, Cudlip SA, Stubbs M, Saunders DE, Murphy M, Wilkins P, Opstad KS, Doyle VL, McLean MA, Bell BA, Griffiths JR.** *Magn Reson Med* 2003;49:223-232.
23. **Dula AN, Arlinghaus LR, Dortch RD, Dewey BE, Whisenant JG, Ayers GD, Yankeelov TE, Smith SA.** *Magn Reson Med* 2013;70:216-224.
24. **Jia G, Abaza R, Williams JD, Zynger DL, Zhou J, Shah ZK, Patel M, Sammet S, Wei L, Bahnson RR, Knopp MV.** *J Magn Reson Imaging* 2011;33:647-654.

25. **Zhou J, Tryggestad E, Wen Z, Lal B, Zhou T, Grossman R, Wang S, Yan K, Fu D, Ford E, Tyler B, Blakeley JO, Lateria J, Van Zijl P.** *Nat Med* 2011;17:130-134.
26. **Seip R, Chin CT, Hall CS, Raju BI, Ghanem A, Tiemann K.** *IEEE Trans Biomed Eng* 2010;57:61-70.
27. **Matsumura Y, Maeda H.** *Cancer Res* 1986;46:6387-6392.
28. **Bellmann K, Charette SJ, Nadeau PJ, Poirier DJ, Loranger A, Landry J.** *Cell Stress Chaperones* 2010;15:101-113.
29. **Zhang Y, Calderwood SK.** *Int J Hyperthermia* 2011;27:409-414.
30. **Reinhold HS, Endrich B.** *Int J Hyperthermia* 1986;2:111-137.
31. **Griffiths JR.** *Br J Cancer* 1991;64:425-427.
32. **Delli Castelli D, Terreno E, Aime S.** *Angew Chem Int Ed Engl* 2011;50:1798-1800.
33. **Longo DL, Dastru W, Digilio G, Keupp J, Langereis S, Lanzardo S, Prestigio S, Steinbach O, Terreno E, Uggeri F, Aime S.** *Magn Reson Med* 2011;65:202-211.
34. **Kim M, Gillen J, Landman BA, Zhou J, van Zijl PC.** *Magn Reson Med* 2009;61:1441-1450.
35. **Scheidegger R, Vinogradov E, Alsop DC.** *Magn Reson Med* 2011;66:1275-1285.
36. **van Zijl PC, Zhou J, Mori N, Payen JF, Wilson D, Mori S.** *Magn Reson Med* 2003;49:440-449.
37. **Desmond KL, Moosvi F, Stanisz GJ.** *Magn Reson Med* 2013;doi: 10.1002/mrm.24822.
38. **Zhao X, Wen Z, Huang F, Lu S, Wang X, Hu S, Zu D, Zhou J.** *Magn Reson Med* 2011;66:1033-1041.
39. **Jones CK, Polders D, Hua J, Zhu H, Hoogduin HJ, Zhou J, Luijten P, van Zijl PC.** *Magn Reson Med* 2012;67:1579-1589.
40. **Sun PZ, Murata Y, Lu J, Wang X, Lo EH, Sorensen AG.** *Magn Reson Med* 2008;59:1175-1182.
41. **Zhao X, Wen Z, Zhang G, Huang F, Lu S, Wang X, Hu S, Chen M, Zhou J.** *Mol Imaging Biol* 2013;15:114-122.
42. **Zhu H, Jones CK, van Zijl PC, Barker PB, Zhou J.** *Magn Reson Med* 2010;64:638-644.
43. **Wijlemans JW, Deckers R, van den Bosch MA, Seinstra BA, van Stralen M, van Diest PJ, Moonen CT, Bartels LW.** *Invest Radiol* 2013;48:381-386.
44. **Aulino P, Berardi E, Cardillo VM, Rizzuto E, Perniconi B, Ramina C, Padula F, Spugnini EP, Baldi A, Faiola F, Adamo S, Coletti D.** *BMC Cancer* 2010;10:363.
45. **Ogawara K, Un K, Minato K, Tanaka K, Higaki K, Kimura T.** *Int J Pharm* 2008;359:234-240.
46. **Wu F, Chen WZ, Bai J, Zou JZ, Wang ZL, Zhu H, Wang ZB.** *Ultrasound Med Biol* 2002;28:535-542.

Chapter 5

T_{1ρ} Mapping for the Evaluation of High Intensity Focused Ultrasound Tumor Treatment

Stefanie Hectors, Rik Moonen, Gustav Strijkers, Klaas Nicolay

Published in Magn Reson Med 2014;doi:10.1002/mrm.25269

Abstract

Purpose

This study was aimed to assess the effects of High Intensity Focused Ultrasound (HIFU) thermal ablation on tumor $T_{1\rho}$.

Materials and Methods

In vivo $T_{1\rho}$ measurements of murine tumors at various spin-lock amplitudes ($B_1=0-2000$ Hz) were performed before ($n=13$), directly after ($n=13$) and 3 days ($n=7$) after HIFU treatment. T_2 maps were obtained from the measurements at $B_1=0$ Hz.

Results

Average tumor $T_{1\rho}$ distributions at the different experimental time points showed a shift toward lower $T_{1\rho}$ values after HIFU for all spin-lock amplitudes, which became larger with increasing spin-lock amplitude at 3 days after treatment. Statistical analysis confirmed a significant effect of spin-lock amplitude on the average change in $T_{1\rho}$ ($\Delta T_{1\rho}$) as compared to baseline at 3 days after HIFU. At 3 days after treatment, $\Delta T_{1\rho}$ values at B_1 above 100 Hz were significantly lower (more negative) than at $B_1=0$ Hz (T_2).

Conclusions

Significant changes in tumor $T_{1\rho}$ were observed after HIFU treatment. These $T_{1\rho}$ changes were distinctly more pronounced than HIFU-induced changes in T_2 . The results indicate that $T_{1\rho}$ imaging is sensitive to HIFU-induced tissue changes and may thus be a suitable MR method for the evaluation of HIFU treatment.

Introduction

Magnetic resonance-guided High Intensity Focused Ultrasound (MR-HIFU) is extensively being investigated as a non-invasive technique for thermal treatment of tumors (1). During HIFU ablation, coagulative necrosis is induced in the tissue by rapid heating to a temperature of approximately 60°C (2). Currently, the main clinical application of MR-HIFU is the ablation of benign uterine fibroids (3,4). The last decade, the clinical use of MR-HIFU has been expanded to the treatment of malignant tumors, such as prostate (5,6) and breast (7) tumors. For the application of MR-HIFU for the treatment of malignant lesions, it is of key importance that the success of the ablation intervention can be accurately determined and that residual or recurrent tumor tissue can be detected after the procedure. In **chapter 3**, it was shown by quantitatively comparing MRI data with histology that residual non-treated tumor tissue can be distinguished from successfully treated tumor tissue by multiparametric MRI analysis based on a combination of T₁, T₂ and apparent diffusion coefficient (ADC) data. The HIFU-treated and non-treated tumor tissue could not be accurately segmented with any of the individual MRI parameters. Despite the promising results of the above multiparametric MR analysis as a method for HIFU evaluation, other MRI parameters may be more specific to the nature of HIFU-induced changes in the tumor tissue. Tissue destruction by HIFU is mainly based on protein denaturation, which results in cell death by coagulative necrosis. Several advanced MRI methods may report more directly on protein denaturation than T₁, T₂ and ADC. In **chapter 4**, it was shown for example that amide proton transfer (APT) imaging is a promising MR technique for the evaluation of HIFU treatment. Both directly and 3 days after HIFU treatment distinct regions of decreased APT-weighted signal were observed that corresponded with non-viable tissue observed in histology.

Another MRI parameter that is potentially sensitive to HIFU-induced protein denaturation is the longitudinal relaxation time in the rotating frame (T_{1ρ}). T_{1ρ} is a measure of the decay of magnetization in the transverse plane during a spin-lock pulse which is applied parallel to the magnetization vector. Tissue T_{1ρ} values are predominantly influenced by protein-water interactions (8). While APT measurements are sensitive to the relatively slowly exchanging amide protons in tissue, on-resonance T_{1ρ} measurements are mainly sensitive to fast exchanging protons. T_{1ρ} imaging may thus provide another yet related source of contrast between HIFU-treated and non-treated tumor tissue. T_{1ρ} imaging has previously been used for multiple applications, including the characterization of cartilage composition and degeneration (9,10), tumors (11-13), stroke (8,14), myocardial infarction (15,16) and neurodegenerative diseases (17). Several preclinical studies have reported on changes in T_{1ρ} after chemotherapy (18) and gene therapy (19-21) of tumors. In these studies, prolonged T_{1ρ} values were observed after treatment. Modeling of the T_{1ρ} dispersion showed that the rise in T_{1ρ} was caused by water accumulation in the tumor tissue and an increase in both the correlation time of water associated with macromolecules and the exchange correlation time (20).

The goal of the present study was to assess the effects of HIFU treatment on the $T_{1\rho}$ of tumor tissue. To that aim, $T_{1\rho}$ measurements at spin-lock strengths varying between 0 and 2000 Hz were performed before, directly after and at 3 days after HIFU treatment of a murine subcutaneous tumor model. The HIFU treatment consisted of partial ablation of the tumors to allow for internal reference between successfully treated tumor tissue and residual non-treated tumor tissue.

Materials and Methods

Murine tumor model

CT26.WT murine colon carcinoma cells (American Type Culture Collection (ATCC; CRL-2638)) were cultured as a monolayer at 37°C and 5% CO₂ in RPMI-1640 medium (2 mM L-glutamine, 10 mM HEPES, 1 mM sodium pyruvate, 4500 mg/L glucose, and 1500 mg/L sodium bicarbonate) (Invitrogen, Breda, The Netherlands), supplemented with 10% fetal bovine serum (Greiner Bio-One, Alphen a/d Rijn, The Netherlands) and 50 U/ml penicillin/streptomycin (Lonza Bioscience, Basel, Switzerland). Early passages (5-10) of the original ATCC batch were used for inoculation.

10-12 week-old male Balb/c mice (Charles River, Maastricht, The Netherlands) were inoculated with 2×10^6 CT26.WT cells subcutaneously in the right hind limb. Approximately 10 days after inoculation, tumors became visible in all animals. The first MRI experiment was performed when tumors had reached a size of approximately 300 mm³. The animal experiments were approved by the animal experiment committee of Maastricht University (The Netherlands).

Study design

Both HIFU-treated (n=13) and non-treated control (n=7) animals were included in this study. The HIFU-treated animals were subjected to MRI 1 day before (n=13), directly after (n=13) and 3 days after (n=7) HIFU treatment. The time points of the MRI examinations of the control animals corresponded with the MRI examinations of the HIFU-treated animals and are referred to as day -1, day 0 and day 3. The study design comprised three different experimental groups: HIFU-treated animals sacrificed after the MRI examination directly after HIFU (n=6), HIFU-treated animals sacrificed after the MRI examination at 3 days after HIFU (n=7) and non-treated control animals that were sacrificed after the MRI examination at day 3 (n=7).

HIFU treatment

The HIFU treatment was performed outside the MR scanner with the preclinical Therapy Imaging Probe System (TIPS, Philips Research, Briarcliff Manor, NY, USA) (22). Treatment was performed under general anesthesia (1-2% isoflurane) and precautionary analgesia (buprenorphine, 0.1 mg/kg s.c., administered 30 min before treatment). The control animals received an equal dose of analgesia at the corresponding time point. A square 4x4 mm² treatment grid consisting of 25 equally-spaced treatment points was defined within the tumor area. The treatment volume typically covered approximately 50%

of the total tumor volume to allow for presence of both HIFU-treated and residual non-treated tumor tissue after the HIFU procedure. Treatment settings were: frequency 1.4 MHz, pulse repetition frequency 20 Hz, acoustic power 12 W, duty cycle 50%, treatment time 30 s. A wait time of 120 s was applied between sonication of consecutive treatment points to allow cooling of the tissue to body temperature. During pilot experiments of three mice, a bare-wire thermocouple (80- μ m-diameter T-type thermocouple; T-150A, Physitemp Instruments, Clifton, NJ, USA) was inserted into the tumor tissue to monitor temperature development during HIFU treatment. A temperature of approximately 65°C was reached during sonication with the above-mentioned HIFU settings. The thermocouple was not used during HIFU treatment of the experimental groups to prevent non-HIFU-induced damage to the tumor tissue.

MRI measurements

The MRI examinations were performed with a 7T scanner, equipped with a 72-mm-diameter quadrature RF coil (Bruker BioSpin, Ettlingen, Germany). The mice were positioned in a cradle with an anesthesia mask (1-2% isoflurane). Respiration and body temperature were monitored with a balloon sensor and rectal probe, respectively. The body temperature was maintained at approximately 37°C with a warm water pad. The tumor-bearing paw was covered with degassed ultrasound gel (Aquasonic® 100, Parker Laboratories, Fairfield, NJ, USA) for reduction of susceptibility artifacts in the echo planar imaging (EPI) sequence.

Higher-order local shimming (Bruker MAPSHIM routine) was performed on the tumor-bearing paw to improve B₀ field homogeneity. The T_{1ρ} pulse sequence was performed in 2 segments and consisted of a spin-lock preparation compensated for B₁ and B₀ field imperfections (23) followed by gradient-echo EPI read-out (echo time TE=5 ms, repetition time TR=2000 ms, number of averages NA=2). The acquisition was performed with 6 different spin-locking times (5, 10, 20, 40, 60 and 80 ms) and 8 different spin-lock amplitudes (B₁ = 0, 100, 250, 500, 750, 1000, 1500 and 2000 Hz). The acquisitions with the amplitude of 0 Hz can be considered as a T₂ measurement, as the B₀- and B₁-compensated spin-lock preparation in the absence of a spin-lock pulse is T₂-weighted.

In addition to the T_{1ρ} acquisitions, T₂-weighted imaging (spin-echo, TE=30 ms, TR=1000 ms, NA=1) and contrast-enhanced T₁-weighted imaging (spin-echo, TE=8 ms, TR=800 ms, NA=2, acquisitions before and directly after intravenous injection of Dotarem (0.3 mmol Gd/kg)) were performed.

For all MRI acquisitions a matrix size of 128 x 128 and a field of view of 4 x 4 cm² were used. Eight to 12 slices with a slice thickness of 1 mm were defined covering the whole tumor volume.

Data analysis

Image analysis was performed in Mathematica 8.0 (Wolfram Research, Champaign, IL, USA). T_{1ρ} maps at each spin-lock amplitude were generated by mono-exponential fitting

of the signal intensities at the different spin-lock times. Regions of interest (ROIs) were manually drawn around the tumor tissue on each slice of the T_2 -weighted acquisitions. In addition, small ROIs (10-20 pixels) in the muscle tissue surrounding the tumor were drawn on each slice. These muscle tissue ROIs were used to assess the repeatability of the $T_{1\rho}$ measurements.

To analyze the effects of HIFU treatment on the $T_{1\rho}$ in the tumor tissue, histograms of $T_{1\rho}$ in the tumor ROI were generated for each tumor at each time point. The histograms were made for all spin-lock amplitudes. The histogram properties were: 20 bins, bin width 5 ms and a $T_{1\rho}$ range from 0 to 100 ms. Histograms were averaged for all animals within the different groups (HIFU-treated and control) and spline fitting was performed through these averaged histograms to visualize the $T_{1\rho}$ distributions at the different experimental time points.

From the contrast-enhanced T_1 -weighted acquisitions, maps of the signal enhancement (SE) after Gadolinium injection were generated according to the following formula:

$$SE = [(SI_{\text{after injection}} - SI_{\text{before injection}}) / SI_{\text{before injection}}] * 100\%,$$

in which $SI_{\text{before injection}}$ and $SI_{\text{after injection}}$ are the signal intensities in the images before and after contrast agent injection, respectively.

Histological analysis

Dissected tumors were snap-frozen in isopentane and stored at $-80\text{ }^\circ\text{C}$. Subsequently, tumors were cut into $5\text{ }\mu\text{m}$ thick sections with a distance of approximately $300\text{ }\mu\text{m}$ between the sections. Multiple sections were collected at each position to allow for different staining procedures. The cryo-sections were briefly air-dried and subsequently stained for nicotinamide adenine dinucleotide (NADH) diaphorase activity to assess cell viability. Sections were incubated at $37\text{ }^\circ\text{C}$ for 1 h in Gomori-Tris-HCl buffer (pH 7.4) containing β -NAD reduced disodium salt hydrate (Sigma-Aldrich, St. Louis, MO, USA, 0.71 mg/ml buffer solution) and nitro blue tetrazolium (Sigma-Aldrich, 0.29 mg/ml buffer solution). Adjacent cryo-sections were stained with haematoxylin and eosin (H&E) to analyze general morphology. Brightfield microscopy was performed on a selection of the stained sections and consisted of mosaic acquisition of the entire section at 5x magnification.

Statistical analysis

All data are presented as mean \pm standard deviation (SD). To assess the repeatability of the $T_{1\rho}$ measurements, the effect of time on the average $T_{1\rho}$ values in the muscle ROI in the control animals was tested for significance using an Analysis of Variance (ANOVA) method for repeated measures. For both the HIFU-treated and control animals, the average $T_{1\rho}$ values in the tumor ROI at the different time points were statistically compared with a two-sided paired t-test for each spin-lock amplitude. The effect of spin-lock amplitude on the difference in average tumor $T_{1\rho}$ ($\Delta T_{1\rho}$) between before and after

HIFU treatment was tested for significance using ANOVA for repeated measures with the spin-lock amplitude as the within-subject factor. The $\Delta T_{1\rho}$ value was obtained by subtraction of the average $T_{1\rho}$ value in the tumor ROI before HIFU from the average $T_{1\rho}$ value after treatment. In the case the influence of spin-lock amplitude on the $\Delta T_{1\rho}$ proved to be significant, $\Delta T_{1\rho}$ values at the different spin-lock amplitudes were compared separately with a one-sided paired t-test. For all tests, the level of significance was set at $\alpha=0.05$.

Results

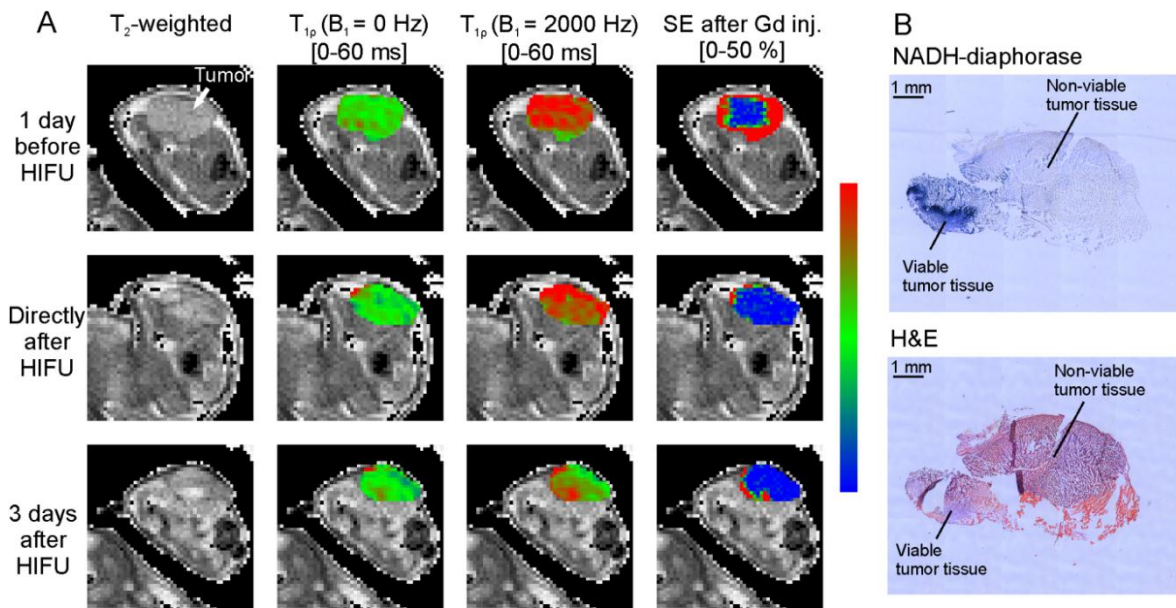


Figure 1. A) Representative example of the MRI results of a tumor-bearing leg before, directly after and 3 days after HIFU treatment. T₂-weighted images of an axial slice in the tumor-bearing leg are shown in the first column of panels. In the second and third column the T_{1ρ} maps at B₁=0 Hz, which can be considered as T₂ maps, and at B₁=2000 Hz are overlaid on the tumor pixels, respectively. In the fourth column the signal enhancement (SE) maps after Gd injection are overlaid on the tumor pixels. The parameter maps were scaled according to the color scale bar which is shown at the right-hand side of the figure. The corresponding parameter range for this scale bar is shown above each column. B) NADH-diaphorase (top) and H&E-stained tumor sections (bottom) obtained at 3 days after HIFU treatment at approximately the same location as the MRI slice at 3 days after treatment. A large region of non-viable (NADH-diaphorase negative) and necrotic (H&E) tumor tissue was observed. A small region of residual viable tumor tissue was observed in the left bottom of the section.

Figure 1A shows representative MRI results as obtained before, directly after and 3 days after HIFU treatment. No clear effects of the HIFU treatment were observed on the T₂-weighted images. This was confirmed by absence of visible changes after HIFU in the T_{1ρ} maps at B₁=0 Hz, which essentially represent T₂ maps. In contrast, the T_{1ρ} maps at B₁=2000 Hz showed a pronounced decrease in T_{1ρ} in a large portion of the tumor at 3 days after HIFU treatment. Directly after treatment, only a minor decrease was observed in tumor T_{1ρ} at B₁=2000 Hz. The signal enhancement maps before HIFU treatment showed an area of decreased perfusion in the tumor core surrounded by regions of high perfusion in the tumor rim. After HIFU treatment, the area of decreased perfusion

extended throughout almost the entire tumor tissue. NADH-diaphorase- and H&E-staining on tumor sections obtained at 3 days after HIFU treatment confirmed extensive necrosis in the tumor tissue (Figure 1B). This necrotic, non-viable region visually corresponded to the areas of decreased $T_{1\rho}$ at $B_1=2000$ Hz.

Average tumor $T_{1\rho}$ distributions of the HIFU-treated animals at the different experimental time points are displayed in Figure 2 for all assessed spin-lock amplitudes. $T_{1\rho}$ shifted toward higher $T_{1\rho}$ values at larger spin-lock amplitudes, indicative of presence of tumor $T_{1\rho}$ dispersion in the used range of spin-lock amplitudes. After HIFU treatment, a shift toward lower $T_{1\rho}$ values was observed for all spin-lock amplitudes. At 3 days after HIFU treatment, the tail of the $T_{1\rho}$ distributions toward lower values became larger with increasing spin-lock amplitude, indicative of a larger contrast between non-treated and HIFU-treated tumor tissue at higher spin-lock amplitudes.

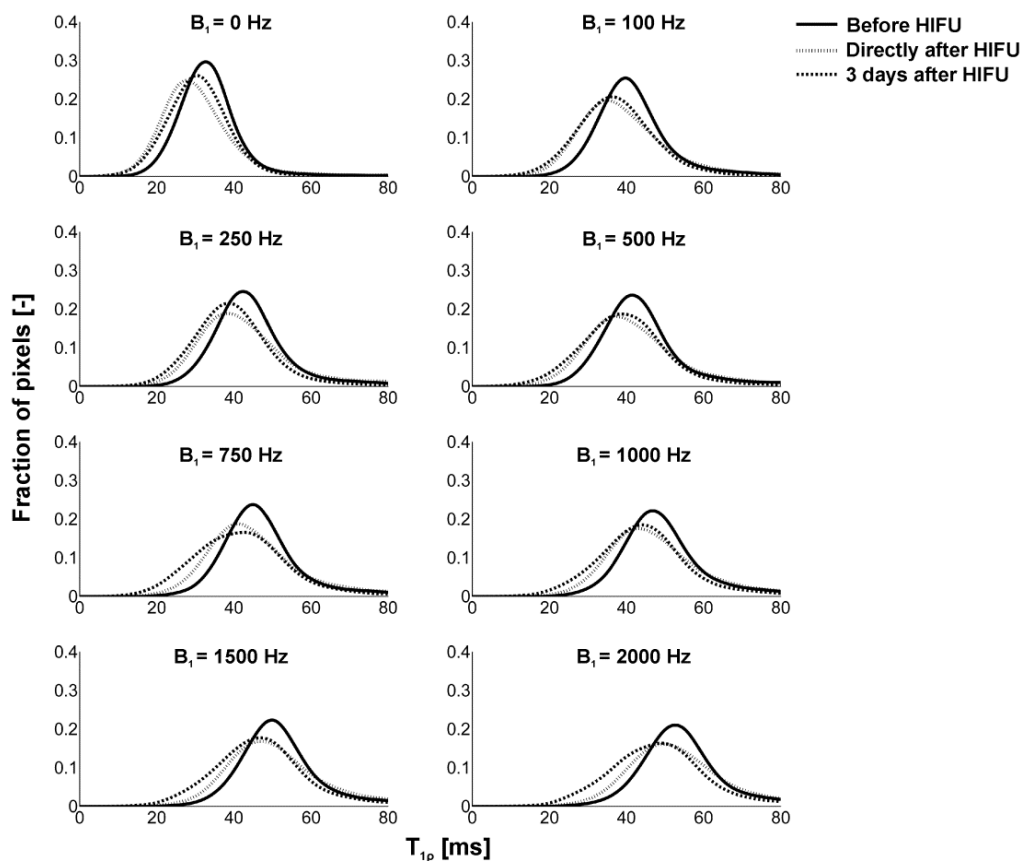


Figure 2. Average $T_{1\rho}$ distributions in the HIFU-treated tumors at the different experimental time points for all assessed spin-lock amplitudes. The lines were generated by spline fitting through averaged histograms.

Quantitative analysis of the average $T_{1\rho}$ value in the tumors of the HIFU-treated animals at the different experimental time points (Figure 3A) showed a significant decrease in the average $T_{1\rho}$ at 3 days after HIFU treatment as compared to before treatment for spin-lock amplitudes higher than or equal to 100 Hz. No significant differences between the average $T_{1\rho}$ values before HIFU and directly after HIFU were observed. To further evaluate the contrast between the $T_{1\rho}$ of HIFU-treated and non-treated tumor tissue, average changes in $T_{1\rho}$ values (i.e., $\Delta T_{1\rho}$) were calculated for the entire tumor ROIs (Figure 3B). No

significant effect of spin-lock amplitude on the $\Delta T_{1\rho}$ value between directly after and before HIFU was observed. The average $\Delta T_{1\rho}$ between 3 days after HIFU treatment and before HIFU clearly decreased to larger negative values with increasing spin-lock amplitude. Statistical analysis confirmed a significant effect of spin-lock amplitude on $\Delta T_{1\rho}$ at 3 days after HIFU ($P=0.048$). The $\Delta T_{1\rho}$ values at B_1 strengths above 100 Hz were significantly lower (more negative) than at $B_1=0$ Hz at 3 days after treatment. Furthermore, the $\Delta T_{1\rho}$ value at 2000 Hz was significantly lower than the $\Delta T_{1\rho}$ values at B_1 strengths between 0 and 1000 Hz.

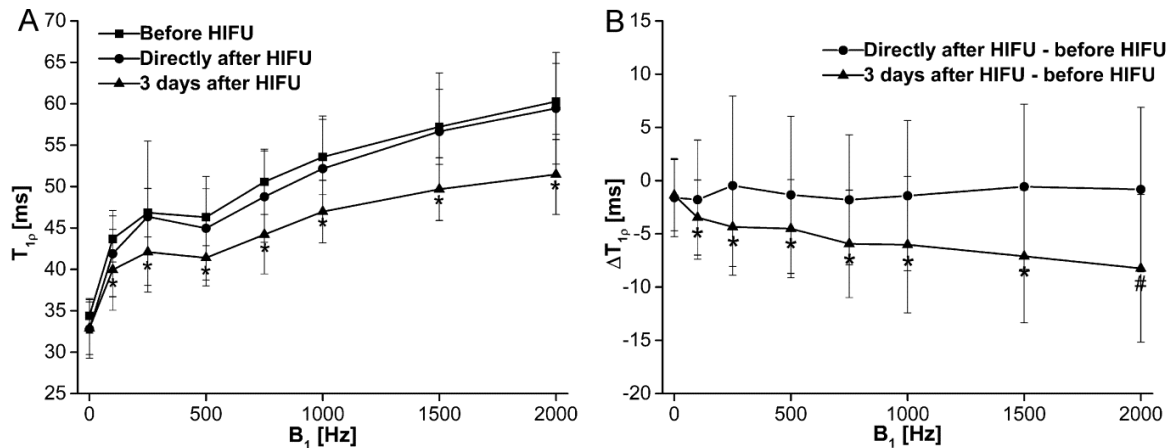


Figure 3. A) Average $T_{1\rho}$ values in the HIFU-treated tumors at the different experimental time points as a function of the spin-lock amplitude. The error bars represent the SD. * indicates a significant difference between the average $T_{1\rho}$ before and after treatment ($P<0.05$). B) Average $T_{1\rho}$ changes ($\Delta T_{1\rho}$) when comparing both time points after HIFU with before HIFU as function of the spin-lock amplitude. The error bars represent the SD. * indicates a significantly lower (more negative) $\Delta T_{1\rho}$ value than at $B_1=0$ Hz ($P<0.05$). # indicates a significantly lower (more negative) $\Delta T_{1\rho}$ value than at all other spin-lock amplitudes, except 1500 Hz.

Representative MRI results of the non-treated control animals, which were scanned at three equivalent time points, are shown in Figure 4A. Homogeneous appearance of the tumor tissue was observed on the T_2 -weighted images at all three time points. No visible changes of the $T_{1\rho}$ of the tumor tissue in time were observed, both at 0 Hz and 2000 Hz. The signal enhancement pattern after Gd injection was similar at all time points and consisted of a less perfused tumor core surrounded by a highly perfused tumor rim. The NADH-diaphorase- and H&E-stained tumor sections, obtained at approximately the same location as the MRI slice at day 3, confirmed general viability of the tumor tissue with small areas of non-viable tumor tissue.

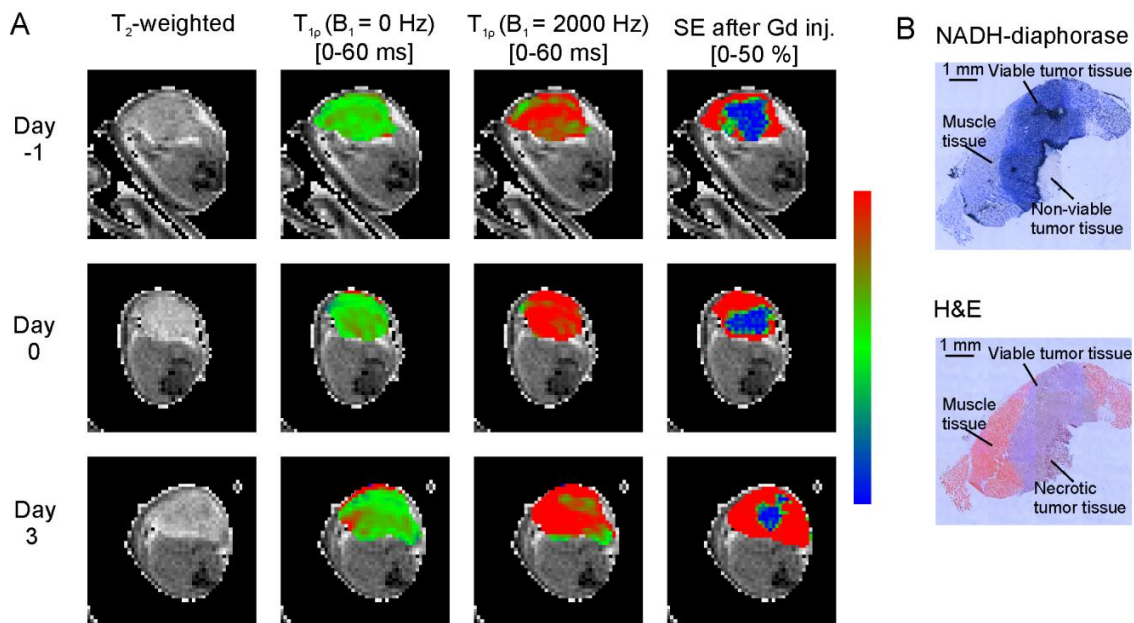


Figure 4. A) Representative example of MRI results of the tumor-bearing leg of a non-treated control animal at day -1, day 0 and day 3. The layout of the figure is identical to that of Figure 1A. B) NADH-diaphorase and H&E-stained tumor sections obtained at day 3 at approximately the same location within the tumor as the MRI slice measured at day 3.

The average tumor $T_{1\rho}$ distributions of the control animals at the different experimental time points are shown in Figure 5. Similar $T_{1\rho}$ distributions were observed for day -1 and day 3 at all spin-lock amplitudes. At day 0, the $T_{1\rho}$ distribution slightly, but not significantly, shifted toward higher $T_{1\rho}$ values as compared to day -1 and day 3.

Figure 6A shows the average $T_{1\rho}$ value in the tumor tissue of the control animals at all time points as a function of the spin-lock amplitude. For all assessed spin-lock amplitudes, the average $T_{1\rho}$ values did not change significantly in time. In Figure 6B the average $T_{1\rho}$ value in the muscle tissue is plotted versus the spin-lock amplitude for the control animals at all time points. For each spin-lock amplitude, no significant effect of time on the muscle $T_{1\rho}$ was observed.

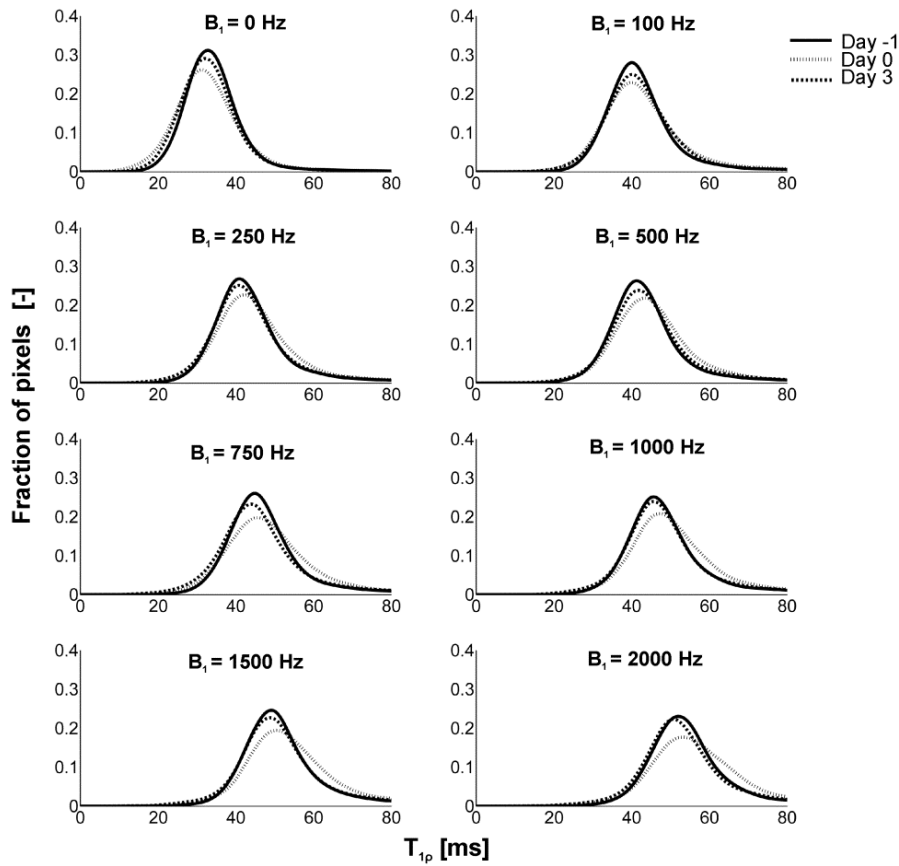


Figure 5. Average $T_{1\rho}$ distributions in the non-treated control tumors at the different experimental time points for all assessed spin-lock amplitudes. The lines were generated by spline fitting through averaged histograms.

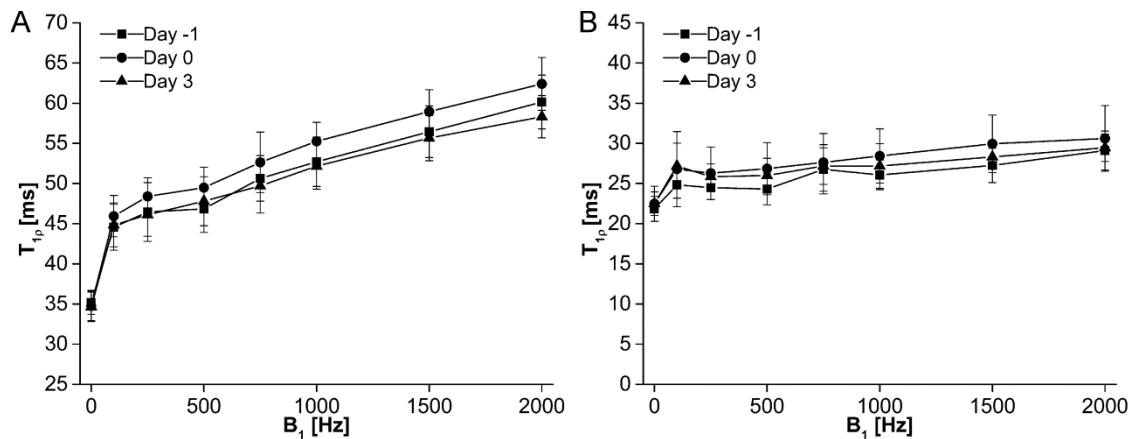


Figure 6. A) Average $T_{1\rho}$ values in the non-treated control tumors at the different experimental time points as a function of the spin-lock amplitude. The error bars represent the SD. No significant differences between the average $T_{1\rho}$ values at the different experimental time points were observed for all assessed spin-lock amplitudes. B) Average $T_{1\rho}$ values in the muscle tissue surrounding the non-treated control tumors at the different experimental time points as a function of the spin-lock amplitude. The error bars represent the SD. For each spin-lock amplitude, there was no significant effect of time on the $T_{1\rho}$ value of the muscle tissue.

Discussion and Conclusions

In this study, the effect of HIFU treatment on the $T_{1\rho}$ of tumor tissue was assessed. A significant decrease in tumor $T_{1\rho}$ was observed at 3 days after HIFU treatment. The $T_{1\rho}$ decline became significantly larger at higher spin-lock amplitudes. Directly after HIFU treatment, no significant changes of the tumor $T_{1\rho}$ values were observed as compared to before HIFU. As indicated in the Introduction, HIFU-induced tissue damage is mainly based on protein denaturation, which occurs instantly during treatment. The absence of significant effects of the HIFU treatment on the tumor $T_{1\rho}$ immediately after treatment indicates that $T_{1\rho}$ may not be directly sensitive to HIFU-induced protein denaturation.

The significant decrease in tumor $T_{1\rho}$ at 3 days after HIFU treatment was likely caused by latent effects of the HIFU treatment. In contrast to the results presented here, in other preclinical studies on the effect of tumor treatment (gene therapy (19-21) and chemotherapy (18)) increased values of $T_{1\rho}$ were observed after treatment. In the studies on $T_{1\rho}$ after gene therapy, the rise in $T_{1\rho}$ occurred at 4 days after gene therapy, whereas a significant increase in $T_{1\rho}$ was observed already at 18 hours after chemotherapy (18). Modeling of the $T_{1\rho}$ dispersion of non-treated tumor tissue and gene-therapy-treated tumor tissue showed that the observed $T_{1\rho}$ rise was caused by an increase of free water and an increase in both the correlation time of water associated with macromolecules and the exchange correlation time (20). The observed decline in tumor $T_{1\rho}$ at 3 days after HIFU treatment reported in the present study was likely caused by opposite effects. HIFU-induced protein denaturation and aggregation could have led to extrusion of water from the tumor tissue because of increased hydrophobic interactions, as has been described in an ex vivo study on thermal treatment of various tissues (24). This extrusion of water could have led to a decrease of the free water proton fraction and thereby have decreased the tumor $T_{1\rho}$ values after HIFU treatment. Furthermore, the correlation time of the exchange between protons of proteins and water molecules could have changed after HIFU treatment. Accumulation of the above-mentioned effects probably led to the significant contrast between HIFU-treated and non-treated tumor tissue observed at 3 days after HIFU treatment.

Modeling of the $T_{1\rho}$ dispersion in the tumors before and after HIFU treatment could give additional insights in the effects of HIFU treatment on the macromolecular tissue status. However, accurate fitting of the $T_{1\rho}$ dispersion in the presented data could not be performed, as the maximum spin-lock amplitude (2000 Hz) was too low. In a previous study on $T_{1\rho}$ imaging of gene-therapy-treated gliomas, the $T_{1\rho}$ dispersion could be modeled based on $T_{1\rho}$ data with spin-lock amplitudes up to approximately 6000 Hz (20). In the current study, inclusion of $T_{1\rho}$ values at similarly high spin-lock amplitudes would probably have improved sampling of the $T_{1\rho}$ dispersion. Furthermore, $T_{1\rho}$ measurements at higher spin-lock amplitudes could even further increase the contrast between non-treated and HIFU-treated tumor tissue, since the absolute $\Delta T_{1\rho}$ value at 3 days after HIFU was still increasing at 2000 Hz (Figure 3B). Unfortunately, $T_{1\rho}$ measurements at higher spin-lock amplitudes were not possible with our current setup, because of hardware restrictions on

the maximum coil power. In addition, analysis of the level of protein denaturation in the excised treated tumors could have allowed for further validation of the observed changes in T_{1ρ}. Recently, a method for measurement of the concentration of denatured proteins in ex vivo heart and liver samples that were treated with HIFU-induced histotripsy was described (25). However, the goal of the current study was to initially assess the effects of HIFU treatment on tumor T_{1ρ}. Therefore, ex vivo analysis of the excised tumors was for now restricted to conventional H&E and NADH-diaphorase histology.

Large error bars were observed on the average $\Delta T_{1\rho}$ values (Figure 3B), both directly and at 3 days after HIFU treatment, indicative of a large variation in the HIFU-induced T_{1ρ} change in the different tumors. This was probably caused by the fact that the tumors were treated partially. A fixed treatment area of 4x4 mm² was used, which led to a variation in the tumor volume fractions that were ablated. A lower treated tumor fraction leads to presence of a relatively large region of residual, non-treated tumor tissue, causing a smaller change between the tumor T_{1ρ} values before and after treatment. Consequently, the absolute $\Delta T_{1\rho}$ values would likely be even larger if the residual, non-treated tumor tissue after HIFU treatment was excluded from this analysis. However, since significant changes between the $\Delta T_{1\rho}$ values at the different spin-lock amplitudes were already observed with analysis based on all tumor pixels, analysis with exclusion of non-treated tumor pixels after HIFU was not necessary to demonstrate the enhanced contrast between HIFU-treated and non-treated tumor tissue at higher spin-lock amplitudes.

To investigate the effect of tumor progression on the tumor T_{1ρ} values, non-treated control animals were scanned at the same time points as the HIFU-treated animals. The tumor T_{1ρ} values of the control animals did not significantly change in time, which shows that the observed changes in T_{1ρ} in the HIFU-treated animals could be purely attributed to the effects of HIFU treatment on the tumor tissue. In addition, the average T_{1ρ} value in the muscle tissue surrounding the tumor remained constant for all MRI examinations of the control animals, which is indicative of good repeatability of the T_{1ρ} measurements.

The T_{1ρ} data were qualitatively compared to T₂-weighted imaging and contrast-enhanced T₁-weighted imaging. The effects of HIFU treatment were not visible on the T₂-weighted images, which was supported by absence of visible contrast after HIFU on the T₂ maps (T_{1ρ} at B₁=0 Hz). The inadequacy of T₂-weighted imaging for the evaluation of HIFU treatment has been pointed out before in a clinical study of HIFU treatment of prostate tumors (26). The areas of decreased perfusion derived from the contrast-enhanced acquisitions were apparently larger than the areas of decreased T_{1ρ} (Figure 1). A similar finding was reported in the study on APT imaging of HIFU-treated tumor tissue (**chapter 4**), in which we observed that the areas of decreased contrast agent uptake after HIFU treatment were significantly larger than the areas of decreased APT-weighted signal. Since the areas of decreased APT signals visually corresponded with areas of non-viable tissue in histology, contrast-enhanced T₁-weighted imaging was found to overestimate the extent of necrosis. This overestimation is probably caused by HIFU-induced destruction of

tumor-feeding blood vessels (27,28). Vessel destruction leads to diminished perfusion of the tissue that is supplied by the damaged vessel. If this poorly perfused tissue is outside the treatment volume, it will not undergo coagulative necrosis, but may become necrotic in a later stage.

$T_{1\rho}$ measurements have been linked to chemical exchange saturation transfer (CEST) imaging experiments (29,30). Both methods are sensitive to the chemical exchange between protons of different molecules. In **chapter 4**, it was shown that APT imaging, which is a variant form of CEST imaging, provides significant contrast between HIFU-treated and non-treated tumor tissue. APT imaging employs the chemical exchange of protons between amide groups of mobile proteins and water molecules. The on-resonance spin-lock measurements as performed in this study are mainly sensitive to fast exchanging protons for which the exchange rate is much higher than the offset frequency from water, whereas amide protons are in slow exchange with water with an exchange rate of approximately 10-30 Hz (31). The APT and $T_{1\rho}$ measurements are thus sensitive to different proton pools and could therefore provide complementary information on changes in the macromolecular characteristics of the tissue. Nevertheless, the spin-lock measurements can be made sensitive to amide protons by using off-resonance spin-lock pulses. Strong similarities between off-resonance spin-lock measurements and CEST imaging of amide proton-containing phantoms have been observed (29).

Clinical translation of $T_{1\rho}$ imaging for the evaluation of HIFU treatment seems feasible. However, the specific absorption rate (SAR) associated with the relatively long spin-lock pulses limits the maximum spin-lock amplitude. In clinical studies, typically B_1 strengths of 500 Hz are used with spin-lock times up to 60 ms (17,32). In the present study, significant contrast between non-treated and HIFU-treated tumor tissue was already observed at $B_1=100$ Hz, which suggests that evaluation of HIFU treatment with $T_{1\rho}$ would be feasible within the clinical SAR constraints. Nevertheless, the $T_{1\rho}$ contrast after HIFU treatment should be tested in different human tumor types to assess its clinical potential, since the changes in $T_{1\rho}$ after HIFU could be different in other tumors. Furthermore, the dependence of $T_{1\rho}$ on the strength of the B_0 field should be taken into account. $T_{1\rho}$ has shown to decrease with increasing field strength (33). Since clinical MR scanners generally have a lower field strength than the 7T preclinical scanner used here, the contrast in $T_{1\rho}$ between treated and non-treated tumor tissue may be influenced by the difference in B_0 field. In addition, the generally lower signal-to-noise ratio and spatial resolution of clinical MR measurements may affect the sensitivity of $T_{1\rho}$ imaging to HIFU-induced tissue changes.

To fully assess the suitability of $T_{1\rho}$ imaging as a biomarker for the evaluation of HIFU treatment, $T_{1\rho}$ imaging should be compared to other MRI parameters in terms of their sensitivity to HIFU-induced changes in the tumor. We have previously shown that APT imaging (**chapter 4**) and multiparametric MRI analysis (**chapter 3**) are both promising methods for the evaluation of HIFU treatment. While a significant change in the tumor APT-weighted signal was already observed directly after HIFU treatment, the

multiparametric MR analysis method based on combined T₁, T₂ and ADC data had the largest sensitivity for HIFU-induced necrosis at 3 days after HIFU treatment. The larger change in T_{1ρ} compared to T₂ at 3 days after HIFU that was observed in the current study suggests that T_{1ρ} is of substantial additive value to the previously described multiparametric analysis. In addition, the T_{1ρ} measurements could be performed at later time points after treatment to assess the effects of tissue repair (34) on tumor T_{1ρ}. The 3-days time point in the current study was chosen because it has been reported that the necrotic ablation region is largest in size at that time point after treatment (35).

In conclusion, we have shown that T_{1ρ} mapping gives superior contrast between thermally ablated and non-treated tumor tissue as compared to T₂ mapping. Although only partial tumor ablation was performed, global analysis of the average T_{1ρ} values in the whole tumor already showed a significant difference between tumor T_{1ρ} before and at 3 days after HIFU, indicative of substantial T_{1ρ} contrast between HIFU-treated and non-treated tumor tissue. T_{1ρ} imaging may thus be a suitable MR method for the evaluation of HIFU-induced changes in tumor tissue.

Acknowledgements

The authors thank Igor Jacobs for useful discussions. This research was performed within the framework of CTMM, the Center for Translational Molecular Medicine (www.ctmm.nl), project VOLTA (grant 05T-201).

References

1. **Hynnen K.** *Ultrasonics* 2010;50:221-229.
2. **Kennedy JE.** *Nat Rev Cancer* 2005;5:321-327.
3. **Voogt MJ, Trillaud H, Kim YS, et al.** *Eur Radiol* 2012;22:411-417.
4. **Hesley GK, Gorny KR, Woodrum DA.** *Cardiovasc Intervent Radiol* 2013;36:5-13.
5. **Murat FJ, Poissonnier L, Pasticier G, Gelet A.** *Cancer Control* 2007;14:244-249.
6. **Rouviere O, Girouin N, Glas L, Ben Cheikh A, Gelet A, Mege-Lechevallier F, Rabilloud M, Chapelon JY, Lyonnet D.** *Eur Radiol* 2010;20:48-55.
7. **Schmitz AC, Gianfelice D, Daniel BL, Mali WP, van den Bosch MA.** *Eur Radiol* 2008;18:1431-1441.
8. **Grohn OH, Lukkarinen JA, Silvennoinen MJ, Pitkanen A, van Zijl PC, Kauppinen RA.** *Magn Reson Med* 1999;42:268-276.
9. **Regatte RR, Akella SV, Borthakur A, Reddy R.** *J Magn Reson Imaging* 2003;17:114-121.
10. **Ellermann J, Ling W, Nissi MJ, Arendt E, Carlson CS, Garwood M, Michaeli S, Mangia S.** *Magn Reson Imaging* 2013;31:1537-1543.
11. **Markkola AT, Aronen HJ, Lukkarinen S, Ramadan UA, Tanttu JI, Sepponen RE.** *Invest Radiol* 2001;36:531-538.
12. **Santyr GE, Henkelman RM, Bronskill MJ.** *Magn Reson Med* 1989;12:25-37.
13. **Poptani H, Duvvuri U, Miller CG, Mancuso A, Charagundla S, Fraser NW, Glickson JD, Leigh JS, Reddy R.** *Acad Radiol* 2001;8:42-47.
14. **Grohn OHJ, Kettunen MI, Makela HI, Penttonen M, Pitkanen A, Lukkarinen JA, Kauppinen RA.** *J Cereb Blood Flow Metab* 2000;20:1457-1466.
15. **Witschey WR, Zsido GA, Koomalsingh K, Kondo N, Minakawa M, Shuto T, McGarvey JR, Levack MM, Contijoch F, Pilla JJ, Gorman III JH, Gorman RC.** *J Cardiovasc Magn Reson* 2012;14:37.
16. **Witschey WR, Pilla JJ, Ferrari G, Koomalsingh K, Haris M, Hinmon R, Zsido G, Gorman III JH, Gorman RC, Reddy R.** *Magn Reson Med* 2010;64:1453-1460.
17. **Borthakur A, Sochor M, Davatzikos C, Trojanowski JQ, Clark CM.** *Neuroimage* 2008;41:1199-1205.
18. **Duvvuri U, Poptani H, Feldman M, Nadal-Desbarats L, Gee MS, Lee WM, Reddy R, Leigh JS, Glickson JD.** *Cancer Res* 2001;61:7747-7753.

19. **Hakumaki JM, Grohn OH, Tyynela K, Valonen P, Yla-Herttuala S, Kauppinen RA.** *Cancer Gene Ther* 2002;9:338-345.
20. **Sierra A, Michaeli S, Niskanen JP, Valonen PK, Grohn HI, Yla-Herttuala S, Garwood M, Grohn OH.** *Magn Reson Med* 2008;59:1311-1319.
21. **Kettunen MI, Sierra A, Narvainen MJ, Valonen PK, Yla-Herttuala S, Kauppinen RA, Grohn OH.** *Radiology* 2007;243:796-803.
22. **Seip R, Chin CT, Hall CS, Raju BI, Ghanem A, Tiemann K.** *IEEE Trans Biomed Eng* 2010;57:61-70.
23. **Witschey II WR, Borthakur A, Elliott MA, Mellon E, Niyogi S, Wallman DJ, Wang C, Reddy R. J** *Magn Reson* 2007;186:75-85.
24. **Graham SJ, Stanis GJ, Kecojevic A, Bronskill MJ, Henkelman RM.** *Magn Reson Med* 1999;42:1061-1071.
25. **Wang YN, Khokhlova T, Bailey M, Hwang JH, Khokhlova V.** *Ultrasound Med Biol* 2013;39:424-438.
26. **Kirkham AP, Emberton M, Hoh IM, Illing RO, Freeman AA, Allen C.** *Radiology* 2008;246:833-844.
27. **McDannold N, Tempany CM, Fennessy FM, So MJ, Rybicki FJ, Stewart EA, Jolesz FA, Hynynen K.** *Radiology* 2006;240:263-272.
28. **Wu F, Chen WZ, Bai J, Zou JZ, Wang ZL, Zhu H, Wang ZB.** *Ultrasound Med Biol* 2002;28:535-542.
29. **Jin T, Autio J, Obata T, Kim SG.** *Magn Reson Med* 2011;65:1448-1460.
30. **Zaiss M, Bachert P.** *NMR Biomed* 2013;26:507-518.
31. **Zhou J, Payen JF, Wilson DA, Traystman RJ, van Zijl PC.** *Nat Med* 2003;9:1085-1090.
32. **Wang YX, Zhao F, Griffith JF, Mok GS, Leung JC, Ahuja AT, Yuan J.** *Eur Radiol* 2013;23:228-234.
33. **Makela HI, De Vita E, Grohn OH, Kettunen MI, Kavec M, Lythgoe M, Garwood M, Ordidge R, Kauppinen RA.** *Magn Reson Med* 2004;51:4-8.
34. **Cheng HL, Purcell CM, Bilbao JM, Plewes DB.** *J Magn Reson Imaging* 2004;19:329-341.
35. **Wijlemans JW, Deckers R, van den Bosch MA, Seinstra BA, van Stralen M, van Diest PJ, Moonen CT, Bartels LW.** *Invest Radiol* 2013;48:381-386.

Chapter 6

Cluster analysis of DCE-MRI-derived pharmacokinetic parameters to identify regional vascular changes after tumor treatment with High Intensity Focused Ultrasound

Stefanie Hectors*, Igor Jacobs*, Matthias Schabel, Holger Gröll, Gustav Strijkers, Klaas Nicolay

Under review

* authors contributed equally

Abstract

Evaluation of High Intensity Focused Ultrasound (HIFU) treatment with MRI is generally based on the assessment of the non-perfused volume from contrast-enhanced T_1 -weighted images. However, the vascular status of the tissue surrounding the non-perfused volume has not been extensively investigated with MRI. In this study, cluster analysis of the transfer constant K^{trans} and extravascular extracellular volume fraction v_e , that were derived from dynamic contrast-enhanced MRI (DCE-MRI) data, was performed in the tumor tissue surrounding the non-perfused volume to identify subregions of tissue with distinct vascular characteristics.

DCE-MRI was performed in CT26.WT colon carcinoma-bearing Balb/c mice before ($n=12$), directly after ($n=12$) and 3 days after ($n=6$) partial tumor treatment with HIFU. In addition, a non-treated control group ($n=6$) was included. The non-perfused volume was identified based on the level of contrast enhancement. Quantitative comparison between non-perfused tumor fractions and non-viable tumor fractions derived from NADH-diaphorase histology showed that there was a stronger agreement between these fractions at 3 days after treatment (R^2 to line of identity=0.91), compared to directly after treatment ($R^2=0.74$). Next, k-means clustering with 4 clusters was applied on the K^{trans} and v_e parameter values of all significantly enhanced pixels. The fraction of pixels within two clusters, that were characterized by a low K^{trans} and either a low or high v_e , significantly increased after HIFU treatment. Changes in the composition of these clusters were considered to be HIFU-induced. Qualitative H&E histology showed that the HIFU-induced alterations in these clusters may be associated with hemorrhage and structural tissue disruption.

In conclusion, it was demonstrated that, in addition to assessment of the non-perfused tumor volume, the presented methodology gives further insight in HIFU-induced effects on the tissue vascular status. This method may aid in the assessment of the consequences of the observed vascular alterations for the fate of the tissue.

Introduction

High Intensity Focused Ultrasound (HIFU) is an emerging technique for the non-invasive thermal treatment of tumors (1). While routine clinical use of HIFU treatment is mainly restricted to noncancerous growths, such as uterine fibroids (2-4), its application range is now being extended to malignant tumors, such as breast (5,6), prostate (7-10) and liver cancer (11-13). The clinical introduction of HIFU treatment of such malignant lesions has benefited from the development of ultrasound-guided and magnetic resonance imaging-guided HIFU (MR-HIFU) systems, which provide spatial guidance of the treatment (1,14-16). In an MR-HIFU system, the HIFU transducer is integrated in the patient bed of a clinical MR scanner (17). Apart from accurate treatment planning, this system also facilitates treatment monitoring by measuring the temperature rise during HIFU treatment using MR thermometry, providing direct feedback to the ultrasound transducer (18,19).

Dependent on the treatment conditions, hyperthermia may lead to alterations in tumor physiological properties. Whereas mild hyperthermia may (temporarily) enhance microvascular functions, higher temperature elevations or longer treatment times may damage the microvasculature and impair the microcirculation (20). It has been described that hyperthermic ablation induces a lesion that consists of three zones: a central zone, in which temperatures of approximately 60°C result in protein denaturation and coagulative necrosis; a peripheral zone with sublethal temperature elevations between 40-45°C resulting from thermal conduction; and the surrounding tissue that is not affected by the HIFU treatment (21). Appropriate treatment evaluation is required to confirm that tumor is non-viable in the intended treatment zone and to assess potential damage in the surrounding tissue.

Contrast-enhanced T₁-weighted imaging is one of the most commonly used MRI methods for the evaluation of HIFU treatment (8,9,22). A lack of contrast enhancement is generally observed in the central ablation volume, due to vascular destruction. Therefore, the non-perfused volume serves as an important readout parameter (9,22-24). In the transition zone between the central ablation volume and tumor tissue that is not affected by the HIFU treatment, milder temperature elevations may result in indirect heat-induced injury and more subtle vascular alterations. The vascular changes in the peripheral zone around the central ablation volume are strongly dependent on the exact temperature and/or thermal dose that is reached during the HIFU intervention. In addition, these peripheral vascular effects can be transient in nature. Directly after HIFU, hyperthermic conditions in the peripheral zone could (transiently) increase tumor blood flow and microvascular permeability and increase tumor oxygenation (20,25). At a later time point, heat-induced injury could result in apoptosis (21). Destruction (26) or (transient) occlusion (27) of the tumor vasculature could cause ischaemia or ischaemia-reperfusion injury and result in delayed cell death (21,26,28). In addition, the immune response may be enhanced in the transition zone and inflammation-associated hyperemia may be observed (8,21,22). At a later stage (approximately 7 days (29)) after treatment, also fibrosis and revascularization may alter the tumor vascular status (28-30). On contrast-enhanced T₁-weighted images,

often an enhancing rim is reported in the region surrounding the central ablation zone, which may be due to these vascular alterations or result from residual unaffected tumor tissue in case of incomplete ablation (8,22). Since the observed contrast enhancement is almost equal in regions of different vascular changes and in unaffected residual tumor tissue, conventional contrast-enhanced MRI does not have a high specificity for the identification of subtle vascular effects after HIFU treatment.

It is however important to gain further insights in the vascular status of the peripheral tumor zone, since HIFU-induced changes in the microvascular function of the tumor tissue in this region may have substantial consequences for the microenvironment and fate of the tumor. In addition, if residual tumor is present after HIFU treatment, this may be treated with adjuvant tumor therapies. The sensitivity of the tumor to these therapies may also be affected by the vascular status (21). The perfusion status could affect the oxygenation of the tumor and thereby its sensitivity to radiotherapy. In addition, residual tumor tissue could be treated with additional chemotherapy, which requires a proper vascular supply. Also strategies in which HIFU is exploited for hyperthermia-mediated drug delivery require a detailed knowledge of the tumor vascular status (31,32). Therefore, it is of great importance that regional changes in tumor vascular status in the transition zone can be identified.

Compared to conventional contrast-enhanced MRI, assessment of changes in contrast-agent uptake kinetics by dynamic contrast-enhanced MRI (DCE-MRI) may be a more suitable method to gain insight in the altered vascular status in the tissue around the coagulated lesion. It has been previously shown that semi-quantitative DCE-MRI parameters obtained at 3-14 days after HIFU treatment of human breast tumors correlated well with the histology-derived percentage of residual tumor (33). A fully quantitative analysis of the DCE-MRI data may lead to an improved insight in changes in contrast agent uptake-kinetics after HIFU treatment. Pharmacokinetic modeling of DCE-MRI data can be applied to determine biomarkers that are sensitive to vascular changes; e.g. with the widely employed Tofts model the transfer constant K^{trans} and the extravascular extracellular volume fraction v_e can be determined (34). Hijnen et al. have used these kinetic parameters for HIFU therapy assessment in a rat tumor model (35). Cheng et al. have shown that these parameters could give insight in regional changes in the microvasculature after HIFU treatment of rabbit muscle tissue (29,36). Adjacent to the central ablation region without contrast enhancement, a region with low K^{trans} and high v_e was identified, which was associated with restricted flow due to vascular congestion and hemorrhage and an increased capacity for contrast agent accumulation due to structural disruption and vacuolation. In addition, an outer region with higher K^{trans} and v_e was observed, which was characterized by edema and mild inflammation in the first few days after treatment and by revascularization at a later stage. To the best of our knowledge, there are no studies in which the anticipated subtle changes in tumor vascular status around the HIFU ablation volume have been investigated with pharmacokinetic modeling of DCE-MRI data.

In the present study, DCE-MRI was performed before, directly after and at 3 days after HIFU treatment of a murine subcutaneous tumor model. Partial tumor treatment was performed to allow for the presence of both HIFU-treated and residual tumor tissue after the HIFU procedure. Tracer-kinetic modeling was performed on the tumor pixels outside the non-perfused volume to assess HIFU-induced changes in contrast agent uptake-kinetics. Cluster analysis based on K^{trans} and v_e was employed to identify subregions with different uptake kinetics and the regional distribution of these clusters within the tumor was determined. These kinetic parameters derived from DCE-MRI may provide a more refined picture of HIFU-induced regional changes in vascular status compared to conventional contrast-enhanced MRI.

Materials and Methods

Ethics Statement

All animal experiments were performed according to the Directive 2010/63/EU of the European Parliament and approved by the Animal Care and Use Committee of Maastricht University (protocol: 2010-097 and 2010-132).

Murine tumor model

CT26.WT murine colon carcinoma cells (American Type Culture Collection (ATCC; CRL-2638)) were cultured as a monolayer at 37°C and 5% CO₂ in RPMI-1640 medium (Invitrogen, Breda, The Netherlands), supplemented with 10% fetal bovine serum (Greiner Bio-One, Alphen a/d Rijn, The Netherlands) and 50 U/ml penicillin/streptomycin (Lonza Bioscience, Basel, Switzerland). Early passages (5-10) of the original ATCC batch were used for inoculation.

10-12 week-old Balb/c mice (Charles River, Maastricht, The Netherlands) were inoculated with 2×10^6 CT26.WT cells subcutaneously in the right hind limb. Approximately 10 days after inoculation, tumors became palpable in all animals.

Study design

MRI was performed 1 day before (n=12), directly (2-3 h) after (n=12) and 3 days after HIFU treatment (n=6). A control group of non-treated animals (n=6) was included that underwent MRI at the same time points as the HIFU-treated animals. The time points of the control animals are referred to as day -1, day 0 and day 3. Directly after the last MRI experiment, the mice were sacrificed, and the tumors were excised for histological analysis. This study design led to three different groups for quantitative histology: animals sacrificed after the MRI examination directly after HIFU treatment (n=6, referred to as 'Directly after HIFU'), animals sacrificed after the MRI examination at 3 days after HIFU treatment (n=6, referred to as '3 days after HIFU') and non-treated control animals (n=6, referred to as 'Control').

HIFU treatment

HIFU treatment was performed outside the MR scanner with the preclinical Therapy

Imaging Probe System (TIPS, Philips Research, Briarcliff Manor, NY, USA) (37). Treatment was performed under general anesthesia (1-2% isoflurane) and precautionary analgesia (buprenorphine, 0.1 mg/kg s.c., administered at least 30 min before treatment). Control animals received an equal dose of analgesia at the corresponding time point. Partial tumor treatment was performed by definition of a square 4x4 mm² treatment grid within the tumor area, consisting of 25 equally-spaced ablation volumes (1x1x9 mm³) that were placed within the tumor under guidance of an ultrasound imaging system (HDI5000 imaging system combined with a P7-4 phased array transducer, Philips Ultrasound, Bothell, WA, USA). This resulted in the presence of both HIFU-treated and non-treated tumor tissue after the HIFU procedure. Treatment settings were: frequency 1.4 MHz, pulse repetition frequency 20 Hz, acoustic power 12 W, duty cycle 50%, treatment time 30 s. A wait time of 120 s was applied between sonication of consecutive treatment points to allow for sufficient cooling of the treated tissue. A temperature increase to 66°C during HIFU treatment was confirmed by insertion of a thermocouple into the tumor in 3 pilot experiments, as described previously (**chapter 3**).

MRI measurements

MRI measurements were performed with a 6.3 T horizontal-bore scanner (Bruker BioSpin, Ettlingen, Germany) using a 3.2-cm-diameter quadrature birdcage RF coil (Rapid Biomedical, Rimpfing, Germany) under general anesthesia (1-2% isoflurane). The mice were positioned in a custom-made cradle, equipped with a mask for anesthetic gas. Respiration was monitored with a balloon sensor. Body temperature was monitored and maintained with a warm water pad. For reduction of susceptibility artifacts in echo planar imaging (EPI), the tumor-bearing paw was covered with degassed ultrasound gel (Aquasonic® 100, Parker Laboratories). Artifacts were further reduced by local shimming.

A fat-suppressed T₂-weighted spin-echo sequence (TE=30 ms, TR=1000 ms, number of averages NA=1) was used for anatomical reference.

Pre-contrast T₁ mapping was performed using an inversion recovery Look-Locker EPI sequence (TE=8 ms, TR=10000 ms, inversion time=30 ms, flip angle=20°, pulse separation=400 ms, number of points=15, NA=2).

DCE-MRI measurements were performed using a gradient-spoiled dual gradient echo EPI sequence (TR=1250 ms, TE₁/TE₂=7.5/26.1 ms, NA=2, number of segments=2, flip angle=80°, temporal resolution=5 s, number of repetitions=100). At 1.5 min after start of the acquisition, a bolus of 0.3 mmol/kg Gd-DOTA (Dotarem; Guerbet, Villepinte, France) with a saline flush was injected in 5 s via the tail vein using an infusion pump (Chemyx Fusion 100, Stafford, TX, USA).

All images were acquired with a matrix size of 128x128, FOV of 4x4 cm² and 1 mm slice thickness. 12-16 slices were acquired covering the whole tumor volume.

DCE-MRI data processing

Image analysis was performed in Mathematica 8.0 (Wolfram Research, Champaign, IL, USA) and MATLAB R2013a (The MathWorks, Natick, MA, USA). Regions of interest (ROIs) were defined on the T_2 -weighted images by manually drawing contours around the tumor tissue on each slice. From these ROIs the tumor volumes at the different experimental time points were determined. Pre-contrast T_1 maps were generated as described previously (38).

A T_2^* correction was performed on the dynamic signal intensities to account for the T_2^* changes caused by contrast agent influx (39,40). The dynamic T_2^* values in the tumor pixels were determined based on the ratio of the signal intensities at the two echo times. Dynamic T_1 values were calculated from the signal equation for a spoiled gradient-echo sequence using the T_2^* -corrected dynamic signal intensities and the pre-contrast T_1 values. A B_1 correction was applied to the flip angle used in the dynamic acquisition, using a B_1 map acquired with the same RF coil in a 2% agarose/0.05 mM CuSO_4 phantom. Dynamic T_1 values were converted to dynamic contrast agent concentrations ([CA]) using the Dotarem plasma relaxivity at 7 T at 37°C ($3.53 \text{ mM}^{-1}\text{s}^{-1}$ (41)).

Pharmacokinetic analysis of DCE-MRI data

Pharmacokinetic analysis of the DCE-MRI data was performed with a custom-written MATLAB tool. For determination of K^{trans} and v_e in each tumor pixel, the standard Tofts model (34,42) was used, in which the dynamic contrast agent concentration in the tumor tissue is defined as:

$$C_t(t) = K^{\text{trans}} \int_0^t C_p(\tau) e^{-k_{\text{ep}}(t-\tau)} d\tau$$

in which C_t and C_p are the contrast agent concentrations in the tumor tissue and the blood plasma, respectively and k_{ep} is the rate constant ($k_{\text{ep}} = K^{\text{trans}}/v_e$). A delay term (t_d) was included in the model to allow for a delay between bolus arrival in the blood and the tissue response. A literature-based bi-exponential arterial input function (AIF), measured in the mouse iliac artery upon injection of a similar dose of Dotarem (43), was used and modified to match with our data. The bi-exponential AIF is described by:

$$C_p(t) = \begin{cases} 0 & t < t_i \\ a_1 e^{-m_1 t} + a_2 e^{-m_2 t} & t \geq t_i \end{cases}$$

in which t_i is the injection time.

The peak amplitude of the AIF was adapted based on the injected dose and the mouse plasma volume. In addition, the second exponent of the AIF, describing the AIF tail, was adapted based on blood kinetics data of Dotarem from five separate CT26.WT tumor-bearing Balb/c mice. For this purpose, the gadolinium concentration of blood plasma samples acquired at different time points after CA injection was determined by means of Inductively Coupled Plasma-Atomic Emission Spectrometry or Inductively Coupled

Plasma-Mass Spectrometry. These adaptations resulted in the following bi-exponential AIF parameters: $a_1=5.36$ (mM), $m_1=11.20$ (min^{-1}), $a_2=1.27$ (mM), $m_2=0.0655$ (min^{-1}).

The standard Tofts model was fitted to the dynamic [CA] curves using the MATLAB function `lsqcurvefit`, with constraints $K^{\text{trans}} \geq 0 \text{ min}^{-1}$, $k_{\text{ep}} \geq 0 \text{ min}^{-1}$ and $0 \leq t_d \leq 7$ repetitions.

Identification of non-perfused tumor volume

Non-perfused pixels were selected based on the level of contrast enhancement. Pixels were considered non-perfused if the median [CA] after injection was lower than 5 times the standard deviation (SD) of the data points in the dynamic [CA] curve before injection. Non-perfused volumes were calculated from the total number of non-perfused pixels in each tumor multiplied by the pixel volume. Non-perfused fractions were derived from the ratio between the non-perfused volume and the total tumor volume. The non-perfused pixels were not included in the subsequent histogram and cluster analyses.

Selection of pixels for cluster analysis

A number of criteria were defined to select the perfused tumor pixels that were included in the cluster analysis. Pixels in which the dynamic T_1 became lower than 250 ms or the dynamic T_2^* became lower than the first echo time (7.5 ms) were excluded for further analysis, since such low T_1 and T_2^* values could not be accurately determined with the present DCE-MRI acquisition settings. A second criterion included a constraint on the goodness-of-fit R^2 of the curves fitted to the data. Curves with an R^2 value lower than 0.8 were excluded from analysis. In addition, pixels with non-physiological v_e values higher than 1 were omitted.

To get insight in the K^{trans} and v_e distribution in the perfused tumor tissue of the HIFU-treated and control animals at the different experimental time points, histograms of K^{trans} (20 bins, bin width 0.025 min^{-1} , range 0-0.5 min^{-1}) and v_e (20 bins, bin width 0.025, range 0-0.5) in the selected perfused tumor pixels were made.

Cluster analysis

k-means clustering with 3, 4, 5 and 6 clusters was performed on the combined K^{trans} and v_e data of the selected perfused pixels of all (HIFU-treated and non-treated) animals at all time points simultaneously with a custom-written Mathematica function. Prior to clustering, data were normalized (mean=0, SD=1) to remove scaling differences between K^{trans} and v_e . Changes in the fraction of pixels in the different clusters were defined as treatment-associated if the fraction of pixels assigned to the particular cluster increased significantly (one-sided paired t-test, $P < 0.05$) after HIFU treatment (either directly or at 3 days after HIFU) compared to before HIFU treatment.

Regional distribution of clusters

To assess the spatial distribution of the different clusters with respect to the non-perfused volume, the distance of each pixel in each cluster to the closest non-perfused pixel was determined. Histograms (6 bins, bin width 1 pixel, range 1-7 pixels) of these minimal

distances to the non-perfused volume were made for each cluster at each time point after HIFU treatment to visualize the regional distribution of the different clusters with respect to the non-perfused volume. In addition, the median minimal distance of each cluster to the non-perfused volume was calculated for each HIFU-treated mouse at both time points after HIFU treatment.

Histological analysis

Dissected tumors were snap-frozen in isopentane and stored at -80°C . Tumors were cut into $5\ \mu\text{m}$ thick sections with a distance of approximately $300\ \mu\text{m}$ between the sections. The cryo-sections were briefly air-dried and subsequently stained for nicotinamide adenine dinucleotide (NADH) diaphorase activity to assess cell viability. Sections were incubated at 37°C for 1 h in Gomori-Tris-HCl buffer (pH 7.4) containing β -NAD reduced disodium salt hydrate (Sigma-Aldrich, St. Louis, MO, USA, 0.71 mg/ml buffer solution) and nitro blue tetrazolium (Sigma-Aldrich, 0.29 mg/ml buffer solution). Brightfield microscopy was performed on all sections and consisted of mosaic acquisition of the entire section at 5x magnification. Analysis of the microscopy images was performed in Mathematica 7.0. ROIs were manually drawn around the pale non-viable tumor tissue and the entire tumor tissue on all sections of each tumor. From the ratio between the ROI areas of non-viable tumor tissue and entire tumor tissue on all tumor sections, a histology-derived non-viable tumor volume fraction was determined for each tumor. Subsequently the MRI-derived non-perfused tumor fractions were compared to the histology-derived non-viable tumor fractions.

Apart from the NADH-diaphorase staining, haematoxylin and eosin (H&E) staining was performed on paraffin sections of a separate CT26.WT tumor that was treated with the same HIFU settings. This tumor was excised at ~ 2.5 h after HIFU treatment. Brightfield microscopy was performed to inspect morphological changes in the tumor tissue after treatment.

Statistical analysis

Data are presented as mean \pm SD. At all experimental time points, the relative tumor sizes of the HIFU-treated and non-treated tumors were statistically compared with a two-sided t-test assuming equal variances. The non-perfused tumor volumes at the different experimental time points were compared for statistical significance with a two-sided paired t-test. Correlation analysis between the MRI-derived non-perfused tumor fractions and histology-derived non-viable tumor fractions was performed for all groups by calculation of the Pearson correlation coefficient. In addition, the one-to-one correspondence between the non-viable and non-perfused tumor fractions was determined by calculation of the R^2 of the data points to the line of identity. The difference between non-viable tumor fractions of the HIFU-treated and non-treated control tumors at the last experimental time point was tested for significance with a two-sided t-test assuming equal variances. Changes in the K^{trans} and v_e histograms between the two time points after HIFU and before HIFU were tested for significance with a two-sided paired t-test. A one-sided paired t-test was

performed for each cluster to assess if the fraction of pixels in that cluster was increased after HIFU. The median minimal distances to the non-perfused volume of the different clusters were statistically compared with a two-sided paired t-test. For all tests, the level of significance was set to $\alpha=0.05$.

Results

The partial tumor ablation with HIFU resulted in a significantly lower relative tumor size at day 3 compared to the control mice (Figure 1).

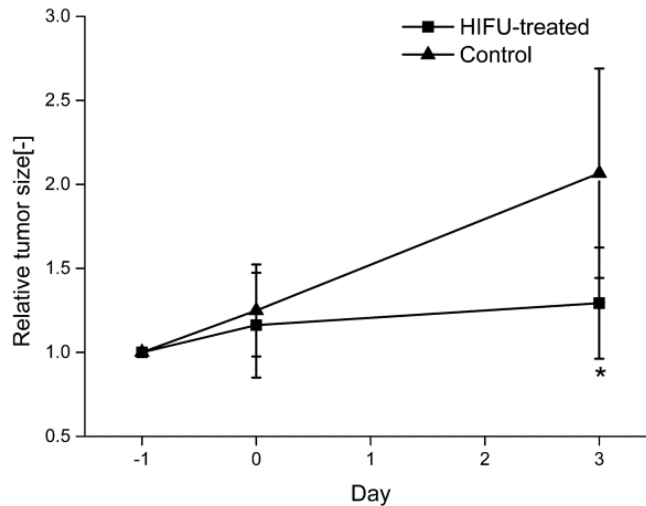


Figure 1. Tumor growth. Mean±SD relative tumor size, based on ROIs drawn on the anatomical MRI images, at the different experimental time points for the HIFU-treated and the control animals. For the HIFU-treated animals day 0 corresponds to the day of treatment. * indicates a significant difference in relative tumor size between the HIFU-treated and control animals at measurement day 3 (two-sided t-test, $P<0.05$).

Representative pharmacokinetic parameter maps in the tumor tissue before and at both time points after HIFU treatment are shown in Figure 2A (for the same animal). Before HIFU treatment, the tumor vasculature was characterized by higher K^{trans} values in the tumor rim than in the tumor center. Furthermore, a small region of low K^{trans} was observed in the tumor core. The v_e values were also generally higher in the tumor rim than in the center. Directly after partial HIFU treatment of the tumors, a large area of decreased K^{trans} emerged. Such area of decreased K^{trans} was also present at 3 days after HIFU treatment. At both time points after HIFU treatment, the area of decreased K^{trans} corresponded to regions with low v_e with small subregions of high v_e . No substantial differences in K^{trans} and v_e were detected for the non-treated control animals between measurement day -1 and day 0, although a reduction in K^{trans} was observed at day 3 (Figure 2B).

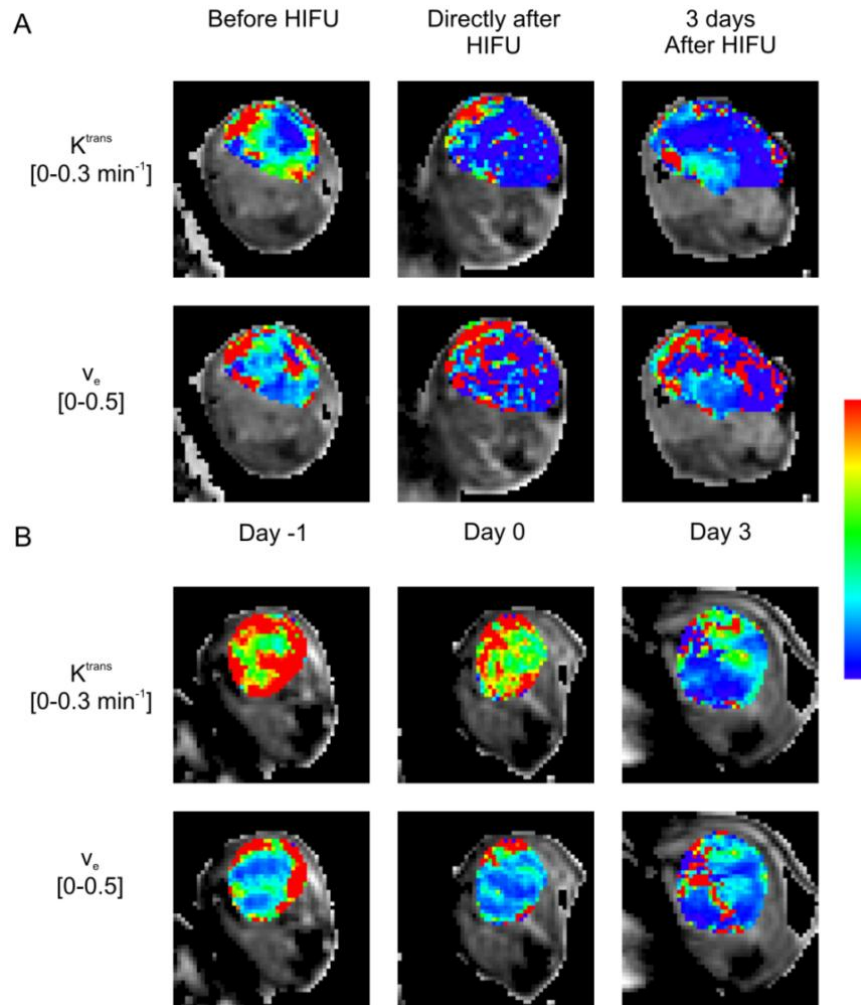


Figure 2. Pharmacokinetic parameter maps. A) Representative pharmacokinetic parameter maps overlaid on the tumor pixels of an axial T_2 -weighted image of a tumor-bearing paw before, directly after and at 3 days after HIFU treatment. B) Representative pharmacokinetic parameters maps for a control animal at the corresponding experimental time points. The parameters were scaled according to the color bar shown at the right side of the figure. The corresponding parameter range for this scale bar is indicated at the left side of the parameter maps.

To assess the effect of the partial ablation on tumor perfusion, non-perfused tumor volumes were determined first, based on the level of contrast enhancement in the tumor pixels. The average non-perfused tumor volumes of the HIFU-treated and control animals at the different experimental time points are displayed in Figure 3A and B, respectively. Directly after HIFU treatment, the non-perfused tumor volume significantly increased compared to before HIFU treatment. No significant difference between the non-perfused tumor volume 3 days after HIFU compared to either before or directly after HIFU was observed. For the control animals, the non-perfused tumor volume remained constant between measurement day -1 and 0, whereas the non-perfused tumor volume was significantly increased at day 3.

The average histology-derived non-viable tumor fraction at the last experimental time point was higher for the HIFU-treated animals than for the control animals, although this difference was not significant (Figure 3C). Correlation plots between the MRI-derived non-perfused tumor volume fractions and histology-derived non-viable tumor volume fractions are displayed in Figure 3D for the different experimental groups. For the HIFU-treated animals sacrificed directly after HIFU, a high, significant correlation ($r=0.866$) was observed between the MRI-derived non-perfused and histology-derived non-viable tumor fractions. However, the non-perfused tumor fractions were generally higher than the non-viable tumor fractions at that time point after HIFU treatment, resulting in a relatively low one-to-one correspondence (R^2 to line of identity = 0.74). At 3 days after HIFU treatment, also a high correlation ($r=0.933$) was observed between the non-perfused and non-viable tumor fractions. At this time point after HIFU treatment, a good one-to-one correspondence between the non-perfused and non-viable tumor fractions was observed ($R^2=0.91$). For the control animals, both the correlation ($r=0.242$) and one-to-one correspondence ($R^2=0.57$) between the non-perfused and non-viable tumor volume fractions were low.

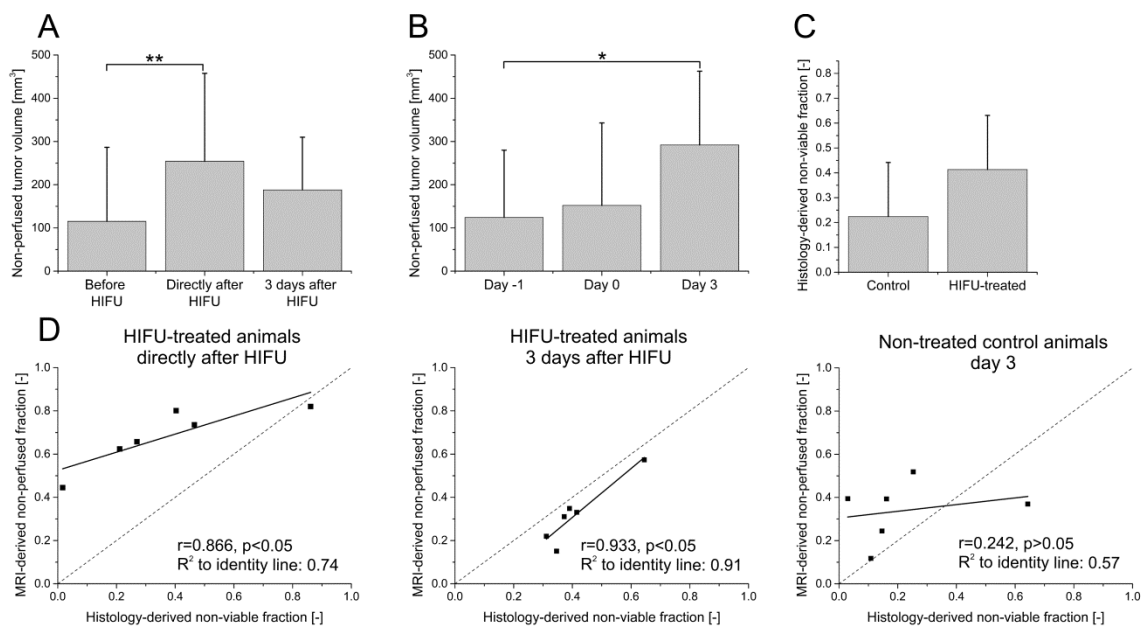


Figure 3. Non-perfused tumor volumes. A) Mean±SD non-perfused tumor volumes before, directly after and at 3 days after HIFU treatment. ** indicates a significant increase in the non-perfused tumor volume directly after HIFU compared to before HIFU (two-sided paired t-test, $P<0.001$). B) Mean±SD non-perfused tumor volumes at measurement day -1, 0 and 3 for the control animals. * indicates a significant increase in the non-perfused tumor volumes between measurement day 0 and 3 (two-sided paired t-test, $P<0.05$). C) Mean±SD histology-derived non-viable tumor fractions of the control and HIFU-treated animals at measurement day 3. D) Correlation plots of MRI-derived non-perfused tumor fractions vs. histology-derived non-viable tumor fractions for the three different experimental groups. The line of identity is shown as a visual reference. The correlation coefficient and the R^2 to the line of identity are displayed in the right bottom corner of each figure.

In addition to the above measurements of non-perfused tumor fractions and volumes, a detailed analysis of the pharmacokinetic parameters in the perfused tumor surrounding the non-perfused ablation volume was performed. The average distributions of K^{trans} and

v_e in the perfused pixels in the HIFU-treated tumors at all time points are shown in Figure 4A and B, respectively. Directly after HIFU treatment, the fraction of pixels with a K^{trans} value between 0 and 0.025 min^{-1} was significantly increased compared to before HIFU. In addition, the fraction of pixels in a number of bins with a higher K^{trans} ($>0.1 \text{ min}^{-1}$) was significantly decreased directly after HIFU. At this time point, the fraction of pixels with a v_e value between 0.05 and 0.15 was significantly lower than before HIFU, whereas a significant increase in the fraction of pixels with both a lower v_e value (0-0.025) and a higher v_e value (>0.25) was observed. At 3 days after HIFU treatment, the fraction of pixels in most bins was not significantly different from that before treatment. The average K^{trans} and v_e distributions in the perfused pixels of the non-treated control animals at the different time points are displayed in Figure 4C and D, respectively. No significant changes in the K^{trans} and v_e of the perfused pixels were observed between the different time points, except for one bin in the v_e histogram in which the fraction of pixels was significantly increased at day 3 compared to day -1.

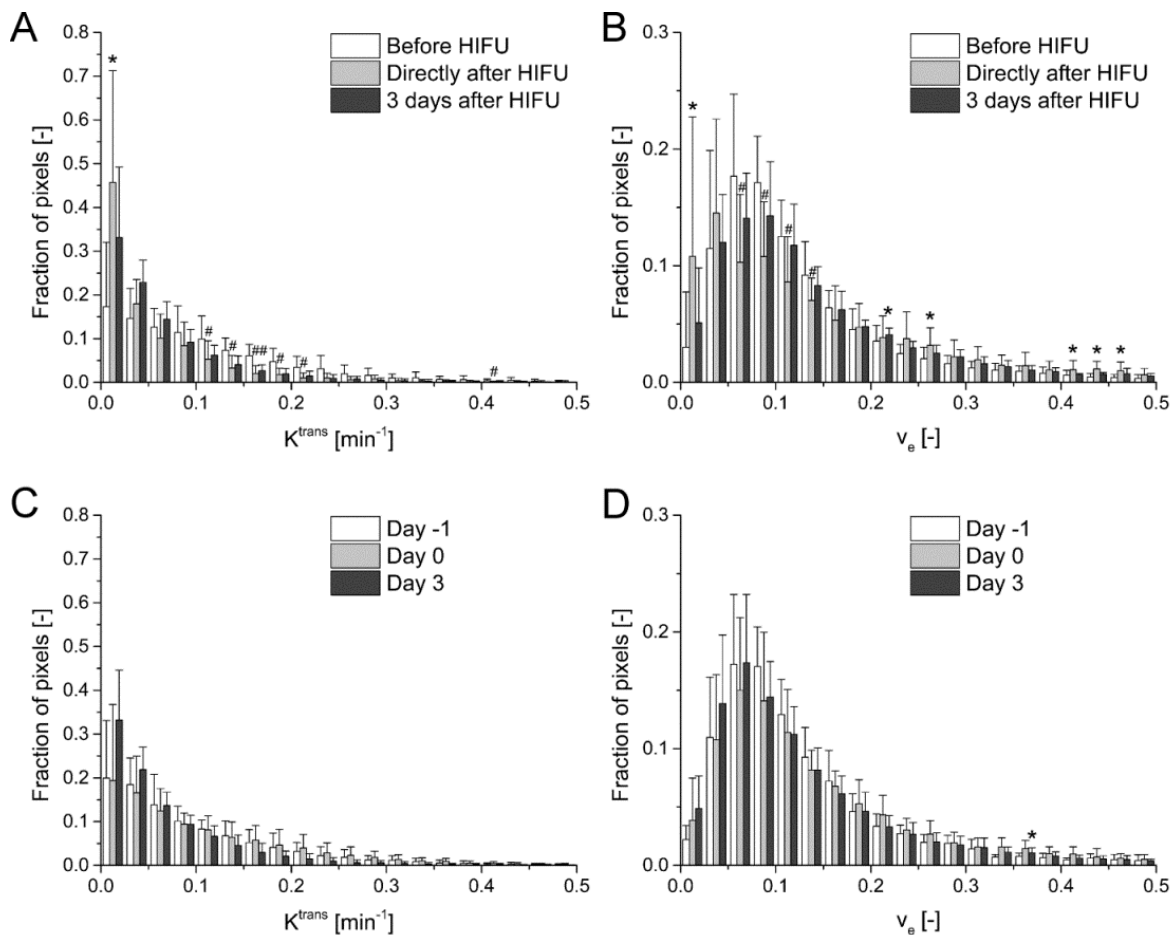


Figure 4. Pharmacokinetic parameter histograms. A and B) Average K^{trans} and v_e histograms in the HIFU-treated tumors at the different experimental time points, respectively. The error bars represent the SD. * and # indicate a significant increase and decrease in the fraction of pixels after HIFU compared to before HIFU, respectively (two-sided paired t-test, $P < 0.05$). C and D) Average K^{trans} and v_e histograms in the non-treated control animals at the different experimental time points, respectively. The error bars represent the SD. * indicates a significant increase in the fraction of pixels at day 3 compared to day -1 (two-sided paired t-test, $P < 0.05$).

Cluster analysis was performed on the perfused pixels of all tumors and all time points to identify subregions with different contrast agent uptake kinetics. Four clusters appeared to be the optimal number of clusters with which the most prominent vascular changes could be identified. In Figure 5 the results of the cluster analysis with four clusters are overlaid on the tumor pixels of the same slice from the same animal as shown in Figure 2. The white region represents the non-perfused tumor pixels. The different colors represent the four clusters that were identified. The median dynamic [CA] curves of all pixels assigned to the different clusters are shown in the bottom of Figure 5. After HIFU treatment, the number of pixels assigned to the blue and green clusters strongly decreased. The DCE-MRI curves in these clusters were characterized by a rapid upslope, a clear wash-out and substantial contrast agent influx. At both time points after HIFU, a large region of non-perfused tissue emerged. Curves in the non-perfused tumor area, shown at the right of the figure, were characterized by a lack of contrast agent inflow. The area around the non-perfused volume consisted mostly of pixels assigned to the red and yellow clusters. Contrast agent uptake in pixels assigned to the red cluster was small and relatively slow. The curves in the yellow cluster typically indicated slow uptake kinetics, but pronounced contrast agent influx. The area of non-perfused pixels visually corresponded well to the area of non-viable tissue on the NADH-diaphorase stained section obtained at 3 days after HIFU treatment at approximately the same location in the tumor, in agreement with the data presented in figure 3D.

In Figure 6 the average fraction of pixels assigned to the four clusters is shown for the HIFU-treated animals at the different time points. Directly after HIFU treatment, the fraction of pixels in the yellow and red cluster was significantly increased compared to before HIFU. At 3 days after HIFU treatment, the fraction of pixels in these clusters was not significantly higher than before HIFU. Because of the HIFU-induced increase in the fraction of pixels in the yellow and red clusters, changes in these clusters were considered as treatment-associated.

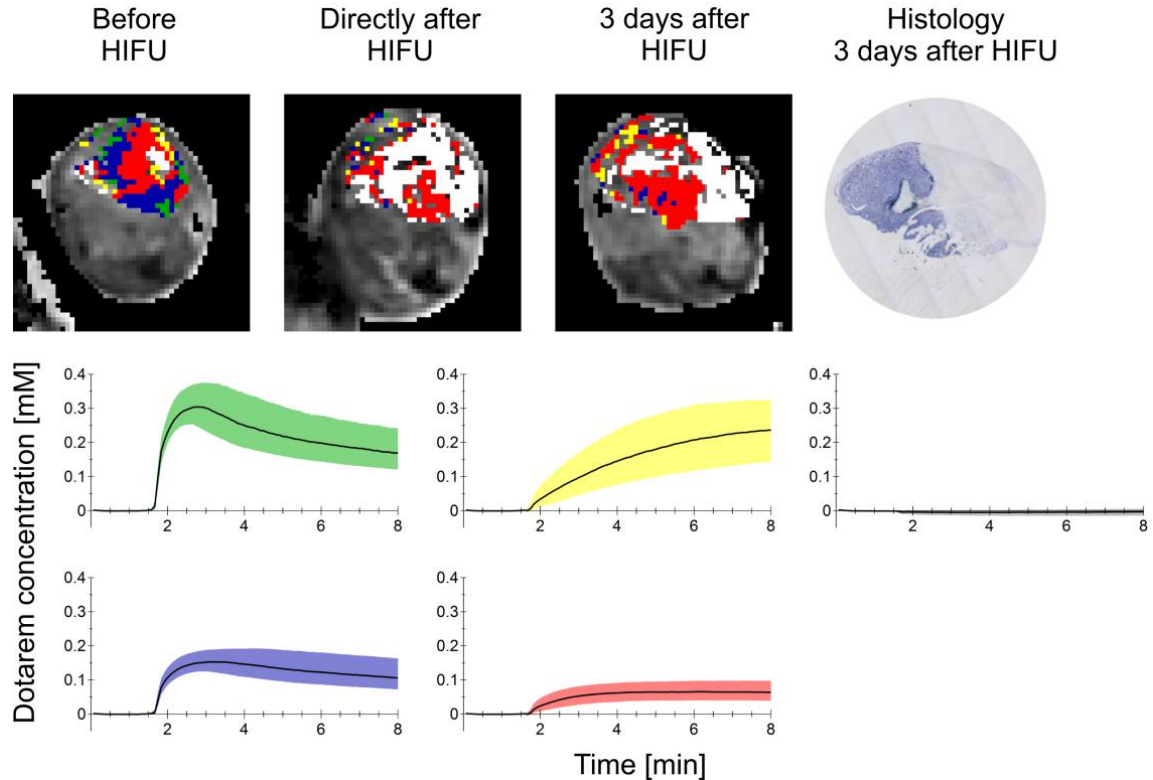


Figure 5. Clustering of pharmacokinetic parameter values. Representative clustering results overlaid on the tumor pixels of the T_2 -weighted image of the tumor-bearing paw of the same animal as shown in figure 1 before, directly after and at 3 days after HIFU treatment. The four clusters are represented by the different colors (yellow, green, red and blue). The non-perfused pixels, that were excluded from cluster analysis, are represented by the white color. An NADH-diaphorase stained tumor section obtained at approximately the same location as the MRI slice at 3 days after HIFU treatment is shown at the top right corner of the figure. A clear pale, non-viable tumor region was observed next to NADH-diaphorase positive, viable tumor tissue. The median dynamic [CA] curves of all pixels in each of the 4 clusters (shown by the different colors) and the non-perfused pixels are shown in the figure bottom (from top to bottom, left to right: green cluster, yellow cluster, non-perfused pixels, blue cluster and red cluster). The bands around the curves represent the range between the 25th and 75th percentiles.

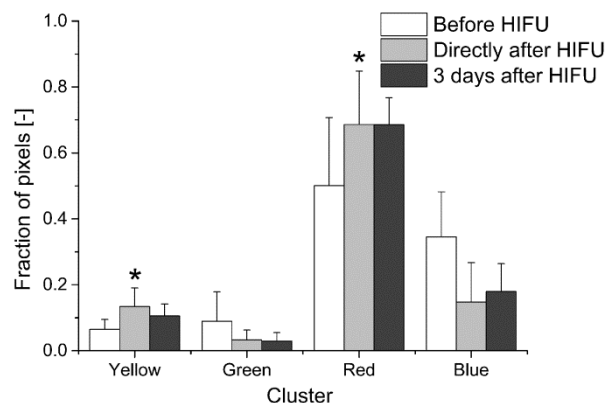


Figure 6. Cluster composition at the different experimental time points. Mean \pm SD fraction of pixels assigned to the four different clusters before, directly after and at 3 days after HIFU treatment. * indicates a significant increase in the fraction of pixels directly after HIFU compared to before HIFU ($P < 0.05$, one-sided paired t-test).

In Table 1 the K^{trans} and v_e parameter values in the different clusters are displayed. In the clusters with a treatment-associated increase in fraction of pixels (yellow and red clusters), K^{trans} was lower than in the other (green and blue) clusters. The v_e in these clusters was either higher (yellow cluster) or lower (red cluster) than in the other clusters.

Table 1. K^{trans} and v_e values (mean \pm SD) in the four clusters.

Cluster	K^{trans} [min^{-1}]	v_e [-]
Yellow	0.066 \pm 0.054	0.495 \pm 0.170
Green	0.356 \pm 0.107	0.223 \pm 0.098
Red	0.039 \pm 0.026	0.095 \pm 0.061
Blue	0.150 \pm 0.044	0.138 \pm 0.067

To gain insight in the regional distribution of the different clusters with respect to the non-perfused volume, the minimal distance of each perfused pixel in each cluster to the closest non-perfused pixel was determined. The histograms in Figure 7 show the distribution of these minimal distances for all clusters at the two time points after HIFU treatment and provide information on the proximity of the different clusters to the non-perfused volume. Both directly and at 3 days after HIFU treatment, the red cluster was most closely located to the non-perfused volume. The yellow cluster was more closely located to the non-perfused volume than the green and blue clusters, but further away from the non-perfused volume than the red cluster. The median minimal distances between the four clusters and the non-perfused volume, averaged for all HIFU-treated animals, are given in Table 2 for both time points after treatment. Directly after HIFU, the average distance to the non-perfused volume was significantly smaller for the red cluster compared to all other clusters. Furthermore, a significantly smaller distance to the non-perfused volume was observed for the yellow cluster compared to the blue cluster. At 3 days after HIFU treatment, the red cluster was still significantly closer to the non-perfused volume than the blue cluster.

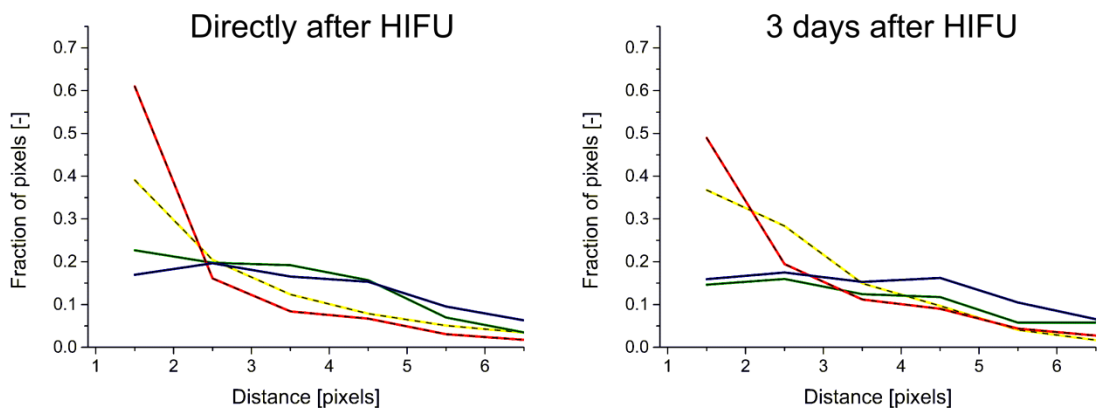


Figure 7. Spatial distribution of clusters with respect to non-perfused volume. Distribution of the minimal distance of the pixels in each of the four different clusters to the closest non-perfused pixel directly after and at 3 days after HIFU treatment. The yellow, green, red and blue lines represent the different clusters. The dashed lines represent the clusters with a treatment-associated increase in the fraction of pixels (yellow and red clusters) and the solid lines represent the other (blue and green) clusters.

Table 2. Distance of clusters to the non-perfused volume. Median minimal distance from the different clusters to the non-perfused volume averaged for all HIFU-treated animals, at both time points after HIFU treatment. Data are presented as mean±SD. # and ## indicate a significantly smaller distance of a cluster to the non-perfused volume compared to the cluster(s) indicated between the parentheses, with $P < 0.05$ and $P < 0.001$, respectively.

Cluster	Distance directly after HIFU [pixels]	Distance 3 days after HIFU [pixels]
Yellow	2.31±0.67 # (blue)	2.51±0.34
Green	2.79±1.67	3.67±1.78
Red	1.52±0.51 #(green, blue) ##(yellow)	2.15±0.68 # (blue)
Blue	3.13±1.50	3.41±1.25

Representative microscopy images of H&E-stained sections of a tumor excised at ~2.5 h after HIFU treatment are shown in Figure 8. A region of viable tumor tissue was observed, which was structurally intact (Figure 8A). The cells in the viable tumor tissue were densely packed and cell nuclei had a normal appearance. In addition, a zone of coagulated tissue was observed, surrounded by a region characterized by structural disruption (Figure 8B). The nuclei of the cells in the coagulated zone were typically dark and shrunken. Gaps between the tumor cells were visible in the structurally disrupted tumor tissue (Figure 8B and C). Disrupted tumor blood vessels and presence of red blood cells in the extravascular space were observed, indicative of hemorrhages (Figure 8B and D). These hemorrhages were mainly located close to the coagulated areas.

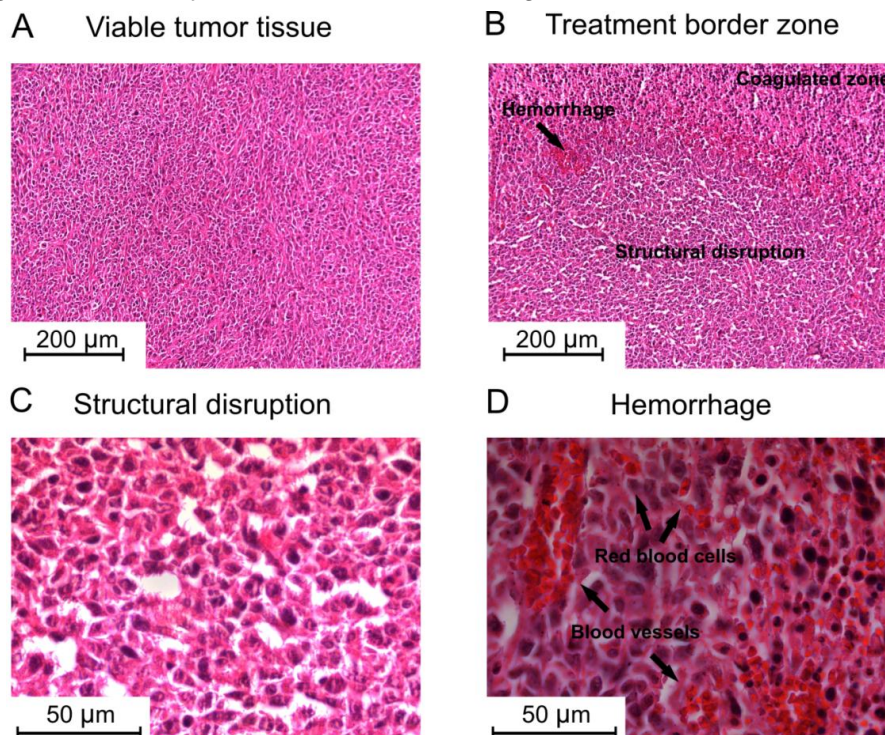


Figure 8. H&E microscopy. Representative brightfield microscopy images of H&E-stained sections of a HIFU-treated CT26.WT tumor excised at ~2.5 h after treatment. A) Viable tumor tissue at 20x magnification. B) Border zone of coagulated tumor tissue surrounded by structurally disrupted tumor tissue at 20x magnification. C) Structurally disrupted tumor tissue at 100x magnification. D) Region with hemorrhage at 100x magnification.

Discussion and Conclusions

In this study, pharmacokinetic analysis of DCE-MRI data was performed to identify tumor regions with different contrast agent uptake kinetics longitudinally after HIFU treatment. In addition to the commonly performed assessment of non-perfused volumes, cluster analysis of pharmacokinetic parameters was performed to gain insight in more subtle underlying changes in vascular status in the area surrounding the non-perfused central ablation volume.

A significant increase in the non-perfused tumor volume was observed directly after HIFU treatment (Figure 3A). At this time point, the non-perfused tumor fractions were generally higher than the histology derived non-viable tumor fractions (Figure 3D). This finding is possibly caused by HIFU-induced destruction of tumor vasculature in the zone surrounding the ablated region, which could lead to delayed cell death (20,21,26,28). This delayed cell death may explain the better agreement between the non-viable and non-perfused tumor fractions at 3 days after treatment. Temporary HIFU-induced vascular constriction (27) could also have contributed to the higher non-perfused fraction directly after treatment, although this contribution is probably minor since the non-perfused tumor volume at 3 days after HIFU was not significantly lower than directly after HIFU (Figure 3A). The correlation between non-viable and non-perfused tumor fractions for the non-treated control animals was low, in contrast to the treated animals (Figure 3D). For the control animals, the non-perfused tumor fraction was generally higher than the non-viable tumor fraction. Likely, part of the non-perfused pixels represented hypoxic, yet viable, tumor tissue, which is also known to be poorly perfused (44,45). This hypoxic tissue may become necrotic at a later stage of tumor progression. Therefore, non-perfused pixels do not necessarily represent necrosis leading to a disagreement between the non-viable and non-perfused tumor fractions. This complicates the classification of tumor as non-viable solely based on the lack of contrast enhancement after HIFU in a setting in which tumors were already relatively non-perfused before treatment.

Nevertheless, pharmacokinetic analysis can still give additional insights in uptake-kinetics and thereby provide information on changes in the underlying vascular status in the zone peripheral to the central ablation volume. Histogram and cluster analysis of the pharmacokinetic parameters in the perfused pixels showed that there were subtle yet significant HIFU-induced changes in the pharmacokinetic parameter values in the areas surrounding the non-perfused volume. Since in two clusters the fraction of pixels significantly increased after HIFU treatment (Figure 6), these alterations were assumed to be treatment-associated. One of these clusters was characterized by a low K^{trans} and high v_e (yellow cluster) and the second by a low K^{trans} and low v_e (red cluster) combination (Table 1). The uptake kinetics (Figure 5) characterizing the region with low K^{trans} and high v_e could be explained by a more difficult contrast agent access due to HIFU-induced vascular congestion and hemorrhage, but a higher capacity for accumulation due to the presence of vacuolation and structural disruption in the extravascular tissue space. The

low K^{trans} and low v_e in the other cluster with a treatment-associated increase in fraction of pixels (red cluster) was likely caused by more severe vascular damage, which may include vascular disruption, congestion and hemorrhage. Regions with these types of vascular characteristics around the central region of coagulative necrosis were previously also identified with DCE-MRI analysis and confirmed by extensive histological evaluation in a study on HIFU treatment of rabbit thigh muscle (36).

The pixels in the clusters with treatment-associated changes (yellow and red clusters) were located more closely to the non-perfused pixels than pixels in the other clusters (Figure 7). In addition, H&E staining confirmed the presence of tumor regions with structural disruption and hemorrhage after HIFU (Figure 8). However, although the observed changes in the fractions of pixels in the different clusters were induced by HIFU treatment and histological evidence was presented for these changes, the kinetic uptake characteristics of the red and yellow clusters cannot be regarded as specific for HIFU-treated tumor based on the presented results. The relatively high fraction of pixels in the red cluster before treatment (Figure 6), indicates that pixels with these characteristics can be naturally present in this tumor model. This could be explained by the fact that for this tumor model perfusion was relatively low in the tumor center. Therefore, most likely hypoxic regions with an impaired perfusion are naturally present. More pronounced HIFU-induced changes in contrast agent uptake-kinetics and clusters that are more specific for HIFU-induced vascular alterations may be detected if the cluster analysis would be applied in better perfused tumor models.

Extensive histological analysis, in which the clusters with specific vascular characteristics are spatially compared to histological features, could give further insights in the underlying effects causing the observed vascular changes. In the present study however, histological evaluation was mainly focused on the definition of the non-viable tumor volume fraction in order to compare these with non-perfused tumor fractions. Furthermore, HIFU treatment was performed outside the MR system, since the preclinical therapeutic ultrasound transducer is not MR-compatible. In a HIFU set-up with MRI guidance, temperature maps could be acquired during the treatment allowing changes in the pharmacokinetic parameters to be compared with the applied thermal dose (36). This information would also allow for a better definition of the danger zones around the central ablation volumes and a more detailed comparison between applied thermal dose, temperature-dependent changes in uptake kinetics and histological appearance of these regions.

The HIFU treatment generally led to a decreased blood flow in the region around the coagulated zone. No evidence for an increased blood flow or enhanced microvascular permeability due to mild hyperthermia was observed. Hyperthermia of 43.5°C has shown to induce a gradual perfusion increase during the first 30 min after treatment, followed by a substantial decrease in perfusion up to 24 h after treatment (46). In our case, the heating times were most likely too short to induce any considerable perfusion increase. In case one would want to exploit the increased perfusion or vascular permeability, for

example if adjuvant chemotherapy is applied after the HIFU intervention, it is important to verify that the hyperthermic conditions have indeed led to these vascular conditions. The cluster analysis performed in the present study provides a way to identify the existence and location of tumor regions with such vascular status.

The DCE-MRI data in the current study were acquired up to 3 days after treatment. Measurements performed longitudinally during a longer time period after HIFU treatment would give further insight in the temporal response of tumor tissue to HIFU treatment. Whereas early after HIFU treatment mainly acute HIFU-induced vascular damage and inflammation are expected, repair processes such as regeneration, fibrosis and revascularization may be observed at a later time point after treatment (29). The described cluster analysis could be applied to identify regions of tissue repair with corresponding vascular characteristics. In a previous study on DCE-MRI analysis of HIFU-treated muscle tissue, it has been shown that regions at the outer edge of the HIFU-treated lesion exhibited higher K^{trans} and v_e values compared to the surrounding unaffected tissue at 7 days after treatment. These regions corresponded to areas of tissue repair in histology (29). In addition to analysis of vascular changes at late time points after HIFU treatment, it would also be of specific interest to assess whether vascular changes observed at an early time point after treatment have prognostic value for the ultimate fate of the tissue. Knowledge of the implications of the different vascular changes in the tumor tissue for the long-term outcome could ultimately increase the specificity of DCE-MRI for the detection of residual tumor tissue after treatment. Importantly, the proposed analysis of vascular changes by clustering of DCE-MRI-derived pharmacokinetic parameters is not restricted to HIFU treatment. The methodology could also be employed to evaluate other tumor therapies that have substantial effect on the tumor vasculature, such as treatment with vascular-disrupting agents.

In conclusion, it was demonstrated that analysis of DCE-MRI data by means of cluster analysis on pharmacokinetic parameters can be used to identify regions with different contrast agent uptake-kinetics after HIFU treatment, that may be reflective of their vascular status. In addition to the commonly performed analysis of non-perfused tumor volume after HIFU treatment, the presented methodology gives additional insight in uptake-kinetics in the transition zone adjacent to central ablation volume. This method could aid in assessment of the consequences of the different vascular alterations after HIFU for the microenvironment and fate of the tissue and the sensitivity of the tumor to additional therapies.

Acknowledgements

The authors acknowledge Ralf Seip from Philips Research for his advice on the HIFU treatment settings. This research was supported by the Center for Translational Molecular Medicine (VOLTA).

References

1. **Tempany CM, McDannold NJ, Hynynen K, Jolesz FA.** *Radiology* 2011;259:39-56.
2. **Hesley GK, Gorny KR, Woodrum DA.** *Cardiovasc Intervent Radiol* 2013;36:5-13.
3. **Voogt MJ, Trillaud H, Kim YS, Mali WP, Barkhausen J, Bartels LW, Deckers R, Frulio N, Rhim H, Lim HK, Eckey T, Nieminen HJ, Mougnot C, Keserci B, Soini J, Vaara T, Kohler MO, Sokka S, van den Bosch MA.** *Eur Radiol* 2012;22:411-417.
4. **Napoli A, Anzidei M, Ciolina F, Marotta E, Cavallo Marincola B, Brachetti G, Di Mare L, Cartocci G, Boni F, Noce V, Bertaccini L, Catalano C.** *Cardiovasc Intervent Radiol* 2013;36:1190-1203.
5. **Schmitz AC, Gianfelice D, Daniel BL, Mali WP, van den Bosch MA.** *Eur Radiol* 2008;18:1431-1441.
6. **Merckel LG, Bartels LW, Kohler MO, van den Bongard HJ, Deckers R, Mali WP, Binkert CA, Moonen CT, Gilhuijs KG, van den Bosch MA.** *Cardiovasc Intervent Radiol* 2013;36:292-301.
7. **Murat FJ, Poissonnier L, Pasticier G, Gelet A.** *Cancer Control* 2007;14:244-249.
8. **Rouviere O, Girouin N, Glas L, Ben Cheikh A, Gelet A, Mege-Lechevallier F, Rabilloud M, Chapelon JY, Lyonnet D.** *Eur Radiol* 2010;20:48-55.
9. **Kirkham AP, Emberton M, Hoh IM, Illing RO, Freeman AA, Allen C.** *Radiology* 2008;246:833-844.
10. **Rouviere O, Gelet A, Crouzet S, Chapelon JY.** *Nat Rev Clin Oncol* 2012;9:721-727.
11. **Leslie T, Ritchie R, Illing R, Ter Haar G, Phillips R, Middleton M, Bch B, Wu F, Cranston D.** *Br J Radiol* 2012;85:1363-1370.
12. **Wijlemans JW, Bartels LW, Deckers R, Ries M, Mali WP, Moonen CT, van den Bosch MA.** *Cancer Imaging* 2012;12:387-394.
13. **Leslie TA, Kennedy JE, Illing RO, Ter Haar GR, Wu F, Phillips RR, Friend PJ, Roberts IS, Cranston DW, Middleton MR.** *Br J Radiol* 2008;81:564-571.
14. **Kennedy JE.** *Nat Rev Cancer* 2005;5:321-327.
15. **Hynynen K.** *Ultrasonics* 2010;50:221-229.
16. **ter Haar G.** *Prog Biophys Mol Biol* 2007;93:111-129.
17. **Kohler MO, Mougnot C, Quesson B, Enholm J, Le Bail B, Laurent C, Moonen CT, Ehnholm GJ.** *Med Phys* 2009;36:3521-3535.
18. **Ishihara Y, Calderon A, Watanabe H, Okamoto K, Suzuki Y, Kuroda K.** *Magn Reson Med* 1995;34:814-823.
19. **de Senneville BD, Mougnot C, Quesson B, Dragonu I, Grenier N, Moonen CT.** *Eur Radiol* 2007;17:2401-2410.
20. **Vaupel PW, Kelleher DK.** *Int J Hyperthermia* 2010;26:211-223.
21. **Chu KF, Dupuy DE.** *Nat Rev Cancer* 2014;14:199-208.
22. **Zhou YF.** *World J Clin Oncol* 2011;2:8-27.
23. **Venkatesan AM, Partanen A, Pulanic TK, Dreher MR, Fischer J, Zurawin RK, Muthupillai R, Sokka S, Nieminen HJ, Sinaii N, Merino M, Wood BJ, Stratton P.** *J Vasc Interv Radiol* 2012;23:786-794 e784.
24. **Kim YS, Lim HK, Kim JH, Rhim H, Park BK, Keserci B, Kohler MO, Bae DS, Kim BG, Lee JW, Kim TJ, Sokka S, Lee JH.** *Invest Radiol* 2011;46:639-647.
25. **Kong G, Braun RD, Dewhirst MW.** *Cancer Res* 2001;61:3027-3032.
26. **Wu F, Chen WZ, Bai J, Zou JZ, Wang ZL, Zhu H, Wang ZB.** *Ultrasound Med Biol* 2002;28:535-542.
27. **Hynynen K, Chung AH, Colucci V, Jolesz FA.** *Ultrasound Med Biol* 1996;22:193-201.
28. **Luo W, Zhou X, Gong X, Zheng M, Zhang J, Guo X.** *J Ultrasound Med* 2007;26:477-485.
29. **Cheng HL, Purcell CM, Bilbao JM, Plewes DB.** *J Magn Reson Imaging* 2004;19:329-341.
30. **Khiat A, Gianfelice D, Amara M, Boulanger Y.** *Br J Radiol* 2006;79:308-314.
31. **Grull H, Langereis S.** *Journal of controlled release : official journal of the Controlled Release Society* 2012;161:317-327.
32. **Hijnen N, Langereis S, Grull H.** *Advanced Drug Delivery Reviews* 2014;72:65-81.
33. **Gianfelice D, Khiat A, Amara M, Belblidia A, Boulanger Y.** *Breast Cancer Res Treat* 2003;82:93-101.
34. **Tofts PS, Brix G, Buckley DL, Evelhoch JL, Henderson E, Knopp MV, Larsson HB, Lee TY, Mayr NA, Parker GJ, Port RE, Taylor J, Weisskoff RM.** *J Magn Reson Imaging* 1999;10:223-232.
35. **Hijnen NM, Heijman E, Kohler MO, Ylihautala M, Ehnholm GJ, Simonetti AW, Grull H.** *Int J Hyperthermia* 2012;28:141-155.
36. **Cheng HL, Purcell CM, Bilbao JM, Plewes DB.** *J Magn Reson Imaging* 2003;18:585-598.
37. **Seip R, Chin CT, Hall CS, Raju BI, Ghanem A, Tiemann K.** *IEEE Trans Biomed Eng* 2010;57:61-70.
38. **Karlsson M, Nordell B.** *Magn Reson Imaging* 1999;17:1481-1488.
39. **Kleppesto M, Larsson C, Groote I, Salo R, Vardal J, Courivaud F, Bjornerud A.** *J Magn Reson Imaging* 2014;39:1314-1319.
40. **Yu Y, Jiang Q, Wang H, Bao S, Haacke EM, Hu J.** *Proceedings of the 19th Annual Meeting ISMRM, Montréal, Canada* 2011:2060.
41. **Vander Elst L, Raynaud J-S, Vives V, Santus R, Louin G, Robert P, Port M, Corot C, Muller R.** *Proceedings of the 21st Annual Meeting ISMRM, Salt Lake City, USA* 2013:746.

42. **Tofts PS, Kermode AG.** Magn Reson Med 1991;17:357-367.
43. **Fruytier AC, Magat J, Colliez F, Jordan B, Cron G, Gallez B.** Magn Reson Med 2013:doi:10.1002/mrm.24682.
44. **Gillies RJ, Schornack PA, Secomb TW, Raghunand N.** Neoplasia 1999;1:197-207.
45. **Tozer GM, S. L, Michalowski A, Aber V.** Br J Cancer 1990;61:250-257.
46. **Song CW, Lin JC, Chelstrom LM, Levitt SH.** Int J Radiat Oncol Biol Phys 1989;17:799-802.

Chapter 7

Multiparametric Magnetic Resonance Imaging analysis for the evaluation of Magnetic Resonance-guided High Intensity Focused Ultrasound treatment

Stefanie Hectors*, Igor Jacobs*, Edwin Heijman, Jochen Keupp, Monique Berben, Gustav Strijkers, Holger Gröll, Klaas Nicolay

Under review

* authors contributed equally

Abstract

For the clinical application of High Intensity Focused Ultrasound (HIFU) for the thermal ablation of malignant tumors, accurate treatment evaluation is of key importance. In this study, we have employed a multiparametric MRI protocol, consisting of quantitative T_1 , T_2 , ADC, amide proton transfer (APT), $T_{1\rho}$ and DCE-MRI measurements, to evaluate MR-guided HIFU treatment of subcutaneous tumors in rats. K-means clustering using all different combinations of the endogenous contrast MRI parameters (feature vectors) was performed to segment the multiparametric data into tissue populations with similar MR parameter values. The optimal feature vector for identification of the extent of non-viable tumor tissue after HIFU treatment was determined by quantitative comparison between clustering-derived and histology-derived non-viable tumor fractions. The highest one-to-one correspondence between these clustering-based and histology-based non-viable tumor fractions was observed for feature vector {ADC, APT-weighted signal} (R^2 to line of identity ($R^2_{y=x}$)=0.92) and the strongest agreement was seen at 3 days after HIFU ($R^2_{y=x}$ =0.97). To compare the multiparametric MRI analysis results with conventional HIFU monitoring and evaluation methods, the histology-derived non-viable tumor fractions were also quantitatively compared with non-perfused tumor fractions (derived from the level of contrast enhancement in the DCE-MRI measurements) and 240EM tumor fractions (i.e. thermal dose > 240 equivalent minutes at 43°C). The correlation between histology-derived non-viable tumor fractions directly after HIFU and the 240EM fractions was high, but not significant. The non-perfused fractions overestimated the extent of non-viable tumor tissue directly after HIFU, whereas an underestimation was observed at 3 days after HIFU. In conclusion, we have shown that a multiparametric MR analysis, based on the ADC and the APT-weighted signal, can accurately determine the extent of non-viable tumor tissue after HIFU treatment. We expect that this method can be incorporated in the current clinical workflow of MR-HIFU ablation therapies.

Introduction

High Intensity Focused Ultrasound (HIFU) is a promising technique for the non-invasive thermal treatment of tumors (1,2). For the clinical introduction of HIFU for thermal ablation of malignant tumors, accurate treatment planning, monitoring and therapy assessment are of critical importance to ensure a successful and safe treatment. To fulfill these needs, HIFU treatment is generally performed under image guidance, either by magnetic resonance imaging (MRI) or ultrasound. In an MR-guided HIFU system (MR-HIFU), the HIFU transducer is integrated in the patient bed of a clinical MR scanner. MR thermometry can be utilized to monitor the temperature evolution in real-time (3) allowing for the definition of thermal dose areas which are lethal to the tumor tissue (i.e. tumor regions in which the delivered thermal dose was at least 240 equivalent minutes (EM) at 43°C) (4,5). In addition, the excellent soft tissue contrast of MRI offers unique possibilities for treatment planning and evaluation. Clinical evaluation of HIFU treatment with MRI has been mainly restricted to T_2 -weighted and contrast-enhanced T_1 -weighted imaging. Although these methods provide useful information about treatment response (6-10), they often lack the sensitivity and/or specificity to accurately identify the non-viable tumor tissue after HIFU (10-12).

In **chapter 3** it was shown that HIFU-treated non-viable tumor tissue can be accurately identified at 3 days after HIFU treatment using a multiparametric MRI analysis of combined T_1 , T_2 and apparent diffusion coefficient (ADC) data. However, directly after treatment, the multiparametric analysis performed less well with respect to the identification of non-viable tumor tissue. Other MRI methods, especially those that are sensitive to protein denaturation and aggregation which occur instantly during HIFU treatment, may be more suitable for direct treatment evaluation. Amide proton transfer (APT) imaging is a very promising method for tumor tissue characterization (13-18) and treatment evaluation (19). APT imaging selectively measures the saturation transfer from amide protons of mobile proteins and peptides to bulk water protons. Another MR parameter that is sensitive to macromolecular changes in the tumor tissue is the longitudinal relaxation time in the rotating frame ($T_{1\rho}$). $T_{1\rho}$ is primarily sensitive to protein-water interactions. In **chapter 4** and **chapter 5**, respectively, it was shown that APT imaging and $T_{1\rho}$ mapping are both promising MRI methods for the detection of HIFU-induced macromolecular tissue changes.

We hypothesized that inclusion of these advanced MR contrast parameters in the previously described multiparametric analysis leads to a more accurate identification of successfully HIFU-treated tumor tissue. Therefore, the goal of the current study was to identify a subset of MRI parameters that are suitable for accurate early HIFU therapy assessment. In addition, we aimed to compare the performance of this optimal multiparametric analysis with conventional HIFU monitoring and evaluation methods, namely MR thermometry and contrast-enhanced MRI. Such quantitative comparison with conventional techniques could not be performed in the previous studies described in **chapter 3, 4 and 5**, mainly because the HIFU treatment was performed outside the MR

system. In the present study, the HIFU treatment was performed in a rat tumor model on a clinical 3 Tesla MR-HIFU system, allowing for real-time acquisition of MR temperature maps during treatment. The multiparametric MRI protocol, consisting of quantitative T_1 , T_2 , ADC, APT and $T_{1\rho}$ mapping was performed in the same MR-HIFU system before, directly after and at 3 days after HIFU treatment. In addition, dynamic contrast-enhanced MRI (DCE-MRI) was performed after HIFU to assess changes in the tumor vascular status and to determine the non-perfused tumor volume after treatment. Cluster analysis, that segments the multiparametric data into tissue populations with similar MR parameter values, was performed on all possible combinations of the endogenous MR contrast parameters. The optimal subset of MRI parameters for HIFU treatment evaluation was determined by quantitative comparison between clustering-derived and histology-derived non-viable tumor fractions. The performance of the proposed multiparametric analysis with respect to the identification of non-viable tumor tissue was compared to contrast-enhanced MRI and MR thermometry by quantitative correlation analyses between clustering-derived non-viable tumor fractions, non-perfused tumor fractions, 240EM tumor fractions (i.e. the fraction of the tumor in which the thermal dose exceeded 240EM) and histology-derived non-viable tumor fractions.

Materials and Methods

Ethics statement

All animal experiments were performed according to the Directive 2010/63/EU of the European Commission and approved by the Animal Care and Use Committee of Maastricht University (protocol: 2012-171).

Rat tumor model

5 to 7-week old female Fischer 344 rats (Charles River, Maastricht, The Netherlands) were inoculated with 1×10^6 GS 9L cells (early passages of the original batch obtained from Public Health England, London, UK) in 100 μ L phosphate buffered saline (PBS, Sigma-Aldrich), subcutaneously in the left hind limb. The average tumor size at the time of the first MRI examination was 878 ± 533 mm³ as determined from region-of-interest (ROI) analysis on the anatomical MR images.

Study design

The tumor-bearing rats underwent MRI directly before (n=12), directly after (n=12) and 3 days after (n=6) HIFU treatment. A non-treated control group (n=6) was included that underwent MRI at the same time points, but did not undergo MR-HIFU treatment. Immediately after the final MRI measurement, rats were sacrificed by cervical dislocation and tumors were excised for histological analysis. This study design resulted in three different groups for histology; rats that were sacrificed immediately after the MRI scan directly after MR-HIFU ablation (referred to as 'Directly after HIFU', n=6), rats that were sacrificed directly after the MRI scan at 3 days after MR-HIFU ablation (referred to as '3 days after HIFU', n=6) and a non-treated control group (referred to as 'Control', n=6).

MR-HIFU system and small animal setup

HIFU treatment was performed using a clinical 3T MR-HIFU system (Philips Sonalleve, Philips Healthcare, Vantaa, Finland). A dedicated small animal HIFU-compatible MR receiver coil (Philips Healthcare, Vantaa, Finland) with a multi-channel volumetric design was used to obtain optimal signal to noise ratio. The utilized MR-HIFU system and small animal set-up have been described in detail previously (20).

Animal handling

Animals were anesthetized with 3% isoflurane in medical air (0.6 L/min) and maintained with 1.0-2.5% isoflurane during the HIFU treatment and MRI measurements. At least 30 minutes prior to HIFU treatment, precautionary analgesia was given (carprofen; rhymadyl, 4 mg/kg s.c.). An equal dose of analgesia was administered to the control animals before the first MRI measurement. For optimal coupling of the ultrasound to the skin, fur was removed from the tumor and hind limb by shaving and application of a depilatory cream (Veet, Hoofddorp, The Netherlands). During MRI measurements and MR-HIFU treatment, the animal's respiration rate was monitored with a pressure balloon sensor (Graseby, Smiths Medical, St Paul, MN, USA) and body temperature was monitored using a rectal temperature probe (Neoptix, Québec City, Canada) and maintained at 37°C.

HIFU treatment

A 4-mm diameter treatment cell was planned within the tumor using anatomical MR images. Volumetric thermal ablation of the tumor tissue was performed with a 256-element spherical phased array transducer by electronic steering of a single focus point along a circular trajectory perpendicular to the direction of ultrasound propagation, as described previously (20,21). Ultrasound was applied as a continuous wave with a frequency of 1.44 MHz. Thermal ablation was performed by 90 seconds of sonication at 35 W acoustic power (resulting in an average maximum ablation temperature of 58.5 ± 5.6 °C (n=12)). The sonication time was intentionally kept constant rather than using the MR thermometry-based feedback control to stop the sonication when a certain target temperature or thermal dose was reached. It has previously been described that HIFU treatment using a constant power and sonication time without feedback results in a wider spread of temperatures in the treatment volume and subsequently to a larger variation in the thermal lesion size, as compared to sonications with MR thermometry feedback (22). Since a large spread in thermal lesion size and subsequently a large range of non-viable tumor fractions was beneficial for the correlation analyses between MRI-derived and histology-derived non-viable tumor fractions in the current study, the sonications were performed without thermometry feedback. Tumors were only partially treated with a single treatment cell, which was smaller than the typical tumor diameter, to allow for the presence of both treated and untreated tumor tissue in the multiparametric MR images.

MRI protocol

The MRI protocol started with a T_2^* -weighted 3D gradient-echo acquisition (repetition time (TR)=15 ms, echo time (TE)=12 ms, field of view (FOV)=280x280x20 mm³, reconstructed

voxel size=0.28x0.28x2 mm³, flip angle (FA)=10°, number of averages (NA)=2, scan duration=1 min 58 s) to check for the presence of air bubbles in the HIFU beam path or in close proximity to the tumor tissue.

The HIFU treatment cell was planned on anatomical images covering the entire tumor, acquired with a multi-slice steady-state gradient-echo sequence (TR=793 ms, TE=13 ms, FOV: 40x48x20 mm³, reconstructed voxel size: 0.25x0.25x1 mm³, FA=20°, NA=2, scan duration=5 min 6 s).

The temperature rise in the treatment area during MR-HIFU ablation was monitored with a dynamic gradient-echo EPI acquisition (TR=38ms, TE=20ms, FOV=250x250 mm², reconstructed voxel size=1.42x1.42x4.08 mm³, FA=19.5°, EPI factor=7, NA=2, temporal resolution=4.8 s) in 3 adjacent slices perpendicular and 1 slice parallel to the acoustic beam path.

The multiparametric MRI protocol consisted of quantitative assessment of the T₁, T₂, ADC, APT-weighted signal and T_{1ρ} as well as a DCE-MRI acquisition. For the HIFU-treated animals, DCE-MRI was only performed after the HIFU treatment, since the presence of the paramagnetic Gd could affect the assessment of the endogenous contrast parameters directly after treatment and induce inaccuracies in the temperature mapping due to magnetic susceptibility changes (23). The acquisitions of the multiparametric protocol were performed with a FOV of 150x150x10 mm³ and reconstructed at a voxel size of 0.94x0.94x2 mm³, resulting in a 3D matrix size of 160x160x5. For the DCE-MRI sequence the FOV was extended to 150x150x30 mm³ (matrix size 160x160x15) to avoid aliasing artifacts, with the same center slice positions and reconstructed voxel size as for the other sequences. The orientation of the central slice of all imaging methods of the multiparametric MRI protocol was aligned with the central slice of the temperature mapping sequence, perpendicular to the acoustic beam axis.

T₁ mapping was performed using a 3D Look-Locker segmented gradient-echo (turbo field echo) sequence. T₁-weighted images were acquired with inversion times ranging from 18-6418 ms in steps of 100 ms. Further acquisition parameters were: TR=5.6 ms, TE=2.8 ms, FA=5°, turbo-factor 10, NA=1, scan duration: 8 min.

T₂ mapping was performed by acquisition of T₂-weighted images with TE ranging from 4.1-251.7 ms in steps of 16.5 ms using a multi-slice fast spin-echo sequence (TR=14526 ms, NA=1, scan duration=12 min 35 s).

For ADC mapping a diffusion-weighted echo planar imaging (EPI) sequence was used, with b-values of 0, 100, 200, 400, 600, 800, 1200 s/mm². Other imaging parameters were: TR=1000 ms, TE=71 ms, FA=90°, EPI factor=11, NA=2, scan duration=9 min 22 s.

For APT imaging, a z-spectrum was recorded using a 3D turbo gradient-echo sequence with irradiation offsets ranging from -6 to 6 ppm with 0.5 ppm steps. The saturation pulses were continuous wave RF pulses with a duration of 2 s at a saturation power level corresponding to a field amplitude of B_{1, rms}=1.8 μT. In addition, a control acquisition (S₀)

was performed with irradiation at ~ -1560 ppm. Further acquisition parameters were: TR=7.5 ms, TE=3.8 ms, FA=20°, turbo-factor=75, NA=2, scan duration=17 min 50 s. B_0 homogeneity was improved by local second-order pencil-beam shimming.

$T_{1\rho}$ was acquired with a 3D gradient-echo sequence (TR=3.6 ms, TE=2.1 ms, FA=20°, NA=8, scan duration 3 min 54 s), with a spin-lock preparation compensated for B_1 and B_0 field imperfections (24). Images were acquired with 2 different spin-lock durations (5 and 40 ms) using a spin-lock amplitude of 350 Hz.

DCE-MRI was performed with an RF-spoiled 3D T_1 -weighted turbo gradient-echo sequence with the following acquisition parameters: TR=5.2 ms, TE=2.6 ms, FA=15°, turbo-factor=51, NA=1, dynamic scan time=4.3 s, total scan duration=10 min 46 s. After 1 minute of pre-contrast images acquisition, a bolus of 0.2 mmol/kg Gd-DOTA (Dotarem; Guerbet, Villepente, France) with a saline flush was injected in 5 s at a rate of 3 mL/min by use of an infusion pump (Chemyx Fusion 100, Stafford, TX, USA).

The total acquisition time of the multi-slice multiparametric protocol was approximately 75 minutes.

Image processing and generation of parameter maps

Data analysis was performed with Mathematica 8.0 and MATLAB R2013a. Tumor ROIs were manually drawn using the image with TE=37.1 ms of the T_2 mapping dataset. Diffusion-weighted images were used as a visual reference for the correct identification of tumor tissue. Parameter maps were calculated on a pixel-by-pixel basis in each slice. Only the central slice of the multiparametric images was selected for all further analyses, since the orientation of this slice corresponded to the central slice of the temperature maps perpendicular to the HIFU beam axis. T_1 maps were generated as described previously (25). To calculate the T_2 maps, mono-exponential fitting was performed through the multi-echo data, omitting the first two echoes due to signal fluctuations. The ADC was determined by mono-exponential fitting through the signal intensities at the 4 highest b-values (400, 600, 800, 1200 s/mm²).

For analysis of the APT data, first the minimum of the z-spectrum was determined by fitting a 23rd-order polynomial function through the z-spectrum after which the minimum of this function was calculated. Subsequently, the minimum of the z-spectrum was centered at 0 ppm and the APT-weighted signal maps were generated via a magnetization transfer asymmetry (MTR_{asym}) analysis using $MTR_{\text{asym}} = (S_{\text{sat}}(-3.5 \text{ ppm}) - S_{\text{sat}}(3.5 \text{ ppm})) / S_0$, in which $S_{\text{sat}}(-3.5 \text{ ppm})$ and $S_{\text{sat}}(3.5 \text{ ppm})$ are the signal intensities in the z-spectrum at -3.5 ppm and 3.5 ppm from the water frequency, respectively, and S_0 is the signal intensity in the acquisition with the saturation offset far from the water peak (~ -1560 ppm).

The $T_{1\rho}$ values were determined by calculation of $(t_{\text{sl},2} - t_{\text{sl},1}) / \ln(SI_{\text{sl},1} / SI_{\text{sl},2})$, where $t_{\text{sl},1}$ and $t_{\text{sl},2}$ are the different spin-lock durations and $SI_{\text{sl},1}$ and $SI_{\text{sl},2}$ are the corresponding signal intensities.

From the DCE-MRI data, dynamic T_1 values were calculated in the tumor ROIs from the dynamic signal intensities and the pre-contrast T_1 values using the signal equation for an RF-spoiled gradient-echo sequence (26). Dynamic T_1 values were converted to dynamic contrast agent concentrations ([CA]) using the relaxivity of Dotarem ($3.78 \text{ mM}^{-1}\text{s}^{-1}$), which was measured *ex vivo* in rat plasma at 3 T at 37°C . Tracer-kinetic analysis of the DCE-MRI data was performed with a custom-written MATLAB tool. The standard Tofts model (27) was fitted to the DCE-MRI data to determine the transfer constant K^{trans} and extravascular extracellular volume fraction v_e in each tumor pixel. A delay term (t_d) was included in the model to allow for a delay between bolus arrival in the blood and the tissue response. A population-averaged bi-exponential arterial input function (AIF) was used as proposed by McGrath et al. (28). The bi-exponential AIF is described by:

$$C_p(t) = \begin{cases} 0 & t < t_i \\ a_1 e^{-m_1 t} + a_2 e^{-m_2 t} & t \geq t_i \end{cases}$$

in which t_i is the injection time. The exponents of the bi-exponential function were determined based on blood kinetics data of Dotarem acquired in 3 separate female Fischer 344 rats. Blood sampling in these separate animals was performed from the saphenous vein at different time points (0.5, 2, 5, 10, 15, 20, 30 min) after contrast agent injection. The Gd^{3+} concentration in the blood samples was determined by means of Inductively Coupled Plasma-Atomic Emission Spectrometry (ICP-AES) or ICP-Mass Spectrometry (ICP-MS). The blood concentrations of Gd^{3+} were converted to plasma concentrations using a hematocrit value of 53.8% (29). Subsequently, the bi-exponential model was fitted to the time-plasma concentration data points. The a_1 and a_2 parameters following from this fit were adapted such that the sum of a_1 and a_2 was equal to the theoretical peak concentration, which was calculated based on the injected dose and the rat plasma volume. These adaptations led to the following bi-exponential AIF parameters: $a_1=5.38 \text{ mM}$, $a_2=1.38 \text{ mM}$, $m_1=2.82 \text{ min}^{-1}$, $m_2=0.04 \text{ min}^{-1}$.

The Standard Tofts model was fitted to the dynamic [CA] curves using the MATLAB function `lsqcurvefit`, with constraints $K^{\text{trans}} \geq 0 \text{ min}^{-1}$, $k_{\text{ep}} (=K^{\text{trans}}/v_e) \geq 0 \text{ min}^{-1}$ and $0 \leq t_d \leq 7$ repetitions. Tumor pixels were considered non-perfused if the median dynamic [CA] after injection was lower than 5 times the standard deviation (SD) of the data points in the dynamic [CA] curve before injection.

Maximum temperature maps were generated from the acquired MR thermometry data. Thermal dose maps were calculated using the Sapareto-Dewey equation (30) with 43°C as reference temperature. Although the slice orientation was the same for the temperature maps and the multiparametric MR images, the image resolution and position within the slice plane of the temperature maps and multiparametric MR images were different. Therefore, registration of the temperature maps to the multiparametric images was performed by translation and interpolation in the slice plane. 240EM thermal dose areas were defined and MR parameter changes directly after MR-HIFU treatment were related to the maximum temperature and thermal dose.

Histograms of the parameter values in the tumor pixels at the different time points were calculated for all MRI parameters to assess HIFU-induced changes in the parameter distributions.

Cluster analysis

k-means cluster analysis was performed to segment the multiparametric MRI data into groups of pixels, i.e. clusters, with similar MR parameter values (31). Prior to clustering, the parameter values were normalized (mean=0, standard deviation=1) to prevent scaling bias between the different MR parameters. Clustering was performed with a custom-written Mathematica tool with 2 to 6 clusters and all possible feature vectors (i.e. all different combinations of MR parameters). The pharmacokinetic parameters resulting from the DCE-MRI analysis were not included in the cluster analysis, since DCE-MRI was only performed after treatment.

After clustering with the different feature vectors, clusters were defined as non-viable if the fraction of pixels that was assigned to that cluster significantly increased after MR-HIFU ablation (either directly or at 3 days after ablation) compared to before treatment (one-sided paired Student's t-test, $P < 0.05$). The remaining clusters were defined as viable. Subsequently, all tumor pixels were classified as either viable or non-viable based on the cluster to which they were assigned. Based on this classification, the k-means clustering-derived non-viable tumor fractions were calculated for each tumor and for each feature vector.

Histology

After sacrifice, tumors were excised for histological processing and analysis. A tissue marking dye kit (Sigma-Aldrich) was utilized to draw lines of four different colors on the tumor, to aid in retrieval of the same orientation as the MRI slices. The tumor was sliced in two pieces, such that the cutting face matched with the central slice of the multiparametric and MR thermometry acquisitions. Subsequently, one of the pieces was processed to prepare paraffin sections and the other to prepare cryosections. For cryosections, tumors were embedded in Cryomatrix (Shandon, Thermo Scientific, Waltham, MA, USA), snap-frozen in isopentane of -40°C and stored at -80°C . For paraffin sections, the tumors were fixed in 4% formaldehyde solution for approximately 40 hours and then stored in 70% ethanol until they were embedded in paraffin. Both the paraffin-embedded and the snap-frozen tumor pieces were subsequently cut in 5-6 μm thick sections.

For quantitative assessment of the non-viable tumor fraction, cryosections were briefly air-dried and subsequently stained for nicotinamide adenine dinucleotide (NADH) diaphorase activity as a marker for cell viability. Tumor sections were incubated in filtered Gomori-Tris-HCl buffer of pH 7.4, with 0.71 mg/mL β -NAD reduced disodium salt hydrate (Sigma-Aldrich) and 0.29 mg/mL nitro blue tetrazolium (Sigma-Aldrich) for 1 hour at 37°C .

The paraffin sections were used for hematoxylin and eosin (H&E; Sigma-Aldrich) staining to assess morphological tumor changes after MR-HIFU ablation.

After staining, one paraffin section and one cryosection were selected (blinded from the MRI results) for each tumor and brightfield microscopy was performed on a Panoramic MIDI digital slide scanner (3DHitech Ltd, Budapest, Hungary) at 41x magnification to obtain images of the entire tumor section.

Analysis of the microscopy images of the NADH diaphorase-stained tumor sections was performed in Mathematica 8.0 (Wolfram Research, Champaign, IL, USA). For quantification of the non-viable tumor fraction, ROIs were manually drawn around the entire tumor tissue and around the pale non-viable tumor tissue. For each tumor the non-viable tumor fraction was determined from the ratio between the two ROI areas.

Comparison between MRI and histology

The cluster results of the different feature vectors were analyzed by quantitative comparison between clustering-derived and histology-derived non-viable tumor fractions. This comparison was done by assessment of the Pearson's correlation coefficient and the one-to-one correspondence between the fractions. The latter was determined by calculation of the coefficient of determination ($R^2_{y=x}$) between the data points and the line of identity. All groups ('Directly after HIFU', '3 days after HIFU' and 'Control') were combined in this analysis. The feature vector with the highest one-to-one correspondence between clustering-derived and histology-derived non-viable tumor fractions was selected as the optimal feature vector for the identification of non-viable tumor tissue. After selection of the optimal feature vector, the one-to-one correspondence and Pearson's correlation coefficient between clustering-derived non-viable tumor fractions and histology-derived non-viable tumor fractions were also determined separately for the different experimental groups. The histology-derived non-viable fractions were also quantitatively compared to the DCE-MRI-derived non-perfused fractions and the 240EM fractions, again by calculation of the $R^2_{y=x}$ and the correlation coefficient.

Statistical analysis

All data are shown as mean \pm SD. Two-sided paired t-tests were used to compare: the average parameter values in the tumor ROI before and at both time points after HIFU treatment; the histograms of the endogenous contrast MRI parameters before and at both time points after HIFU treatment; and the average parameter values in the 240EM area before and directly after HIFU ablation. Two-sided t-tests assuming equal variances were used to compare: the average parameter values in the HIFU-treated and non-treated control tumors; and the K^{trans} and v_e histograms of the HIFU-treated and non-treated control animals at corresponding time points. The calculated Pearson's correlation coefficients were tested for significance with a one-sample t-test. For all tests, the level of significance was set to $\alpha=0.05$.

Results

MR parameter maps and average parameter values

Representative MR parameter maps at the different experimental time points ('Before HIFU', 'Directly after HIFU' and '3 days after HIFU') are shown in Figure 1A. The observed changes in the individual endogenous MR parameter values after HIFU treatment were rather subtle and heterogeneous between the different endogenous contrast parameters. The K^{trans} maps derived from the DCE-MRI measurements showed that the tumor was largely non-perfused directly after treatment, while the perfusion was partly restored at 3 days after treatment. On the maximum temperature maps (Figure 1B) a circular region was observed in which a significant temperature increase was measured. This circular region was more distinctly visible on the thermal dose maps (Figure 1B), because of the exponential increase of thermal dose at higher temperatures. The NADH-diaphorase-stained tumor section shown in Figure 1C, obtained at approximately the same position and orientation in the tumor as the MRI slice at 3 days after HIFU treatment, shows mostly non-viable tumor (pale) with a small amount of viable tumor (blue) on either side of the non-viable region.

Table 1 shows average MRI parameter values in the entire center slice, consisting of both HIFU-treated and non-treated tumor tissue because of the partial tumor ablation. HIFU treatment resulted in a subtle, yet significant, decrease in ADC directly after HIFU, whereas ADC values were pronouncedly, and significantly, increased at 3 days after HIFU. In addition, T_1 values were significantly decreased at 3 days after HIFU compared to before HIFU. Directly after HIFU treatment, the average T_1 values in the HIFU-treated tumors were significantly higher than those in the control tumors at the corresponding time point, although the increase in T_1 between before and directly after treatment in the HIFU-treated tumors was not significant. The K^{trans} and v_e values were significantly lower in the HIFU-treated tumors directly after HIFU compared to the control tumors at day 0. At 3 days after HIFU treatment, K^{trans} remained significantly lower in the HIFU-treated tumors compared to the control tumors.

Further insight in the MR parameter distributions in the tumor tissue at the different experimental time points is provided by the histograms of MR parameter values in all tumor pixels in the center slice, which can be found in the supplemental information (Part I). The most notable changes in these histograms were observed at 3 days after HIFU treatment. At that time point, a pronounced significant shift toward high ADC values and a slight, non-significant, shift toward low APT-weighted signal values were observed. Results of the analysis of the relation between temperature/thermal dose and changes in MR parameter values directly after treatment can also be found in the supplemental information (Part II).

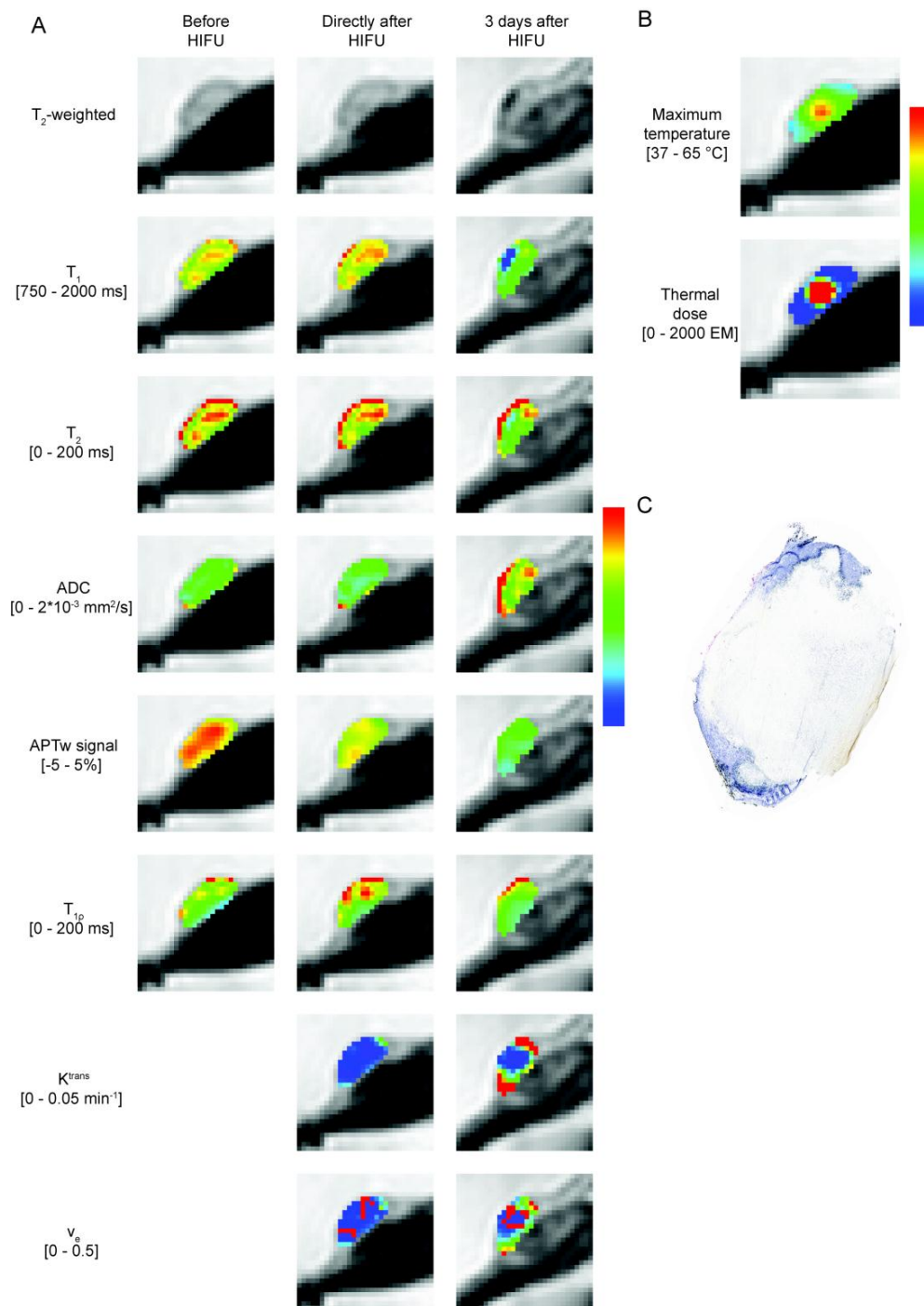


Figure 1. A) Representative T_2 -weighted images and MR parameter maps (T_1 , T_2 , ADC, APTw signal, $T_{1\rho}$, K^{trans} and v_e) superimposed on the T_2 -weighted images in the center slice of the tumor-bearing hind limb, before, directly after and at 3 days after HIFU treatment. The parameter maps of K^{trans} and v_e before HIFU are absent, since DCE-MRI was not performed at this time point. The color coding represents the MR parameter values in the tumor, of which the scaling is given by the scale bar on the right and the range is indicated on the left side of each row. B) Maps of the maximum temperature that was reached (top) and the applied thermal dose in each tumor pixel (bottom). The scale bar on the right and the numbers on the left represent the range in parameter values. C) The NADH diaphorase-stained tumor section at the same location as the shown MRI slice, excised at 3 days after HIFU treatment. The blue region is viable tumor and the pale region is non-viable tumor.

Table 1. MR parameter values (mean±SD) in the entire center tumor slice of the HIFU-treated rats before HIFU, directly after HIFU, 3 days after HIFU, as well as in the control animals at day 0 and day 3. For the HIFU-treated animals, the p-values next to the average parameter values result from a paired two-sided Student's t-test between the 'Directly after HIFU' or '3 days after HIFU' data and the 'Before HIFU' data. The p-values between the parentheses result from a two-sided Student's t-test between the HIFU-treated and non-treated control tumors at corresponding time points. The p-values given for the control animals at day 3 result from a two-sided paired Student's t-test ($P < 0.05$) between the data at day 0 and day 3. The p-values are highlighted bold if the mean MR parameter values showed statistically significant differences ($P < 0.05$).

Parameter	HIFU-treated animals			Control animals	
	Before HIFU	Directly after HIFU	3 days after HIFU	Day 0	Day 3
T_1 [ms]	1674±41 (P=0.061)	1694±57;P=0.085 (P=0.030)	1520±134; P=0.041 (P=0.386)	1624±63	1581±96;P=0.347
T_2 [ms]	183±16 (P=0.313)	173±29;P=0.152 (P=0.175)	160±17;P=0.111 (P=0.372)	198±45	177±39;P=0.423
ADC [10^{-3} mm^2/s]	1.14±0.14 (P=0.360)	1.04±0.14; P=0.030 (P=0.036)	1.65±0.17; P=0.001 (P=0.001)	1.21±0.19	1.27±0.13;P=0.614
APTw signal [%]	2.23±0.71 (P=0.261)	2.39±0.66;P=0.538 (P=0.458)	1.55±1.35;P=0.150 (P=0.186)	2.67±0.86	2.63±1.25;P=0.925
T_{1p} [ms]	127±9 (P=0.118)	136±18;P=0.178 (P=0.050)	119±15; P=0.604 (P=0.727)	116±20	115±22;P=0.918
K^{trans} [min^{-1}]	-	0.013±0.010 (P=0.013)	0.044±0.013 (P=0.048)	0.076±0.034	0.085±0.041;P=0.560
V_e [-]	-	0.093±0.046 (P=0.000)	0.205±0.068 (P=0.095)	0.258±0.040	0.332±0.151;P=0.301

Cluster analysis and feature vector selection

After evaluation of the changes in the individual MR parameters, cluster analysis was performed to combine information of the different endogenous contrast MR parameters to identify HIFU-treated non-viable tumor tissue. Clusters were classified as non-viable when the fraction of pixels within the clusters significantly increased after HIFU treatment. Subsequently, the one-to-one correspondence ($R^2_{y=x}$) between the non-viable tumor fractions derived from clustering with all different feature vectors and the histology-derived non-viable tumor fractions was determined. All experimental groups were included in this analysis. Clustering with 4 clusters led to a stronger one-to-one correspondence between histology and clustering compared to other numbers of clusters. $R^2_{y=x}$ values between histology-derived non-viable tumor fractions and non-viable tumor fractions derived from clustering with 4 clusters are displayed in Table 2 for all feature vectors. Feature vector {ADC, APTw signal} was identified as the optimal feature vector, since clustering with these two MR parameters resulted in the best one-to-one correspondence ($R^2_{y=x} = 0.92$) between the histology-derived and clustering-derived non-viable tumor fractions.

Table 2. One-to-one correspondence ($R^2_{y=x}$) between histology-derived non-viable tumor fractions and non-viable tumor fractions resulting from k-means clustering with 4 clusters and all possible feature vectors (i.e. combinations of MR parameters). The $R^2_{y=x}$ values are given for all feature vectors, grouped per number of MR parameters of which the feature vector consisted, and ordered from low to high values. The highest $R^2_{y=x}$ value is highlighted in bold (for feature vector {ADC, APTw signal}).

	Feature vector	$R^2_{y=x}$
1 parameter	{T _{1ρ} }	-21.7
	{T ₂ }	0.00
	{APTw signal}	0.00
	{T ₁ }	0.16
	{ADC}	0.63
2 parameters	{T ₂ , APTw signal}	0.00
	{T ₂ , T _{1ρ} }	0.00
	{APTw signal, T _{1ρ} }	0.23
	{T ₁ , ADC}	0.29
	{T ₁ , APT}	0.37
	{T ₁ , T _{1ρ} }	0.48
	{T ₁ , T ₂ }	0.58
	{ADC, T _{1ρ} }	0.60
	{T ₂ , ADC}	0.81
	{ADC, APTw signal}	0.92
3 parameters	{T ₁ , T ₂ , T _{1ρ} }	0.50
	{T ₁ , APTw signal, T _{1ρ} }	0.51
	{T ₂ , APTw signal, T _{1ρ} }	0.59
	{T ₁ , T ₂ , APTw signal}	0.61
	{T ₂ , ADC, T _{1ρ} }	0.61
	{T ₁ , T ₂ , ADC}	0.68
	{T ₁ , ADC, T _{1ρ} }	0.71
	{T ₂ , ADC, APTw signal}	0.72
	{T ₁ , ADC, APTw signal}	0.74
4 parameters	{T ₁ , T ₂ , ADC, T _{1ρ} }	0.55
	{T ₁ , T ₂ , APTw signal, T _{1ρ} }	0.55
	{ADC, APTw signal, T _{1ρ} }	0.73
	{T ₂ , ADC, APTw signal, T _{1ρ} }	0.74
	{T ₁ , T ₂ , ADC, APTw signal}	0.86
	{T ₁ , ADC, APTw signal, T _{1ρ} }	0.91
5 parameters	{T ₁ , T ₂ , ADC, APTw signal, T _{1ρ} }	0.77

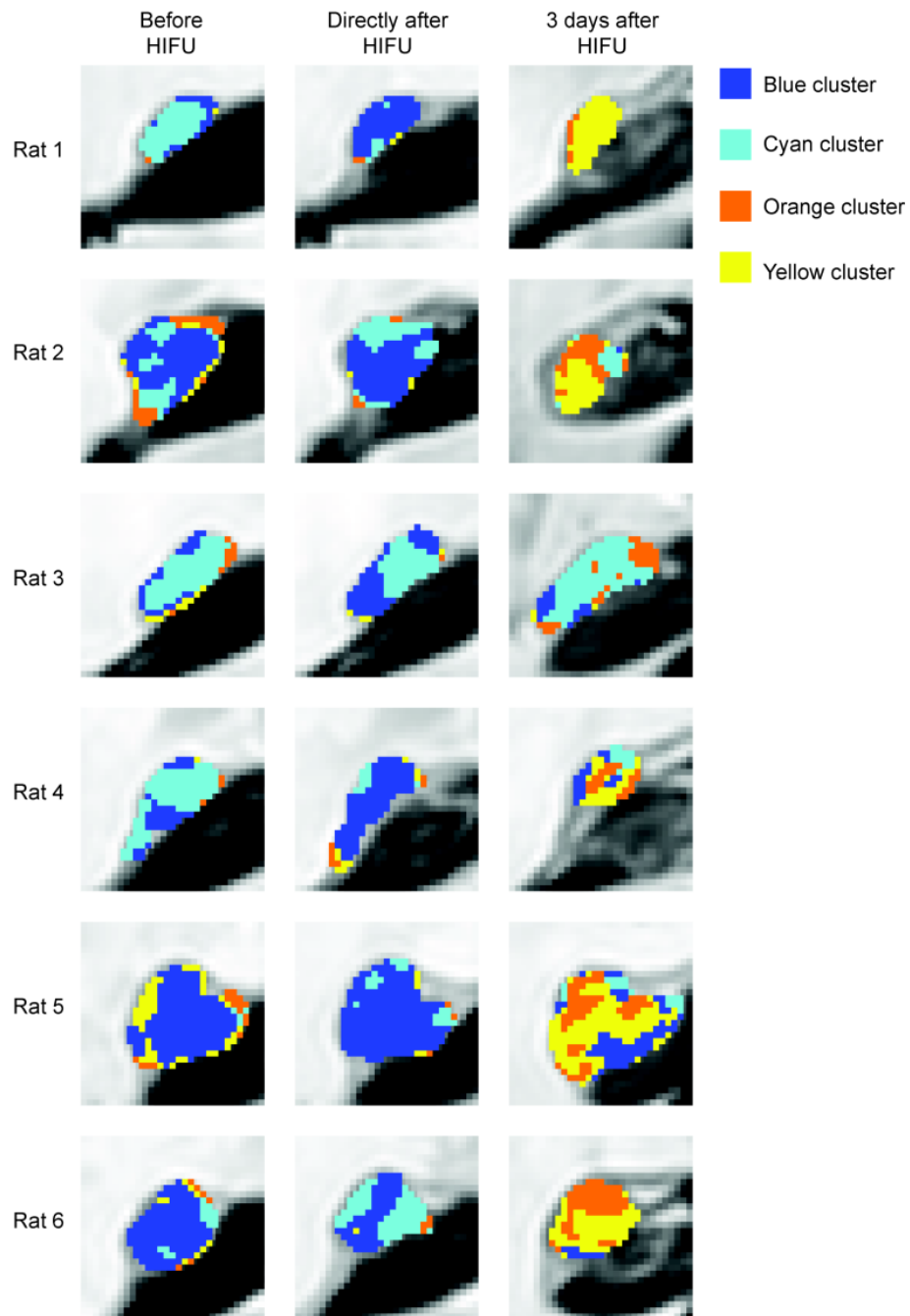


Figure 2. Representative results of k-means clustering with feature vector {ADC, APTw signal} and 4 clusters at the different experimental time points of all animals in the experimental group '3 days after HIFU', superimposed on the tumor pixels in the T₂-weighted images. The MR slice of rat 1 is the same as the slice shown in Figure 1. The four colors (cyan, blue, orange and yellow) represent the different clusters.

Representative cluster maps, resulting from clustering with the optimal feature vector {ADC, APTw signal} and 4 clusters, for all rats that underwent MRI follow-up until 3 days after MR-HIFU are shown in Figure 2 at the three experimental time points. Before HIFU, almost all tumor pixels were assigned to the cyan and blue clusters. Also directly after HIFU treatment, only a minor number of pixels was assigned to the yellow and orange clusters. However, at 3 days after HIFU treatment large regions emerged in which pixels were assigned to the yellow and orange clusters. Remarkably, in rat 3 most tumor pixels remained in the blue and cyan clusters at 3 days after treatment, indicative of presence of a substantial amount of residual viable tumor tissue, which was confirmed by histology (see later in this section). However, the MR thermometry measurements suggested a successful ablation of this particular tumor (maximum temperature = 65.3°C, 240EM fraction = 0.32).

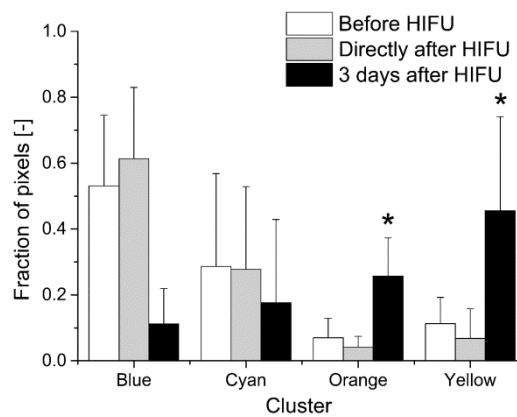


Figure 3. Bar chart of the fraction of pixels within the different clusters at the different experimental time points. * denotes a significant increase in the fraction of pixels within the cluster compared to before HIFU (one-sided paired Student's t-test, $P < 0.05$).

The fractions of pixels assigned to the different clusters following from segmentation with feature vector {ADC, APTw signal} at the three time points of the HIFU-treated animals are shown in Figure 3. Indeed, a significantly increased fraction of pixels in the yellow and orange clusters was observed at 3 days after HIFU compared to before treatment. These clusters were therefore classified as non-viable.

The average MR parameter values in the clusters resulting from segmentation with the optimal feature vector {ADC, APTw signal} are listed in Table 3. The clusters that were classified as non-viable were characterized by a high ADC value and either a low APT-weighted signal (yellow cluster) or an APT-weighted signal that is comparable to values measured before HIFU (orange cluster).

Table 3. MR parameter values (mean±SD) in the different clusters resulting from k-means clustering with feature vector {ADC, APTw signal} and 4 clusters.

Cluster	ADC [10^{-3} mm ² /s]	APTw signal [%]
Blue	0.97±0.18	1.83±0.62
Cyan	1.11±0.26	3.69±0.76
Orange	2.20±0.36	2.24±1.13
Yellow	1.52±0.26	0.97±0.95

The qualitative visual agreement between the clustering-derived and histology-derived non-viable tumor tissue at 3 days after HIFU treatment is depicted in Figure 4. Large tumor regions were classified as non-viable by the cluster analysis. These regions were generally in good visual agreement with areas of non-viable tumor tissue in histology. The remarkable cluster results of rat 3, that showed that the major part of the tumor was classified as viable at 3 days after treatment in contrast to what would be expected from the lethal thermal dose maps, were supported by histology. The NADH-diaphorase stained tumor section of this rat also indicated that a large part of the tumor was still viable at 3 days after HIFU.

The correlation plot in Figure 5A demonstrates that clustering with 4 clusters and the optimal feature vector {ADC, APTw signal} resulted in a strong correlation ($r=0.92$) and good one-to-one correspondence ($R^2_{y=x}=0.92$, corresponding to the value in Table 2) between clustering-derived and histology-derived non-viable tumor fractions, when all data points of all experimental groups were combined. Directly after HIFU treatment, the agreement with histology was less ($r=0.63$, $R^2_{y=x}=0.62$; Figure 5B). Nevertheless, Figure 5C demonstrates that there was a strong correlation ($r=0.87$) and excellent one-to-one correspondence ($R^2_{y=x}=0.97$) between clustering-derived and histology-derived non-viable tumor fractions at 3 days after HIFU treatment. For the control animals (Figure 5D) the correlation with histology was strong ($r=0.95$), although the clustering-derived non-viable tumor fractions were consistently higher than the histology-derived non-viable tumor fractions ($R^2_{y=x}=0.67$).

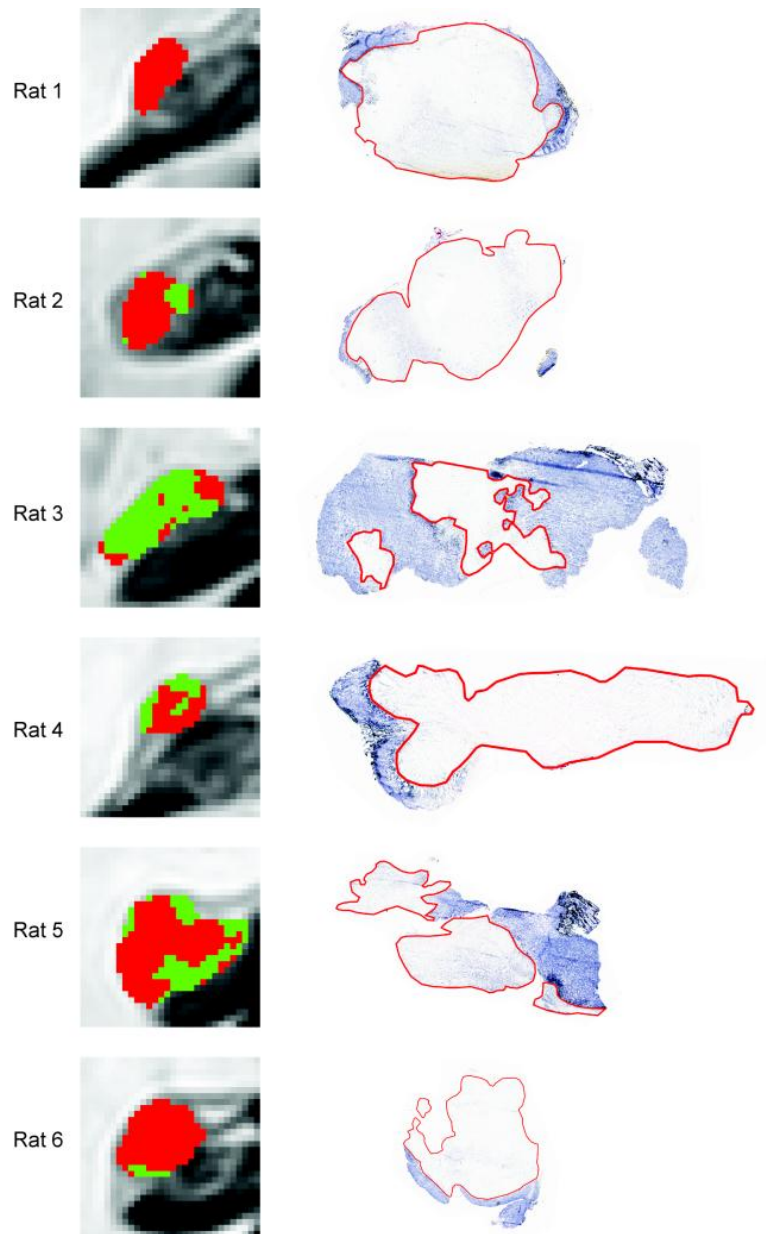


Figure 4. Classification of the tumor pixels as viable (green) or non-viable (red) from clustering with 4 clusters and feature vector {ADC, APTw signal} for all animals in the experimental group '3 days after HIFU', superimposed on the tumor pixels in the T_2 -weighted images. The MR slice of rat 1 is the same as the slice shown in Figure 1. On the right side of the figure, the corresponding NADH-diaphorase-stained tumor sections are shown. The tumor regions that were identified as non-viable on histology is delineated by red contours.

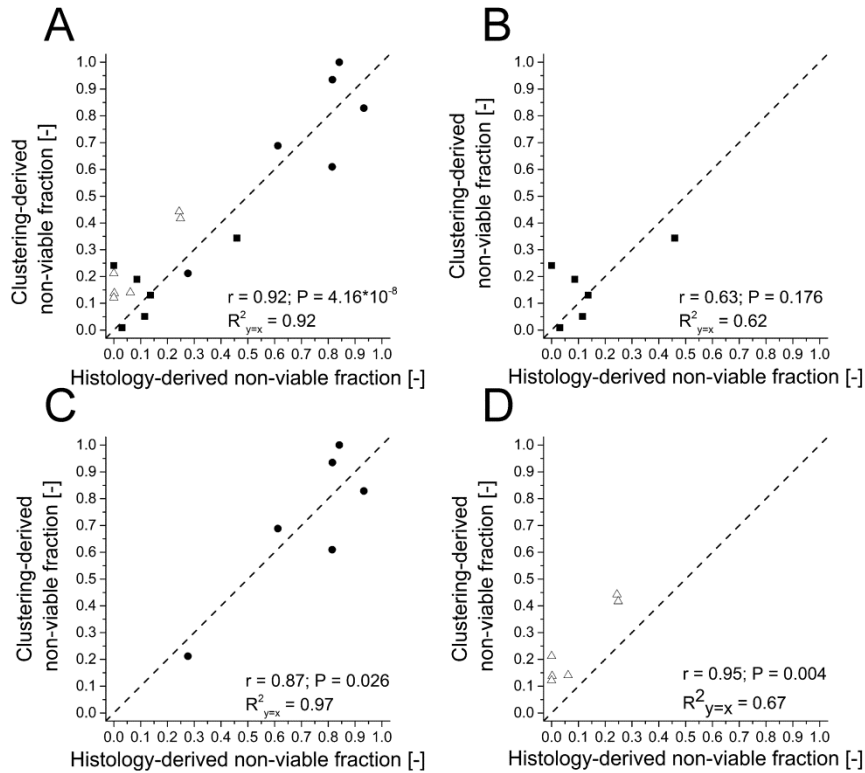


Figure 5. Correlation plots between clustering-derived and histology-derived non-viable tumor fractions resulting from k-means clustering with 4 clusters and feature vector {ADC, APTw signal}, for all data ('Directly after HIFU', '3 days after HIFU' and 'Control') (A) and for the individual experiment time points (B, C and D). The symbols \blacksquare , \bullet and \triangle indicate the experimental groups 'Directly after HIFU', '3 days after HIFU' and 'Control', respectively. The dashed lines represent the line of identity $y=x$. The Pearson's correlation coefficient with corresponding p-value and $R^2_{y=x}$ are listed in each correlation plot.

Correlation between 240EM fractions, non-perfused tumor fractions and histology

In order to compare the performance of the proposed multiparametric analysis with conventionally used HIFU treatment monitoring and evaluation methods, a similar correlation analysis between 240EM fractions, non-perfused fractions, deduced from DCE-MRI, and histology-derived non-viable fractions was performed (Figure 6). A trend ($P=0.070$) toward a strong correlation between the 240EM fraction and the histology-derived non-viable tumor fraction directly after HIFU was observed (Figure 6A). Directly after treatment, no relation was found between the non-perfused and histology-derived non-viable tumor fractions (Figure 6B). The non-perfused tumor fractions were consistently larger than the histology-derived non-viable tumor fractions. At 3 days after HIFU, a strong positive correlation ($r=0.90$) between the non-perfused fraction and histology-derived non-viable fraction was observed, although the non-perfused tumor fraction was consistently lower than the histology-derived non-viable tumor fraction (Figure 6C).

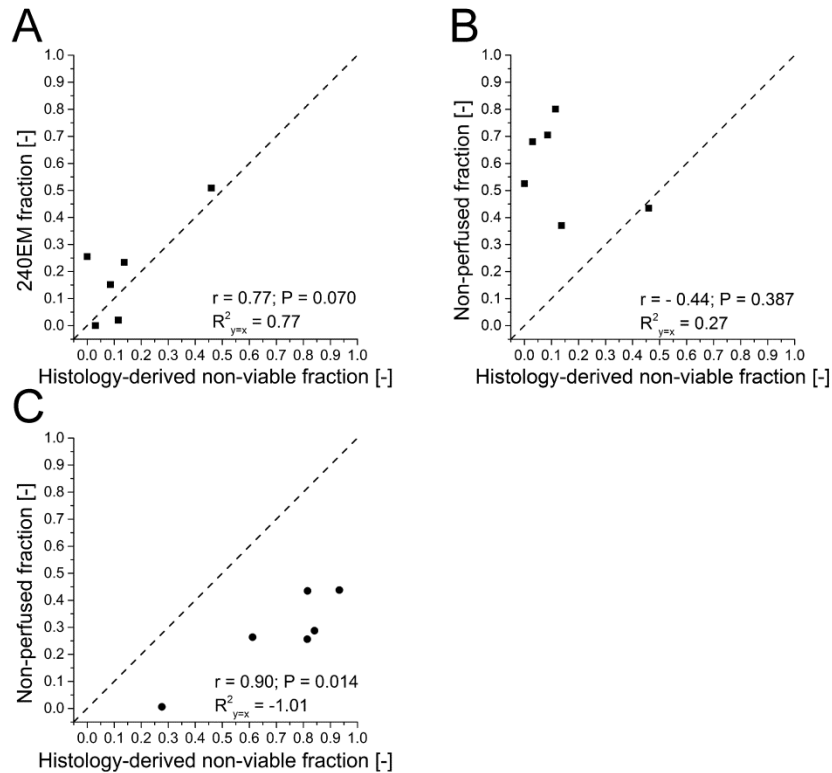


Figure 6. Correlation plots between the 240EM fractions and histology-derived non-viable fractions (A), non-perfused fractions and histology-derived non-viable fractions directly after HIFU (B) and non-perfused fractions and histology-derived non-viable fractions at 3 days after HIFU (C). The symbols ■ and ● represent the experimental groups ‘Directly after HIFU’ (A-B) and ‘3 days after HIFU’ (C), respectively. The dashed line represents the line of identity $y=x$. The Pearson’s correlation coefficient with corresponding p-value and $R^2_{y=x}$ are listed in each correlation plot.

A summary of the results of the correlation analyses between the histology-derived non-viable fractions and the 240EM, non-perfused and clustering-derived non-viable tumor fractions is displayed in Table 4. This table further illustrates that only the clustering-derived non-viable fractions at 3 days after HIFU had a significant correlation and good agreement with the histology-derived non-viable tumor fractions.

Table 4. Overview of the results of the correlation analysis between the histology-derived non-viable fractions and the 240EM, non-perfused and clustering-derived (feature vector {ADC, APTw signal} and 4 clusters) non-viable fractions. S and NS indicate whether there was a significant or non-significant correlation ($P < 0.05$), respectively. The symbols $>$, $<$, \approx and $=$ indicate whether the fractions indicated in the corresponding row heading were generally larger, smaller, almost equal or equal compared to the histology-derived non-viable fractions. - indicates that the correlation analysis was not performed, because it was practically impossible to spatially register the MR data at 3 days after treatment to those directly after treatment (see Discussion).

		Histology-derived non-viable fraction	
		Directly after	3 days after
240 EM fraction		NS, \approx	-
Non-perfused fraction	Directly after	NS, $>$	-
	3 days after	-	S, $<$
Clustering-derived non-viable fraction	Directly after	NS, \approx	-
	3 days after	-	S, $=$

H&E histology

Representative microscopy images of H&E-stained sections of tumors excised directly and at 3 days after HIFU are shown in Figure 7. At both time points, extensive necrosis was observed throughout the tumor tissue. Other major morphological changes observed directly after HIFU treatment were dilated and coagulated blood vessels and the infiltration of immune cells. HIFU-induced tissue damage was more pronouncedly visible at 3 days after treatment. At that time point, extensive inflammation was seen in areas around the central zone of coagulative necrosis. In addition, cell debris and hemorrhages were observed.

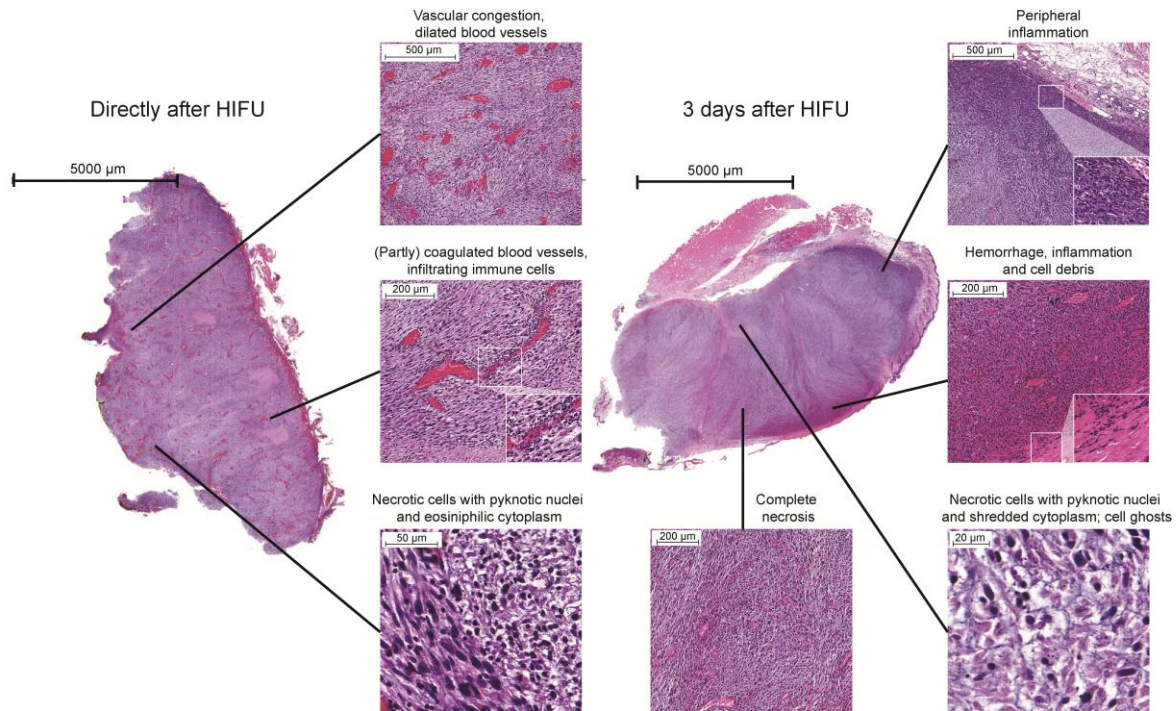


Figure 7. Representative brightfield microscopy images of H&E-stained sections of tumors excised directly (~2 h) and at 3 days after treatment. Regions of specific interest are magnified and shown as separate images. The position of these regions within the tumor section is indicated with the black lines. The inset in the center image of the tumor section obtained directly after HIFU shows a magnification of infiltrating immune cells. The insets in the top-right and center-right image of the tumor section obtained 3 days after HIFU show magnifications of inflammatory cells and cell debris, respectively.

Discussion and conclusions

In the present study, a multiparametric analysis was employed to identify treated (non-viable) and residual non-treated tumor tissue after MR-HIFU treatment. Global analysis of the MRI parameter values in the tumor tissue in the central MRI slice showed that HIFU-induced changes in the MRI parameters were more pronounced at 3 days after HIFU compared to directly after treatment (Table 1). For the individual MR parameters only a subtle, yet significant, change in the average ADC in the tumor was observed directly after HIFU treatment. The detected decrease in ADC may be caused by cytotoxic cell swelling (32,33). In contrast, a strong increase in ADC was observed at 3 days after HIFU treatment. This more pronounced change is likely attributable to necrosis-induced cell shrinkage, increased cell membrane permeability and disruption of diffusion barriers in the necrotic tumor region (9,34). Related to that, the significant decrease in T_1 at 3 days after treatment was probably caused by an increased access of water molecules to paramagnetic sites and an increased macromolecular content in the interstitial space (34). Furthermore, a population of pixels with decreased APT-weighted signal intensity was identified in the APT parameter distribution at 3 days after HIFU (Supplemental Information, Part I). This can be explained by protein aggregation due to thermal stress, which results in a decreased availability of mobile amide protons for exchange with the bulk water (**chapter 4**). In addition, changes in pH, for example due to ischemia, may have contributed to the decrease in APT-weighted signal (**chapter 4**). These above

alterations in tumor morphology, to which the different MRI parameters are sensitive, apparently require time to develop and seem too subtle to allow for detection of endogenous MR contrast changes shortly after the thermal ablation. This was supported by the qualitative assessment of morphological changes after HIFU treatment with H&E staining (Figure 7), which indicated that HIFU-induced tissue damage was more pronounced at 3 days after treatment compared to directly after treatment.

The cluster analysis, in which multiple MRI parameters were combined in a single analysis, also showed the overall highest sensitivity for HIFU-induced cell death at 3 days after treatment. At that time point, a strong correlation and high one-to-one correspondence was observed between histology-derived non-viable tumor fractions and non-viable tumor fractions derived from clustering with 4 clusters and feature vector {ADC, APTw signal}. In the study on multiparametric MRI analysis of HIFU-treated tumor tissue in **chapter 3**, the largest correlation between MRI and histology was also found at 3 days after treatment. In that particular study, { T_1 , T_2 , ADC} was identified as the optimal feature vector for the identification of HIFU-treated, non-viable tumor tissue. In the current study it was hypothesized that addition of the advanced MRI parameters APT-weighted signal and $T_{1\rho}$ to the multiparametric MR analysis would improve its efficacy for early HIFU treatment evaluation, because these advanced MRI methods are expected to be sensitive to early HIFU treatment effects including protein denaturation. However, even with inclusion of these advanced parameters, the overall correlation between clustering and histology was lower directly after MR-HIFU ablation compared to 3 days after treatment. Directly after HIFU treatment, the highest one-to-one correspondence between clustering-derived and histology-derived non-viable fractions was observed for feature vector { T_1 , $T_{1\rho}$ }. At that time point, the $R^2_{y=x}$ value was 0.63 for that particular feature vector, which was substantially lower than the $R^2_{y=x}$ value of the feature vector that was identified as optimal ({ADC, APTw signal}) at 3 days after treatment ($R^2_{y=x}=0.97$; Figure 5C). Nevertheless, the APT-weighted signal appeared to be a valuable addition to the multiparametric analysis. In contrast to our previous study, in which three MRI parameters were needed for the accurate identification of non-viable tumor tissue at 3 days after treatment (**chapter 3**), in the current study the combined ADC and the APT data were sufficient to obtain an excellent agreement between the extent of non-viable tumor tissue identified by clustering and histology.

Importantly, measurement of a single endogenous contrast MRI parameter appeared to be unsuitable for accurate identification of HIFU-treated tumor tissue. No clear demarcation of the HIFU-treated tumor region could be observed in the different MR parameter maps (Figure 1). In addition, the one-to-one correspondence between clustering-derived and histology-derived non-viable tumor fractions was low for all feature vectors consisting of one single MRI parameter (Table 2), which strongly indicates the additional value of multiparametric analysis for the evaluation of HIFU treatment as compared to therapy assessment based on analysis of separate MR images.

Inclusion of the DCE-MRI data to the cluster analysis may increase its sensitivity to early HIFU treatment effects by measuring changes in tumor vascular status. A significant reduction in K^{trans} and v_e was observed in the HIFU-treated tumors compared to control tumors. This decline in the DCE-MRI-derived pharmacokinetic parameters was probably caused by vascular destruction (35,36), which results in a lack of contrast agent inflow in the treated tumor. However, although (D)CE-MRI may be more sensitive to HIFU-induced tissue changes directly after HIFU, the changes in contrast enhancement after HIFU treatment do not necessarily represent cell death. In fact, a poor agreement between non-perfused and histology-derived non-viable tumor fractions was observed both directly and at 3 days after HIFU treatment. Directly after HIFU treatment, the non-perfused fraction was consistently larger than the non-viable fraction. This may be explained by the fact that HIFU-induced vascular destruction could extend beyond the central ablation zone, due to heat stress in regions surrounding this zone. It has been found in multiple studies that the non-perfused volume is generally larger than the estimated treatment volume (37-39) directly after HIFU thermal ablation. While coagulative necrosis is immediately induced in the central zone of ablation due to protein denaturation, cellular and nuclear membrane damage and halted metabolism (40), the vascular destruction in the peripheral zone may not directly result in tumor necrosis. Furthermore, temporary vascular occlusion (41) could have contributed to the relatively high non-perfused tumor fractions directly after HIFU. In contrast to directly after HIFU, at 3 days after treatment the non-perfused tumor fraction was consistently lower than the non-viable tumor fraction, which might be due to contrast agent diffusion into the borders of the non-viable tumor area. A similar underestimation of the extent of non-viable tumor tissue by contrast-enhanced MRI has been reported in a study on HIFU treatment of rabbit tumors (42).

The 240EM thermal dose threshold can also not be regarded suitable for predicting the extent of non-viable tissue after HIFU treatment. The thermal sensitivity varies largely between tissue types and therefore 240EM cannot be regarded as a universal threshold for lethal thermal dose (4,5). In the present study we observed a strong, but non-significant, correlation between histology-derived non-viable fractions and 240EM fractions (Figure 6A). One should however take into account that HIFU-induced necrosis can extend beyond the thermal coagulation zone, because of delayed cell death due to vascular damage. Identification of non-viable tumor tissue after HIFU treatment solely based on the 240EM fraction would therefore likely underestimate the total extent of HIFU-induced cell death. An underestimation of the extent of tumor necrosis by the 240EM fraction was also reported in a pre-clinical study of HIFU-treated rabbit tumors (42).

A limitation of the current study is the lack of spatial registration between the subsequent MRI examinations of the same animal. Repositioning the tumor-bearing paw in exactly the same position as during the first MRI examination was practically impossible, mainly due to tumor progression between the examinations. Hence, quantitative analysis between MRI findings directly and at 3 days after HIFU treatment was mainly restricted to global

analysis of MRI parameter changes across the entire tumor. The effect of HIFU treatment on the MRI parameters is likely underestimated in this global analysis of average tumor parameter values, since both successfully treated and non-treated tumor tissue were included because of the partial tumor treatment. In addition, although best effort was taken to match the cutting plane of histology with the center MRI slice, tissue deformation during histological processing is inevitable and therefore exact spatial registration between MRI and histology remained difficult. Consequently, the correlation analyses were based on tumor fractions rather than on absolute tumor areas. Furthermore, one should take into account that the thickness of the histological sections (5-6 μm) was substantially smaller than the MR slice thickness (2 mm), which can further explain deviations in the appearance of the tumor on MRI and in histology. For clinical application of the proposed multiparametric analysis a reduction of scan time of the multiparametric protocol may be necessary. The total acquisition time of the ADC and APT measurements was approximately 27 minutes. The scan time could possibly be shortened, without affecting accuracy, by decreasing the number of b-values and irradiation offsets in the ADC and APT measurements, respectively. In addition, acceleration techniques such as parallel imaging (43,44) and compressed sensing (45) could be employed.

In summary, we demonstrated that a multiparametric MR analysis, based on ADC and the APT-weighted signal, can accurately determine the extent of non-viable tumor tissue after HIFU treatment. The presented analysis outperformed the conventional methods that are used for monitoring and evaluation of HIFU therapy, *i.e.* thermal dose mapping and CE-MRI, respectively, with respect to the identification of non-viable tissue after treatment. We expect that, after extensive validation in different human tumor types, the proposed method can be incorporated in the current clinical workflow of MR-HIFU therapies.

Acknowledgements

The authors thank professor Paul van Diest (University Medical Center Utrecht) and Nathalia Vykhodtseva (Harvard Medical School) for their assistance with the evaluation of the H&E-stained tumor sections. In addition, Marije Janssen and Caren van Kammen (both from Maastricht University) are acknowledged for their support with the animal experiments. This research was performed within the framework of CTMM, the Center for Translational Molecular Medicine (www.ctmm.nl), project VOLTA (grant 05T-201).

References

1. **Kennedy JE.** *Nat Rev Cancer* 2005;5:321-327.
2. **ter Haar G.** *Prog Biophys Mol Biol* 2007;93:111-129.
3. **de Senneville BD, Mougnot C, Quesson B, Dragonu I, Grenier N, Moonen CT.** *Eur Radiol* 2007;17:2401-2410.
4. **Yarmolenko PS, Moon EJ, Landon C, Manzoor A, Hochman DW, Viglianti BL, Dewhirst MW.** *Int J Hyperthermia* 2011;27:320-343.
5. **Dewhirst MW, Viglianti BL, Lora-Michiels M, Hanson M, Hoopes PJ.** *Int J Hyperthermia* 2003;19:267-294.
6. **Zhou YF.** *World J Clin Oncol* 2011;2:8-27.
7. **Venkatesan AM, Partanen A, Pulanic TK, Dreher MR, Fischer J, Zurawin RK, Muthupillai R, Sokka S, Nieminen HJ, Sinaii N, Merino M, Wood BJ, Stratton P.** *J Vasc Interv Radiol* 2012;23:786-794 e784.
8. **Kim YS, Lim HK, Kim JH, Rhim H, Park BK, Keserci B, Kohler MO, Bae DS, Kim BG, Lee JW, Kim TJ, Sokka S, Lee JH.** *Invest Radiol* 2011;46:639-647.
9. **Zhang Y, Zhao J, Guo D, Zhong W, Ran L.** *Eur J Radiol* 2011;79:347-352.
10. **Rouviere O, Girouin N, Glas L, Ben Cheikh A, Gelet A, Mege-Lechevallier F, Rabilloud M, Chapelon JY, Lyonnet D.** *Eur Radiol* 2010;20:48-55.
11. **Kirkham AP, Emberton M, Hoh IM, Illing RO, Freeman AA, Allen C.** *Radiology* 2008;246:833-844.
12. **Sung HY, Jung SE, Cho SH, Zhou K, Han JY, Han ST, Kim JI, Kim JK, Choi JY, Yoon SK, Yang JM, Han CW, Lee YS.** *Pancreas* 2011;40:1080-1086.
13. **Zhou J, Lal B, Wilson DA, Laterra J, van Zijl PC.** *Magn Reson Med* 2003;50:1120-1126.
14. **Salhotra A, Lal B, Laterra J, Sun PZ, van Zijl PC, Zhou J.** *NMR Biomed* 2008;21:489-497.
15. **Jones CK, Schlosser MJ, van Zijl PC, Pomper MG, Golay X, Zhou J.** *Magn Reson Med* 2006;56:585-592.
16. **Zhou J, Blakeley JO, Hua J, Kim M, Laterra J, Pomper MG, van Zijl PC.** *Magn Reson Med* 2008;60:842-849.
17. **Dula AN, Arlinghaus LR, Dortch RD, Dewey BE, Whisenant JG, Ayers GD, Yankeelov TE, Smith SA.** *Magn Reson Med* 2013;70:216-224.
18. **Jia G, Abaza R, Williams JD, Zynger DL, Zhou J, Shah ZK, Patel M, Sammet S, Wei L, Bahnson RR, Knopp MV.** *J Magn Reson Imaging* 2011;33:647-654.
19. **Zhou J, Tryggestad E, Wen Z, Lal B, Zhou T, Grossman R, Wang S, Yan K, Fu D, Ford E, Tyler B, Blakeley JO, Laterra J, Van Zijl P.** *Nat Med* 2011;17:130-134.
20. **Hijnen NM, Heijman E, Kohler MO, Ylihautala M, Ehnholm GJ, Simonetti AW, Grull H.** *Int J Hyperthermia* 2012;28:141-155.
21. **Kohler MO, Mougnot C, Quesson B, Enholm J, Le Bail B, Laurent C, Moonen CT, Ehnholm GJ.** *Med Phys* 2009;36:3521-3535.
22. **Köhler MO, Enholm J, Mougnot C, Andreae T.** 2011; Available at: http://www.healthcare.philips.com/pwc_hc/ru_ru/about/Events/RSNA/pdfs/MR_Sonalleve_HIFU_whit_epaper.pdf. Accessed August 29, 2014.
23. **Hijnen NM, Elevelt A, Grull H.** *Invest Radiol* 2013;48:517-524.
24. **Witschey II WR, Borthakur A, Elliott MA, Mellon E, Niyogi S, Wallman DJ, Wang C, Reddy R.** *J Magn Reson* 2007;186:75-85.
25. **Karlsson M, Nordell B.** *Magn Reson Imaging* 1999;17:1481-1488.
26. **Deoni SC, Rutt BK, Peters TM.** *Magn Reson Med* 2003;49:515-526.
27. **Tofts PS, Brix G, Buckley DL, Evelhoch JL, Henderson E, Knopp MV, Larsson HB, Lee TY, Mayr NA, Parker GJ, Port RE, Taylor J, Weisskoff RM.** *J Magn Reson Imaging* 1999;10:223-232.
28. **McGrath DM, Bradley DP, Tessier JL, Lacey T, Taylor CJ, Parker GJ.** *Magn Reson Med* 2009;61:1173-1184.
29. **CharlesRiverLaboratories.** 2012; Available at: http://www.criver.com/files/pdfs/rms/fischer-cdf/rm_rm_r_cdf_fisher_rat_clinical_pathology_data.aspx. Accessed September 1, 2014.
30. **Sapareto SA, Dewey WC.** *Int J Radiat Oncol Biol Phys* 1984;10:787-800.
31. **Omran MGH, Engelbrecht AP, Salman A.** *Intelligent Data Analysis* 2007;11:583-605.
32. **Jacobs MA, Ouwerkerk R, Kamel I, Bottomley PA, Bluemke DA, Kim HS.** *J Magn Reson Imaging* 2009;29:649-656.
33. **Jacobs MA, Gultekin DH, Kim HS.** *Med Phys* 2010;37:4768-4776.
34. **Graham SJ, Stanisiz GJ, Kecojevic A, Bronskill MJ, Henkelman RM.** *Magn Reson Med* 1999;42:1061-1071.
35. **Wu F, Chen WZ, Bai J, Zou JZ, Wang ZL, Zhu H, Wang ZB.** *Ultrasound Med Biol* 2002;28:535-542.
36. **Cheng HL, Purcell CM, Bilbao JM, Plewes DB.** *J Magn Reson Imaging* 2003;18:585-598.
37. **Pilatou MC, Stewart EA, Maier SE, Fennessy FM, Hynynen K, Tempny CM, McDannold N.** *J Magn Reson Imaging* 2009;29:404-411.
38. **Tempny CM, Stewart EA, McDannold N, Quade BJ, Jolesz FA, Hynynen K.** *Radiology* 2003;226:897-905.

39. **McDannold N, Tempny CM, Fennessy FM, So MJ, Rybicki FJ, Stewart EA, Jolesz FA, Hynynen K.** Radiology 2006;240:263-272.
40. **Chu KF, Dupuy DE.** Nat Rev Cancer 2014;14:199-208.
41. **Hynynen K, Chung AH, Colucci V, Jolesz FA.** Ultrasound Med Biol 1996;22:193-201.
42. **Wijlemans JW, Deckers R, van den Bosch MA, Seinstra BA, van Stralen M, van Diest PJ, Moonen CT, Bartels LW.** Invest Radiol 2013;48:381-386.
43. **Pruessmann KP, Weiger M, Scheidegger MB, Boesiger P.** Magn Reson Med 1999;42:952-962.
44. **Griswold MA, Jakob PM, Heidemann RM, Nittka M, Jellus V, Wang J, Kiefer B, Haase A.** Magn Reson Med 2002;47:1202-1210.
45. **Geethanath S, Reddy R, Konar AS, Imam S, Sundaresan R, D RR, Venkatesan R.** Crit Rev Biomed Eng 2013;41:183-204.

Supplemental Information

Part I - Tumor MR parameter distributions

Histograms of MR parameter values in all tumor pixels in the center slice at the different experimental time points are displayed in Figure S1. A significant increase in the fraction of pixels with T_1 values between 1250 and 1450 ms was observed at 3 days after HIFU (Figure S1A). In the distribution of T_2 , a slight but significant shift towards lower T_2 values was visible both directly and at 3 days after HIFU (Figure S1B). The distributions of the ADC values (Figure S1C) show that the fraction of pixels with a low ADC (between $0.65 \cdot 10^{-3}$ and $0.75 \cdot 10^{-3}$ mm²/s) was significantly higher directly after HIFU compared to before HIFU. In contrast, at 3 days after HIFU, a pronounced shift towards high ADC (larger than $1.4 \cdot 10^{-3}$ mm²/s) values was observed. In the APT-weighted signal histograms (Figure S1D) a population of pixels with APT-weighted signal between -2.25 and 0.25 % emerged at 3 days after HIFU, although these changes were not significant. The $T_{1\rho}$ distribution (Figure S1E) was not evidently altered at either of the time points after HIFU treatment compared to before HIFU, except for a minor decrease in fraction of pixels with a relatively low $T_{1\rho}$ value (45-75 ms).

In the distributions of the pharmacokinetic parameters K^{trans} (Figure S1F) and v_e (Figure S1G), the data from the control rats at the same experimental time points are shown as a reference since no DCE-MRI was performed before HIFU in the treatment groups. The fraction of pixels with a K^{trans} close to zero (0.0 - 0.0075 min⁻¹) was significantly higher directly after HIFU than for the control rats. At 3 days after HIFU, the fraction of pixels with low K^{trans} values (0.0 - 0.0225 min⁻¹) was still significantly higher than for the control rats. For the control rats, a significantly higher fraction of pixels with intermediate K^{trans} values between 0.01125 - 0.1425 min⁻¹ was observed at day 0 compared to day 3. In the distribution of v_e , the fraction of pixels with a low v_e , mainly between 0.0 - 0.045 , was significantly higher for the HIFU-treated rats than for the control rats, at both experimental time points.

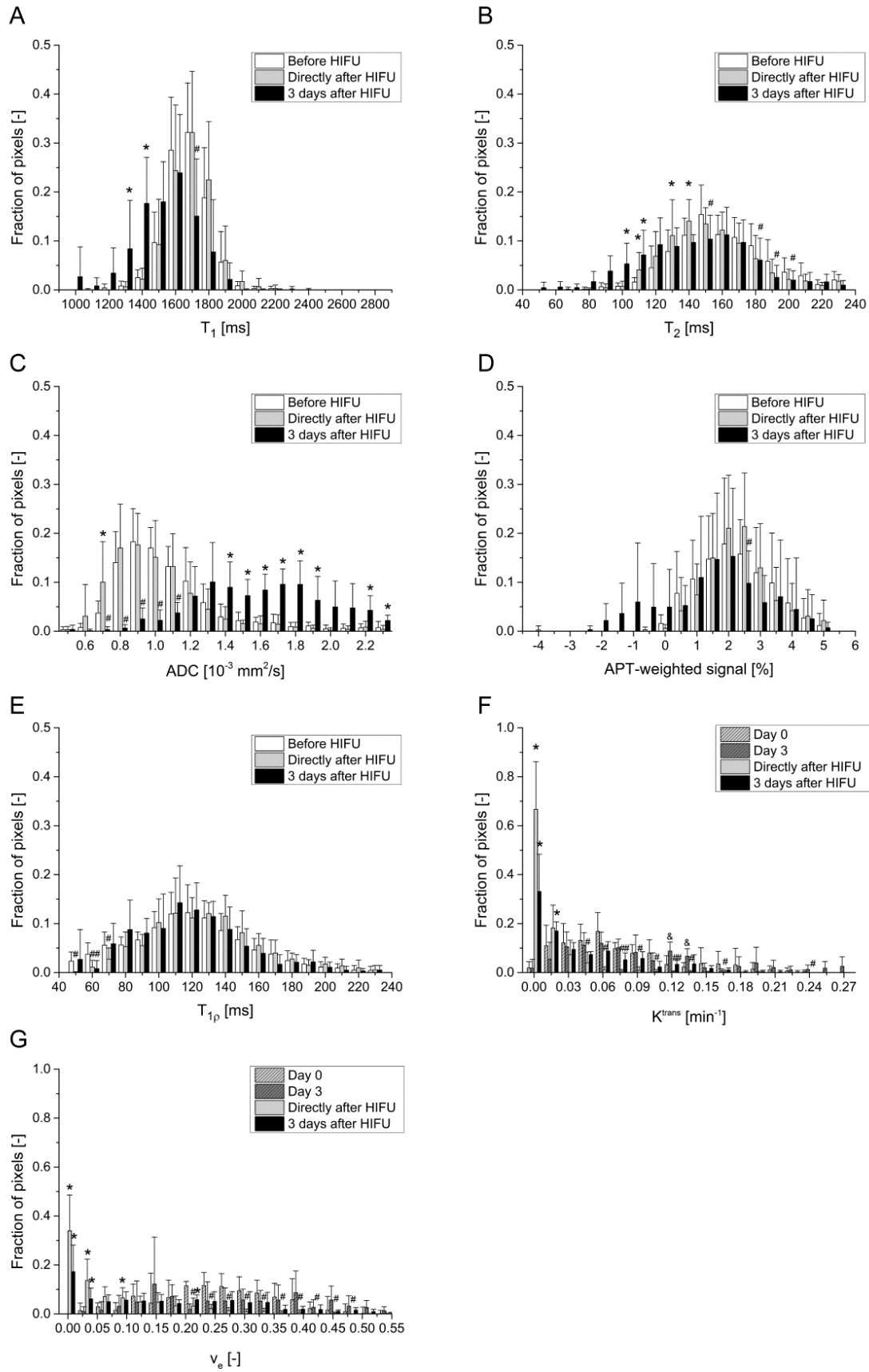


Figure S1. Average MR parameter distributions in the central tumor slice for the HIFU-treated animals at the different time experimental points ('Before HIFU', 'Directly after HIFU', '3 days after HIFU'). Since DCE-MRI was not performed before HIFU, in the histograms of K^{trans} and v_e the mean parameter values of the control

animals at the corresponding measurement days (day 0 and day 3) are shown. The error bars represent the standard deviation. For all endogenous MR parameters (T_1 , T_2 , ADC, APT-weighted signal, $T_{1\rho}$) * and # denote a significant increase and decrease in the fraction of pixels after HIFU compared to before HIFU, respectively (two-sided paired Student's t-test, $P < 0.05$). For the DCE-MRI parameters (K^{trans} and v_e), * and # denote a significantly higher or lower fraction of pixels after HIFU compared to the control animals, respectively (two-sided paired Student's t-test, $P < 0.05$). & denotes a significant difference in fraction of pixels at day 3 compared to day 0 for the control animals.

Part II - Relation between temperature, thermal dose and MR parameter changes

In addition to evaluation of MR parameter changes in the entire center tumor slice, the relation between HIFU-induced temperature elevation and changes in MR parameter values directly after treatment was more closely investigated. For all endogenous MR parameters, the average MR parameter values within the 240EM area (*i.e.*, the area in which the thermal dose is generally considered as lethal to cells), directly after HIFU and in the same tumor area before HIFU are shown in Table S1. In this area, only the T_2 was significantly changed directly after HIFU compared to before HIFU.

For the pharmacokinetic parameters, the average K^{trans} and v_e in a population of pixels are plotted versus the maximum temperature that was reached in these pixels in Figure S2. All tumor pixels in the center slice, regardless of the reached thermal dose, were included in this analysis. A slight increase in K^{trans} values could be observed at temperatures around 41-42°C. Thereafter, the K^{trans} generally seemed to decrease with increasing temperature (Figure S2A). A gradual reduction in v_e values for increasing temperatures was observed (Figure S2B). A similar analysis of maximum temperature vs. parameter value was performed for the endogenous MR contrast parameters. However, no correlation between any of the endogenous MRI contrast parameters and maximum temperature was identified directly after HIFU (data not shown).

Table S1. MR parameter values (mean±SD) in the 240EM thermal dose area directly after HIFU and in the same tumor area before HIFU. The p-values result from a two-sided paired Student's t-test between the 'Directly after HIFU' and 'Before HIFU' data. K^{trans} and v_e are not shown, since DCE-MRI was only performed after HIFU. The p-values are highlighted bold if there was a significant difference in the MR parameter values between before and directly after HIFU ($P < 0.05$).

Parameter	Before HIFU	Directly after HIFU
T_1 [ms]	1679±56	1656±46 (P=0.119)
T_2 [ms]	161±13	149±15 (P=0.002)
ADC [10^{-3} mm ² /s]	1.01±0.10	1.00±0.18 (P=0.901)
APT-weighted signal [%]	2.45±1.04	2.81±1.25 (P=0.474)
$T_{1\rho}$ [ms]	121±21	121±22 (P=0.954)

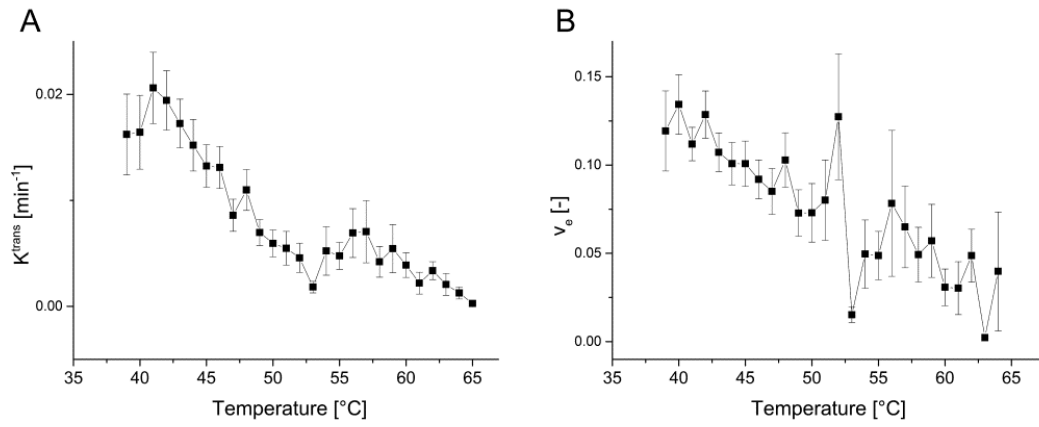


Figure S2. Plot of the relation between pharmacokinetic parameter values (mean±standard error) and ablation temperature. The graph was assembled by determination of the population of pixels in which a certain maximal temperature had been reached and estimation of the mean K^{trans} and v_e values in this population of pixels directly after HIFU.

Chapter 8

General discussion and future directions

Thermal ablation using HIFU is an upcoming method for tumor treatment. To date, the main clinical application of focused ultrasound therapy is the thermal ablation of uterine fibroids. For these benign lesions partial HIFU treatment is generally sufficient to achieve substantial symptom relief. However, the extension of HIFU for the thermal therapy of malignant lesions does require that the treatment covers the entire tumor, while the surrounding tissue is minimally affected. The development of MR-guided HIFU systems can be considered as an important step toward clinical introduction of HIFU treatment of malignant lesions. Apart from treatment monitoring based on MR thermometry, MRI can also be used for accurate tumor localization before the HIFU intervention as well as for early treatment evaluation and long-term follow-up. The aim of this thesis was to develop suitable MRI methods for accurate HIFU treatment planning and evaluation. It was shown in a preclinical research setting that the extent of non-viable tumor tissue at 3 days after HIFU treatment can be accurately determined with a multiparametric MRI analysis that combines the data of different MRI contrast mechanisms (**chapter 3, 7**). Application of this multiparametric MRI analysis for the evaluation of HIFU treatment could substantially improve the accuracy of the detection of residual tumor tissue compared to conventional approaches in which a single MRI method, such as contrast-enhanced T_1 -weighted imaging, is employed.

Low-field vs. high-field MRI

In the majority of the studies in this thesis, the HIFU treatment evaluation was done on a high-field (6.3 or 7 T) preclinical MR scanner (**chapter 3, 4, 5 and 6**). The HIFU treatment was performed outside the MR system since integration of the preclinical transducer in the MRI scanner was not (yet) possible. Nevertheless, incorporation of HIFU systems in high-field MRI scanners could be preferable compared to conventional clinical MR scanners that operate at 1.5 or 3.0 T. Because the signal-to-noise ratio linearly increases with field strength, generally a higher spatial resolution can be achieved with high-field MRI systems. This higher spatial resolution could allow for more accurate treatment planning and evaluation. However, one also has to take into account that many MRI parameters are field-dependent (e.g. T_1 becomes higher with increasing field strength, while T_2 and $T_{1\rho}$ decrease at higher field strengths). The contrast between tumor tissue and surrounding non-tumor tissue as well as between successfully treated and residual tumor tissue could thus be affected by a difference in field strength. In addition, since magnetic susceptibility effects scale with MR field strength, the implementation of accurate MR thermometry based on the generally used Proton Resonance Frequency Shift method is challenging at high-field, because this method is very sensitive to field fluctuations. Reports on MR thermometry at high-field are very limited, although recently a promising technique for accurate MR thermometry at 7 T was described, in which the temperature-sensitive water phase images were corrected for field fluctuations using images that were acquired alternately in a reference substance, such as fat (1). In the study in **chapter 7** the HIFU treatment was performed within the 3 T MR scanner. The results show that the proposed multiparametric MR protocol is strongly sensitive to HIFU-induced cell death,

despite the lower field strength. However, the spatial resolution in this 3 T study was lower ($0.94 \times 0.94 \times 2 \text{ mm}^3$) compared to the high-field studies ($0.31 \times 0.31 \times 1 \text{ mm}^3$), which implies that the MRI protocol at low field is less suitable for the detection of small regions of residual tumor tissue.

Detection of residual tumor cells

Regardless of the field strength, the sensitivity of MRI is not high enough to allow for detection of small numbers of residual tumor cells after HIFU treatment. It is of high importance that the presence of these residual tumor cells after HIFU treatment can be detected or – even better – prevented. Even a small number of residual tumor cells could lead to substantial tumor progression, especially if these tumor cells are hypoxic due to HIFU-induced vascular damage. Under hypoxic circumstances the hypoxia inducible factors HIF-1 α and HIF-2 α could be activated. This activation may lead to an increased expression of vascular endothelial growth factor (VEGF) (2,3), which is a key stimulator of angiogenesis. The newly formed blood vessels provide nutrients and oxygen to the residual tumor cells, which may lead to tumor progression. Importantly, the tumor cells could also migrate through the neovasculature and enter the circulatory system, which could induce the development of metastases.

However, the growth of residual tumor tissue, even it is far away from the ablated region, could also be inhibited by a systemic anti-tumor immune response that is triggered by the HIFU treatment. In the last few decades both preclinical and clinical studies, that were recently listed in a comprehensive review (4), have been performed, that show evidence for this anti-tumor immune response after the HIFU intervention. The mechanism of this immune response is not well understood yet, but there are a few plausible hypotheses based on the published results (4). First, it could be that the HIFU treatment lessens host immune suppression induced by the tumor cells, which would consequently lead to increased host antitumor immunity. Secondly, HIFU treatment leads to increased levels of heat-shock proteins, which can act as a sort of vaccines to produce a host immune response. Thirdly, the cytokines that are secreted by the immune cells inside the zone of inflammation around the central ablated region may induce the development of mature cytotoxic T lymphocytes. Finally, the extensive cellular debris that is present in the coagulative tissue will lead to the recruitment of macrophages and other cells that can function as antigen presenting cells, which can further boost the antitumor response. Regarding the different mechanisms that are activated after HIFU that can either induce rapid tumor progression or a halt in tumor growth, there is obviously a considerable risk associated with the presence of residual viable tumor cells after treatment. This risk could be reduced, yet not fully eliminated, by treatment of a safety margin around the tumor (5). This safety margin allows for treatment of occult cancer cells that could be present around the primary tumor (6). The possible presence of these occult, MRI-invisible cells should also be taken into account in MR methods for treatment planning, such as described in **chapter 2**. To further increase the therapy efficacy, the HIFU treatment may also be combined with e.g. adjuvant chemotherapy with anti-angiogenic agents to prevent tumor

progression induced by the presence of residual unaffected tumor cells. In addition, HIFU treatment could be combined with immune therapy to further boost the HIFU-induced antitumor immunity (4).

Although the application of a safety margin during HIFU treatment and the adjuvant administration of chemo- or immunotherapeutics seem promising ways to tackle the issues associated with potential presence of residual tumor cells, it would nevertheless be preferable if these tumor cells could be detected in some way to prevent over- or undertreatment. While they are invisible with conventional MRI methods, these residual tumor cells could potentially be detected by molecular MR imaging with tumor-specific probes. However, the detection of targeted MRI probes is often hampered by the relatively low sensitivity of MRI for the detection of contrast agents. This sensitivity issue may be overcome by using targeted nanoparticles that can carry a large payload of contrast-generating materials, such as Gd-chelates and iron oxides. Nevertheless, because of its inherent higher sensitivity, the nuclear imaging technique positron emission tomography (PET) may be favorable for the detection of low numbers of residual tumor cells with tumor-targeted probes (7). PET has been used for the detection of local recurrences after HIFU therapy of solid tumors (8,9). In these studies, the PET tracer ^{18}F -2-fluoro-2-deoxy-D-glucose (^{18}F -FDG) was used, which is a marker for metabolism and thus cell viability. ^{18}F -FDG PET can be regarded as a suitable method to assess the extent of cell death after HIFU treatment. However, it is less specific to detect the presence of residual tumor cells, because ^{18}F -FDG also accumulates in other highly metabolizing tissue regions after treatment, such as areas of inflammation and edema. The use of ^{18}F -fluorothymidine (^{18}F -FLT), which is a PET tracer sensitive to cell proliferation, may be more suitable for the detection of residual tumor cells, since it is known to be more tumor-specific. Despite the apparent superb sensitivity of PET imaging for the detection of residual tumor tissue, it also has distinct disadvantages. PET has a much lower spatial resolution compared to MRI and does not offer anatomical information. Though expensive, the use of a hybrid MR-PET system may allow for complete HIFU treatment assessment by combining the proposed multiparametric MRI approach for determination of the extent of non-viable tumor tissue with ^{18}F -FLT-PET for the detection of residual individual tumor cells.

Multiparametric MRI

Next to the extensive set of MRI biomarkers that was explored in this thesis, there are still a number of other contrast mechanisms that may be suitable for HIFU treatment assessment. Especially contrast mechanisms that are expected to be strongly sensitive to acute treatment effects may increase the sensitivity of the multiparametric MRI analysis to early changes after treatment. Examples of these contrast mechanisms are ^{23}Na MRI and hyperpolarized ^{13}C MR (**chapter 1**). Inclusion of these non-proton MR methods in the multiparametric protocol would require MR hardware set-ups that allow for the use of multinuclear coil designs. Coil setups that allow for combined ^1H and ^{23}Na (10) or ^{13}C (11) acquisitions within the same experiment without the need for moving the RF coil or subject have been described previously.

A potential drawback of the use of a multiparametric MRI protocol is that it usually leads to long acquisition times, which are generally unacceptable in clinical practice. However, the acquisition times of the individual MRI scans could be substantially reduced by the use of acceleration techniques such as compressing sensing (12) and parallel imaging (13,14). In addition, integration of the multiparametric protocol into a magnetic resonance fingerprinting (MRF) acquisition could considerably shorten the acquisition time. MRF is a recently introduced MR method that uses a pseudorandom acquisition by dynamic alteration of several MR acquisition parameters (15). The resulting signal evolutions – or ‘fingerprints’ – obtained in the imaging pixels are unique for each tissue type and a function of multiple MR contrast parameters. The fingerprints are subsequently matched to a predefined dictionary of predicted signal evolutions, which allows for the construction of quantitative maps of the MRI parameters of interest. Up to now only an MRF method that allows for quantification of T_1 , T_2 and proton density has been reported (15). However, the MRF acquisition can be readily adapted to include quantitative assessment of other parameters, such as ADC, MTR and the APT-weighted signal.

Delayed treatment effects

In the studies presented in this thesis, the subcutaneous rodent tumors were intentionally only treated partially by HIFU. This was primarily done to allow for internal reference between successfully treated and non-treated tumor tissue. However, as indicated above, the residual non-treated tumor tissue cannot be considered truly unaffected. Apart from the above-mentioned hypoxia-induced angiogenesis and systemic antitumor immune response, the hyperthermic and possibly ischemic conditions in the residual tumor tissue could also lead to other delayed treatment effects, such as cell death (**chapter 1**). These delayed treatment effects should be taken into account if the success of the HIFU treatment is assessed directly after the intervention to prevent over- or undertreatment. It would be interesting to investigate whether the MRI data obtained directly after HIFU treatment are of predictive value for the fate of the tumor tissue at 3 days – or later – after HIFU treatment. Especially the APT-weighted signal seems to be a promising biomarker for the prediction of delayed treatment effects, since it is not only sensitive to protein denaturation, but also to ischemia (**chapter 1, 4**). However, in the current setting, it was not feasible to assess the predictive value of the MRI results directly after treatment, because the data obtained directly after and at 3 days after HIFU could not be spatially registered due to considerable tumor growth between these time points. Such analysis would be better feasible if applied in more slowly growing tumors or if the tumor would be treated completely. Complete ablation of the small subcutaneous tumors (~1 cm diameter) seems practically impossible, because it would induce considerable damage to the surrounding muscle tissue, leading to massive inflammation and edema. Therefore, future studies on multiparametric MR analysis for the evaluation of HIFU treatment should preferably be performed in larger preclinical tumor models, such as the VX2 tumor in rabbits, or in the clinical setting. Apart from analysis of the predictive value of MRI data obtained early after HIFU treatment, the results of the multiparametric MRI analysis could

then also be quantitatively compared with ultimate treatment outcome. Because of the substantial tumor progression after HIFU treatment, such long-term studies could not be performed in the present setting.

Clinical translation

The use of subcutaneous small rodent tumor models obviously has limitations. Apart from the impossibility to treat the entire tumor, it is challenging to translate the results obtained in the subcutaneous rodent tumors to clinically relevant human tumors. The tumor microenvironment and surrounding tissue are generally very different in these preclinical tumors compared to human tumors. In addition, the tumor to body weight ratio of preclinical ectopic tumor models is generally much larger than in human tumors, which means that systemic responses to treatment may be relatively larger in the laboratory animals compared to patients. The use of orthotopic tumor models, such as animals models of liver or breast cancer, would have been more clinically relevant. However, accurate HIFU treatment of the relatively small orthotopic rodent tumor models is considerably more challenging, if not impossible, with the used HIFU set-ups, because of the effects of respiratory and cardiac motion and the presence of bones or vital organs in the vicinity of the tumor. Despite the shortcomings of subcutaneous tumor models, the results presented here clearly give first insights in the MR contrast mechanisms that are promising for the evaluation of (pre)clinical HIFU treatment. The techniques can be readily translated to clinical studies to investigate whether the multiparametric MR analysis is also suitable for the evaluation of HIFU treatment of human tumors. An important step toward clinical translation of the proposed methodology for the evaluation of HIFU treatment was taken in **chapter 7**, in which the multiparametric MRI protocol was implemented on the 3T clinical MR-HIFU system.

Conclusion

In conclusion, the sensitivity of multiple MRI methods to the responses to HIFU treatment was assessed in this thesis. Several MR contrast parameters, mainly the ADC and APT-weighted signal, seem promising with respect to their sensitivity to HIFU-induced tissue changes, especially if these contrast parameters are combined within a multiparametric MR analysis. As a next step, these MRI methods should be applied to a larger variety of tumor types to fully assess their suitability for the accurate identification of non-viable tissue after HIFU treatment.

References

1. **Streicher MN, Schafer A, Ivanov D, Muller DK, Amadon A, Reimer E, Huber L, Dhital B, Rivera D, Kogler C, Trampel R, Pampel A, Turner R.** *Magn Reson Med* 2013;doi:10.1002/mrm.24681.
2. **Wu L, Fu Z, Zhou S, Gong J, Liu CA, Qiao Z, Li S.** *PLoS One* 2014;9:e88913.
3. **Moon EJ, Sonveaux P, Porporato PE, Danhier P, Gallez B, Batinic-Haberle I, Nien YC, Schroeder T, Dewhirst MW.** *Proc Natl Acad Sci U S A* 2010;107:20477-20482.
4. **Wu F.** *J Acoust Soc Am* 2013;134:1695-1701.
5. **Schmitz AC, van den Bosch MA, Loo CE, Mali WP, Bartelink H, Gertenbach M, Holland R, Peterse JL, Rutgers EJ, Gilhuijs KG.** *Radiother Oncol* 2010;97:225-232.
6. **Mendez Romero A, Verheij J, Dwarkasing RS, Seppenwoolde Y, Redekop WK, Zondervan PE, Nowak PJ, Ijzermans JN, Levendag PC, Heijmen BJ, Verhoef C.** *Int J Radiat Oncol Biol Phys* 2012;82:159-166.
7. **Kircher MF, Willmann JK.** *Radiology* 2012;263:633-643.
8. **Orsi F, Zhang L, Arnone P, Orgera G, Bonomo G, Vigna PD, Monfardini L, Zhou K, Chen W, Wang Z, Veronesi U.** *AJR Am J Roentgenol* 2010;195:W245-252.
9. **Xiong LL, Hwang JH, Huang XB, Yao SS, He CJ, Ge XH, Ge HY, Wang XF.** *JOP* 2009;10:123-129.
10. **Augath M, Heiler P, Kirsch S, Schad LR.** *J Magn Reson* 2009;200:134-136.
11. **Lim H, Thind K, Martinez-Santesteban FM, Scholl TJ.** *J Magn Reson Imaging* 2014;doi:10.1002/jmri.24458.
12. **Geethanath S, Reddy R, Konar AS, Imam S, Sundaresan R, D RR, Venkatesan R.** *Crit Rev Biomed Eng* 2013;41:183-204.
13. **Griswold MA, Jakob PM, Heidemann RM, Nittka M, Jellus V, Wang J, Kiefer B, Haase A.** *Magn Reson Med* 2002;47:1202-1210.
14. **Pruessmann KP, Weiger M, Scheidegger MB, Boesiger P.** *Magn Reson Med* 1999;42:952-962.
15. **Ma D, Gulani V, Seiberlich N, Liu K, Sunshine JL, Duerk JL, Griswold MA.** *Nature* 2013;495:187-192.

Summary

Glossary of abbreviations

List of publications

Acknowledgements

Curriculum Vitae

MRI methods for the planning and evaluation of High Intensity Focused Ultrasound tumor treatment

Summary

High Intensity Focused Ultrasound (HIFU) is an emerging technique for the non-invasive thermal treatment of solid tumors. For HIFU treatment of malignant tumors it is of key importance that the therapy covers the entire tumor volume and that the success of the treatment can be accurately assessed. Thanks to the development of magnetic resonance imaging (MRI)-guided HIFU systems, MRI can be used for planning, monitoring and evaluation of HIFU treatment. The aim of this thesis was to develop suitable MRI methods for accurate HIFU treatment planning and evaluation.

MRI protocols for treatment planning should allow for accurate distinction between tumor and surrounding tissue. These protocols preferably consist of non-contrast-enhanced MRI methods, because the presence of contrast agent in the tumor tissue could interfere with the treatment. In addition, automatic tumor segmentation is preferred compared to manual segmentation, since it is more objective and time-effective. **Chapter 2** describes a fully automatic segmentation algorithm that is based on clustering of endogenous contrast MRI data, consisting of quantitative T_1 , T_2 and apparent diffusion coefficient (ADC) maps. The cluster analysis was performed with all possible combinations of the MRI parameters, i.e. feature vectors, and varying numbers of clusters. A strong linear agreement between automatically and manually segmented mouse subcutaneous tumor volumes was observed when clustering was performed with feature vector $\{T_2, \text{ADC}\}$ and 4 clusters. This indicated that accurate automatic tumor segmentation can be achieved based on endogenous MR contrast.

The major part of the thesis consisted of the identification of MRI biomarkers that are suitable for accurate evaluation of the HIFU treatment. In most studies (**chapter 3, 4, 5 and 6**), HIFU treatment of mouse subcutaneous tumors was performed outside the 6.3 or 7 Tesla MR system with a preclinical therapeutic ultrasound transducer. The mouse tumors were treated partially to allow for internal reference between HIFU-treated and non-treated tumor tissue.

A multiparametric MR analysis was performed on T_1 , T_2 , ADC and magnetization transfer ratio (MTR) data acquired before, directly after and 3 days after treatment (**chapter 3**). Cluster analysis was done on all possible feature vectors to determine the optimal biomarkers for HIFU treatment evaluation. Non-viable tumor fractions derived from NADH-diaphorase histology and non-viable tumor fractions derived from the clustering with different feature vectors were quantitatively compared to define the optimal feature vector for the identification of HIFU-treated tumor tissue. The highest correlation was found for feature vector $\{T_1, T_2, \text{ADC}\}$ (correlation $r=0.80$) at 3 days after HIFU treatment, while this

correlation was less directly after treatment ($r=0.62$). These results indicate that the proposed multiparametric MR analysis is a promising method for the assessment of subacute effects of the HIFU treatment.

In subsequent studies, the more advanced MR methods Amide proton transfer (APT) (**chapter 4**) and $T_{1\rho}$ imaging (**chapter 5**) were assessed for their sensitivity to the identification of HIFU-treated tumor tissue. Both methods have a potential sensitivity to acute HIFU-induced tissue changes, such as protein denaturation. A significant decrease in the APT-weighted signal was observed both directly and at 3 days after HIFU treatment, while the $T_{1\rho}$ was only significantly decreased at 3 days after treatment. These results show that these methods could be of additional value for the multiparametric MRI analysis and that especially the APT-weighted signal may enhance the sensitivity of this analysis to early treatment effects.

To assess changes in the tumor vascular status after HIFU treatment, quantitative dynamic contrast-enhanced-MRI (DCE-MRI) was performed to extract the vascular parameters K^{trans} and v_e (**chapter 6**). Subsequently, cluster analysis on these parameters was done to identify regions of different vascular characteristics. Both directly and at 3 days after treatment a distinct non-perfused tumor volume was identified that was mainly surrounded by pixels in clusters that were characterized by a low K^{trans} and either a low or high v_e . Qualitative haematoxylin and eosin (H&E) staining showed that these clusters corresponded to HIFU-induced hemorrhage and structural disruption of the tumor tissue.

In a final study, all MRI parameters were combined in a single multiparametric MRI protocol to define an optimal subset of MRI parameters for the assessment of HIFU treatment (**chapter 7**). To advance clinical translation of the proposed multiparametric MRI analysis, the HIFU thermal ablation as well as the MRI-based treatment evaluation were performed on a clinical 3 Tesla MR-guided HIFU system. An extensive analysis on the changes in the different MRI parameters was performed. In addition, cluster analysis was carried out with all possible combinations of the MRI parameters. Similarly to the previous multiparametric MRI study, the clustering results were compared to quantitative histology to determine the optimal MRI biomarkers for HIFU treatment evaluation. The largest correlation between histology-derived and clustering-derived non-viable tumor fractions was achieved with feature vector {ADC, APT-weighted signal} ($r=0.87$) at 3 days after HIFU treatment. These results suggest that the inclusion of APT imaging and $T_{1\rho}$ does not enhance the sensitivity of the multiparametric analysis to acute lethal tissue changes after HIFU treatment. Nevertheless, the APT-weighted signal proved to be an additional suitable biomarker for later treatment evaluation.

In summary, this thesis describes multiple MRI methods for the assessment of the success of the HIFU treatment as well as a technique for automatic MRI-based tumor segmentation that is potentially suitable for HIFU treatment planning. Ultimately, the proposed methods could be adapted for clinical translation and thereby potentially advance the clinical application of HIFU for the treatment of malignant lesions.

Glossary of abbreviations and acronyms

ADC	apparent diffusion coefficient
AIF	arterial input function
ANOVA	analysis of variance
APT	amide proton transfer
ASL	arterial spin labeling
BOLD	blood oxygenation-level dependent
CA	contrast agent
CE-MRI	contrast-enhanced MRI
CEST	chemical exchange saturation transfer
DCE-MRI	dynamic contrast-enhanced MRI
EM	equivalent minutes
EPI	echo planar imaging
FA	flip angle
FOV	field-of-view
GE-EPI	gradient-echo echo planar imaging
GUI	graphical user interface
H&E	haematoxylin and eosin
HIFU	High Intensity Focused Ultrasound
ISODATA	Iterative Self Organizing Data Analysis
IVIM	intravoxel incoherent motion
k_{ep}	transfer constant from interstitial space to blood plasma
K^{trans}	transfer constant from blood plasma to interstitial space
MRF	magnetic resonance fingerprinting
MR-HIFU	magnetic resonance-guided high intensity focused ultrasound
MRI	magnetic resonance imaging
MRS	magnetic resonance spectroscopy
MT(R)	magnetization transfer (ratio)
NA	number of averages
NADH	nicotinamide adenine dinucleotide
NOE	nuclear overhauser effect
NPV	non-perfused volume
NSF	nephrogenic systemic fibrosis
PET	positron emission tomography
PRESS	point-resolved spectroscopy
PS	phosphatidylserine
RF	radiofrequency
ROI	region of interest
SAR	specific absorption rate

SD	standard deviation
SE	signal enhancement
SI	similarity index
SNR	signal-to-noise ratio
T_1	longitudinal relaxation time
$T_{1\rho}$	longitudinal relaxation time in the rotating frame
T_2	transverse relaxation time
TE	echo time
TIPS	therapy imaging probe system
TR	repetition time
US	ultrasound
v_e	extravascular extracellular fraction
VEGF	vascular endothelial growth factor

List of publications

Full papers

Hectors SJ, Jacobs I, Strijkers GJ, Nicolay K. Automatic segmentation of murine subcutaneous tumors by multiparametric MR analysis based on endogenous contrast. *Magn Reson Mater Phy* 2014;doi:10.1007/s10334-014-0472-1

Hectors SJ*, Jacobs I*, Strijkers GJ, Nicolay K. Multiparametric MRI Analysis for the Identification of High Intensity Focused Ultrasound-treated Tumor Tissue. *PLoS One*. 2014;9(6):e99936

Hectors SJ, Moonen RP, Strijkers GJ, Nicolay K. $T_{1\rho}$ mapping for the evaluation of High Intensity Focused Ultrasound tumor treatment. *Magn Reson Med*. 2014;doi:10.1002/mrm.25269

Hectors SJ, Jacobs I, Strijkers GJ, Nicolay K. Amide proton transfer imaging of High Intensity Focused Ultrasound-treated tumor tissue. *Magn Reson Med*. 2014;72:1113-22.

Kluza E, Jacobs I, **Hectors SJ**, Mayo KH, Griffioen AW, Strijkers GJ, Nicolay K. Dual-targeting of $\alpha\beta 3$ and galectin-1 improves the specificity of paramagnetic/fluorescent liposomes to tumor endothelium in vivo. *J Control Release*. 2012;158:207-14

Moonen RP, van der Tol P, **Hectors SJ**, Starmans LW, Nicolay K, Strijkers GJ. Spin-Lock MR enhances the detection sensitivity of superparamagnetic iron oxide particles. *Magn Reson Med*. In press.

Hectors SJ*, Jacobs I*, Schabel MC, Strijkers GJ, Nicolay K. Cluster analysis of DCE-MRI-derived pharmacokinetic parameters to identify regional vascular changes after tumor treatment with High Intensity Focused Ultrasound. Under review.

Hectors SJ, Jacobs I, Moonen CT, Strijkers GJ, Nicolay K. MRI methods for the evaluation of High Intensity Focused Ultrasound tumor treatment – current status and future needs. Under review.

Hectors SJ*, Jacobs I*, Heijman E, Keupp J, Berben M, Strijkers GJ, Gröll H, Nicolay K. Multiparametric Magnetic Resonance Imaging analysis for the evaluation of Magnetic Resonance-guided High Intensity Focused Ultrasound treatment. Under review.

Conference proceedings (first author only)

Hectors SJ, Jacobs I, Keupp J, Berben M, Berben M, Strijkers GJ, Grüll H, Nicolay K, Heijman E. Identification of MR-HIFU Ablated Tumor with Multi-parametric MR Analysis at 3T.

Focused Ultrasound 2014 - 4th International Symposium, North Bethesda, USA (poster).

Hectors SJ, Moonen RP, Strijkers GJ, Nicolay K. $T_{1\rho}$ mapping for the evaluation of High Intensity Focused Ultrasound Tumor treatment.

ISMRM 22nd Meeting & Exhibition 2014, Milan, Italy (poster, **magna cum laude merit award**)

6th Benelux ISMRM Meeting 2014, Maastricht, The Netherlands (poster)

Hectors SJ, Moonen RP, Strijkers GJ, Nicolay K. $T_{1\rho}$ mapping for the MRI-based evaluation of High Intensity Focused Ultrasound Tumor treatment.

International Society for Therapeutic Ultrasound meeting 2014, Las Vegas, USA (oral)

Hectors SJ, Jacobs I, Strijkers GJ, Nicolay K. Endogenous MRI biomarkers for the evaluation of HIFU tumor treatment.

International Society for Therapeutic Ultrasound meeting 2014, Las Vegas, USA (poster)

Hectors SJ, Jacobs I, Strijkers GJ, Nicolay K. Amide Proton Transfer Imaging of High Intensity Focused Ultrasound-treated Tumor Tissue.

ISMRM 21st Meeting & Exhibition, 2013, Salt Lake City, USA (oral, **magna cum laude merit award**)

5th Benelux ISMRM Meeting 2013, Rotterdam, The Netherlands (poster)

Hectors SJ, Jacobs I, Strijkers GJ, Nicolay K. Automatic Tumor Delineation by Multiparametric MR Analysis based on Endogenous Contrast.

ISMRM 21st Meeting & Exhibition 2013, Salt Lake City, USA (poster)

Hectors SJ, Jacobs I, Strijkers GJ, Nicolay K. MRI biomarkers for the identification of High Intensity Focused Ultrasound-treated tumor tissue.

TOPIM – ESMI Winter Conference 2013, Les Houches, France (poster)

Hectors SJ, Jacobs I, Strijkers GJ, Nicolay K. Identification of High Intensity Focused Ultrasound treated tumor tissue by Amide Proton Transfer Imaging

OctoberCEST 2012, Annapolis, USA (oral)

Hectors SJ, Jacobs I, Strijkers GJ, Nicolay K. Identification of High Intensity Focused Ultrasound treated tumor tissue using a multiparametric MRI protocol and ISODATA analysis.

ESMRMB 2012, Lisbon, Portugal (oral)

Hectors SJ, Jacobs I, Strijkers GJ, Nicolay K. Identification of High Intensity Focused Ultrasound treated tumor tissue using a multiparametric MRI protocol and ISODATA analysis.

ISMRM 20th Scientific Meeting & Exhibition 2012, Melbourne, Australia (poster)
4th Benelux ISMRM Meeting 2012, Leuven, Belgium (oral)

Hectors SJ, Jacobs I, Strijkers GJ, Nicolay K. MRI assessment of tumor tissue status after High Intensity Focused Ultrasound ablation.

MR-guided Focused Ultrasound Therapy 2011, Rome, Italy (poster)

Hectors SJ, Jacobs I, Strijkers GJ, Nicolay K. MRI assessment of tumor tissue status after High Intensity Focused Ultrasound ablation.

Therapeutic Ultrasound Winter School 2011, Les Houches, France (poster)

Hectors SJ, Jacobs I, Strijkers GJ, Nicolay K. MRI assessment of tumor tissue status before and after High Intensity Focused Ultrasound ablation.

Biomedica 2011, Eindhoven, The Netherlands (poster, **poster award**)

Hectors SJ, de Vries A, Strijkers GJ, Nicolay K, Grüll H. Paramagnetic polymersomes and polymeric micelles for image-guided drug delivery.

2nd Benelux ISMRM Meeting 2010, Utrecht, The Netherlands (oral)

* authors contributed equally

Acknowledgements / dankwoord

Na ruim 4 jaar promotieonderzoek ligt dan hier het resultaat in de vorm van mijn proefschrift. Ik kijk met veel plezier en trots terug op de afgelopen jaren. Een aantal mensen die tijdens mijn promotie een belangrijke rol gespeeld hebben wil ik persoonlijk bedanken.

Allereerst mijn promotor: beste Klaas, bedankt dat u mij de mogelijkheid geboden heeft om in uw groep te promoveren. Ik heb het zeer gewaardeerd dat ik van u alle vertrouwen en vrijheid gekregen heb om mijn onderzoek grotendeels zelfstandig uit te voeren. U bent altijd nauw betrokken geweest bij het onderzoek en ik kon altijd rekenen op bewonderingswaardig snelle en waardevolle correcties op manuscripten. U geeft leiding aan een vakgroep om trots op te zijn.

Gustav, ook jou wil ik bedanken voor de begeleiding tijdens mijn promotieproject. Tijdens de reguliere voortgangsbesprekingen kwam je vaak met goede ideeën wat betreft data-analyse, die de presentatie van de soms toch wel erge vele data net wat overzichtelijker maakten. Ik wil je veel succes wensen in Amsterdam en ik zal je vast in de komende jaren nog wel tegenkomen ofwel in New York of bij de ISMRM.

I would also like to thank the members of my PhD committee, prof. dr. Wladyslaw Gedroyc, dr. Uulke van der Heide, prof. dr. Josien Pluim, prof. dr. Hanneke van Laarhoven, prof. dr. Chrit Moonen and prof. dr. Arend Heerschap. Thank you for reviewing this thesis and for taking part in the committee.

Igor, ik kijk met veel plezier terug op onze intensieve samenwerking de laatste jaren. We vormden altijd een goed team met complementaire vaardigheden. We hebben samen vele avonden en weekenden bij de scanner gezeten. Al dat werk heeft toch maar mooi tot drie, of inmiddels misschien wel vier, succesvolle studies geleid! Ook hebben we samen wat leuke congressen mee kunnen 'pikken' met als hoogtepunt de ISTU in Las Vegas! Daar bleek dat we beiden toch wat gevoelig zijn voor een gokverslaving ;-). Ik wil je veel succes wensen tijdens je postdoc in onze groep en later ook in je verdere carrière!

Rik, het zal erg wennen zijn om je na ruim 10 jaar niet meer elke werkdag te zien. We zijn tegelijk met BMT begonnen, in hetzelfde jaar nog in hetzelfde studentenhuis gaan wonen en vervolgens in dezelfde groep afgestudeerd en gepromoveerd. Erg leuk dat we ook nog samen hebben kunnen werken met de $T_{1\rho}$ projecten. Ik hoop dat we in de toekomst nog vaak met zijn vieren (Ralf, Lieke, jij en ik) zullen afspreken. Altijd gezellig!

Met naast Rik en Igor nog drie anderen was het in onze kamer altijd gezellig druk. Tom, met Igor en mij vormde jij het ijzersterke 'tumorteam'. Het was altijd erg handig om snel met elkaar te kunnen overleggen, al zal de rest daar wellicht anders over denken ;-). Met

zijn drieën skiën, of eigenlijk op congres, in Les Houches was erg geslaagd! Ik wens je veel succes met de rest van je promotie! Valentina, it was nice to have another woman in our room. I always enjoyed your 'Italian temperament'. Jo, als biotechnicus in een kamer vol met aio's was je wellicht een beetje een vreemde eend in de bijt. Je mooie, enthousiaste verhalen over de vogels en je sportieve activiteiten waren echter altijd een fijne afwisseling tussen het harde werken door.

Ook de andere biotechnici mogen zeker niet vergeten worden. Leonie en David, de meeste biotechnische handelingen heb ik zelf gedaan, maar van jullie heb ik de fijne kneepjes van het vak geleerd. Daarnaast was het erg prettig om een back-up te hebben als het aanpakken eens niet lukte. Bedankt daarvoor!

Ik wil ook de andere (oud-)collega's van de Biomedical NMR groep hartelijk bedanken voor de geweldige tijd die ik hier heb gehad! Ondanks dat de samenstelling van de groep vaak verandert omdat er telkens weer mensen gepromoveerd zijn of juist gaan promoveren, blijft de groep onveranderd hecht.

Een verhuizing van het lab tijdens je promotietraject is niet ideaal te noemen. Toch opende de verhuizing naar de High Tech Campus ook weer nieuwe mogelijkheden. Ik ben er trots op dat ik heb mogen werken aan een van de projecten die CIRE heeft voortgebracht. Edwin, bedankt voor je tomeloze inzet tijdens de 'multiparametrische 3T studie'. De studie heeft een lange aanloop gehad door allerlei issues met de sequenties, maar gezien de resultaten is het het wat mij betreft allemaal waard geweest. Jochen, thank you for the useful discussions regarding the APT measurements. Holger, bedankt voor de nuttige commentaren die we van jou kregen op de manuscripten. Het heeft bij Igor en mij weer tot extra inzichten geleid. Monique, je hulp bij de histologische validatie van deze studie is van onschatbare waarde voor ons geweest. Ook wil ik Caren, Carlijn, Marije en Marleen bedanken voor de biotechnische ondersteuning.

Tijdens mijn promotie heb ik ook een aantal studenten begeleid. Nils, Renske, Tom, Evi en Ronald, ondanks dat de resultaten van jullie projecten niet direct in dit proefschrift terug te vinden zijn, heeft jullie werk zeker extra inzicht gegeven in de verandering in MRI parameters na de HIFU behandeling. Ik vond het ook erg leuk om betrokken te zijn bij het project van de studenten die meededen met de iGEM competitie.

Het CTMM Volta consortium heeft wat deuren geopend richting klinische translatie. Roel, Laura en Wilbert, bedankt voor de nuttige discussies wat betreft de implementatie van de MRI sequenties. De automatische segmentatie van borsttumoren op basis van endogene contrastmechanismes bleek, deels naar verwachting, behoorlijk complex. Zowel het aantal datasets als de tijd bleken toch wat te beperkt om dit project tot een succes te maken. Helaas zijn de resultaten hiervan dan ook niet in het proefschrift terecht gekomen.

Ondanks dat het werk regelmatig ook in de avond en in het weekend doorging, heb ik toch geprobeerd om genoeg tijd vrij te maken voor mijn familie en vrienden. Annick en Véronique, jullie ken ik allebei al bijna heel mijn leven. Ik vind het leuk dat we nog steeds zo leuk met elkaar omgaan, terwijl onze levens toch heel verschillend zijn. Esther en Anouk, jullie zijn later 'ingestroomd', maar brachten gelijk ook een hoop gezelligheid! Met zijn vijven vormen we een hecht clubje. De volgende hap-stapavond houden we in New York! Ook de mannen mogen natuurlijk niet vergeten worden: Tijn, Joost, Jean Michel, Dennis en Daan, bedankt voor alle gezelligheid!

Ook in Eindhoven was er altijd genoeg ruimte voor ontspanning. De donderdagborrel halen werd toch wat lastiger door de verhuizing naar de HTC, maar ook de etentjes achteraf waren altijd de moeite waard! Helaas moeten we het nu zonder onze gangmaker Youri stellen. Alexander, Sander, Rik, Fianne en Jasper, bedankt!

Daarnaast ben ik ook gezegend met een hechte (schoon)familie. Joep en Rina, bedankt voor alle leuke avondjes bij jullie in de 'wintertuin'! Lars en Mieke, nog heel veel plezier samen in Vancouver en later in Olen. Roel en Marita, ook jullie veel geluk samen in de toekomst! Pa en ma, bedankt voor alle steun, liefde en gezelligheid. Ma, ik hoop dat we er nog regelmatig een weekendje samen op uit kunnen trekken! Robbert en Linda, jullie mogen trots zijn op jullie mooie gezin! Lize en Veerle maken mij een trotse tante.

Ralf, op het moment van schrijven ben je nog mijn vriend/verloofde, maar bij het drukken van het boekje mijn man! Voor jou zijn de laatste jaren misschien ook niet altijd even makkelijk geweest. De eerste zomer dat we samenwoonden heb ik meer in Eindhoven dan in Breda doorgebracht ;-). Je bent altijd mijn steun en toeverlaat geweest en was nooit te beroerd om ook een zondag bij de scanner door te brengen, zodat we elkaar in elk geval toch nog zagen. Ook een ritje naar Eindhoven was nooit een probleem als de treinen niet (meer) reden. Ik kijk uit naar onze toekomst samen, waar die ook is!

Curriculum Vitae



Stefanie Hectors was born on August 11th, 1986 in Roosendaal, The Netherlands. She completed her pre-university secondary education (gymnasium) cum laude in 2004 at the Gertrudiscollege in Roosendaal. In the same year, she started studying Biomedical Engineering at Eindhoven University of Technology, from which she obtained her BSc degree cum laude in 2007 and her MSc degree with great appreciation in 2010. During her Master studies, she performed an internship at the Icahn School of Medicine at Mount Sinai in New York, USA under supervision of prof. dr. Willem Mulder. Her graduation project was performed under supervision of prof. dr. Holger Gröll in the Biomedical NMR group of prof. dr. Klaas Nicolay at the department of Biomedical Engineering at Eindhoven University of Technology. The project focused on the development of paramagnetic polymersomes and polymeric micelles for image-guided drug delivery. In 2010, she started as a PhD candidate in the same group. The goal of her PhD project was to identify suitable MRI methods for the planning and evaluation of High Intensity Focused Ultrasound tumor treatment. The results of her PhD research are presented in this thesis. Early 2015 she will start a postdoctoral fellowship at Icahn School of Medicine at Mount Sinai in New York.